SPECTRAL CHARACTERIZATION OF ACTINIDE SIGNATURES FOR NUCLEAR REMOTE SENSING APPLICATIONS

BY

EMILY NELUM WEERAKKODY

DISSERTATION

Submitted in partial fulfillment of the requirements
for the degree of Doctor of Philosophy in Mechanical Engineering
in the Graduate College of the
University of Illinois Urbana-Champaign, 2021

Urbana, Illinois

Doctoral Committee:

Professor Nick G. Glumac, Chair and Director of Research
Professor Emeritus Herman Krier
Associate Professor Kelly Stephani
Professor M. Quinn Brewster
Associate Professor Mark Phillips, University of Arizona

ABSTRACT

It is of interest to the defense community to develop new ways to assess a nuclear event at a distance. Distinguishing between a nuclear and non-nuclear fireball and determining the nuclear material and amount present in the fireball are necessary to inform response accordingly. Spectroscopy provides potential avenues for remote detection of nuclear material, and methods can be developed to monitor nuclear proliferation. In this work, signatures of interest are determined for spectroscopic probing of the nuclear fireball. These signatures and their variation with temperature and other environmental factors yield insight into fundamental processes occurring within the nuclear fireball and can be used to generate predictive models that simulate spectra that may be produced from potential devices.

This dissertation focuses on spectral signatures that may be generated from the actinide material and strongly emitting fission products in a nuclear fireball free from the interference of high explosives and engineering materials that may be present in the fireball produced from a conventional weapon. Experiments were performed to determine emission and absorption signatures that result when uranium is subjected to excitation under different conditions (shock tube heating, laser ablation, dust cloud combustion). Using a figure of merit approach to predict which fission product signatures would emit most strongly, selected products assembled in mixtures of varying proportion were subjected to varying degrees of excitation by unconventional and conventional explosives to observe the resulting signatures.

Laser ablation of uranium from prior work aided in the identification of signatures for further study. In controlled conditions reminiscent of the high-temperature, early time nuclear fireball, shock tube heating of uranium powder was performed to determine the appearance and variation of atomic signatures at high temperatures. Dust cloud combustion experiments provided some insight into lower temperature conditions in which uranium does not combust in the vapor phase due to strong oxide containment, thereby producing no emission or absorption signatures. This highlighted the effect of method of excitation on the appearance of U signatures since signatures did appear in laser ablation testing in similar temperature regimes, but were condensing from a high-temperature plasma state instead of being heated from room temperature particulate. This further underscored the need for alternative signatures to glean information about the actinide from

excitation of fission products. Various formulations, different ratios of Cs and Sr containing carbonates, and two fission product mixtures emulating the fast, independent distributions of U^{235} and Pu^{239}, were excited in flash powders to observe differences in the resulting signatures. Further testing was performed on combinations of Cs and Sr in the presence of varying metals and high explosives to determine if they could be detected and differentiated between at a standoff distance. These formulations could be distinguished between using spectral methods, which proved promising for future remote sensing applications.

From these experiments, uranium particle combustion behavior was characterized, high-temperature uranium emission signatures were obtained, and fission product signatures with the greatest potential for future work were determined.

To my teachers.

"Make it a great day or not, the choice is yours,"

-Principal Jon D. Teuscher, 1950-2016,

Exemplar of an educator who made a positive impact.

ACKNOWLEDGEMENTS

First and foremost, I would like to thank Professor Nick Glumac for inviting me to work in this research group as an impressionable sophomore. I have no regrets. As an undergraduate, I was afforded the opportunity perform my own experiments and set off bombs in fields, and as a graduate student I have been allowed to collaborate on a variety of experiments with experts in the fields of energetics and nuclear fireball chemistry. I am immensely grateful for this experience and owe it all to his guidance.

I would not have been able to get this far without the support of my family. My parents instilled the value of education in me at a young age, and frankly, I needed to keep up with my cousins. I would also like to thank my proverbial 'village' for their support all these years.

Furthermore, this would not have been possible without the friendship and camaraderie of the many graduate students that have been here during my tenure. Austin Butler, Damon Chen, Michael Ho, and Lt. Will Morningstar have made these last few semesters of dissertation work go a lot more smoothly, always answering my questions regarding 'whether this thing looks okay' or 'if these words make sense in this order,' and making sure I got home okay after late nights at work. They have truly made my last few months in Chambana enjoyable despite the pandemic. Dr. LtCdr. (USN, ret.) Dave Amondson, Rylie Lodes, Nick Poirier, Dr. Adam Sims, Tearants Yu, Joel Schwallaby, Lt. Daniel Meaney, and Brian Read made my time here all the better. I will always remember fondly our road trips, crossword breaks, and cookouts.

I also owe my 'army of undergrads' a debt of gratitude. Some supported the work detailed in this document directly, and others assisted in completing much needed projects around the lab that made all of our lives easier. Specifically, Grace Lu, Avinash Rao, Avery K. Moore, Sara Jiang, and Mason Rosenberg were instrumental in conducting shock tube experimentation. Alexandra Baumgart, John Venetos, Mary Cate Foley, Alex Torres-Soto, and Michael Schroeder helped orchestrate major updates to the shock tube facility. Matthew Lotarski and many others were a joy to work with over the years.

To my dear friends Rohit Gupta, Georgi Hristov, Prateek Ranjan, Armando Collazo, Vanessa Awate, Christopher Colletti, Michelle Gray, Daphne Lodes, Cary Butler, Kevin Murphy, and

Sharanya Subramaniam—thank you for the movies, trivia, karaoke, dancing, and so many fun times that kept me sane.

Thank you Pranith Lomada, Eleni Georgiadis, Alexandra Baumgart, Maya D'Souza, and Morgan Aavang for ceaselessly being my cheerleaders and confidants from afar, and thanks to Nick Scott, Sullivan Figurskey, Connor Dion, Yamen Mubarak, and Alexander Winter for making me take Tuesday nights off this year.

I was lucky enough to have the opportunity to be an intern at Lawrence Livermore National Laboratory this past couple years. I would like to thank Evan Kahl and David Weisz for their incredible mentorship and encouragement as well as Bill Clark and Kim Knight.

I am grateful to Professor Emeritus Herman Krier for proofreading this document and for his valuable perspective on research and life.

Thanks to researchers at CRAFT Tech, Indian Head Naval Surface Warfare Center, and Sandia National Laboratories for their helpful collaboration at various points throughout my dissertation work, especially with field testing. Thanks also to Catherine Wallace of the Beckman Institute Imaging Technology Group for assistance with ESEM and STEM imaging.

This work was completed under funding from DTRA Grant HDTRA1-17-1-0026 and the Materials Science in Extreme Environments University Research Alliance (MSEE URA). The project or effort depicted was or is sponsored by the Department of the Defense, Defense Threat Reduction Agency under award HDTRA1-20-2-0001. The content of the information does not necessarily reflect the position or the policy of the federal government, and no official endorsement should be inferred.

TABLE OF CONTENTS

LIST OF FIGURES

LIST OF TABLES

CHAPTER 1: INTRODUCTION AND MOTIVATION

1.1. Motivation

There is a need to develop methods to remotely detect and evaluate nuclear events real-time in order to inform response accordingly. There is a further need to distinguish between conventional and nuclear explosions and monitor nuclear weapon proliferation. Spectroscopic methods can be applied to the development of the necessary technologies to do so. Furthermore, such diagnostics may provide insight into the inner machinations of a nuclear fireball, which despite decades of study are still not fully understood.

Laboratory testing can be used to emulate various temperature regimes and conditions in the nuclear fireball in order to characterize reaction mechanisms that can occur and determine what spectroscopic signatures may appear from these processes. Data from this experimentation can be applied to the development of predictive models for signatures from potential nuclear devices.

Furthermore, this research will shed light on fundamental processes that may occur in the nuclear fireball, such as rapid oxidation of uranium, appearance of fission product signatures, and condensation of products formed in the nuclear fireball into higher oxides—information which is of interest to both the scientific and defense communities.

1.2. Historical Background

With Henri Becquerel's discovery of radioactivity and Marie and Pierre Curie's discovery of certain radioactive materials, scientists hoped that this may provide a source of energy among other potential uses. Decades later, Leó Szilárd posited a neutron-induced chain reaction, and fission and radioactivity were observed by several researchers (Irene and Frederic Joliot-Curie, Otto Hahn, Fritz Strassmann, and Enrico Fermi). When war broke out years later, this phenomenon was harnessed in the development of early nuclear weapons, culminating in the Manhattan Project during World War II [1], [2].

J. Robert Oppenheimer spearheaded this effort to create a weapon that utilized fission to create a highly energetic output [3]. This was a collaboration between a number of entities in the USA, UK, and Canada, which led to the Trinity test—the first nuclear detonation—in New Mexico, and

a month later, Hiroshima and Nagasaki. Amidst Cold War tensions, the US and USSR built up their respective nuclear arsenals [4]. Since then, multiple countries have developed their own nuclear weapons programs, including some outside of the Non-Proliferation Treaty of 1968, of which 191 countries are signatories [5], [6]. In recent years, there has been some concern that nuclear material may fall into the wrong hands and be used to create crude weapons for use in terrorist activity. It is thus useful to be able to determine the composition of detonated weapon at a safe standoff distance so that first responders can act accordingly.

The Comprehensive Nuclear Test Ban Treaty in 1996 banned the testing of nuclear weapons in all environments after previous attempts to limit testing over preceding decades [7]. Thus, further study of the nuclear fireball has largely focused on the development of predictive models which can be validated by other experimental methods, such as those employed herein.

1.3. The Nuclear Fireball

There are a series of events that occur in a nuclear detonation that could give rise to emissions of interest to this work. The initial charge could contain actinide material, a term which refers to a subset of elements in the periodic table which exhibit radioactive properties (Section 2.2) [8]. It may also contain high explosives (HEs) or engineering materials like steel. When the device is initially detonated, it appears as an immensely bright, ‘glassy’ sphere, which develops into an opaque shock front that expands rapidly, atomizing and ionizing everything in its wake [9]. Fission occurs in the actinide material. Just behind the shock are high-temperature gaseous products, and within that is a fireball of burning condensed products, which starts to become visible from outside of the event as the opaque shock front dissipates. The fireball continues to burn and expand, incorporating materials from the surrounding environment (land or air). The relations that govern this shock expansion as well as temperature and pressure distribution over the fireball are discussed at length in these works [9], [10]. This process is illustrated in Figure 1.1.

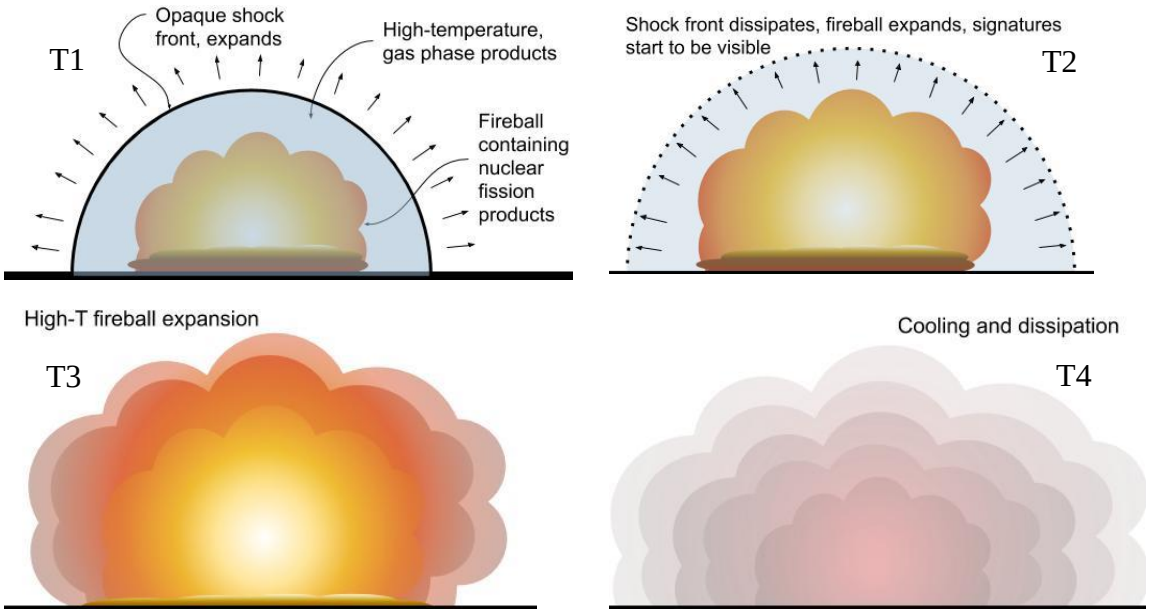

Figure 1.1: Simplified schematic of nuclear fireball. T# denotes sequential time values.

From this series of events, a number of signatures could be expected to appear from any of the materials present in the explosion. There could be atomic or molecular signatures from the actinide material (i.e. U I, U II, UO, etc.), fission product signatures (Zr, Mo, Cs, Sr, etc.), signatures from the high explosives and engineering materials used to construct a device, as well as any compounds these materials may form with the surrounding environment (silicides, etc.). These signatures will also be time-variant as various constituents dissociate and form other products.

Due to the almost unfathomably high-energy resulting from nuclear interactions like fission (Section 2.4.1) or fusion (as opposed to chemical reactions like in high explosives), incredibly high temperatures can be achieved in a nuclear fireball (Figure 1.2) [9], [11].

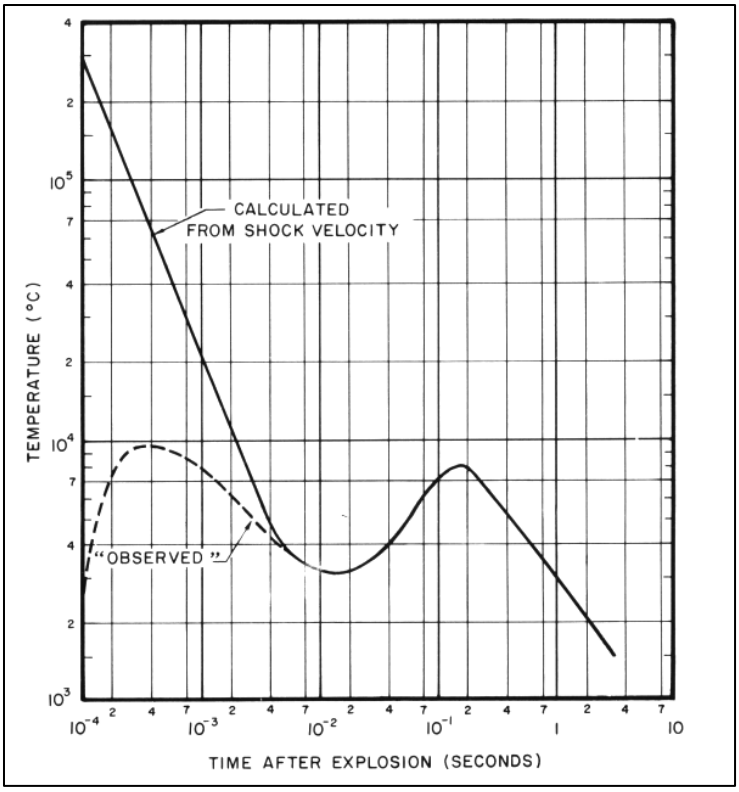

Figure 1.2: Temperature versus time in a nuclear explosion [12].

At early times, temperatures are on the order of 100000s of Kelvin and rapidly decrease. A later peak in temperature is in the 1000s of Kelvin. Higher temperatures engender more populated spectral energy levels and therefore more emission signatures. By performing experiments including the materials of interest and excluding those that might be found in a conventional weapon (high explosives and engineering materials) in relevant conditions, useful signatures can be determined, and diagnostics can be developed to target these.

This description barely begins to scratch the surface of the complex transient thermofluidic environment that constitutes the nuclear fireball, and merely focuses on potential spectral signatures emitted. Detailed descriptions of nuclear weapons effects in terms of thermal and nuclear radiation, shock growth and dissipation, and associated aftereffects have long been studied [9], [10]. Various effects produce additional measurable quantities that have been leveraged for detection of nuclear explosions in the past.

1.4. Prior Methods of Detection

There are several diagnostics that have been employed for decades to detect nuclear events and diagnose them after the fact. These include sampling techniques (air and radioactive debris), remote detection of the characteristic double flash from the interaction of the fireball and shock wave, as well as the radioactivity and electromagnetic interference produced by the event. The event is so energetic that it also creates seismic waves, which can be leveraged for detection of underground testing (Figure 1.3). X-rays—the high energy source of the shock wave's initial opacity—and other electromagnetic radiation can also be detected using both passive and active methods. Gamma-ray and neutron emission from the device and fission can be measured, and the attenuation of X-rays, gamma-rays, or neutrons can be observed [13].

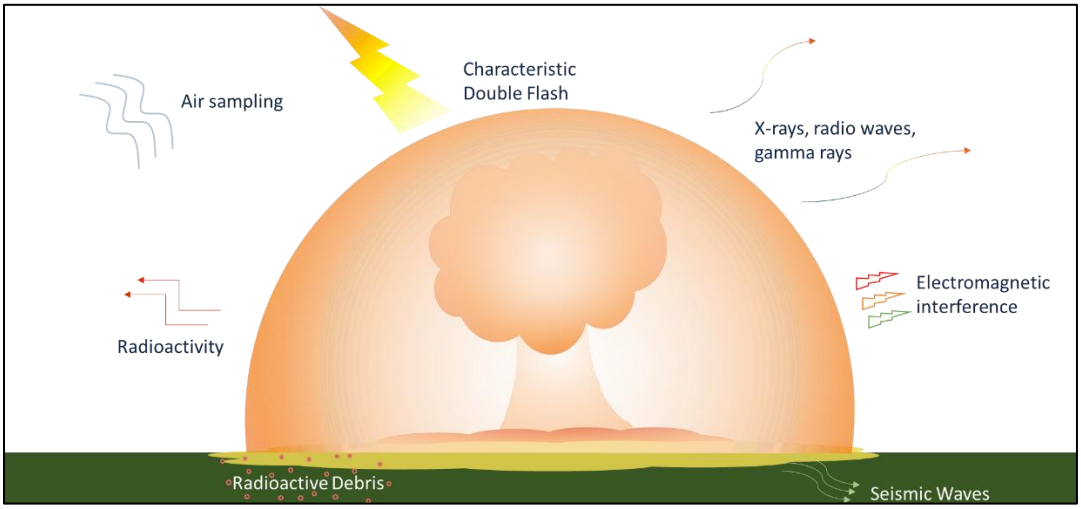

Figure 1.3: Previous nuclear detonation detection methods.

Even radio and acoustic signatures can be observed. All of these techniques have their own pitfalls and generally cannot be used to observe processes occurring real-time inside of the nuclear fireball. Seismic wave detection is subject to imperfections in the Earth's crust. Some electromagnetic waves are subject to attenuation by elements in the atmosphere and can be confused with those produced by lightning. Sampling can only be performed after and in some proximity to the event and therefore does not yield real-time information. Some of these signals do not allow for easily distinguishing between a nuclear and conventional weapon, and others require the use of multiple diagnostics to pinpoint signals from afar [14]. Perhaps targeting carefully selected spectroscopic

signals from materials in a nuclear event will yield useful information free from some of the complications involved with other detection methods.

1.5. Overview of Methodology

In this work several experiments are undertaken to emulate various temperature regimes and conditions in a nuclear fireball in order to determine the appearance of spectral signatures of interest for future remote sensing applications. In previous work laser ablation absorption experiments on uranium were used to study the appearance of high-temperature (10000s K) signatures as well as how they vary in the presence of different amounts of oxygen [15]. Calculations were performed to quantify the amount of uranium monoxide present in previously taken measurements. To investigate lower temperature signatures, uranium powder was combusted using a dust cloud apparatus. Here, temperatures in the low 1000s of Kelvin could be achieved. When uranium signatures did not appear at all under these conditions, a controlled temperature study using the Talbot 13 heterogeneous shock tube facility was used to observe uranium emission at temperatures ranging from 2000-9000 K. From these tests, a general temperature range in which uranium signatures could be observed was determined (> 6000 K). Further tests with higher temporal resolution were performed to determine the temperature and time-resolved development of species' signatures in the high-temperature shock environment as well as to validate temperatures achieved in prior testing. Here, high-temperature early time uranium signatures could be isolated from the late time iron impurity signatures and better evaluated. In tests where uranium particulate was excited from room temperature (shock heating and dust cloud explosions), uranium emissions were not observed until higher temperatures where uranium was no longer protected by oxide and entered the vapor phase; whereas, in laser ablation, U signatures persisted to these lower temperatures, having no such obstacle. Alternate signatures were also explored as indicative of the presence of actinide material in a nuclear fireball.

Since fission products would also be present in a nuclear fireball, selected signatures were studied based on calculations involving detection limits and product abundance. Flash powders containing initially selected fission products (Cs and Sr) were ignited to determine if their signatures would appear in high-temperature conditions. When these signals did appear, small-scale explosive charges doped with Cs and Sr were detonated to achieve even higher temperature conditions, which also produced signatures of interest. When these experiments proved successful, larger scale

tests containing Cs and Sr in different proportions were also performed to observe the resulting signatures and determine interference from HE signatures and other engineering materials.

Additional tests were performed to determine the appearance of signatures from other fission products of interest. Mixtures of flash powders concocted emulating different product distributions were ignited, and signatures were observed throughout the visible and NIR regions of the electromagnetic spectrum to determine which signatures appeared most strongly for future testing in higher temperature conditions.

CHAPTER 2: APPROACH

This section details the underlying theory for experiments later discussed in this document.

2.1. Spectroscopy

Spectroscopy is the study of light and matter. Changes in energy state in an atomic or molecule can lead to absorption or emission of light due to conservation of energy. These phenomena can occur in characteristic patterns as governed by quantum mechanical principles [16]. Emission occurs when a species drops from one energy state to another and emits a photon of the same energy as the difference between the two states. Conversely energy of a characteristic frequency can be absorbed by a species in a lower state, which can then transition to a higher state (absorption). Figure 2.1 shows a schematic of various absorption and emission (spontaneous and stimulated) modes and their corresponding Einstein coefficients, which are parameters representative of the probabilities at which these transitions occur.

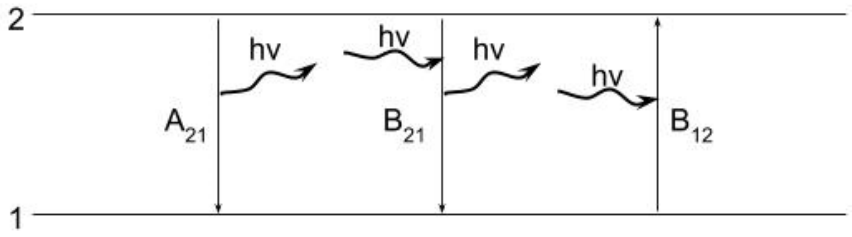

Figure 2.1: Atomic emission and absorption transitions.

A_{21} is the Einstein coefficient of spontaneous emission, B_{21} is the coefficient of stimulated emission (i.e. lasers), and B_{12} is the coefficient of absorption.

There are four forms of excitation/motion in an atom or molecule: translation, rotation, vibration, and electronic. Some of these primarily apply to molecular storage of energy (rotation, vibration). The bulk of this research applies to signatures found in the visible and near UV portions of the electromagnetic spectrum which features many electronic transitions. When changes occur to energy stored in a given atom or molecule, that energy can be absorbed or emitted in the form of photons with energy, E:

$$E = h\upsilon = \frac{hc}{\lambda}$$ *Equation 1*

Here, h is Planck's constant (6.626E-34 Js), ν is the frequency of the transition, λ is the wavelength, and c is the speed of light in vacuum (Equation 1). Due to such factors as energy level distributions and masses and structure of constituents, a given atom or molecule has a characteristic pattern of emission or absorption, and ratios between intensities of the lines produced can be used to determine quantities such as temperature and number density.

Optical spectrometers can be used to observe the patterns formed by emission or absorption of light from the occurrence of these transitions. These are instruments that utilize optics to disperse light so that it may be observed using detectors such as CCDs (charge coupled devices). Light from an experiment can be focused onto an inlet slit which diffracts light into various orders. Using mirrors or lenses and diffraction gratings, a particular range of light can be selected for and focused onto the outlet of a given spectrometer. Focal lengths of optics and grating densities and angles can be modulated to achieve different ranges and resolutions for spectral measurement. Over the years, many permutations of this instrument have been developed for various applications. Figure 2.2 shows a basic diagram of a Czerny-Turner spectrometer with vertical entrance slit, curved mirrors for focusing light onto the grating and the outlet, and an exit aperture. If the exit aperture is a vertical slit, the instrument becomes a monochromator, which selects for a very narrow band of light. Various components of a spectrometer can affect the resolution of the output spectrum, including the width of the entrance slit, the grating density, and the pixel size of the detector chip.

Spectral measurements for this work were primarily performed with Czerny-Turner spectrometers with different dimensions and gratings of various densities to target the desired transitions at appropriate resolutions.

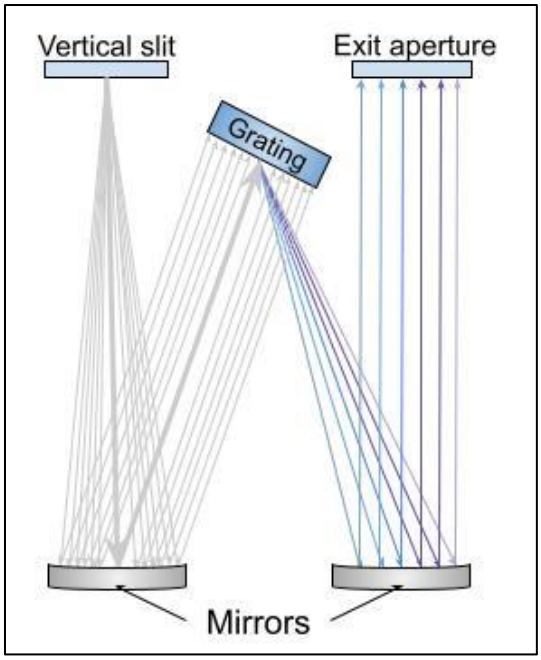

Figure 2.2: Simple spectrometer diagram with reflective grating. The entrance slit diffracts the light which enters the spectrometer into different orders, and the grating diffracts the light into finer resolution and can be adjusted to select the desired output wavelength range.

2.1.1. Boltzmann distribution and temperature determination

As mentioned previously, number density and temperature can be determined from the characteristic spectral patterns formed in the excitation of an atom or molecule. As temperature changes, the populations of different energy levels change; thus, a distribution of species at various energy levels can be correlated to a temperature. An example of spectral change with temperature is shown in Figure 2.3.

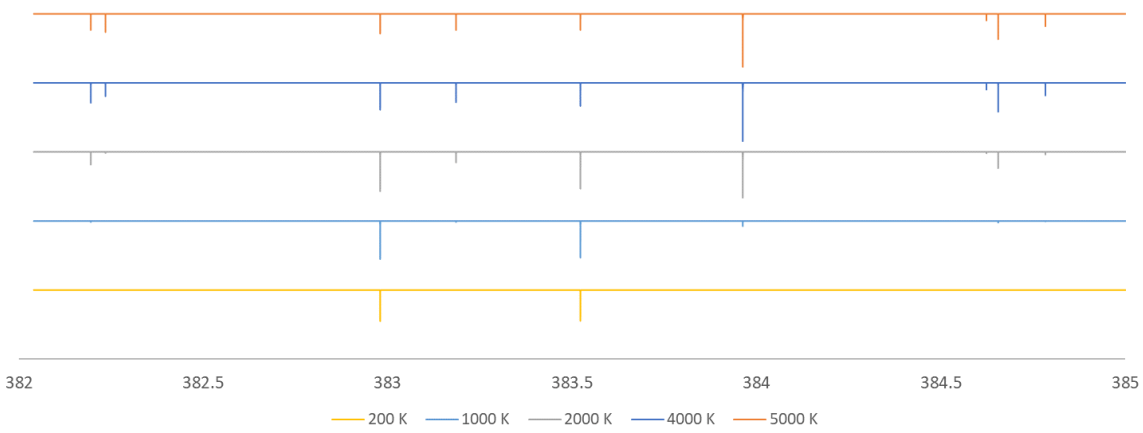

Figure 2.3: Simulated change in U I spectrum with temperature in 382-385 nm range. Reproduced from Ref. [15].

With a known pathlength, number density of a species can be additionally determined from an absorption measurement. Number density can be determined from emission measurements in some cases, but this often requires rigorous calibration or additional assumptions to be made.

The Boltzmann distribution is commonly used to determine temperature from a spectrum given the assumption of local thermodynamic equilibrium, and is of the form:

$$\frac{n_i}{n} = \frac{g_i e^{-\frac{\varepsilon_i}{k_B T}}}{Z} \qquad \textit{Equation 2}$$

Where, n is the total population of the species, n_i is the population of the species at a given energy level, i, g_i is the degeneracy of that level, ε_i is the energy of that level, k_B is the Boltzmann constant T is temperature, and Z is partition function, a number representative of all the possible states of the species (discussed in further detail in Section 4.1). It additionally assumes that the represented constituents do not interact (i.e. combine to form new species) or change in the time frame of the measurement. Using this distribution to calculate temperature requires knowledge of parameters such as energy levels, degeneracies, and Einstein coefficients of the states being transitioned between for a given feature. Temperature is determined by applying Equation 3.

$$T_{el} = \frac{\varepsilon_k - \varepsilon_j}{k_B ln(\frac{g_k n_j}{g_j n_k})} \qquad \textit{Equation 3}$$

An absorption measurement can be taken by using a light source from which the measured species can absorb energy and a spectrometer to read the resulting spectrum. This initially results in a transmission spectrum, which is obtained from dividing the measured spectrum by the original spectrum of the light source (Figure 2.4).

$$T = \frac{I}{I_0} \qquad \textit{Equation 4}$$

Absorbance can then be calculated by taking the negative logarithm of transmittance (Figure 2.4).

$$Abs = -\log_{10} T = -\log_{10} \frac{I}{I_0} \qquad \textit{Equation 5}$$

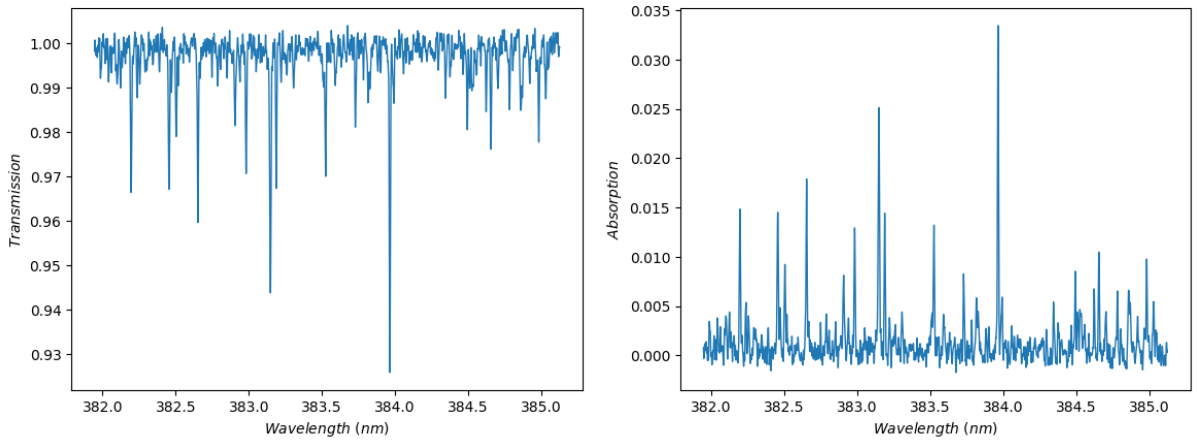

Figure 2.4: Sample transmission (left) and absorption (right) spectra from measurement of a uranium laser ablation plume.

From an absorption measurement, population can be calculated given the integrated area of a transition (Figure 2.5).

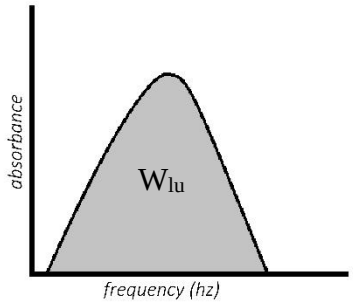

Figure 2.5: Integrated absorption of a peak.

With this measured parameter, W_{lu}, population in a given state, i, can be determined using Equation 6.

$$n_i = \frac{cW_{lu}}{h\upsilon_{ul}B_{lu}L} \qquad \textit{Equation 6}$$

B_{ul} is the Einstein coefficient of absorption. When attempting to determine temperature, these equations can be combined to eliminate parameters like pathlength, L, which may not be known for an emission measurement. If energy level information for appropriately chosen spectral features is plotted against a parameter containing the area underneath the peak, $\ln\left(\frac{W_{lu}*\upsilon_{ul}}{B_{lu}g_l}\right)$, a linear fit can be performed to determine temperature, even for emission measurements. In theory,

only one peak is necessary to determine total population, but multiple lines can be leveraged to determine a more accurate number density [16].

2.1.2. Spectral simulation and databases

The synthetic spectra shown in this work were generated using intensities calculated at various temperatures using line information (i.e. Einstein coefficients, degeneracies, etc.) obtained from spectral databases such as that from Kurucz or NIST (National Institute of Standards and Technology) applied to some of the equations discussed in the previous section. These lines would then be broadened (gaussian) to match the measured data. These synthetic spectra can also be iteratively fit for temperature by using minimizing functions to compare relative strengths of temperature-sensitive lines. Optical thickness was taken into account for initial laser ablation measurements and found to be negligible [15].

The Kurucz Spectral Database was primarily used for calculations and simulations in this work due to its convenient format of tabulation and numerous characterized lines in the near-UV regions studied [17]. NIST's Atomic Spectral Database is more incomplete, with some U I lines identified throughout the VIS and NIR, but further information not characterized [18]. Palmer's Atlas of uranium hollow cathode lines is the most complete, but does not extend into the NIR [19]. Redman did compile a line list which extends into the NIR, but this does not contain Einstein coefficient information [20].

2.2. Actinide Elements

Elements 89-103 are referred to as the actinide elements, named for actinium, which is the first element in the series. This group of metals are in the transition element block and are all radioactive (Figure 2.6) [8]. These materials have primarily been used in nuclear and energy applications since their discovery.

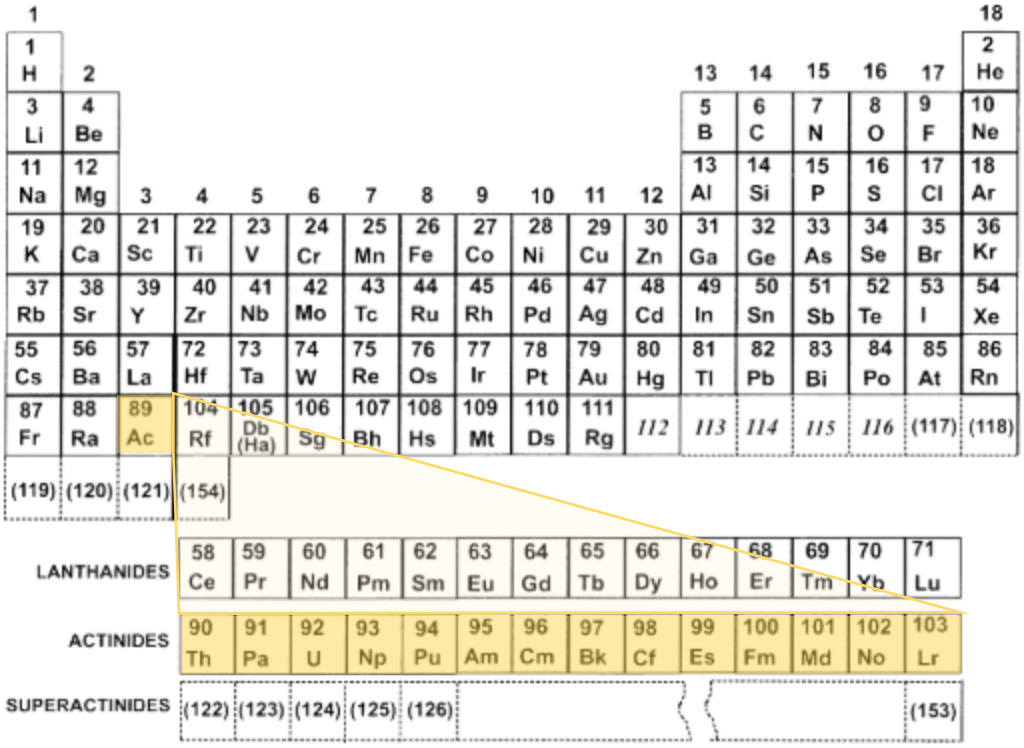

Figure 2.6: Actinide elements on the periodic table. Image adapted from Reference [8].

Of particular interest to this document is uranium, as the appearance of its spectral features and the underlying reasons are discussed. It (like other actinides) is very dense. Uranium is generally reactive, pyrophoric, and readily oxidizes [8], [21]. Its oxide behaves refractorily and in previous testing did not excite in flames of temperatures less than 4800 K [22]. This work does not specify which oxide of uranium is present, but uranium can form several oxides. In condensation from more high temperature, volatile conditions (like a laser ablation plume), UO will form first, followed by UO_2 and subsequently higher oxides, like U_3O_8 [23].

2.3. Uranium Signatures

2.3.1. Laser Ablation

Laser ablation involves focusing a laser beam onto a target material, producing a plasma that can be optically characterized. High-speed, time-resolved, and *in situ* measurements can be used to detect neutral and ion features from atomic and molecular species in both emission and absorption [24]. This technique has been used for a myriad of purposes, ranging from tissue analysis to studying the Martian crust [24]. This plasma environment is considered to be analogous to the

nuclear fireball due to its rapidly induced high-energy, high-temperature conditions and has previously been used to study species of interest to nuclear remote sensing applications. While the laser induced plasma environment is not nearly as energetic as the nuclear fireball, the gas-phase chemistry that occurs in the condensation of a laser ablation plume is similar to that which occurs in the post-detonation nuclear fireball environment.

2.3.1.1. Prior laser ablation study of uranium

Uranium spectral signatures have been catalogued through ablation of uranium powders and ore, as well as uranium-containing soil [25], [26]. These signatures have been investigated under various ambient environments. Skrodzki et al. investigated U absorption and emission features in both N_2 and air at pressures 1-760 torr [27]. Harilal et al. imaged the time-resolved formation of uranium species in a laser plasma in varying air pressure [28]. Time-resolved signatures from different isotopes of uranium have been observed as well [29].

Uranium monoxide has also been studied using laser ablation techniques. Typically, these studies focus on the 593.55 nm band since it tends to emit more strongly than other UO transitions. Mao et al. studied the time-resolved isotopically shifted band in high-resolution as did Weisz et al. [30] [31]. A time-resolved study of the UO band in emission at different oxygen partial pressures was conducted to determine when it would appear and how it would change under these ambient conditions [32]. These plasmas were also spatially imaged for UO and U I emissions. Lower resolution spectra were also obtained in various ambient conditions (Ar, Air, N_2, O_2) [33]. Hartig et al. observed UO formation with trace amounts of O_2 [34]. Time-resolved U I, U II, and UO signatures have been observed in absorption from laser plasmas under various ambient conditions [15], [35]. Figure 2.7 shows an example of some U I and U II transitions tracked for this study [36].

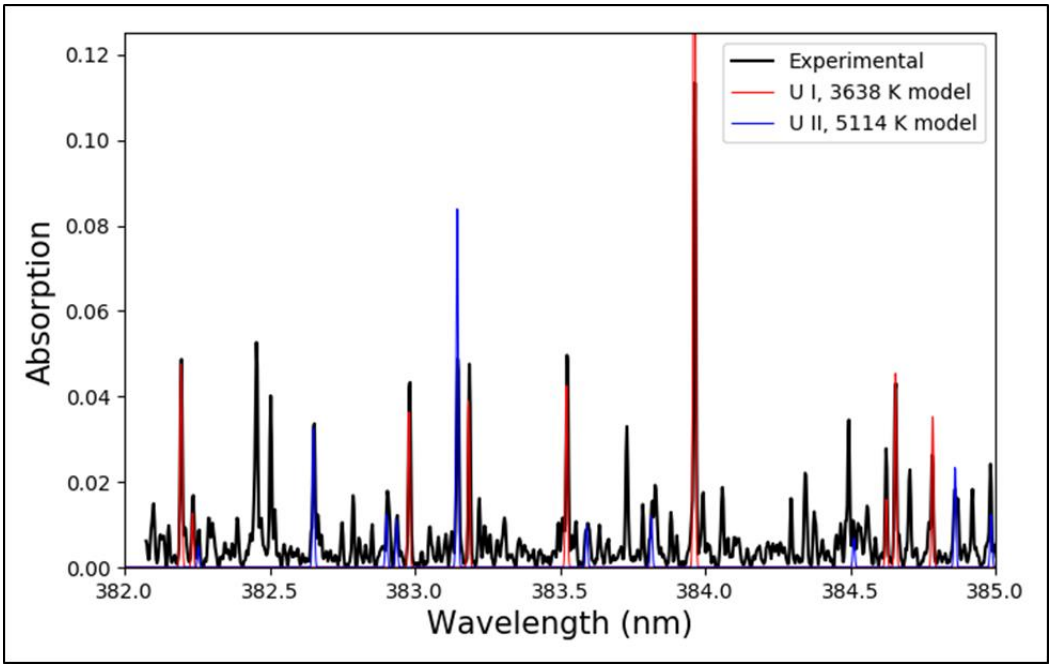

Figure 2.7: Processed absorbance spectrum from Uranium ablation in 15 torr N2 at 7 μs from initial pulse with overlaid model. Red corresponds to U I transitions and blue corresponds to U II transitions [17]. *Unlabeled lines are predominantly attributed to uranium but were not used for calculations* [36].

This methodology was also employed to study a U_3Si_2 sample to study kinetic behavior of the high-temperature U-Si-O system as it might pertain to fractionation processes post-nuclear explosion [37]. Here, the UO band as well as other species were tracked over time as seen in Figure 2.8.

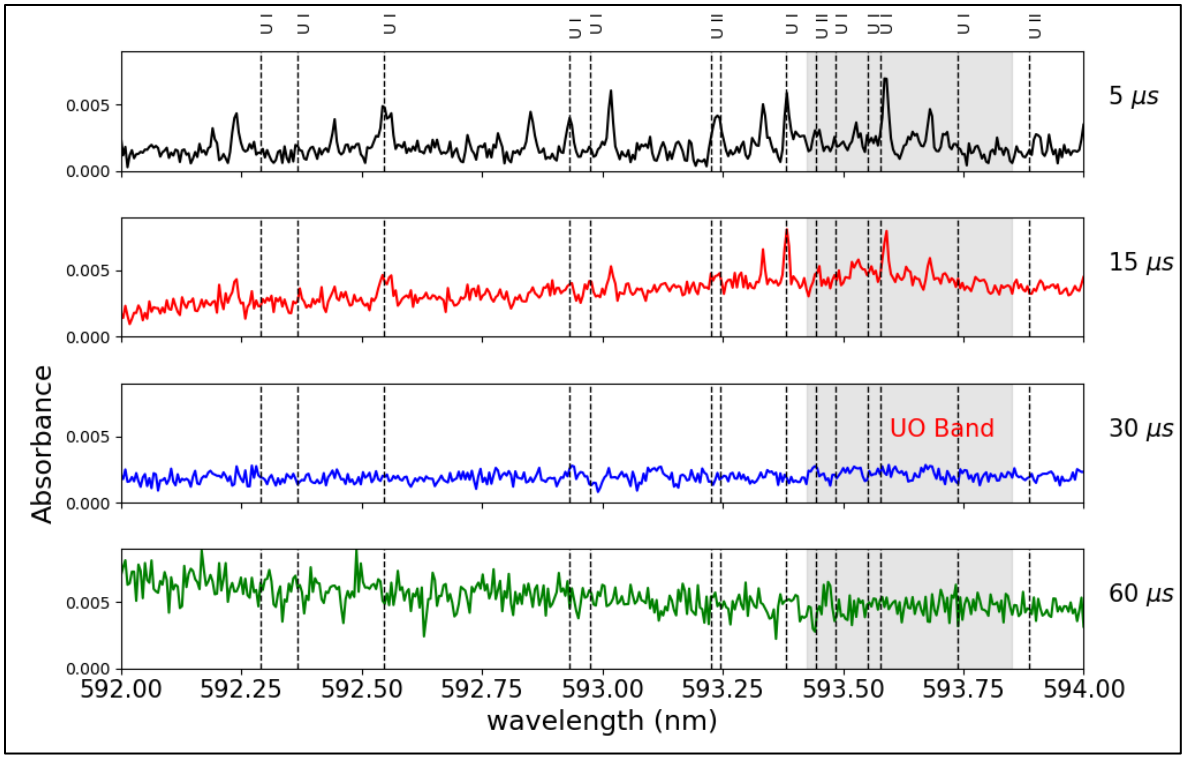

Figure 2.8: Time-resolved absorption spectra for 592-594 nm range observed at 2% O2/98% Ar, 15 torr ambient pressure. The shaded region is the 593.55 nm band, based on determinations by Mao et al. and Harilal et al. [31], [38]–[40]. *U I and U II lines are labeled with dotted vertical lines* [37].

Number densities of U I and U II could be tracked quantitatively, but SiO and UO were tracked in relative terms (Figure 2.9). Due to lack of information about UO, molecular temperature could not be determined (Figure 2.10), but from the temperatures of other species present and the times at which UO appeared, it was concluded that UO forms when the plasma has cooled to around 3000-5000 K.

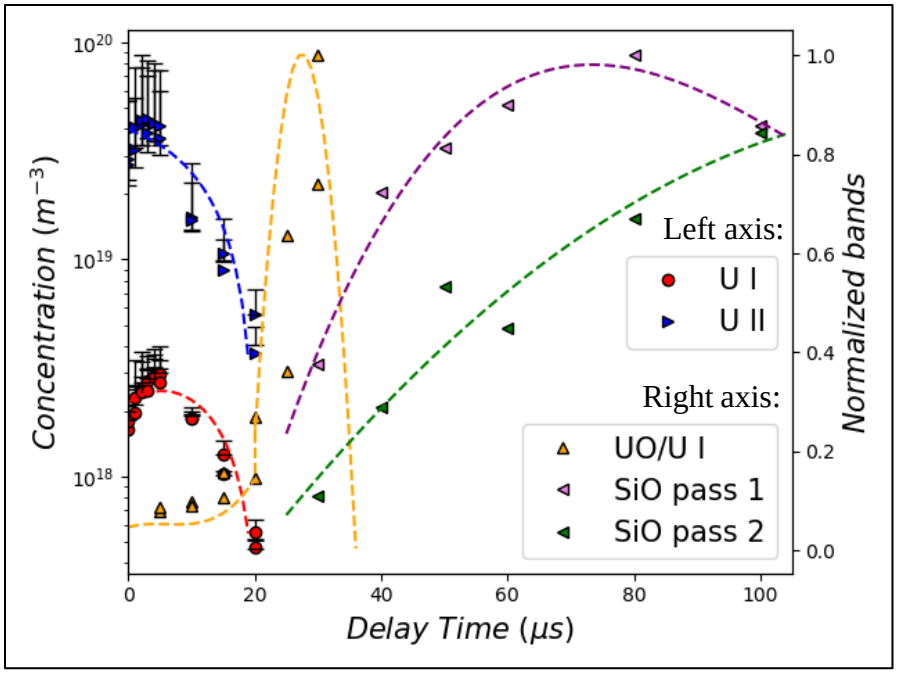

Figure 2.9: Concentration of atomic species (measured from 384-387 nm range, left vertical axis), ratio between UO area and U I 591.54 peak (right vertical axis), and SiO band area (right vertical axis) normalized to background area in absorption versus delay time. Polynomial trend lines are included for ease of visualization of species appearance and decay. Note the logarithmic scale of the left concentration axis. Note also that the SiO data differs in relative intensity between passes [37].

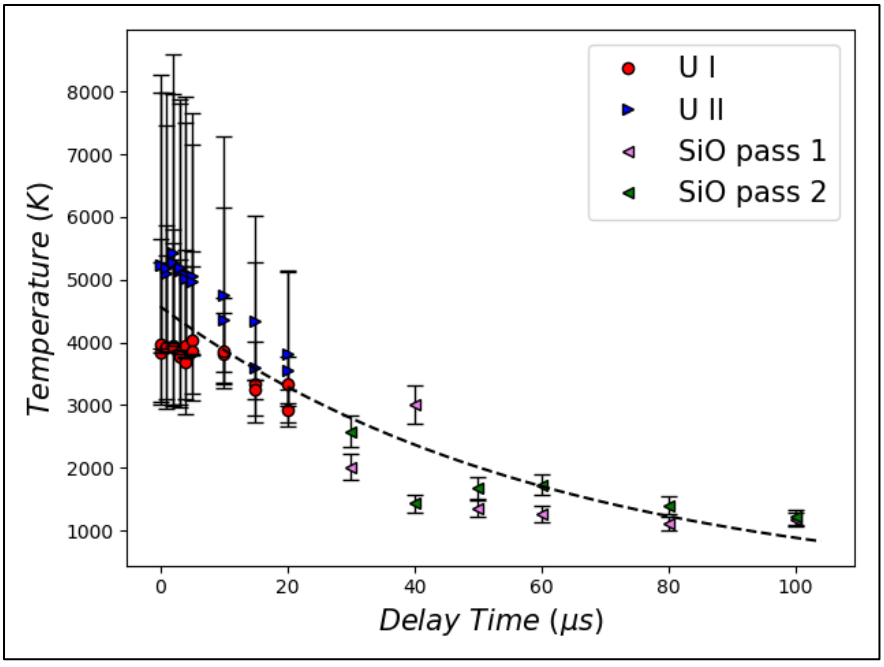

Figure 2.10: Temperature of atomic species and SiO versus delay time [37].

In that previous work, U I and U II temperatures and number densities were quantifiable using Boltzmann methodology, whereas UO could only be tracked in relative terms. Figure 2.11 shows the band in moderate resolution.

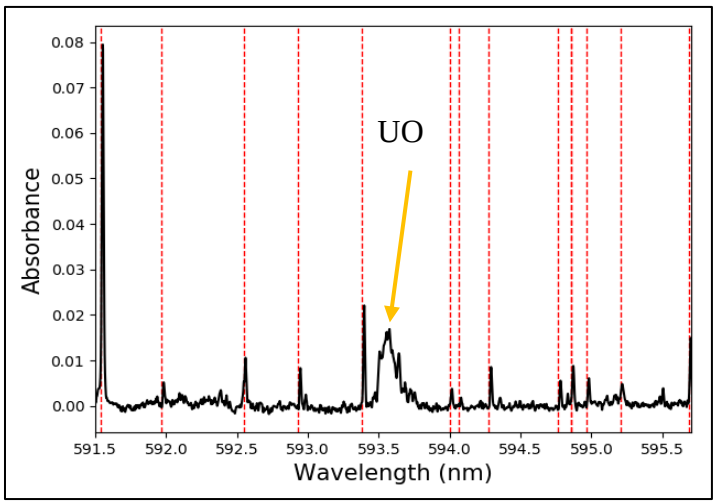

Figure 2.11: Uranium monoxide 593.55 nm band in absorption in 591-596 nm, 10% O_2/90% Ar environment, 100 ns delay. Red vertical lines correspond to U I transitions [17], [31], [32], [38]–[41].

Here, it is difficult to resolve the structure of the band due to its transition density, which has precluded prior investigators' ability to fully characterize the band parameters. Heaven and Kaledin have contributed greatly to this effort, determining rotational information for various electronic transitions of UO [39], [40], [42].

The UO band studied in this work is an electronic transition with rotational and vibrational components. The electronic states follow Hund's case (c) [39]. In this case, the coupling between L and S, the electronic orbital angular momentum and the spin angular momentum, respectively, is stronger than the coupling between L and the internuclear axis [43]. Heaven and Kaledin refer to the upper and lower states of this transition by the Ω quantum number, which is the total electronic angular momentum. These transitions follow $\Delta\Omega = 0, \pm 1$ selection rules [42].

Constants for the 593.55 nm band found in literature are summarized in Table 2.1.

Table 2.1: 593.55 nm UO constants from literature [44]–[47].	
Upper state	$(U^{2+}(5f^{3}7p^{1})O^{2-})$
ν_0 (cm^{-1})	16845.06
Ω’	5
B’ (cm^{-1})	0.330
R’ (Å)	1.830
Oscillator Strength	0.2008
Lower state	$(U^{2+}(5f^{3}7s^{1})O^{2-})$
Ω”	4
B” (cm^{-1})	0.333
R” (Å)	1.838
ν_0 (cm^{-1})	0
ω_0 (cm^{-1})	840-850
$\omega_e x_e$ (cm^{-1})	2.2

These higher resolution absorption and emission spectra obtained by Professor Glumac show a more detailed structure that may lend clarity to an effort to quantify the uranium monoxide band and allow researchers down the line to model this transition [36].

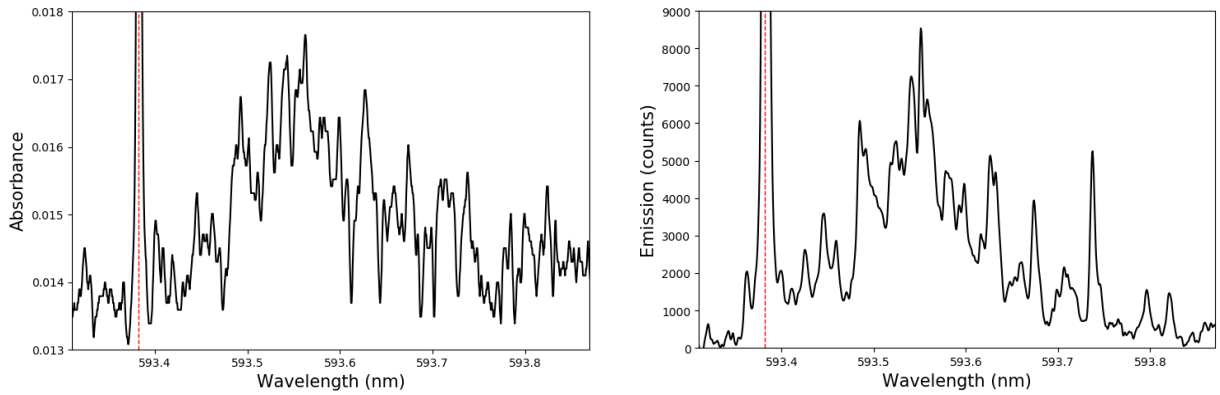

Figure 2.12: High-resolution absorbance and emission spectra of UO 593.55 nm band in a 2% O2/98% Ar environment. The tall peak corresponds to the 593.3817 nm U I transition [17], [31], [35], [38], [41].

2.3.2. Dust Cloud Combustion

2.3.2.1. Dust Combustion

Dust explosions involve the combustion of particulate dispersed in air and require the presence of several components: fuel, oxidation, confinement, mixing and ignition source [48]. These have often been studied in the context of worker safety and the prevention of accidental occurrences in such environments as coal mines [49]. Thermobaric weapons also operate in this manner, wherein

an aerosol or dust-like fuel is dispersed and subsequently detonated [50]. Per electrical safety standards, a uranium dust cloud is considered potentially hazardous and electrically conductive and has a low ignition temperature [51]. A model has also previously been created to simulate aerosolized uranium dispersion in the context of potential health and safety effects [52]. These sorts of experiments have been performed on a variety of metals to determine explosibility and other burning characteristics in the past [53]–[55].

2.3.2.2. Uranium Combustion

Uranium combustion and the observation of resulting spectral signatures is of interest to the scientific and defense communities for the purposes of determining and characterizing appropriate signatures for remote detection applications as well as better understanding uranium combustion [26]. Uranium and oxides are additionally of interest due to deposits produced from depleted uranium containing armor-piercing projectiles [56]. Limited work has been published on the combustion of uranium. There has been much work studying other metal powders, which could potentially be leveraged to understand uranium combustion phenomena [57]–[62].

Due to its pyrophoric nature, uranium powder exposed to air at room temperature forms an oxide layer primarily comprising UO_2 [63]–[66]. Calculations performed using NASA CEA, the National Aeronautics and Space Administration's Chemical Equilibrium with Applications Solver, indicate that the adiabatic flame temperatures of uranium in air and oxygen are 3454 K and 4397 K, respectively [67]. However, NASA CEA makes no allowance for particle size or geometry, nor does it account for the protective oxide layer. Mouradian and Baker Jr. created a model for determining uranium and zirconium burning temperatures in air with respect to sample size, geometry, and airflow whilst making some allowance for the oxide layer [68]. From this, for a spherical particle under natural convention and a size of less than 0.01 cm and decreasing, the burning temperature approaches about 3200 K for particle diameters on the order of 100 microns. Due to the high boiling point of uranium (~4400 K) as compared to its oxide (~3800 K) and burning temperature at atmospheric pressure, it is expected to burn heterogeneously limited by the thickness of oxide [69]–[71].

Various experiments have been performed and models set up to study and emulate uranium combustion phenomena. Many uranium and uranium monoxide transitions were determined in the work of Heaven and Kaledin, where vapor created from the heating of uranium samples was

spectrally characterized using laser-induced fluorescence (LIF) [40]. They further characterized uranium monoxide bands using pulsed laser deposition in a supersonic expansion [39]. Laser-induced breakdown spectroscopy has been used as an analog to fireball conditions to study uranium kinetics in the presence of oxygen [27], [38], [72]–[74]. A reaction mechanism has been determined and calculations performed based on these experimental results [23], [47]. Koroglu et al. observed the formation of gas phase species from a plasma flow reactor in the presence of oxygen whilst cooling from 5000K to 1000K, including the formation of uranium oxides [75]. Work has also been completed regarding the oxidation of uranium, where a diffusion rate law was determined for the oxidation of uranium at lower temperature regimes [63], [76]–[78].

Absorption spectroscopy can be used to determine quantitative temperature and number of species with the knowledge of energy state information of targeted transitions [16], [79]. Few measurements exist on particulate combustion of U, which, in the case of penetrating munitions, occurs after fragmentation from impact. In this work, the dynamics, temperature, and gas phase environment of particulate combustion of natural uranium is characterized using absorption spectroscopy. Burn time measurements and high-speed imaging performed on dust clouds of uranium and other assorted metal powders to characterize and compare burn behavior will be discussed in a later section (Section 4.2).

While signatures from a uranium dust cloud could bear some similarities to the temperature regime in a late-time nuclear fireball, this is a different scenario, in which material must be excited from a room-temperature, particulate state, rather than condensed from incredibly high-temperature plasma conditions. Factors such as the existing oxide layer of uranium particulate will come into play as the U particles combust.

2.3.2.3. Heterogenous and Homogeneous Particle Combustion

Heterogeneous particle combustion occurs when the metal oxide burns at the surface, due to having a lower volatilization temperature than the metal. So long as the temperature remains below the boiling point of the metal, the particle will burn heterogeneously and emit thermal radiation due to the particle heating up but not combusting in the vapor phase (Figure 2.13).

If the temperature is sufficiently high but does not exceed the oxide volatilization temperature or metal boiling point, the oxide will continue to build up on the surface of the particle.

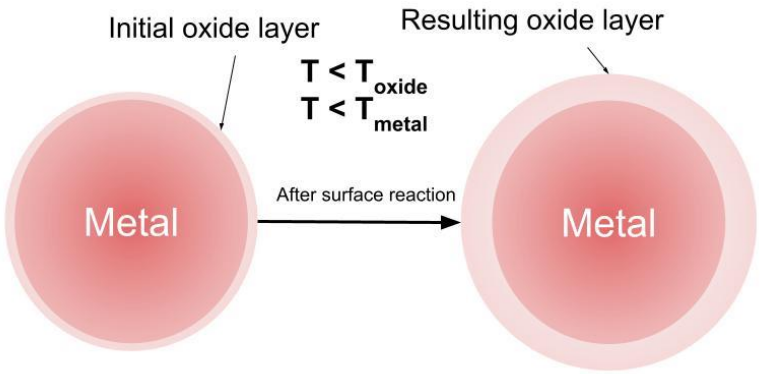

Figure 2.13: Heterogeneous particle combustion: if the ambient temperature is less than the volatilization temperature of the oxide, more oxide will build up on the surface of the metal.

If the particle temperature exceeds the volatilization temperature of the oxide but is less than the boiling point of the metal, the oxide will vaporize, which Markstein refers to as 'surface burning' (Figure 2.14) [71].

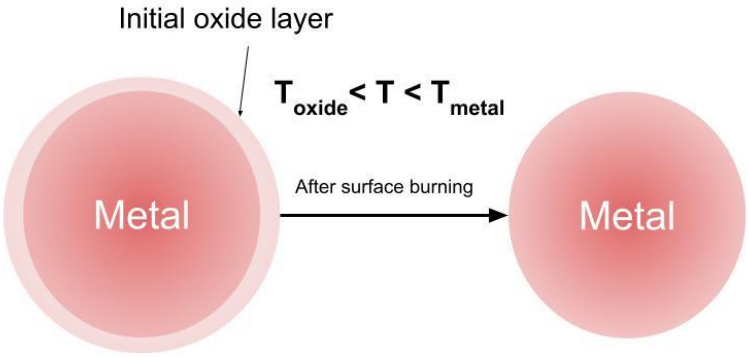

Figure 2.14: Heterogeneous particle combustion: if the ambient temperature is greater than the volatilization temperature of the oxide, but less than the boiling point of the metal, the oxide will vaporize.

Homogeneous particle combustion, also called vapor-phase combustion, occurs when the oxide volatilization temperature is greater than the boiling point of the metal, but combustion temperature will not exceed the boiling point of the metal [80]. Here, the metal vaporizes and heats to the ambient temperature, emitting characteristic molecular and atomic transitions which can be probed spectroscopically.

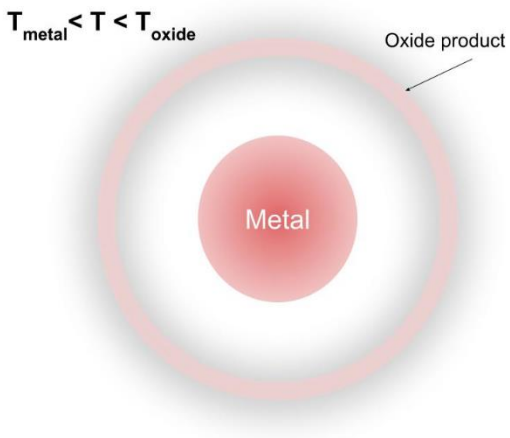

Figure 2.15: Homogeneous (vapor phase) particle combustion. Particle temperature is near the boiling point of the metal. The oxide layer has the peak temperature.

Per Glassman's criterion, for a metal to burn as a vapor, the oxide volatilization temperature must be greater than the temperature of the metal boiling point [80], [81]. The heats and temperatures of volatilization of oxides can change due to factors like ambient pressure, which is important to account for when considering the criterion. This information must be considered when interpreting the results of the dust cloud combustion experiments as well as the shock tube combustion experiments.

2.3.3. Shock Tube Combustion

2.3.3.1. How shock tubes work

The shock tube is one of the most classic examples of materials combustion testing. By varying several parameters, a controllable, high-temperature, high-pressure shock wave can be directed down the tube in order to combust test particles, study fluid dynamics, and calibrate instrumentation [82]. There are several methods of producing a shock wave; these include explosively producing a shockwave in vacuum and creating a large pressure differential on either side of a boundary and puncturing the boundary. However the pressure differential is created, when the high and low pressures meet, a shock wave is formed as the high-pressure gas attempts to equilibrate with the low-pressure gas section. This shock travels at a velocity which can be correlated to the ratio between the high and low pressures and will have a specific after-shock temperature [83]. Because this temperature is well-defined in the context of the velocity and

pressure parameters, shock tubes are immensely useful for combusting particles at or subjecting test materials to specific temperatures. The relevant equations are as follows:

$$\frac{T_1}{T_0} = \frac{[2\gamma M^2 - (\gamma - 1)][(\gamma - 1)M^2 + 2]}{(\gamma + 1)^2 M^2} \qquad \textit{Equation 7}$$

$$\frac{p_1}{p_0} = \frac{2\gamma M^2 - (\gamma - 1)}{\gamma + 1} \qquad \textit{Equation 8}$$

Where T_1 is the temperature after shock, T_0 is a temperature before the shock, γ is the ratio of specific heats, p_1 is the pressure after shock, p_0 is the pressure before shock, and M is the Mach number of the shock wave. When applied directly to the shock tube, the ratio between the driver and driven section can be expressed in this way (Equation 9) [84]:

$$\frac{p_4}{p_1} = \frac{2\gamma_1 M_1^2 - (\gamma_4 - 1)}{\gamma_1 + 1}\left\{1 - \left(\frac{\gamma_4 - 1}{\gamma_1 + 1}\right)\left(\frac{a_1}{a_4}\right)\left(M_1 - \frac{1}{M_1}\right)\right\}^{-\left(\frac{2\gamma_4}{\gamma_4 - 1}\right)} \qquad \textit{Equation 9}$$

Here the subscript of 4 denotes the driver section and the subscript of 1 refers to the driven section.

Figure 2.16 shows qualitatively how a shock would travel down a shock tube and combust test particles [85].

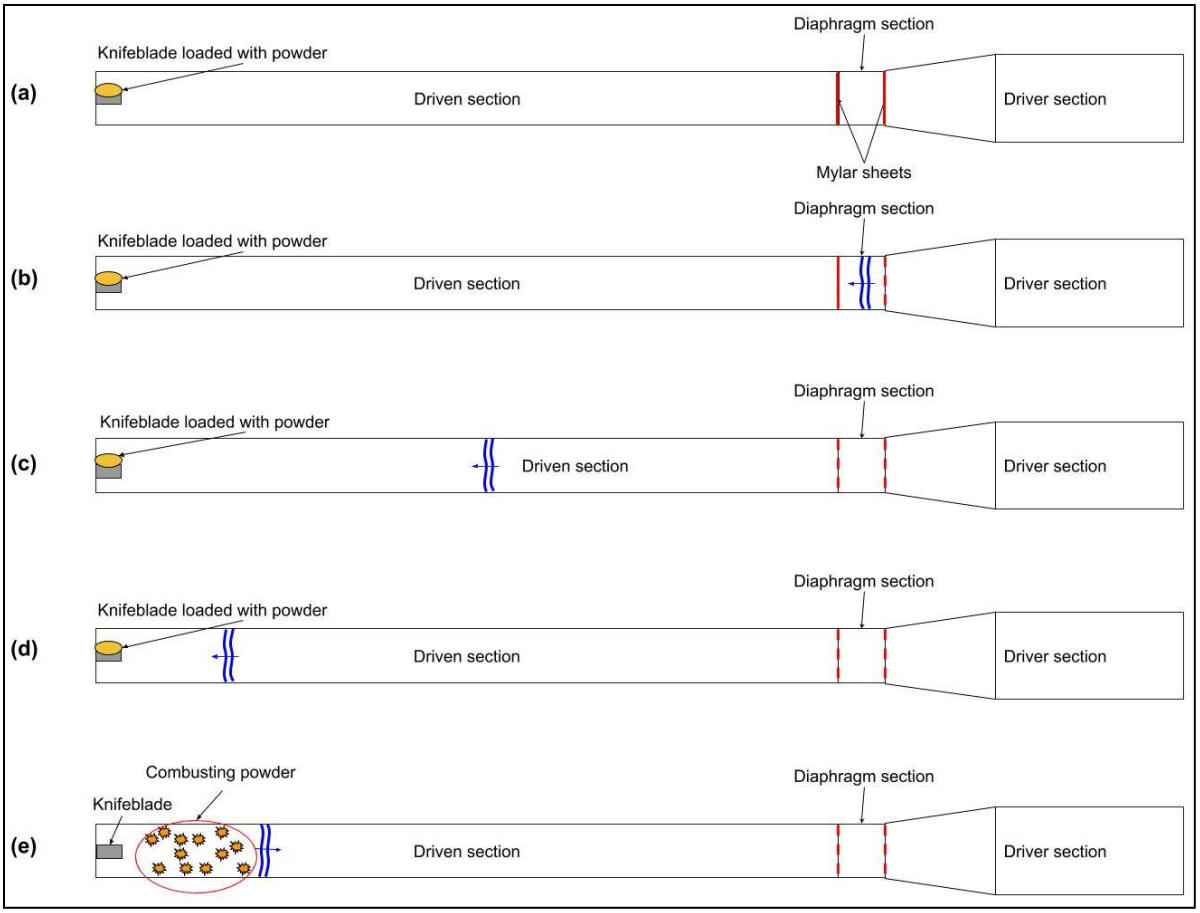

Figure 2.16: Schematic of Shock Tube Operation.

The driven section would be vacuumed down to the desired pressure with gaseous constituents appropriate for the test being conducted. A pressure differential would be induced in the driver and the diaphragm sections. Once the desired pressure has been achieved in the driver section, the diaphragm section would be evacuated and the Mylar would burst, inducing a shock wave to travel down the tube and reflect off of the end wall, combusting particles loaded into the shock tube via knife blade mounted to the end wall (or alternatively an injector in appropriate driven pressure regimes).

This figure is modeled after an existing shock tube setup which will be used to further characterize the spectra of combusted uranium at specified temperatures which will be discussed in more detail later in this document.

2.3.3.2. Previous Shock Tube Metal Combustion Work

Shock tube combustion of metal powders has long been established in characterizing shock-induced emission from metal powders. In terms of using UIUC's heterogeneous shock tube: After creating this setup, Roberts et al. used it to study combustion of aluminum and magnesium alloys in O_2 [86]. Krier et al. observed emission from boron combustion [87]. Bazyn performed spectroscopic measurements on aluminum and aluminum containing powders of varying particle sizes to characterize their burn behavior and draw conclusions about potential applications [88]. Lynch et al. measured absorption and emission from aluminum and drew conclusions about the kinetic behavior of Al and AlO combustion and vaporization and characterized emissivity for pyrometric applications [89], [90]. Allen used this methodology to look at the behavior of energetic metal alloys and nano-aluminum suspensions [91], [92].

2.3.3.3. Shock tube math/NASA CEA

Calculations for shock temperature were performed using NASA CEA, which is a program that can be used to calculate equilibrium properties of complex mixtures [67]. These include shock tube conditions. Use of this program is discussed in Appendix Section 0. Equation 7, Equation 8, and Equation 9 are factored into these calculations. Shock velocity is measured from the experiment, and composition and pressure of the driven section is determined from gas input, factoring in any leaks into the system. Composition matters as it affects the specific heat of the system. Initial temperature of the shock tube is also factored in as it features a heating apparatus.

2.4. Fission Product Signatures

2.4.1. What is fission

Fission is when an atom splits into multiple smaller atoms. It can occur when a neutron impacts a fissionable atom, providing it with enough energy to split. Not all elements or isotopes readily undergo fission, those that do are deemed radioactive. Figure 2.17 shows a schematic of a few fission processes. When a neutron impacts an atom, fission can occur, and this can produce smaller atoms as well as additional neutrons. These additional neutrons may impact other fissionable atoms, causing them to fission in a chain reaction. Some of the fission products may also decay into other products.

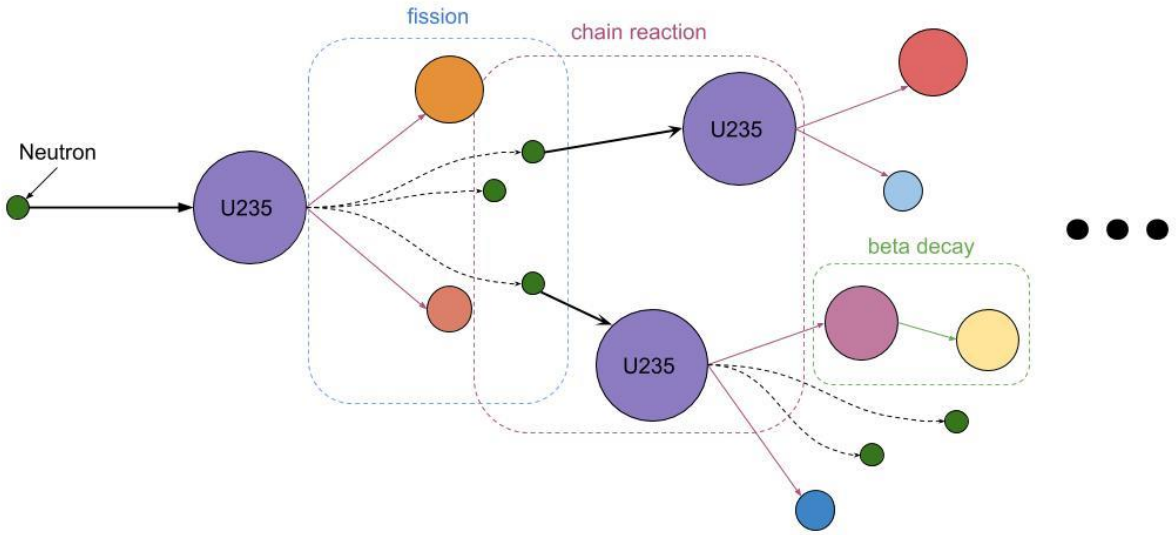

Figure 2.17: Fission processes.

Different fissionable materials may produce different distributions of products, independent and cumulative. Cumulative fission yield refers to the sum of products that form after all fissions occur since fission can also occur in the products of the original actinide material. Independent fission yield refers to the products that are produced directly when fission occurs. Fission yields also vary with initial neutron energy input. For example, thermal fission refers to an energy input of around 2E-2 eV. Fast fission is on the order of 4E5 eV, and 1.4E7 eV is the other echelon of fission distribution typically reported in the IAEA database [93], [94]. Figure 2.18 shows two examples of such distributions for thermal neutron fission yields for radioactive material isotopes, Uranium-235 and Plutonium-239.

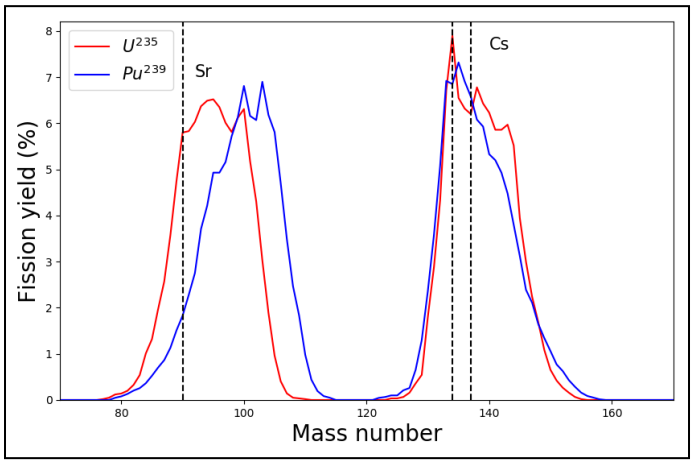

Figure 2.18: Thermal neutron fission yield for $U^{235}$and Pu^{239}. Data digitized from Bleam and IAEA [93], [94].

2.4.2. Why consider this?

Many alternative signatures need to be explored for nuclear forensics applications. The main questions are: can fission product spectral signatures be observed in the fireball environment, and can they vary based upon the fissile material? Since actinide chemistry will evolve over the lifetime of the plume, atomic and ionic signatures of U may not persist, and UO signatures are known to be short-lived in environments where O_2 is abundant. Higher oxide signatures are still being explored by various groups. It is important to consider all potential signatures that may result from a nuclear fireball.

2.4.3. Calculations for initial figure of merit

To determine which elements to study first, a figure of merit was developed to determine what fission products may be most likely to emit under conditions similar to the nuclear fireball so that appropriate spectral transitions could be targeted during experimentation. Initially cumulative thermal fission product yields were considered, as well as the vapor pressure and excited state fractions of each product as shown in Equation 11 and depicted in Figure 2.19.

$$FOM = yield * vapor\ pressure * excited\ state\ fraction \qquad \textit{Equation 10}$$

This parameter accounts for both strongly emitting species and abundance of species. Vapor pressure was considered since gas phase emissions were being targeted—if a material does not enter the gas phase, it would not be able to emit in that phase. Materials with very high first excited states would not be adequately populated to emit, which is why the excited state fraction was considered.

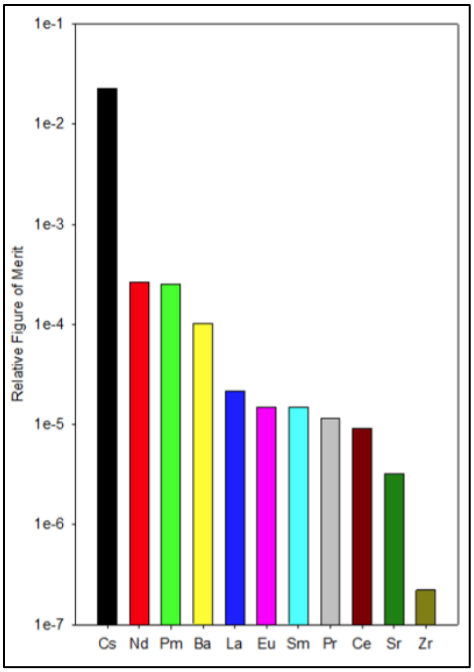

Figure 2.19: First figure of merit (courtesy of Dr. Glumac).

Based on this, Cs and Sr were targeted for initial study—specifically strong atomic Cs and molecular Sr signatures (SrOH) in the near-IR region of the electromagnetic spectrum. Cs has several strong emission lines and tends to emit at combustion temperatures, and Sr is commonly found in fireworks in the form of SrOH, which produces red emissions.

2.4.4. Flash powder and Explosives Testing

Flash powders are mixtures of an oxidizer and fuel typically used for pyrotechnics and were used in this work to observe transitions of interest for remote detection. These flash powders were assembled using aluminum or magnesium and $SrNO_3$, all of which are commonly used in fireworks [95]. A stoichiometric mixture of Al or Mg and $Sr(NO_3)_2$ would be doped with Cs_2CO_3. The relevant chemical equations follow [96]:

$$Sr(NO_3)_2 + Mg \rightarrow SrO + N_2 + 5MgO \qquad \textit{Equation 11}$$

$$3Sr(NO_3)_2 + 10Al \rightarrow 3SrO + 3N_2 + 5Al_2O_3 \qquad \textit{Equation 12}$$

These equations can be used to determine the appropriate amounts of each constituent to add to the mixture. Detonation of flash powder leads to a highly energetic, bright reaction, which can be

optically characterized. Flash powders are typically prepared such that the reaction proceeds to completion, where none of the reactants remain [96].

In order to further energize the Cs and Sr to reach higher temperatures, conventional explosives doped with small amounts of these materials would be detonated. This would help determine if their signatures would appear at all with this amount of excitation and if signatures from high explosives would interfere with their appearance.

2.4.5. Calculations for updated Figure of Merit

After promising results from tests containing Sr and Cs, other fission products were investigated for viability in remote detection from the nuclear fireball. It was determined from testing that it may be more appropriate to consider the independent fast fission product distribution as opposed to the cumulative thermal fission product distribution that had been used to develop the first figure of merit, as the former is better representative of the products present more instantaneously in a nuclear fireball. Figure 2.20 shows examples of these yield curves for U^{235} (orange) and Pu^{239} (blue), which when compared with Figure 2.18, is clearly differently distributed.

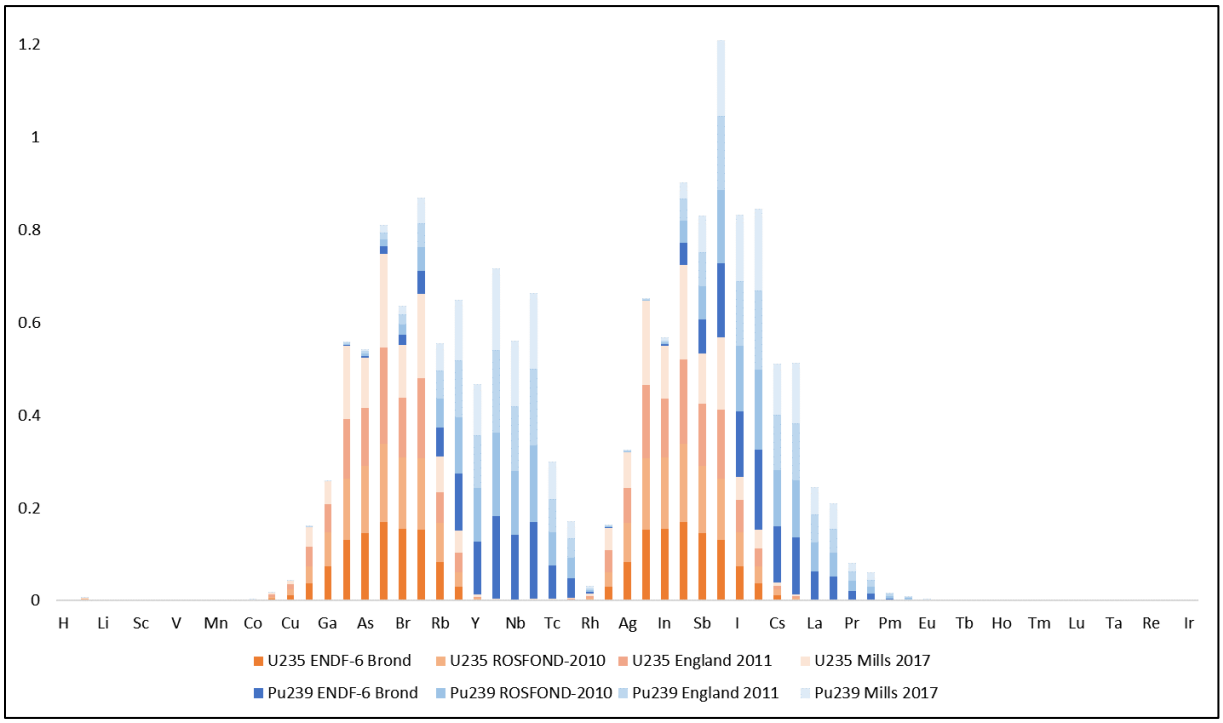

Figure 2.20: Fast independent elemental yields arranged by atomic number (on the x-axis) for U^{235} (orange) and Pu^{239} (blue), 4E5 and 5E5 eV, respectively.

The varying gradations of orange and blue are derived from different sources on the IAEA database [94], [97]. New figures of merit involving the yields above and detection limits for various signatures as reported by Fassel and Golightly [98]. A detection limit is the lowest amount of a species that can be detected using a given type or instrument of measurement. In spectroscopy, these limits can vary with the strength of signatures observed to make this determination, and how these values are reported can depend on the constraints of the spectral acquisition system used (efficiency of optics, etc.) [99]. These can also vary with temperature of species since transition populations vary. For these figures of merit, elemental abundance was divided by detection limit for selected fission products (Figure 2.21 and Figure 2.22). Ergo, species with lower detection limits and higher abundances are more likely to be detected using atomic spectroscopic methods.

Not taken into account in both figures of merit is that some materials may rapidly form polyatomic species or oxides after initial excitation, some of which may also become species of interest in later study.

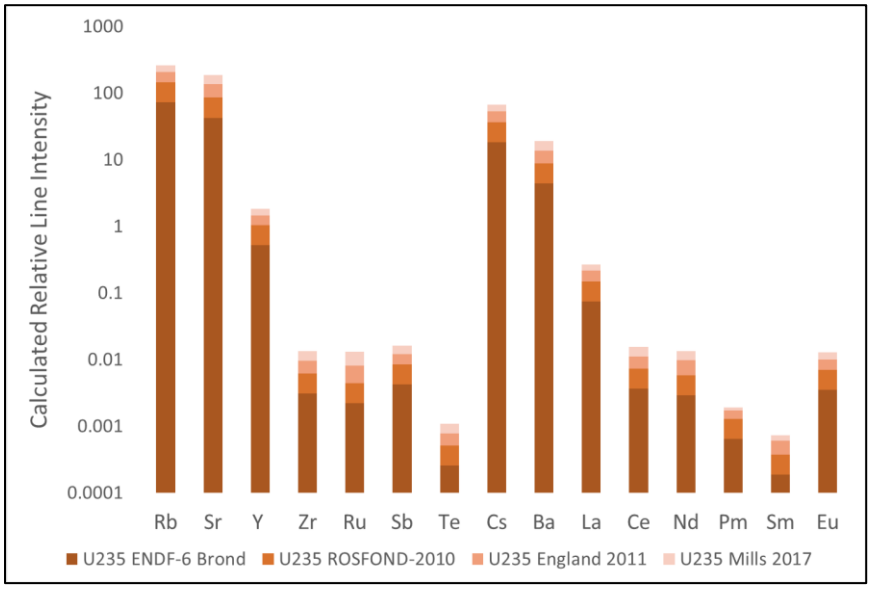

Figure 2.21: Updated figure of merit for U^{235} fission products.

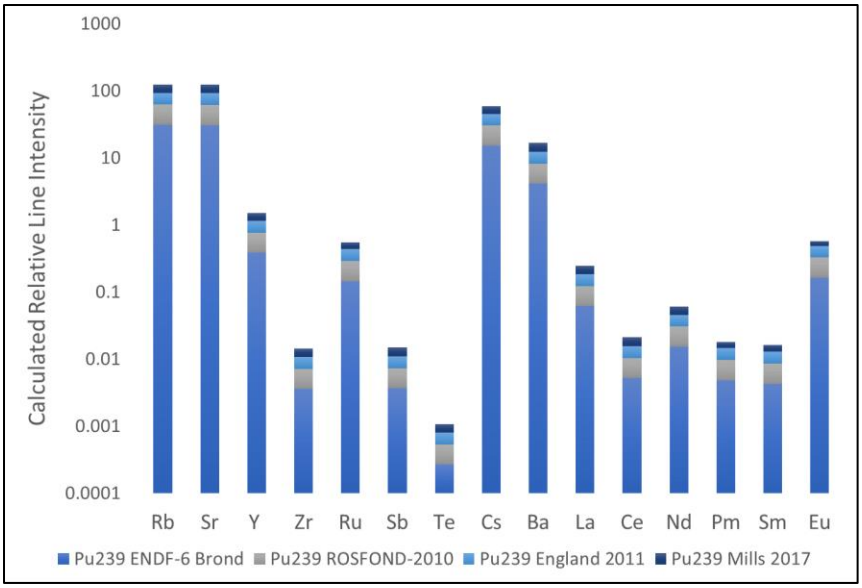

Figure 2.22: Updated figure of merit for Pu^{239} fission products.

From these figures, Rb and Ba were selected for further study, and mixtures containing several of these products in different proportions were created. A similar figure of merit was made for both isotopes using calculations from plasma detection limits as opposed to flame detection limits, as used in the previous figures, for comparison [100]. Plasma detection limit values were not available for Rb, Ru, and Pm (Figure 2.23, Figure 2.24).

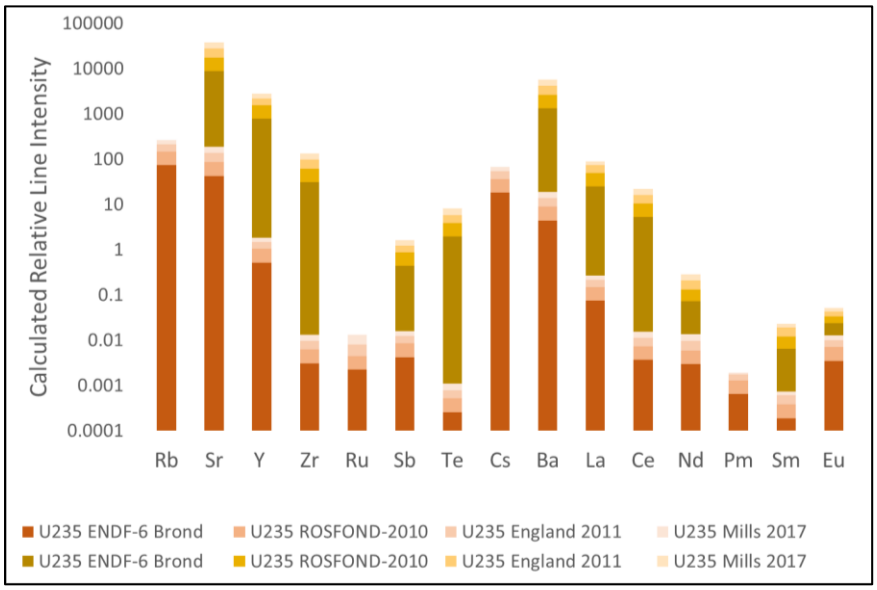

Figure 2.23: Updated figure of merit for U^{235} fission products for both flame (orange) and plasma (yellow) detection limits.

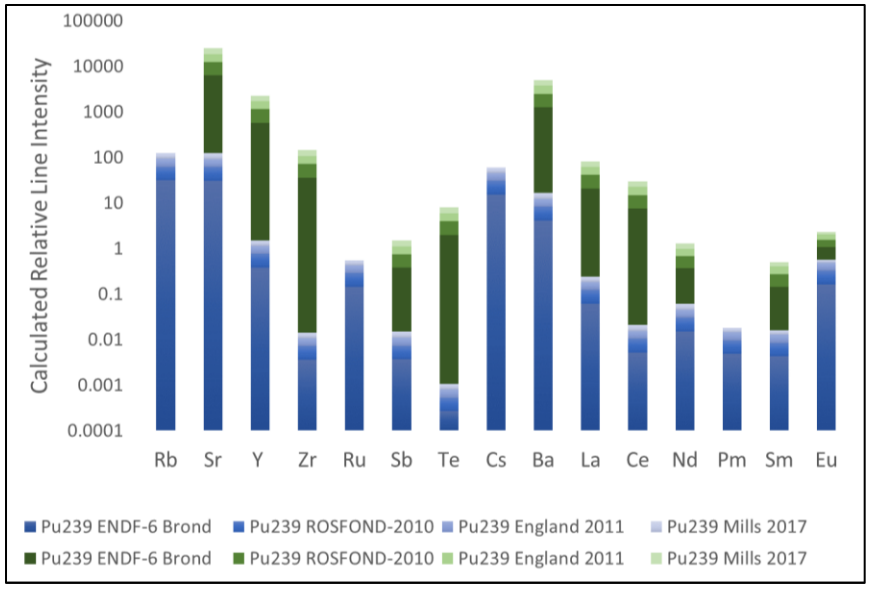

Figure 2.24: Updated figure of merit for Pu^{239} fission products for both flame (blue) and plasma (green) detection limits.

The plasma detection limits tended towards an increased relative line intensity for all products, which was expected due to the higher temperatures and therefore higher likelihood of excitation for a given species/transition, but the distributions only changed slightly—Te and Sb appear different for both the Pu^{239} and U^{235} distributions in the different excitation conditions as do Ce and Nd. Calculations were made to create a mixture of powders mirroring the expected composition of fast independent fission products from materials of interest as determined from these figures.

2.4.6. Rare-Earth Elements

Some of the fission products of interest are rare earth elements or lanthanides (Figure 2.25). These lie in the row of the periodic table above the actinides. Although not in that row, Scandium and Yttrium are included in reference to rare earths [101].

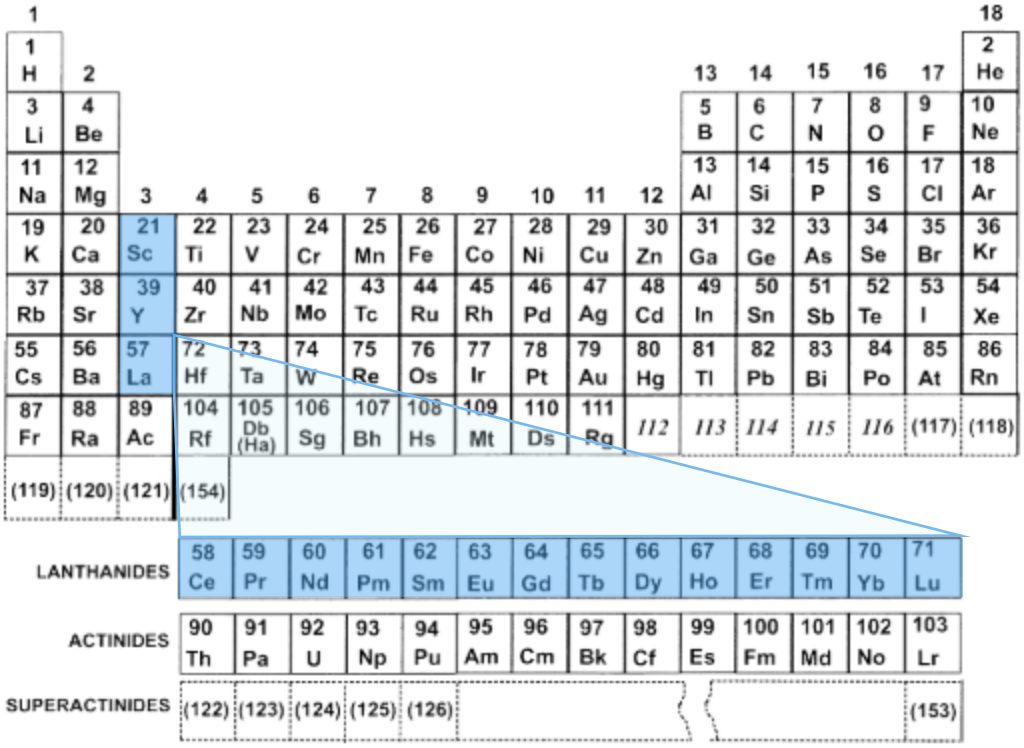

Figure 2.25: Lanthanide elements on the periodic table. Image adapted from Reference [8].

Rare-earth elements are similar in appearance (grey and silvery) and are often found alongside actinides. Like actinides, some lanthanides are radioactive. Although rare-earth elements are abundant in the Earth's crust, these elements are not typically found in concentrated tracts that would be more easily harvested [102].

Nowadays, rare-earth elements are used predominantly in electronic components and other special engineering applications, such as vehicular catalysts, neodymium magnets, and lasing media. They are reactive at high temperatures and/or small particle sizes [101].

2.4.7. Other Elements of Interest

Some of the other potentially strong emitters were strontium, cesium, barium, and rubidium, all of which are metals in the s-block of the periodic table. These are highly reactive and other metals in this block tend to emit even when present as trace impurities in an excitation event (calcium, potassium, sodium).

The remaining materials of interest were transition metals, zirconium, niobium, molybdenum, and ruthenium as well as metalloids, antimony and tellurium, from the p-block [103].

CHAPTER 3: EXPERIMENTAL METHODS

This chapter details the setup of each experiment performed to determine signatures of interest to nuclear forensics applications. These included laser ablation of solid uranium, dust cloud combustion and shock tube heating of uranium powder, and the application of unconventional and conventional explosive excitation to fission products to obtain the resulting spectra.

3.1. Laser Ablation

A schematic of the laser ablation setup used for uranium study discussed in this document is shown in Figure . The setup consists of a chamber that can achieve vacuum down to < 0.01 torr with 0.01 torr precision and has a controllable gaseous environment. A capacitance manometer (Baratron) was used to measure vacuum pressure, and a dial gauge was used for higher pressures. Since tests were done on uranium, which poses an inhalation risk, a HEPA filter was placed in the vacuum line to prevent airborne particulate from escaping into the lab.

The plasma was generated using a Q-switched Nd:YAG laser (3ω, Spectra-physics, model no.: PS-100) with pulse duration of 5 ns and energy of 80 mJ at a frequency of 10 Hz. A xenon lamp (Oriel Instruments 6427, 7-9 µs FWHM) was used to obtain time-resolved absorption measurements in line with a 1.5-meter spectrometer custom-built by Dr. Glumac. Depending on the targeted spectral range, gratings of 300, 2400, and 3600 gr/mm were used. A CCD (Andor iDus 420, 1024 x 255 pixels, 26 x 26 µm pixel size) was used to acquire spectra through this system. System timing was controlled using a Quantum Composers 9514 pulse generator, which allowed for delaying the flash lamp with respect to the onset of the laser ablation plume. The experiment is further detailed in References [35] and [15].

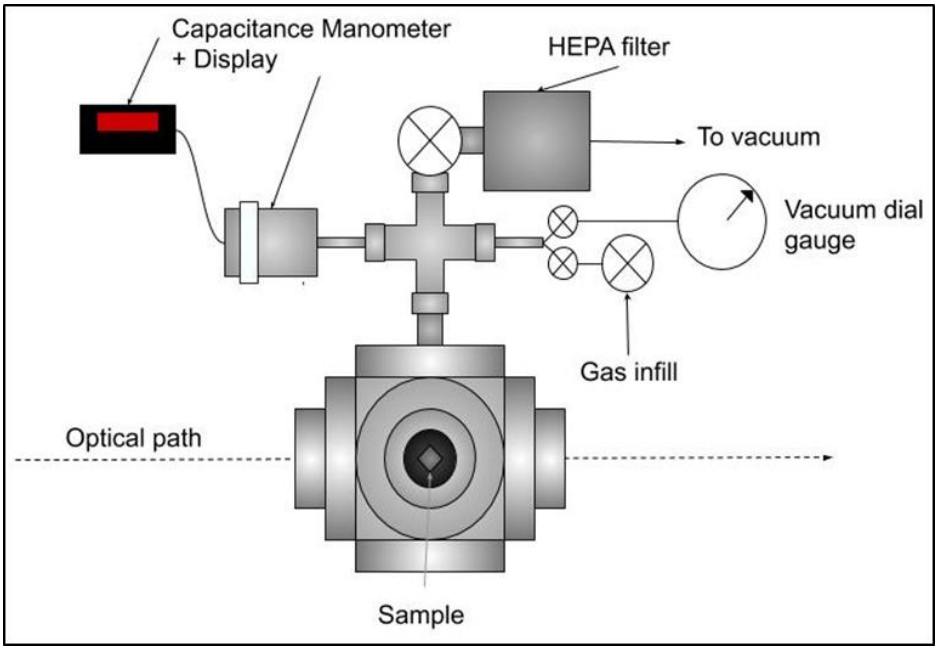

Figure 3.1: Top view of vacuum laser ablation chamber.

Absorption spectra were calculated from spectra of the background, absorption source, plume emission, and when absorption is occurring using the relation below:

$$Transmission = \frac{(Source + Plume) - Plume\ Emission}{Source - Dark} \qquad \textit{Equation 13}$$

Specific experiments are not discussed in detail in this document, but a method for quantifying UO absorption data obtained using this experiment is discussed in Section 4.1.

3.2. Uranium Powder characterization

To better inform experimental results, uranium powder used for both the dust cloud and shock tube experiments needed to be characterized. Powder sizes were derived from images acquired using a Field-Emission Environmental Scanning Electron Microscope (ESEM-FEG) operated by the Beckman Institute Imaging Technology Group's Microscopy Suite. Figure 3.2 shows one of these images.

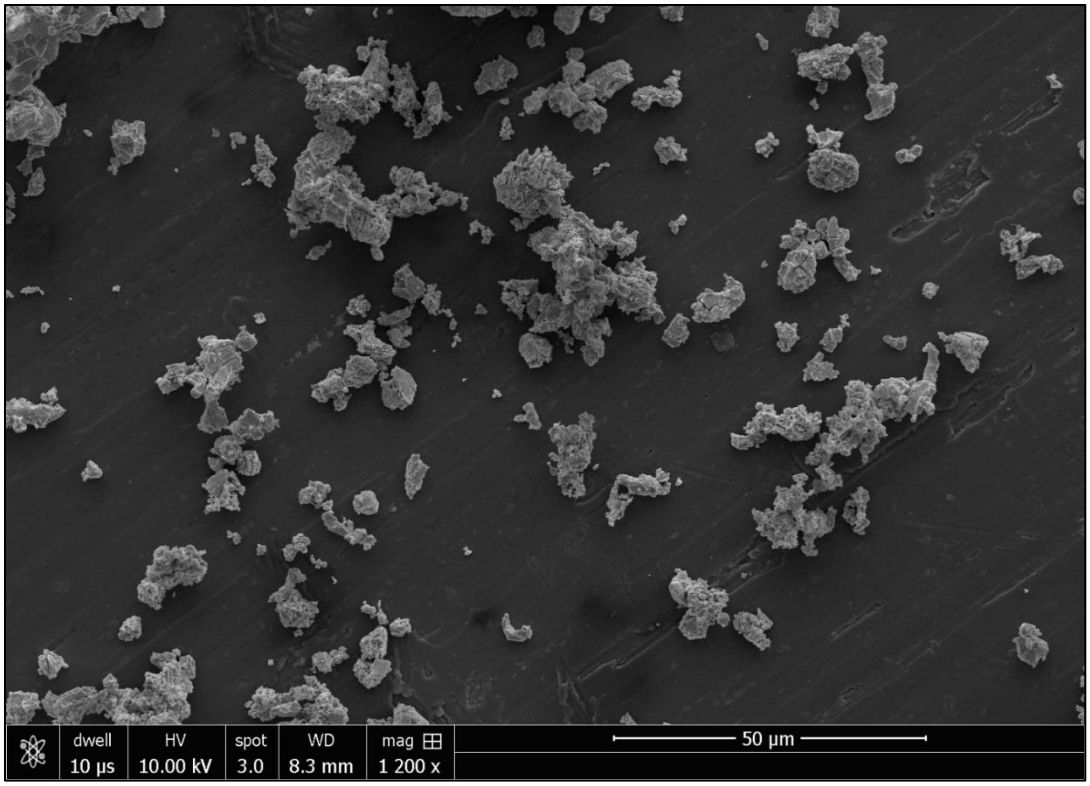

Figure 3.2: ESEM image of uranium powder.

A scanning electron microscope uses a beam of electrons to scan the surface of a sample. This particular machine has an ultimate resolution of 2 nm. A light dusting of uranium powder was adhered to a sample holder with double-stick carbon tape and imaged. Particle areas were found using ImageJ software. Diameters were calculated from these areas as if from a circle of equivalent area since particles were quite irregularly shaped. Figure 3.3 shows the distribution of particle sizes that was obtained from all the images of sufficient resolution to do so. Uranium powder was handled with precautions typically taken to avoid heavy metal inhalation and was on average 1.79 µm in particle diameter with a standard deviation of 2.58 µm.

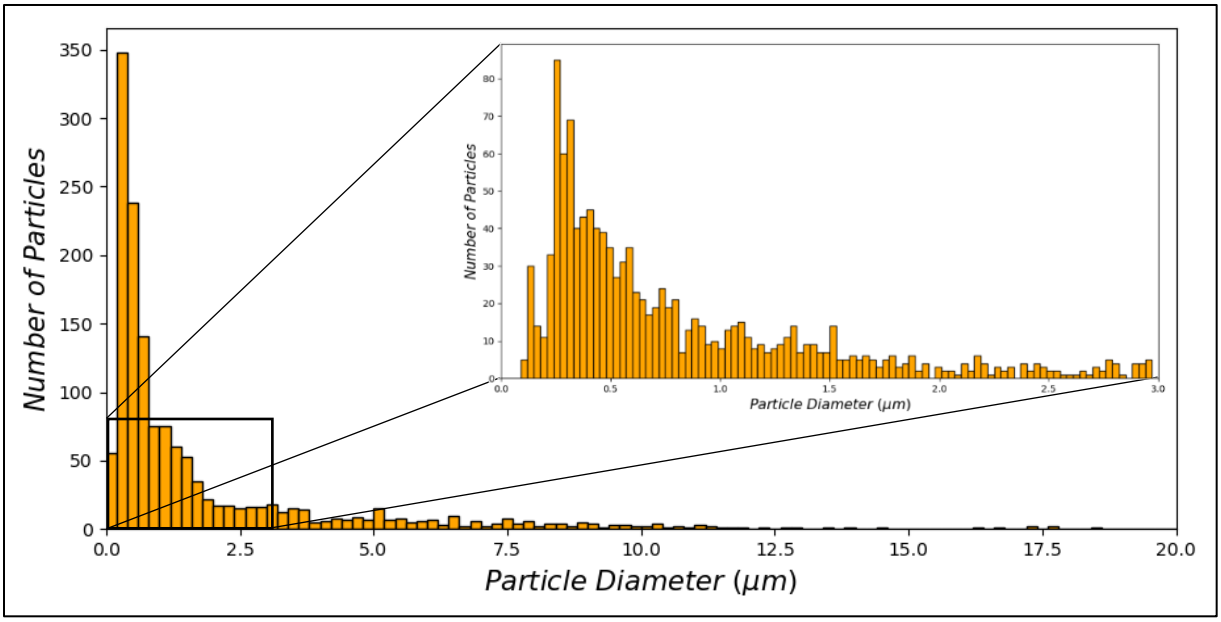

Figure 3.3: Uranium powder size distribution.

Additional imaging was performed to characterize the oxide layer thickness of these particles. Qualitatively, oxide features can be seen on the surface of the ESEM images in the form of flecks and cloud-like features in higher resolution in Figure 3.4. It is reasonable to assume that oxides would form on the surface of uranium powder due to uranium's propensity to oxidize and observation of uranium oxide development in prior literature [21], [22], [66], [104]. Specifically, it is likely to be UO_2 [104].

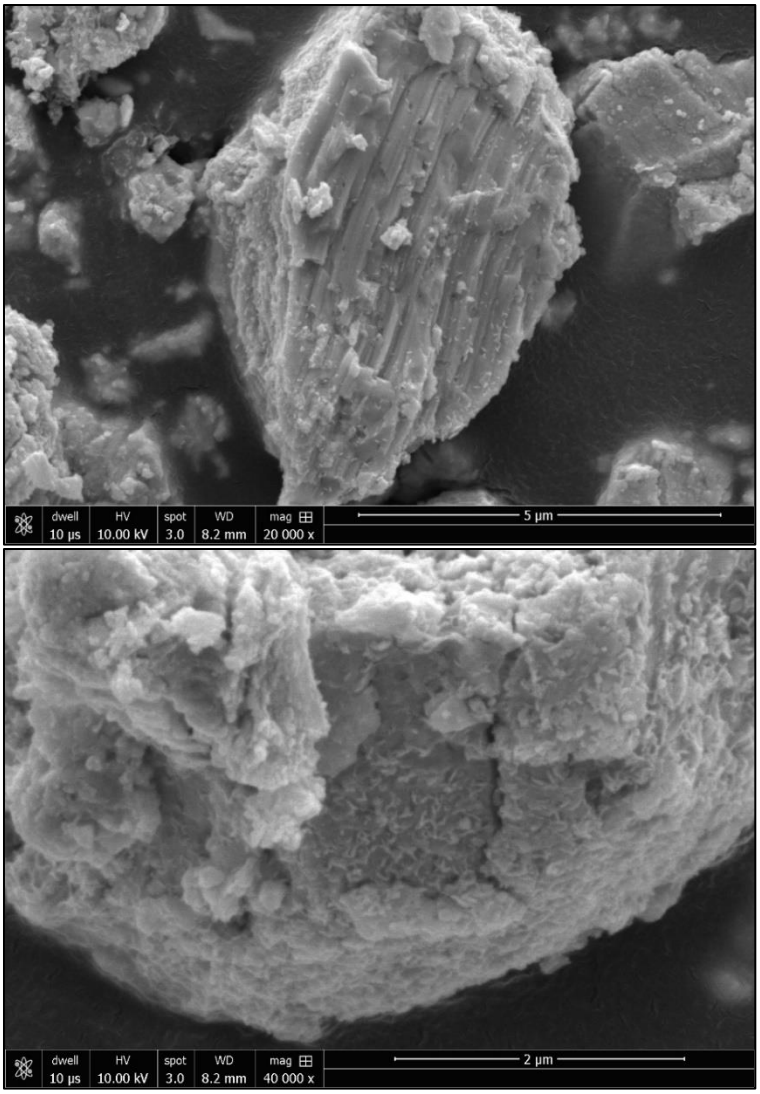

Figure 3.4: High-resolution ESEM image of singular uranium particle. Small flecks and fuzzy irregularities on surface are likely due to a uranium oxide layer.

These images can be compared to that found for uranium powder created under vacuum (therefore having little to no oxide layer) in SEM images from Le Guyadec et al. [65]. Their images appear to be free from these surface features. Images from Ablitzer et al. appear to be somewhat similar to that obtained here [66]. In that work, UH_3 and U powders were synthesized to study their pyrophoric behavior.

Quantitative characterization was performed using Beckman's Scanning Transmission Electron Microscope (STEM). Here, electrons were used to probe individual particles to differentiate between uranium and the oxide layer in order to determine oxide layer thickness. Figure 3.5 shows a few examples of the resulting images in different magnifications.

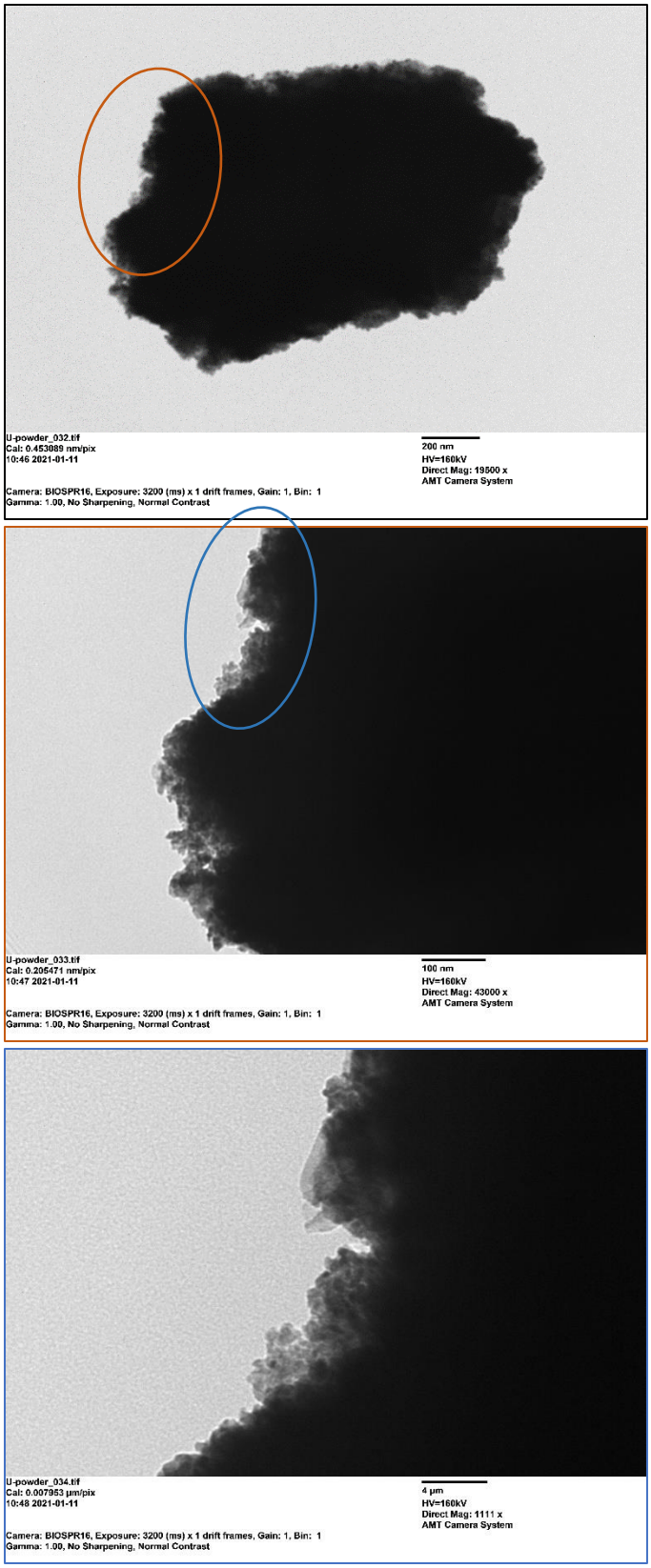

Figure 3.5: STEM images of a particle and its oxide layer in increasing magnification.

The lighter, “fuzzy” regions surrounding the particle are attributed to the uranium oxide layer (UO_2). The oxide thickness was measured using ImageJ at regular intervals along the edges of many particles and a distribution was determined as shown in Figure 3.6.

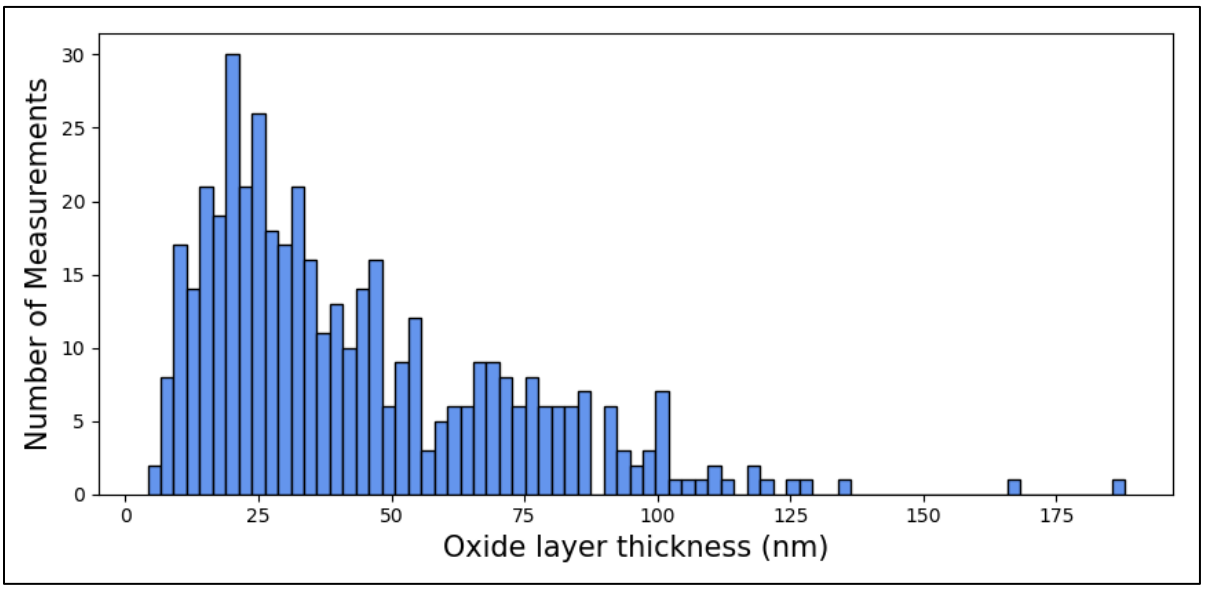

Figure 3.6: Uranium Powder Oxide Layer thickness distribution.

The average oxide layer thickness was about 43.3 nm with a standard deviation of 28.6 nm.

It is important to mention that this method does not characterize any amount of oxide that may be inside the particles and is more so a surface measurement. Other techniques may be used to characterize the total distribution of various uranium and oxide species contained in a sample of powder, such as X-ray diffraction, and would certainly be worth exploring. Other techniques that probe surface morphology may also be helpful to more concretely characterize this oxide layer.

3.3. Dust cloud combustion

A dust cloud chamber was created in order to facilitate the confined dispersal and combustion of 0.025 g of uranium powder (Figure 3.7) [105]. Tungsten electrodes at the base of the chamber were used to excite the powder through a small, tapered hole from a charge produced from a custom-built fire set. The internal volume of the chamber was 2.62E-3 m^3. Assuming complete dispersal of the powder, the maximum concentration of uranium in the chamber should be 9.53 g/m^3 or 2.41E+22 $atoms/m^{-3}$. The chamber is capable of pressurization with a gas mixture of choice as well as vacuum down to a few torr.

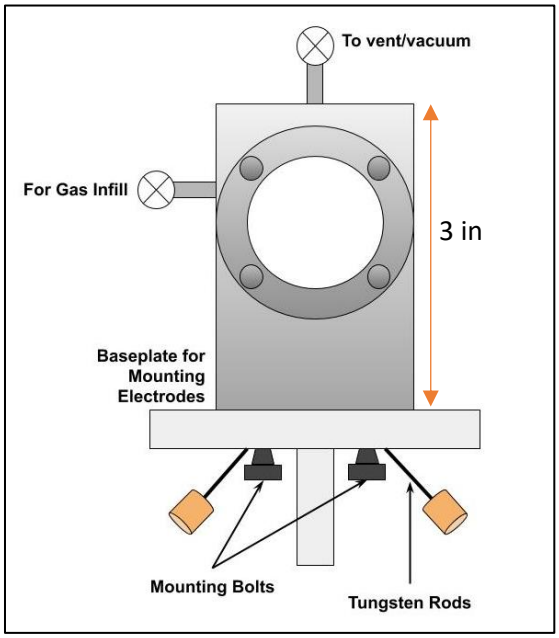

Figure 3.7: Dust Cloud Chamber Schematic from Read [105].

Timing of the system was controlled with a pulse generator (Quantum Composers 9514) which delayed the acquisition of the event with respect to the firing of the dust cloud. An additional pulse generator (Quantum Sapphire 9214) was used to trigger line scan camera acquisition with a duration of 359.5 μs (Hamamatsu C11165-02). A digital oscilloscope (Picoscope 4424) and silicon photodiode were used for burn time measurement (Figure 3.8).

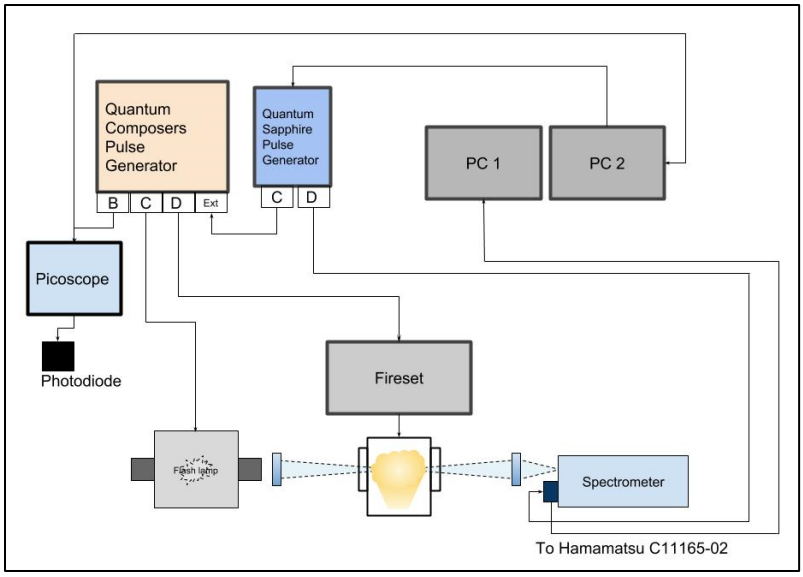

Figure 3.8: Entire Dust Cloud Setup Schematic.

A Xenon flash lamp and custom-built 1.5 m spectrometer with 2400 gr/mm grating used as a broadband source to acquire an absorption spectrum. The flash lamp has a duration of 7 μs FWHM in this region and is spatially and temporally characterized in Figure 3.9. This is the same flash lamp that was used in the laser ablation absorption measurements (Section 3.1).

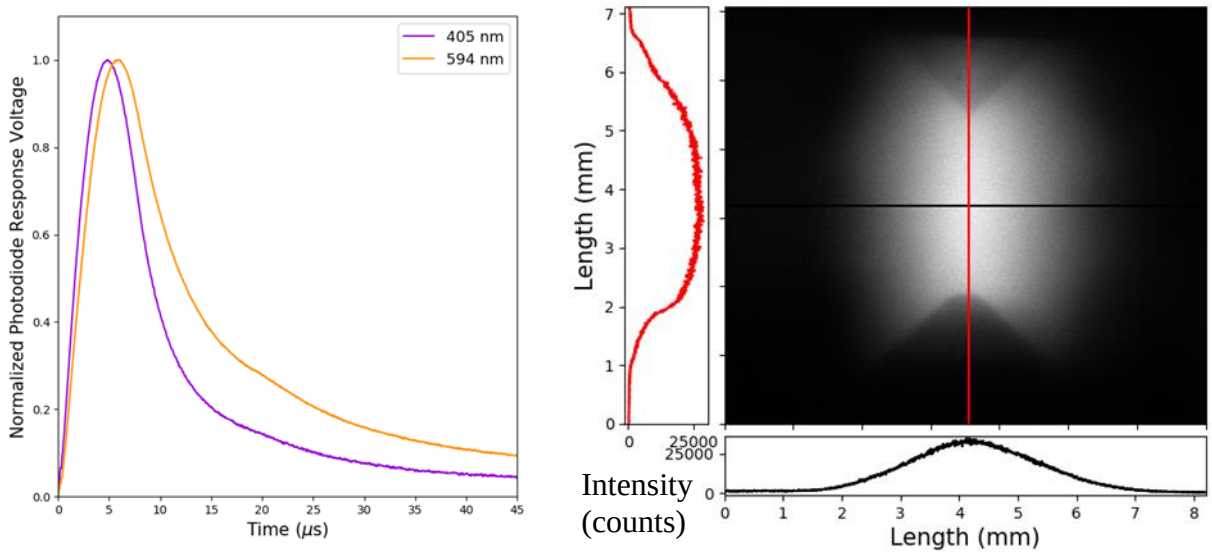

Figure 3.9:Flash lamp response at 594 nm and 405 nm (left) and spatial distribution of flash lamp discharge (right). Image taken through neutral density filters of collective OD 5 [36].

The system has a resolution of 0.0029 nm/pixel. The spectral range targeted was between 381 and 387 nm due to an abundance of ground state U I and U II transitions [17]. Prior to the experiment, a reference spectrum of the flash lamp was taken and divided out from the spectrum acquired

during the experiment, which was taken at 1 ms delay from the initial spark. The pathlength of the system was 5.08 cm. A Chronos 1.4 High-speed Camera was also used to image uranium combustion. For the tests pertaining to this document, the environment was air at atmospheric pressure. Since Fe transitions were prevalent in the spectra obtained from the uranium dust cloud, Table 3.1 shows the information obtained from the Kurucz atomic spectral database used to calculate Boltzmann temperature for Fe I [17].

Table 3.1: Information used to calculate Boltzmann temperature of Fe I from Kurucz Database [17].

λ (nm)	**J_l**	**J_u**	**E_{lower} (cm^{-1})**	**A_{ul} (s^{-1})**
381.584	4	3	11976.24	1.31E+08
382.0425	5	4	6928.268	66740000
382.4444	4	3	0	2829000
382.5881	4	3	7376.764	59750000
382.7822	3	2	12560.93	1.05E+08
383.4222	3	2	7728.059	45240000
384.0437	2	1	7985.784	46990000
384.9966	1	0	8154.713	60530000
385.6371	3	2	415.933	4640000
385.9911	4	4	0	9694000
386.5523	1	1	8154.713	15500000
387.2501	2	2	7985.784	10490000

Metal powder combustion has been studied extensively in the past, and burn time is a commonly used metric for its evaluation [57], [60], [106], [107]. Burn time has strong dependence on particle size, temperature, and oxygen availability. Further tests to characterize burn times of various similarly-sized (<10 μm) metal powder (Ta, W, Zr, Hf, Al, B, Ti, Fe, Mo, Si) dust clouds in air for comparison with uranium were conducted. These powders were prepared using the Gilson Autosiever Sonic Sifter (GA-6) and 3-inch diameter 10 μm sieve (GAA-83). Uranium powder was sifted by hand in a glovebox due to the high toxicity of inhalation, but as characterized earlier (Section 3.2), the uranium particles were predominantly much smaller than 10 μm in diameter to begin with.

These tests focused on both burn time acquisition and imaging to observe the occurrence of the exploding particle effect in an attempt to draw further conclusions about the nature of uranium particle combustion. Many of these powders and their burn characteristics have been studied in the

past, and drawing commonalities between these and uranium can lead to a better understanding of the mechanisms through which uranium burns. Table 3.2 shows the data used to apply Glassman's criterion to data interpretation.

Table 3.2: Powder characterization for burn time testing [108], [109], [118], [110]–[117].

Element	Mass (mg)						Metal $\Delta H^{M}_{vap,298\,K}$ (kJ/mol)	Oxide $\Delta H^{O}_{vap,298\,K}$ (kJ/mol)	Oxide Volatilization Temperature (K)	Metal Boiling Point (K)
U	6	3	2.6	4.1	3.6	5.4	477	621	~3800	4404
Al	2.6	2.2	2.2	2.2	2.8	2.2	284	1860	4000	2791
B	2.4	3.5	2.3	2.3	2.3	-	499	360	2340	4139
Fe	3.3	2.3	3.5	3.2	3.2	2.6	354	610	3400	3133
Hf	3.9	2.8	2.4	-	-	-	648	1461	~4350	4575
Mo	3.8	3.6	3.7	3.4	3.6	-	617	333	900	5833
Si	2.6	2.3	2.7	-	-	-	383	353	2633	3177
Ta	2.2	3.7	3.3	3.6	2.4	-	753	-	1200	5693
Ti	3	2.4	3	3.3	2.4	-	427	1890	3300	3631
W	2.3	2.3	3	3.8	3.1	-	774	452	1970	6203
Zr	2.2	3.9	3.7	-	-	-	591	920	4280	4703

Figure 3.10 shows a top view of the updated setup for these experiments.

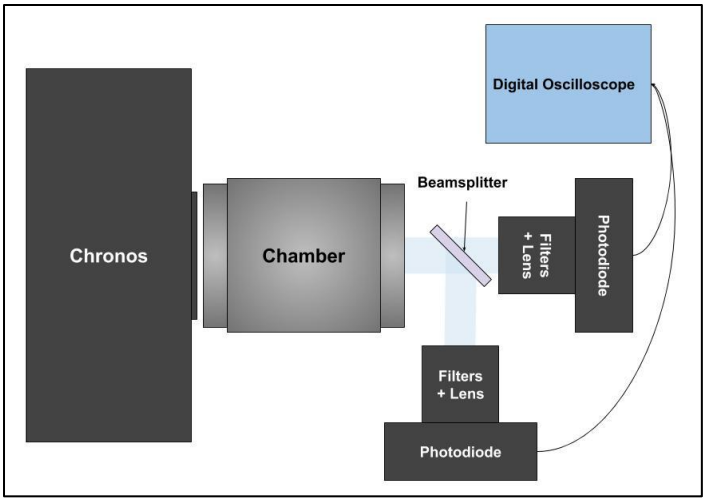

Figure 3.10: Top view schematic for metal powder burn time experiments.

Here, two photodiodes (Thorlabs PDA100A2) measured the intensity of broadband emissions from the combustion of these various metal powders. These were attenuated with neutral density

filters as necessary to prevent detector saturation. A Chronos high-speed camera (CR14-1.0-8C) was used to image combustion as in previous uranium experiments. Uranium tests were also repeated to confirm results from prior testing.

3.4. Shock tube experimentation

3.4.1. Series 1

Shock tube heating was used to obtain temperature-variant spectra of the previous characterized uranium powder from 2000-9000 K. The heterogeneous shock tube is 12 meters long and has an inner diameter of 8.9 cm in the driven test section [106]. Figure 3.11 shows a schematic of the setup. Thus far, shock temperatures as low as 980 K and as high as 9992 K have been reached. It can withstand pressures up to 34 atm and can be vacuumed down to 0 torr with resolution of 0.01 torr as measured by a capacitance manometer (MKS Baratron 122B) and a mercury manometer (Meriam Instrument 11AA10WM).

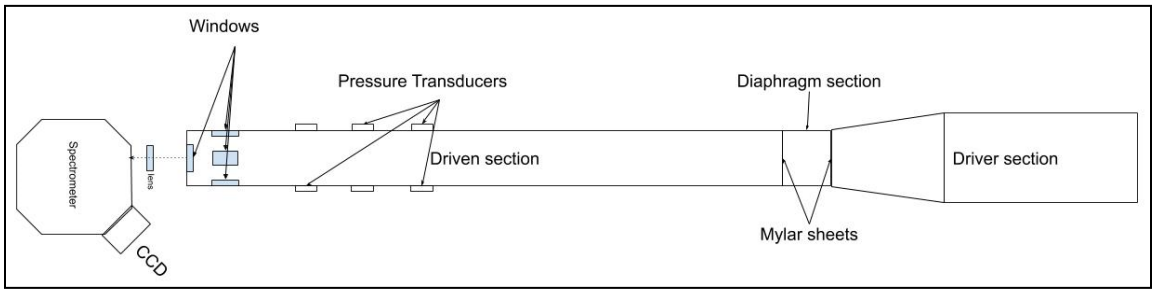

Figure 3.11: Shock Tube Diagnostic Setup (not to scale).

Shock speed is measured using three PCB piezoelectric pressure transducers (PCB 113B27) and digital oscilloscope (Picoscope 4424) with in-line amplification. A Chronos high-speed camera (CR14-1.0-8C) was used to image combustion through a side window on the end section. A spectral acquisition system consisted of a SPEX 270M spectrometer with a 1200 gr/mm grating and a CCD camera (ZWO ASI174mm) was calibrated using an Aluminum hollow cathode lamp (Analyte 22929 Al) to capture a range between 360 and 400 nm which was chosen due to the numerous ground state U I and U II transitions in this spectral region [17]. Light resulting from the high-temperature uranium powder was directed into the slit of the spectrometer with an f-matched lens through a sapphire window at the end of the shock tube.

During operation, the driven section was vacuumed down to < 0.01 torr and filled with 100 torr of the desired gas mixture, here pure Argon, then vacuumed down to 2 torr. This process is timed and used to determine a more accurate composition of gases in the end section, factoring in a potential leak of air into the tube using a previously characterized leak rate. For this series of tests, the resulting pressure and composition in the driven section would be about 2.04 torr of ~98% Ar, ~1.7% N_2, and ~0.4% O_2 on average. The driver section would then be filled to the appropriate pressure of Helium gas to achieve the desired shock speed and temperature conditions and the diaphragm section would be filled to half that pressure. Two mylar partitions separate these sections, the thicknesses of which were varied depending on the desired experimental pressures. Once the desired driver section pressure is achieved, the diaphragm section is evacuated, causing the mylar partitions to break in succession as the resulting pressure differential overwhelms them. Subsequently, the shock travels down the tube and reflects off of the end wall, exciting the uranium powder which is loaded onto a knife blade located at the end of the tube prior to the shot (Figure 2.16). Shock velocities in this series were measured to be between 1400 and 2200 m/s.

Since there was an iron impurity present in the shock tube, and uranium signatures did not appear in every test, a set of temperature sensitive iron transitions were used to corroborate the NASA CEA calculated temperatures (Figure 3.12). These transitions were simulated using a process described in Section 2.3.

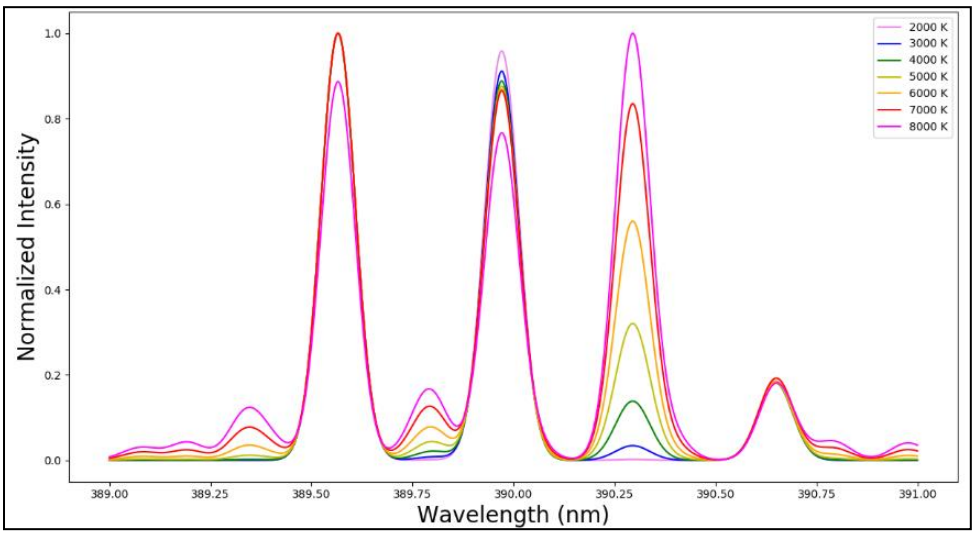

Figure 3.12: Fe I model used to determine spectral temperature for initial shock tube series.

3.4.2. Series 2

After the initial set of experiments, it was determined that additional diagnostics to measure temperature would be desirable to corroborate the high temperatures calculated to have been reached with the NASA CEA program. A three-color pyrometer and a SPEX 270M spectrometer set to the NIR (~1000-1500 nm) were added for this series, which focused on temperatures > 5000 K to isolate when uranium signatures began to appear. The three-color pyrometer features three Thorlabs photodiodes (PDA100A2) and three 10 nm bandpass filters at 620 nm, 700 nm, and 940 nm. These data were logged using a digital oscilloscope (Picoscope 3427). The NIR spectrometer could additionally be used to determine temperature by fitting the continuum spectra produced from the event as well as potential uranium signatures. Figure 3.13 shows the revised setup.

The same visible spectrometer used in the previous round of testing was used for this round. The camera was switched out for the Hamamatsu Line Scan camera (C11165-02). This was so that spectra could be gated for better determination of temperature and isolation of high-temperature uranium signatures from lower temperature iron signatures at later times.

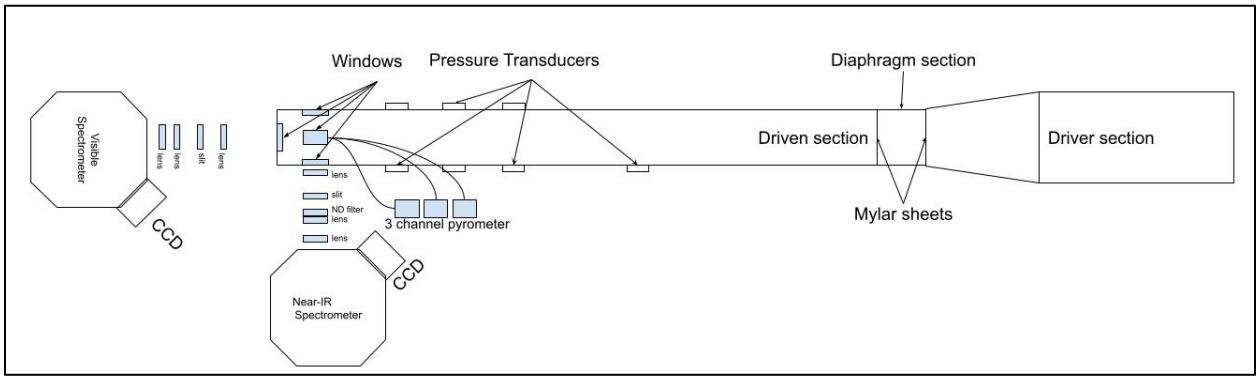

Figure 3.13: Shock Tube Diagnostic Setup for second iteration of experiments (not to scale).

3.4.2.1. Pyrometry

Multi-color pyrometry allows for the determination of a temperature by way of determining the ratio between calibrated photodiode signals of narrow wavelength bands [119]. It is subject to the emissivity of the measured material, so results need to be interpreted accordingly, and some combinations of bands may be less utile in certain temperatures regimes than others. Much of the following is derived from work by Bonefačić and Blecich [120].

Pyrometry depends on Planck's law of blackbody (thermal) radiation (Equation 13):

$$E_\lambda(T) = \frac{C_1}{\lambda^5}\left(e^{C_2/\lambda T} - 1\right)^{-1}$$ *Equation 14*

Here C_1 and C_2 are constants, $2hc^2$ and hc/k, respectively, where h is Planck's constant, c is the speed of light, and k is Boltzmann's constant. Blackbody spectra appear continuous and shift with varying temperature (and therefore energy). If the blackbody is not ideal—either a graybody or otherwise—emissivity, ε, needs to be taken into account otherwise. The blackbody assumption holds that ε = 1, whereas graybody assumption allows for a constant emissivity with $0 < \varepsilon < 1$. It additionally assumes high optical density and that individual spectral features do not occur in the bands being measured.

With pyrometry, multiple wavelengths are considered, and the ratio between two signals is used to determine temperature (Equation 15).

$$\frac{E_{\lambda1}(T)}{E_{\lambda2}(T)} = \frac{\varepsilon_{\lambda1}\frac{C_1}{\lambda_1^5}\left(e^{C_2/\lambda_1 T} - 1\right)^{-1}}{\varepsilon_{\lambda2}\frac{C_1}{\lambda_2^5}(e^{C_2/\lambda_2 T} - 1)^{-1}}$$ *Equation 15*

This expression can be simplified (Equation 16):

$$\frac{E_{\lambda1}(T)}{E_{\lambda2}(T)} = \frac{\varepsilon_{\lambda1}\lambda_2^5\left(e^{C_2/\lambda_1 T} - 1\right)^{-1}}{\varepsilon_{\lambda2}\lambda_1^5(e^{C_2/\lambda_2 T} - 1)^{-1}}$$ *Equation 16*

When solving for temperature, the equation takes this form (Equation 13):

$$T = \frac{C_2\left(\frac{1}{\lambda_2} - \frac{1}{\lambda_1}\right)}{\ln\frac{L_{\lambda1}(T)}{L_{\lambda2}(T)} + \ln A - \ln\frac{\varepsilon_{\lambda1}}{\varepsilon_{\lambda2}} - 5\left(\frac{\lambda_2}{\lambda_1}\right)}$$ *Equation 17*

Here, *L(T)* values refer to photodiode measured signal from a given test, and A is a correction factor determined from a source of known temperature. Emissivity can potentially be neglected so long as they are approximately equal. For the work detailed here, a Quartz Tungsten Halogen (QTH) lamp from (Newport 6332) with a filament temperature of 3400 K was used.

$$A = \frac{Q_{\lambda2}(T)E_{\lambda1}(T)}{Q_{\lambda1}(T)E_{\lambda2}(T)} = \frac{Q_{\lambda2}(T)\varepsilon_{\lambda1}\lambda_2^5\left(e^{C_2/\lambda_1 T} - 1\right)^{-1}}{Q_{\lambda1}(T)\varepsilon_{\lambda2}\lambda_1^5(e^{C_2/\lambda_2 T} - 1)^{-1}}$$ *Equation 18*

Here, *Q(T)* values refer to the photodiode measured signal from the QTH lamp, and ε_λ values refer to calculated emissivity values of the lamp based on manufacturer reported values and a blackbody spectrum of the same temperature.

The bandpass filters utilized for this work had wavelengths of 620, 700, and 940 nm and a FWHM of 10 nm each. These ranges are overlaid with a blackbody spectrum of the same temperature as the QTH lamp as well as spectra from other temperatures in the range of interest to illustrate their change (Figure 3.14). Here $\varepsilon = 1$.

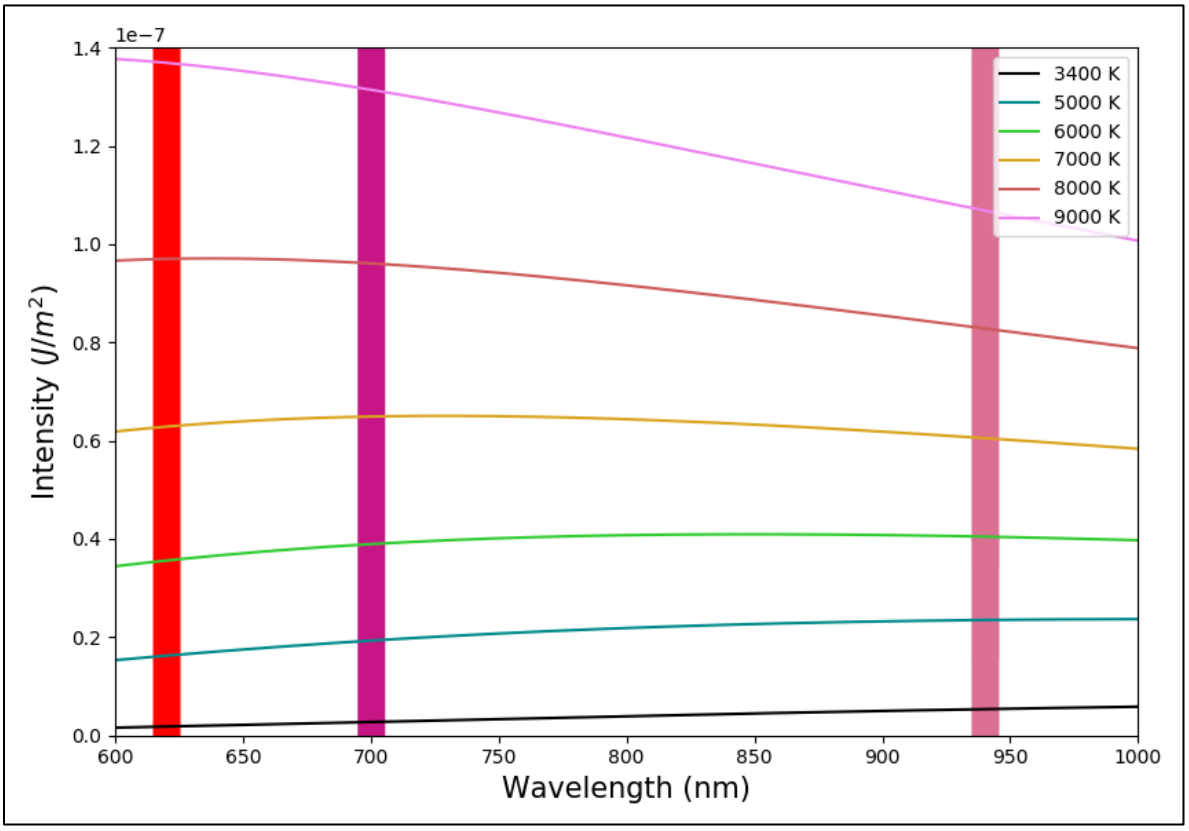

Figure 3.14: Blackbody spectrum at various temperatures with regions of interest highlighted – 620, 700, 940 nm bands.

The temperatures that would be yielded from theoretical ratios of photodiode traces for a few wavelength dependences of emissivity are shown in Figure 3.15.

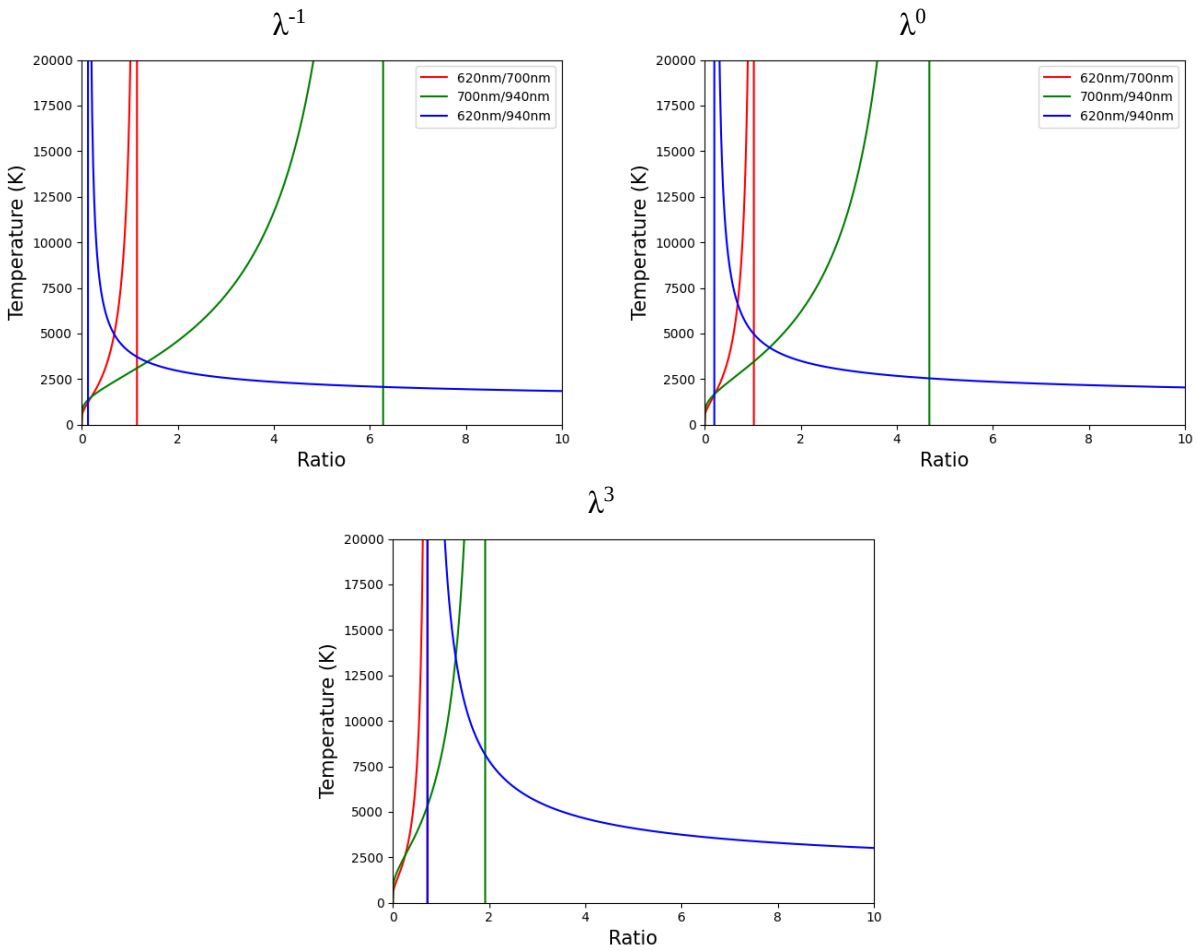

Figure 3.15: Temperatures yielded from bandpass filter ratios for different emissivity-wavelength dependences.

3.5. Flash powder testing

A six-inch cube chamber was set up containing a custom-built sparking apparatus connected to leads from a custom-built fire set (Figure 3.16).

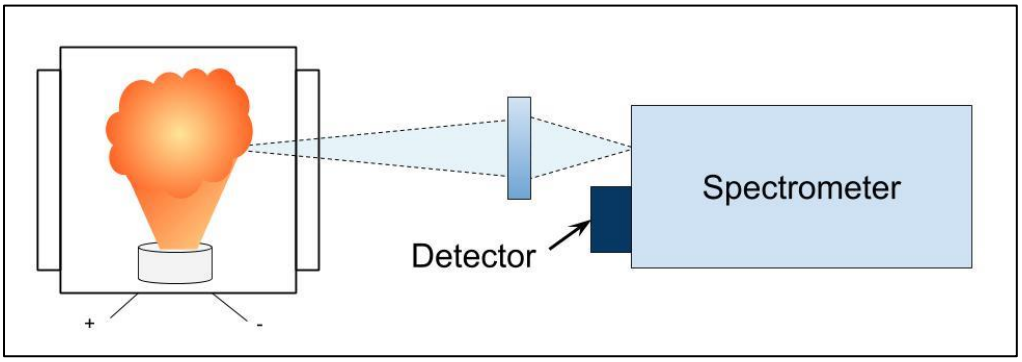

Figure 3.16: Simplified flash powder testing schematic.

A custom-built 1.5-meter Czerny-Turner spectrometer (2400 gr/mm grating) was used to capture high-resolution spectra in the region where atomic and ionic Cs and atomic Sr peaks were expected to appear from flash powder ignition in a table-top chamber setup (around 460 nm). The Andor iDus 420 CCD (1024 x 255 pixels, 26 x 26 µm pixel size) was used to acquire spectra.

A SPEX 270M with 300 gr/mm grating was used to perform standoff testing more closely mirroring planned field-test conditions viewing the 580-980 nm region. Here, signatures from SrOH and Cs I were expected to appear. A Hamamatsu Line Scan camera (C11165-02) was used to acquire spectra.

Using Equation 11 and Equation 12, flash powders of $Sr(NO_3)_2$ and Mg or Al doped with a small amount of Cs_2CO_3 were detonated to view the resulting signatures. Additionally, two mixtures of powders containing a multitude of fission products in different ratios were tested to determine differences in spectra produced. These were not strictly flash powders since the masses were calculated to represent the distributions of independent fast fission products of U^{235} and Pu^{239}. Considering the figures of merit discussed previously, cost, and material availability, the powders used for the mixture are listed in Table 3.3.

For the fission powder mixture tests, the spectral region was tuned between 400 and 900 nm increments of ~130 nm.

Table 3.3: Masses for fission product mixtures.

Material	**U^{235} mixture mass (g)**	**Pu^{239} mixture mass (g)**
Rb_2CO_3	1.5117	0.7065
$Sr(NO_3)_2$	3.9642	2.6292
Zr	1.5086	1.6268
Mo	0.3641	1.5835
Ru	0.0010	0.4189
Sb	0.9730	0.9081
Cs_2CO_3	2.1733	1.9258
$BaCO_3$	2.8028	2.4642
$La_2(CO_3)_3*H_2O$	1.5880	1.4447
$Ce_2(CO_3)_3*H_2O$	0.9200	1.2550
$Nd_2(CO_3)_3*H_2O$	0.0815	0.3698
$Sm_2(CO_3)_3*H_2O$	0.0027	0.0604
$Eu_2(CO_3)_3*H_2O$	0.0002	0.0108
$Y_2(CO_3)_3*H_2O$	2.5944	2.1355

3.6. Small-scale high explosive testing

A high explosive charge containing small amounts of Sr and Cs chlorides was detonated in the black pill blast chamber shown in Figure 3.17.

Figure 3.17: Image of black pill chamber (right, courtesy of Terry Yu).

The same SPEX setup as the flash powder testing for the NIR range was used to observe this experiment and the resulting Cs and Sr signatures, as well as the potential appearance of signatures from the high explosive.

3.7. Field-scale high explosive testing

After the lab-scale preliminary tests were conducted with high explosives, a series of field tests were conducted at the Naval Surface Warfare Center's Blossom Point Facility to determine the appearance of different amounts of Cs and Sr signatures corresponding to different amounts of their carbonates contained in the explosive charges, henceforth referred to as Ratio 1 (6.1 Cs/5.8 Sr) and Ratio 2 (6.6 Cs/2 Sr). Two SPEX 270 spectrometers were fielded as in the flash powder and lab-scale explosive experiments (Figure 3.18 and Figure 3.19). They were at a 115 m standoff from the detonation.

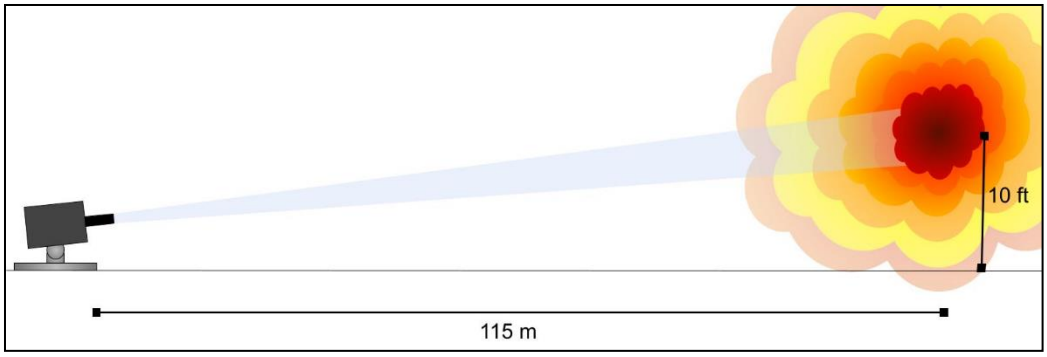

Figure 3.18: Schematic of field testing. Test instruments were located 115 m away from the event. Charge was suspended 10 ft above the ground.

Charges with different metals, copper or magnesium, were assembled with each of the ratios as well as varying explosives to determine how differently oxidizing metals and other components affected spectral output.

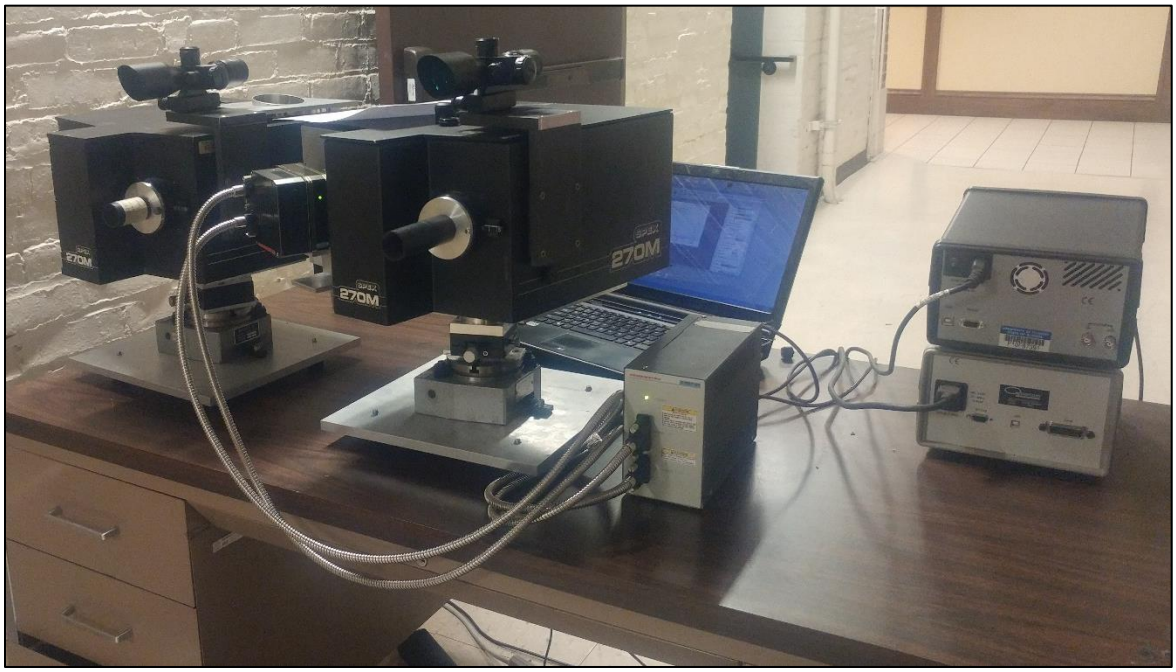

Figure 3.19: Image of mock field test setup.

Both spectrometers were SPEX 270M with 1-inch diameter achromat entrance optics that enabled focus at the distance of the test detonation. They were placed on stages that allowed rotation and tilt for aiming at the event with rifle scopes mounted atop them. One spectrometer targeted the 450-485 nm range with a 2400 gr/mm grating in order to observe Cs and Sr signatures with a Hamamatsu array camera (C7042-01) having an acquisition rate of 110 fps. The other targeted the

580-920 nm range containing SrOH and Cs I signatures with a Hamamatsu line scan camera (C11165-02) having an acquisition rate of 2777 fps. A Chronos high-speed camera (CR14-1.0-8C) was used to image the explosions. Acquisition was timed using three Quantum Composers pulse generators as well as a TTL (transistor-to-transistor logic) signal provided by onsite explosives handlers prior to the explosion. Data generated from this test series was applied to the development of predictive models to generate synthetic spectral signatures by collaborators at CRAFT Tech.

CHAPTER 4: RESULTS AND DISCUSSION

In this chapter, the results of the various experiments performed to investigate and identify signatures of interest to nuclear remote sensing applications are presented. An attempt to estimate the amount of uranium monoxide present in previous laser ablation testing is summarized, and parameters deemed necessary for further quantification are addressed. Uranium combustion behavior and signatures resulting from its combustion in a dust cloud as well shock-induced high-temperature emissions are shown, and implications are discussed. More exploratory testing to identify fission product signatures of interest and results thereof are also presented in this section.

4.1. Uranium Monoxide Estimation

In order to quantify uranium monoxide present from absorption in a given system, a partition function must be determined. Relations presented in this section are informed largely by the works of Laurendeau and Herzberg [16], [43]. The partition function is a temperature variant quantity that is representative of all the energy states of a given atom or molecule. In calculating this, temperature, volume, and total particle number are considered fixed (assumption of equilibrium during the time of measurement). The general form is shown in Equation 19 [16].

$$\mathrm{Z} = \sum_i g_i e^{-\frac{\varepsilon_i}{k_B T}} \qquad \textit{Equation 19}$$

Here, ε_i is the energy of a given state, g_i is degeneracy or the number of states that share the same energy, k_B is Boltzmann's constant, and T is temperature.

As mentioned previously, energy can be stored in different modes in an atom or molecule and each of these modes contribute to the partition function. Thus, the partition function can be represented (Equation 20) [16]:

$$\mathrm{Z} = \mathrm{Z}_t * \mathrm{Z}_r * \mathrm{Z}_v * \mathrm{Z}_e \qquad \textit{Equation 20}$$

Where Z_t, Z_r, Z_v, and Z_e, are the translational, rotational, vibrational, and electronic contributions, respectively. The translational mode is separated from the other three modes, which are considered to be internal energy storage. It is dependent on the mass of the molecule, which is held as a constant and can be neglected for these purposes.

Z_r is a function of the characteristic rotational temperature, θ_r, symmetry, σ, and the temperature of the system. This function can be represented differently depending on the temperature regime. As the temperatures in this document are higher ($T/\theta_r >> 30$), the relevant equation is as follows (Equation 21) [16]:

$$Z_r = \frac{T}{\theta_r \sigma} \qquad \textit{Equation 21}$$

When the appropriate constants are input (Equation 22):

$$\theta_r = \frac{hc}{k_B} B = 0.4789 \qquad \textit{Equation 22}$$

Here, B is the rotational constant of the lower state of the transition, 0.333 cm^{-1}, which is dependent on the distance between the two atoms, 1.838 Å [42], and their reduced mass, $\mu = (m_1 * m_2)/(m_1+m_2)$. Since UO is diatomic, $\sigma = 1$.

Z_v is dependent on the characteristic vibrational temperature, θ_v, and temperature (Equation 23) [16]:

$$Z_v = (1 - e^{-\theta_v/T})^{-1} \qquad \textit{Equation 23}$$

For ω_e = 846.5 cm^{-1} [16], [39]:

$$\theta_v = \frac{hc}{k_B} \omega_e = 1217.93 \qquad \textit{Equation 24}$$

And lastly, the electronic partition function is more reminiscent of the general form, but is applied directly to the many possible electronic states which are tabulated in Reference [40]. It is important to note here that the this is not a complete list of electronic states. Work is currently in process to find and characterize more of these states using techniques like laser ablation. The addition of these states will alter the resulting partition function.

To determine of concentration, Equation 25 must be used [16].

$$\frac{N_i}{N} = \frac{Z_i}{Z} \qquad \textit{Equation 25}$$

Where N_i is the population of a given state, N is the total number of molecules, Z_i is the partition function of a given state, and Z is the total partition function. Z_i/Z for the electronic component of

the UO partition function for the 593.55 nm transition (Figure 2.12, E_l = 0 cm^{-1}, E_u = 16845 cm^{-1}) is shown in Figure .

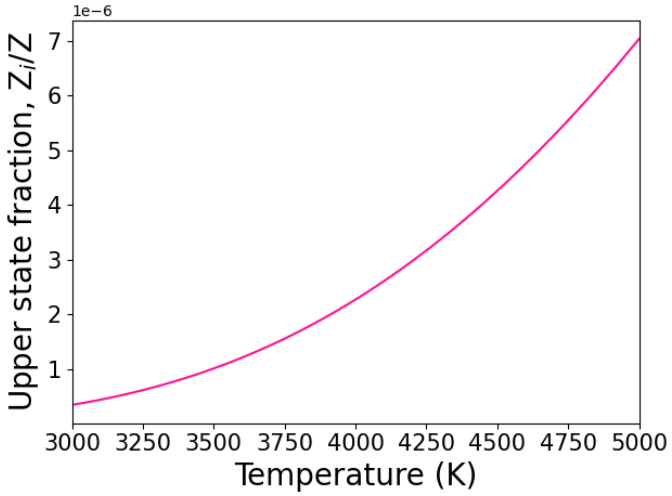

Figure 4.1: Boltzmann upper state fraction variation with temperature for 593.55 nm UO transition, E_u=16845 cm^{-1}.

From an absorption measurement, N_i can be determined (Equation 6) [16]. Recall that W_{lu} is integrated absorption obtained from the measurement, L is the pathlength over which the measurement was taken, B_{lu} is the Einstein absorption coefficient, and υ_{ul} is the wavenumber of the transition.

In the case of uranium monoxide, there is an incomplete set of information available to determine exactly the amount that might appear in an absorption measurement like the one previously shown in Figure 2.12. Much of the work to determine the information that does exist was undertaken by Heaven, Kaledin, and their collaborators over a few decades [39], [40], [42], [45], [46], [121]. Due to the crowded nature of uranium monoxide electronic transitions, it is difficult to isolate individual spectral features to determine more specific information for further analysis. This isolation will require higher resolution techniques such as Tunable Diode Laser Absorption Spectroscopy (TDLAS).

Thus, in estimation of concentration using observed absorption spectra of UO, some liberties must be taken. This is in part due to difficulty in discerning individual transitions. Work by Mulliken suggests that a transition that appears to be a continuous feature can be treated as ‘very broad atomic line’ using several assumptions (the nuclei of the molecule are held in a fixed configuration but allowed to vibrate and rotate) [122]. This text holds that the total strength of the transition

should be independent of temperature since change in temperature should only cause a redistribution of population within the molecule. This assumes that the entire extended structure of the molecule is captured in a given measurement, which is not unreasonable for crowded UO.

The transition chosen for initial calculations is shown in Figure 4.2. Lines that overlap the transition are overlaid from the supplementary material provided for Reference [39]. It is unclear if these lines are characterized for $U^{238}O^{16}$ or $U^{238}O^{18}$, which would exhibit a slight shift in spectrum due to the slightly different mass. This shift has been characterized further in other, more recent sources [30], [31]. This region is bounded on one side by a strong U I transition and has a dearth of identified lines between around 593.55 nm and 593.78 nm. Wavenumbers and lower state J terms for these lines are reported in Table 4.1.

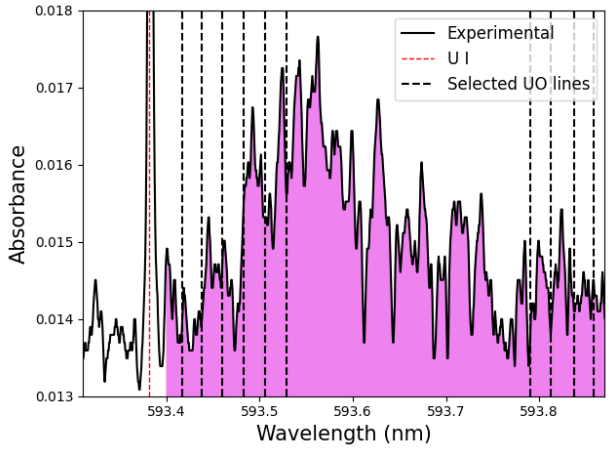

Figure 4.2: Reproduction of Figure 2.12 with shaded area of interest. Black vertical lines were reported by Kaledin and Heaven [39]. *Red vertical line is a U I transition.*

Table 4.1: Lines of interest from Reference [39].		
Line	**Experimentally observed (cm^{-1})**	**J''**
R(9)	16851.57	9
R(8)	16850.97	8
R(7)	16850.34	7
R(6)	16849.69	6
R(5)	16849.04	5
R(4)	16848.39	4
P(6)	16840.97	6
P(7)	16840.34	7
P(8)	16839.62	8
P(9)	16839.03	9

The shaded region represents the area (in frequency) taken to be integrated absorption, W_{lu}. Pathlength, L, of the system was known to be 0.012 m from previous testing under similar conditions [35].

Using Mulliken's work, the dipole strength and oscillator strength can be approximated using two equations [122]:

$$D_{ul} = \frac{3h}{8\pi^2 mcg_u}\frac{f_{lu}}{\upsilon_{lu}} = 0.912\times10^{-11}\frac{f_{lu}}{g_u\upsilon_{lu}} = 3.83\times10^{-19}\frac{W_{lu}}{g_u\upsilon_{lu}} \qquad \textit{Equation 26}$$

$$f_{lu} = \frac{mc^2}{n\pi e^2}W_{lu} = 4.20\times10^{-8}W_{lu} \qquad \textit{Equation 27}$$

Here D_{ul} is dipole strength, which appears analogous to transition moment, f_{lu} is oscillator strength, m is the mass of an electron, e is the elementary charge, g_u is the upper state degeneracy, and n is a value that Mulliken obtained from Ladenburg and Van Voorhis [123]. For the constants Mulliken determined, υ_{lu} must be input in units of cm^{-1}.

The Einstein coefficients remain to be determined (Equation 28 and Equation 29):

$$A_{ul} = \frac{64\pi^4{\nu_{ul}}^3e^2}{3h}g_l\mathrm{D}_{ul} = \frac{64\pi^4{\nu_{ul}}^3}{3h\varepsilon_0 g_l}|R^{ul}|^2 \qquad \textit{Equation 28}$$

$$B_{lu} = \frac{8\pi^3e^2}{3h^2c}g_uD_{ul} = \frac{A_{ul}}{8\pi hc{\nu_{ul}}^3}\frac{g_u}{g_l} \qquad \textit{Equation 29}$$

Here, $|R^{ul}|$ is the transition dipole moment, which for UO is unknown. The last unknown is temperature, which partition function is dependent on. Since this was unknown, N was estimated for a range of temperatures from 3000-5000 K based on UO appearance a test series in which U_3Si_2 was ablated (Figure 2.9, Figure 2.10) [37]. For these equations, degeneracy should be a value less than 3 [122]. In a calculation performed using the J terms reported by Kaledin and Heaven, the degeneracy of the lower state of the transition was found to be 9, and the upper state is estimated to be the similar [40]. Thus, this may be one source of deviation. Another lies in the *n* input to the equation for oscillator strength (Equation 27). This parameter was determined in the context of an oxygen band in the VUV, and while it was found to be a decent approximation to molecular gases, UO is larger and perhaps more complex than O_2 [123].

Thankfully, Tyagi et al. has tentatively determined the oscillator strength of this transition to be 0.2008 using computational methods [47]. This allows for the use of slightly altered relations from Equation 28 and Equation 29 in terms of f_{lu} as determined by Hilborn (Equation 30 and Equation 31) [124].

$$A_{ul} = \frac{g_l 2\pi f^2 e^2}{g_u \varepsilon_0 m c^3} f_{lu} \qquad \textit{Equation 30}$$

$$B_{lu} = \frac{e^2}{4\varepsilon_0 m h f} f_{lu} \qquad \textit{Equation 31}$$

Where f is the frequency of the transition, and ε_0 is the permittivity of free space, 8.854E-12 F/m. As is well-outlined in Hilborn, all of these parameters (oscillator strength, transition moment, and Einstein coefficient) are interrelated and if one of them is found, the others shall be known. Using Equation 31 and Equation 24, N, the total number density of UO was calculated for g_l = 1 and 2 per Milliken's parameters and g_l = 9 from Heaven and Kaledin (Figure 4.3).

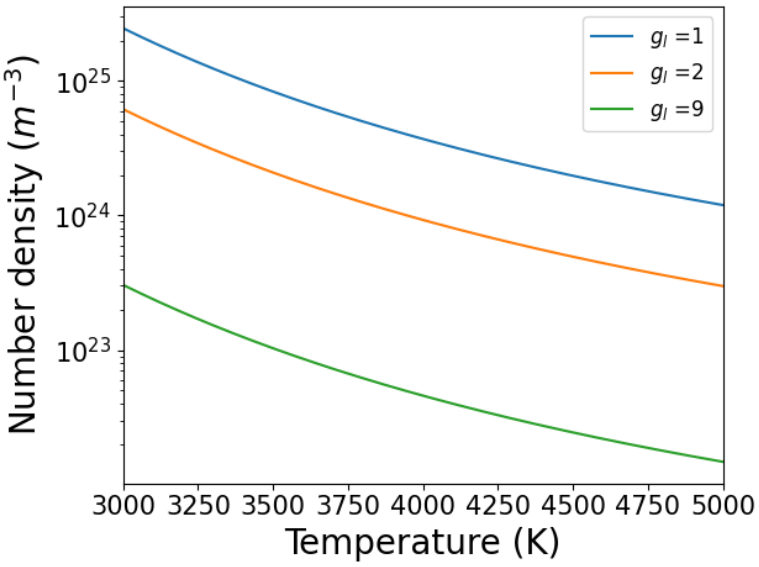

Figure 4.3: Calculated UO number density for possible degeneracies over 3000-5000 K.

A model developed by Finko et al. suggests that the number density of UO should be on the order of that of U I species in these conditions [23]. Data tracking U I and U II number densities in similar conditions to this spectrum would suggest that the number density of UO should be higher—U I and U II number densities on the order of 10^{20} m^{-3} and 10^{19} m^{-3}, respectively (Figure 4.4).

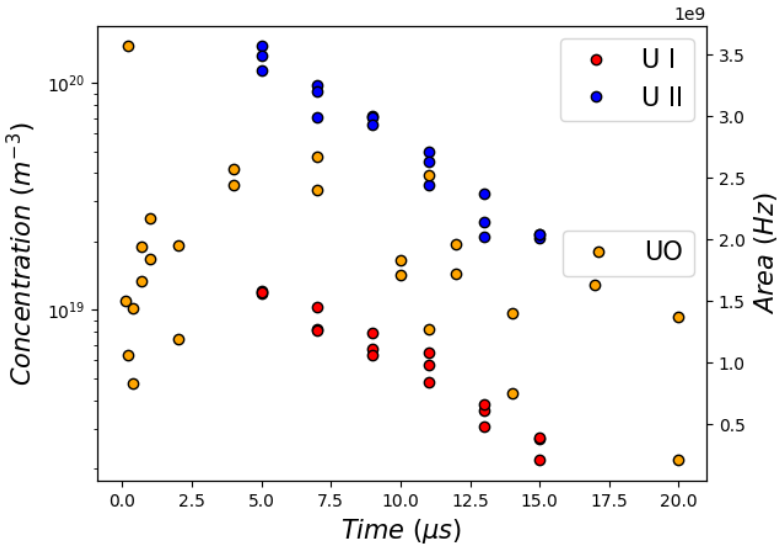

Figure 4.4: Concentration of U I and U II (left axis) and band area of UO (right axis) in laser ablation absorption tracked over delay time in a 15 torr, 10%/ 90% Ar environment.

Temperatures were averaged for each delay time between those calculated for U I and U II (shown in Figure 4.5 for the same experiment), and were fit to delay time since temperature decreased over time, and UO temperature could be directly measured due to lack of information available.

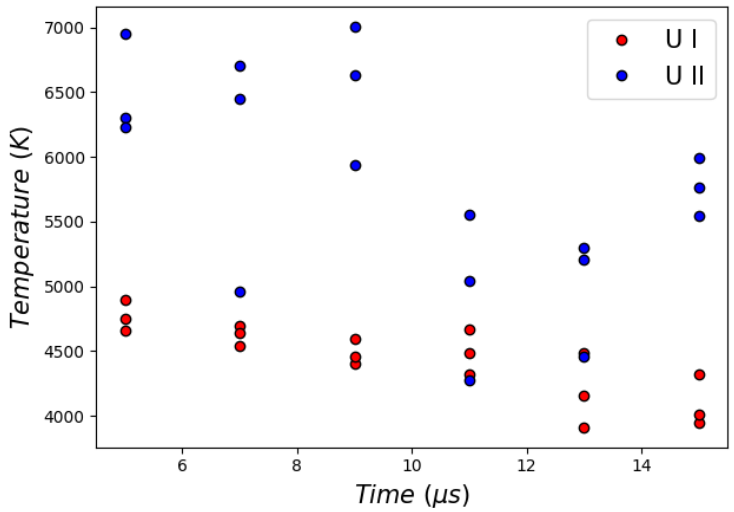

Figure 4.5: Temperature of U I and U II in laser ablation absorption tracked over delay time in a 15 torr, 10%/ 90% Ar environment.

With the assumption of local thermodynamic equilibrium, temperature should be approximately the same for all species measured in the optical path at a given time. From Figure 4.5, this is inaccurate, but without a better determination of UO temperature, this will have to do for now. Selecting $g_l = 9$ and with fit temperatures, the UO band area data in Figure 4.4 yields the number density data shown in Figure 4.6(a). Figure 4.6(b) shows number density data if temperature is fixed at 4000 K.

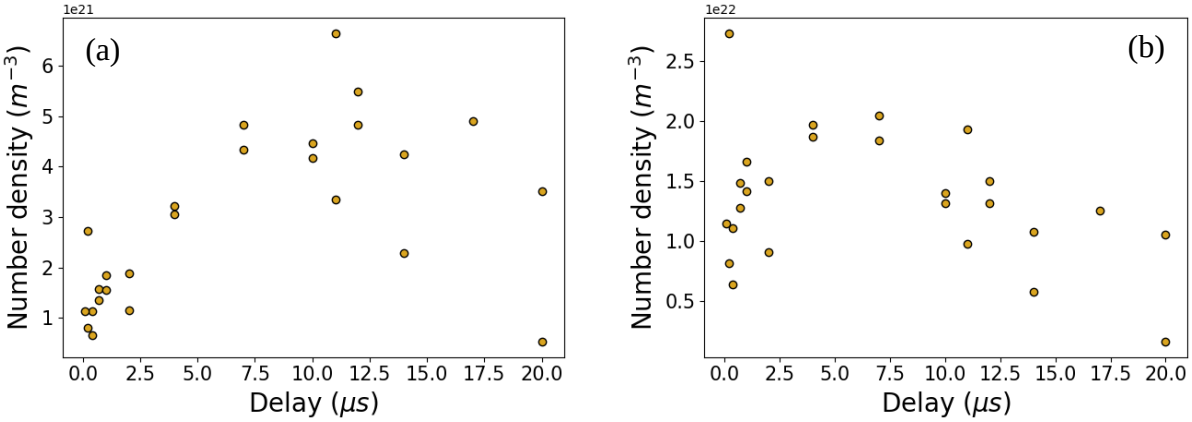

Figure 4.6: Number density of UO over time after initial ablation: (a) temperature variant based on LTE assumption, (b) T = 4000 K.

These numbers are not completely unreasonable, but are a few orders of magnitude higher than would be expected. More concrete determination of the transition moment for this band would also be helpful for absolute quantification of number density. Both oscillator strength and transition moment are quantities that can be used to determine Einstein coefficients for diatomic transitions, so accurate determination of these is necessary for absolute measurement from an absorption spectrum. Using the oscillator strength from Tyagi et al., B_{lu} was found to be 4.77E20 m/kg (m^3/Js^2). Hilborn also has a relation for transition moment in terms of oscillator strength [124]:

$$|\mathrm{R}^{ul}|^2 = \frac{3g_l h e^2}{8\pi^2 g_u m f} f_{lu} \qquad \textit{Equation 32}$$

If we set $g_u = 9$, R^{ul} comes out to around 1.679E-29 Cm. This degeneracy value is gleaned from the J term nearest to the null gap of this system [39]. Again, Tyagi et al.'s determination of oscillator strength is tentative, and these results should be evaluated thusly. There are several sources of uncertainty for this number density determination including the use of an averaged-temperature for calculations; the underlying principle that one Einstein coefficient can be representative of the entire band may also be problematic. Energy level information for UO is currently incomplete which affects the resulting electronic partition function necessary for this number density calculation. These uncertainties can be remedied by future research: higher-resolution measurements of UO to determine variation with temperature, exploration of new low-lying UO signatures using laser-ablation and similar techniques, and more definitive determination of oscillator strength or transition moment.

4.2. Dust cloud combustion

4.2.1. Burn time measurement and comparison

Burn time data was obtained for several metal powders that had been sifted to <10 μm in diameter (Figure 4.7). These experiments were designed to provide relative information on uranium combustion kinetics in the test configuration. Burning time data based on luminosity traces for Al, B, Hf, Fe, Mo, Si, Ta, Ti, W, Zr, and U were obtained. The Al burn times were found to be comparable to those reported by Gill et al. for similar diameters [125]. B particle burn times were slightly longer than those previously reported for single-particle measurements in acetylene flames, but were similar to those from laser ignition [126]. Fe burn time was also comparable [127]. Titanium burn times were similar to those reported by Badiola and Dreizin for laser spark

ignition, and Zr burn times were slightly longer [57]. Similar data for Hf, Mo, Si, Ta, and W were not found in the literature for particles of similar size.

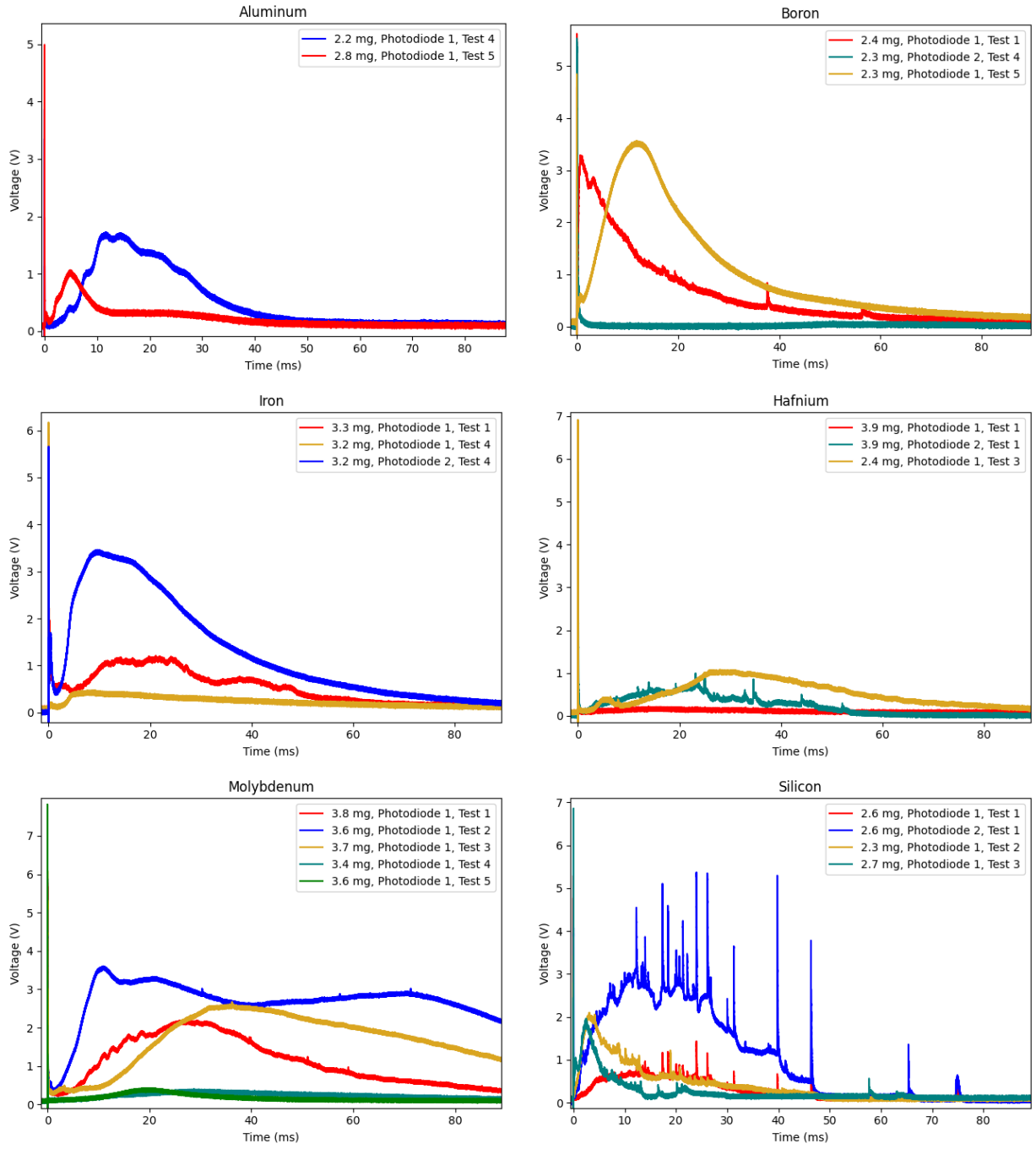

Figure 4.7: Selected photodiode traces used to determine burn times for various metals tested.

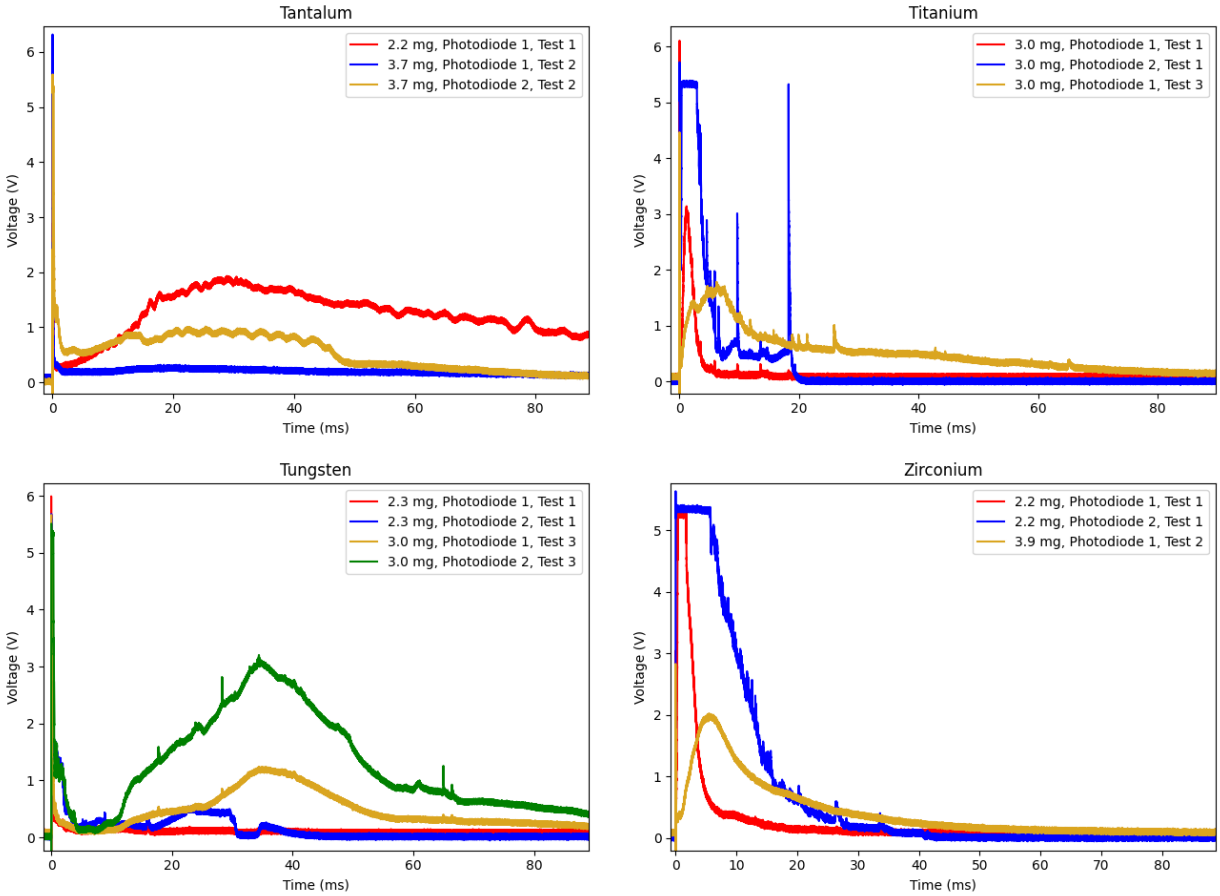

Figure 4.7 continued.

As for uranium, Read did some preliminary measurements in his thesis [105]. These burn times were much shorter than those reported in this document on average, possibly due to the much lower ambient pressures, different neutral density filtration (to prevent detector saturation), and larger masses tested (Figure 4.8).

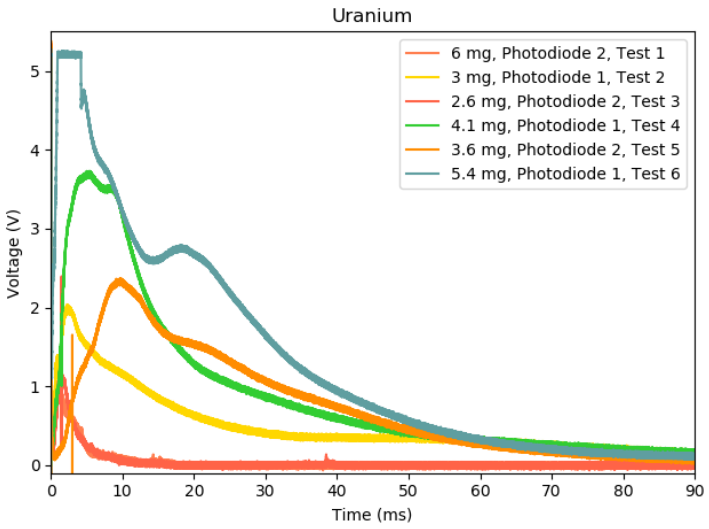

Figure 4.8: Uranium combustion burn time traces.

Multiple of these materials were founded to burn heterogeneously in the literature. Based on the previous work for the system, it is unlikely that temperatures over 4000 K were reached [105]. Burn times for each material tested are summarized in Figure 4.9. For some species, there is considerable variation in measurements.

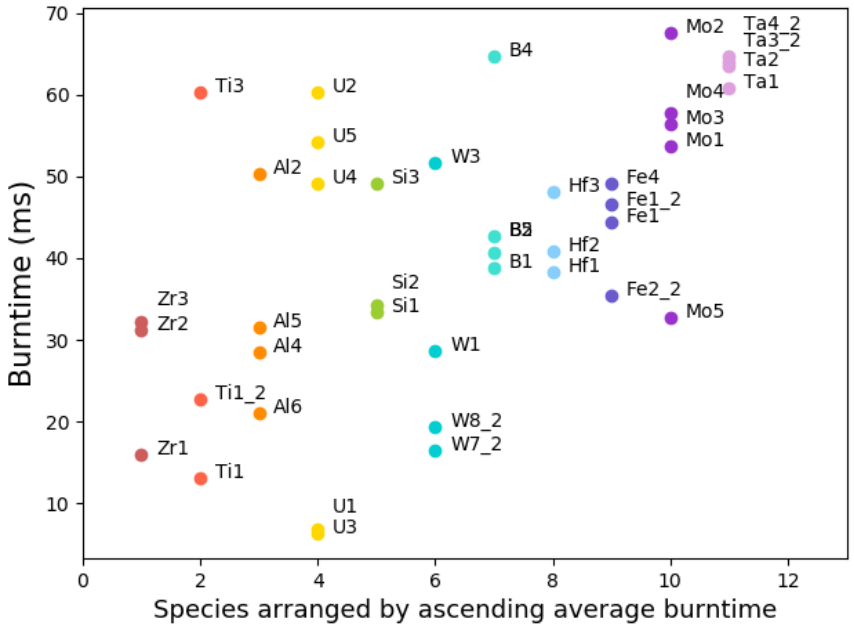

Figure 4.9: Burn time comparison between various metal powders.

These results on average correlate to relative burn time data in which Zr had shorter burn times than Ti for particles of roughly the same size [57] and results in which Al had longer burn times

than Ti powders [128]. In tests of small amounts of high explosive materials doped with Al and B, B exhibited the slower burn rate [129]. Since these data correlate with relative burn times found in other publications, it may be reasonable to conclude that U burn times are on average longer than that of Zr, Ti, and Al, and shorter than that of other species tested for particles of the same size.

4.2.2. Particle combustion behavior

Burn behavior was also observed for each material tested. At the temperature range tested, uranium is expected to burn heterogeneously, since its oxide volatilization temperature is lower than the metal boiling point. A storyboard of uranium dust cloud combustion is shown in Figure 4.10 in a 1 atm air environment.

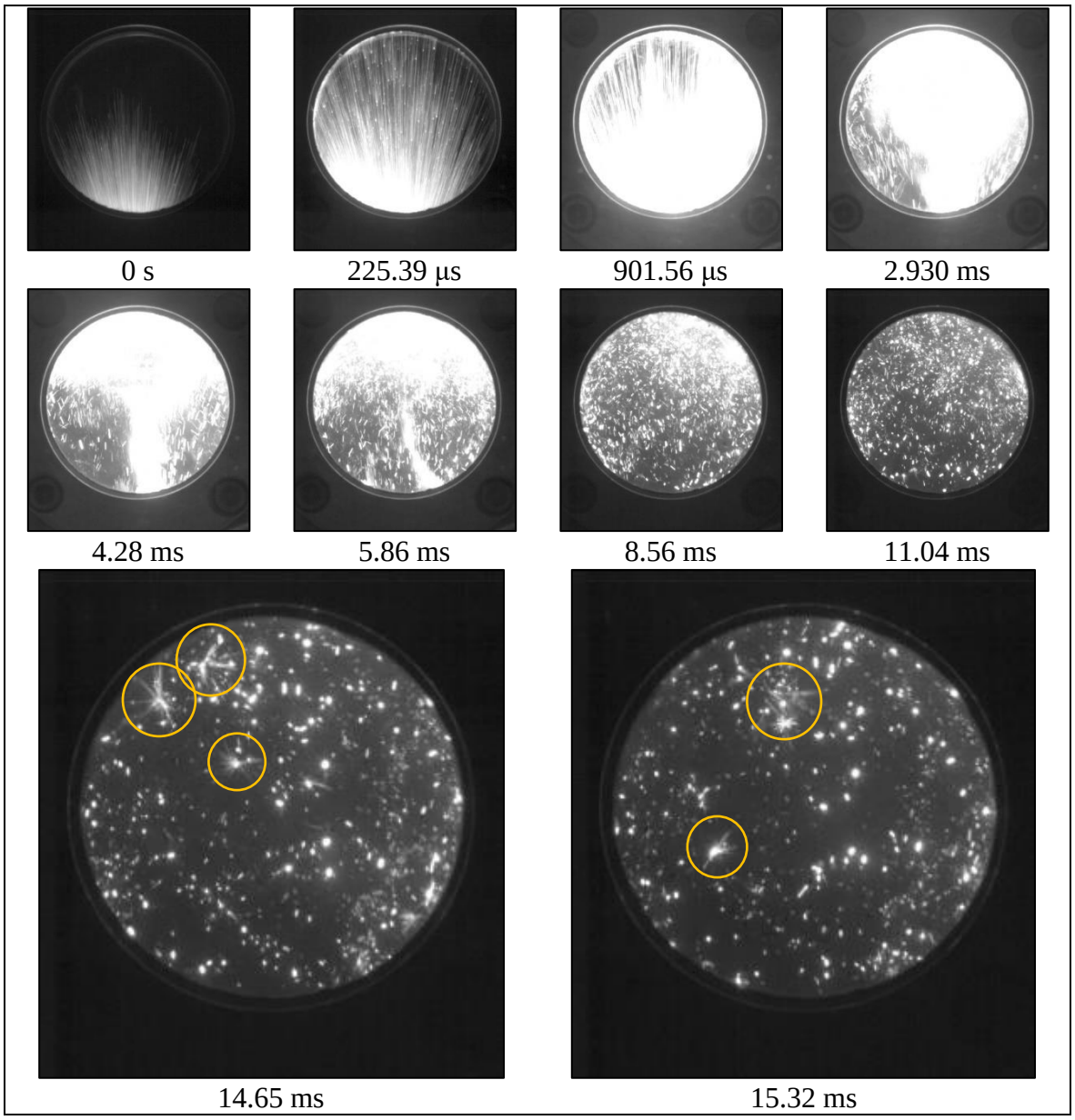

Figure 4.10: Storyboard of dust cloud combustion of 0.0287 g uranium in 1 atm air environment. Circles indicate exploding agglomerates.

There is an exploding particle agglomerate effect at later times, circled on the images. This phenomenon is similar that seen by Zepper et al. in aluminum combustion and by Dreizin in refractory materials such as zirconium and titanium [58], [59], [130]–[132]. As zirconium combusts in the presence of air, liquid ZrO_xN_y intermediates form with gaseous nitrogen contained in voids. ZrO_2 precipitates out, and newly exposed Zr burns with gaseous oxygen as the previously contained nitrogen escapes [58], [59]. A similar process occurs in titanium combustion, wherein a liquid solution of Ti, O, and N containing gaseous nitrogen contain voids simultaneously forms

stable titanium oxides and an unreacted Ti surface whilst gaseous nitrogen escapes [133]. It stands to reason that this sequence of events is also occurring in the exploding particles of uranium.

Figure 4.11 shows images for the aluminum dust cloud. Since the oxide volatilization temperature is higher than that of the metal boiling point, Al is expected to burn in the vapor phase.

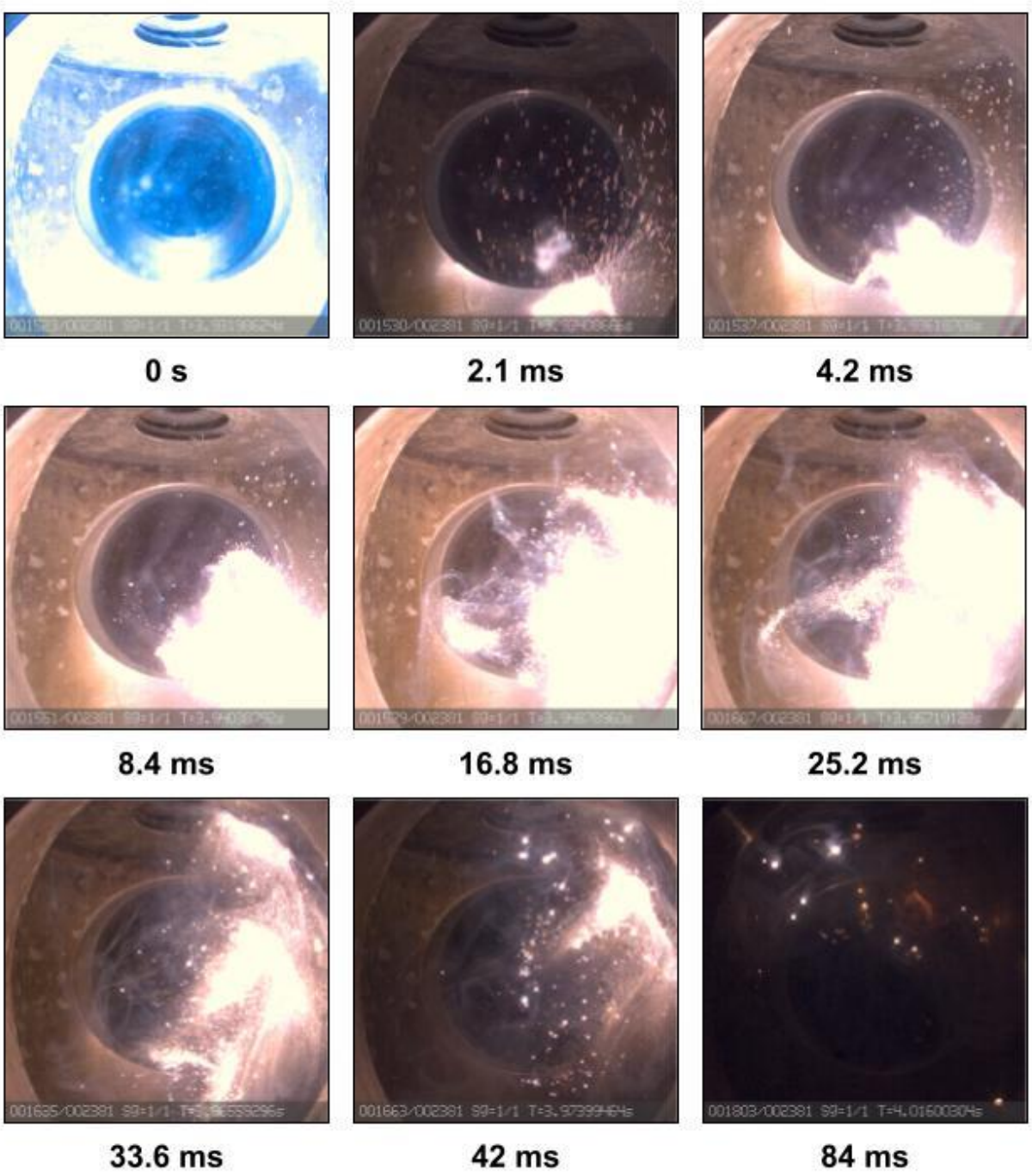

Figure 4.11: Aluminum dust cloud storyboard (2.2 mg).

Like uranium, boron is expected to burn heterogeneously (Figure 4.12). This is corroborated in other references [87][126].

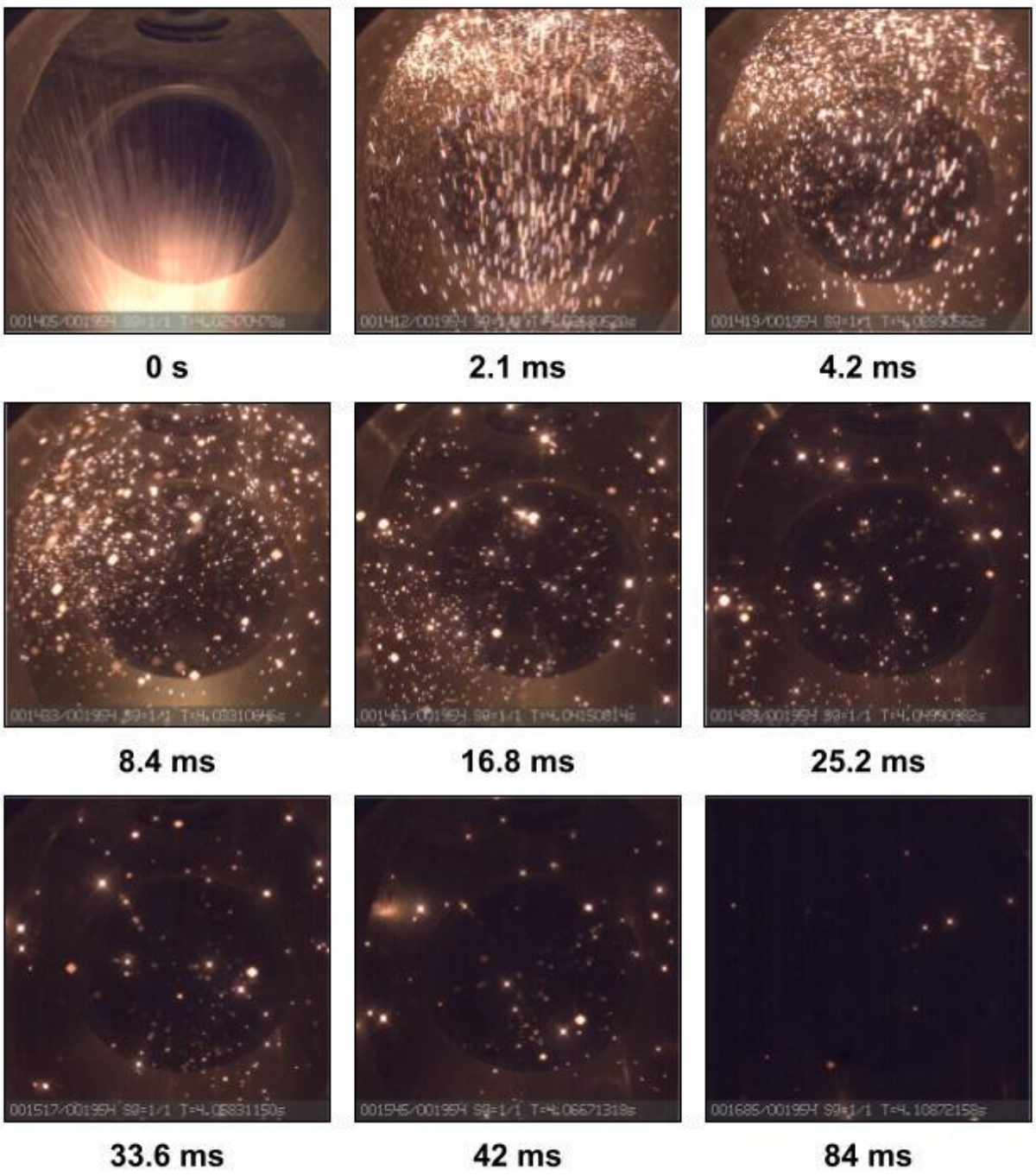

Figure 4.12: Boron dust cloud storyboard (2.4 mg).

Since iron oxide volatilization is higher than the metal, homogeneous combustion is expected to occur. As in the aluminum images, clouds of vapor appear to combust (Figure 4.13).

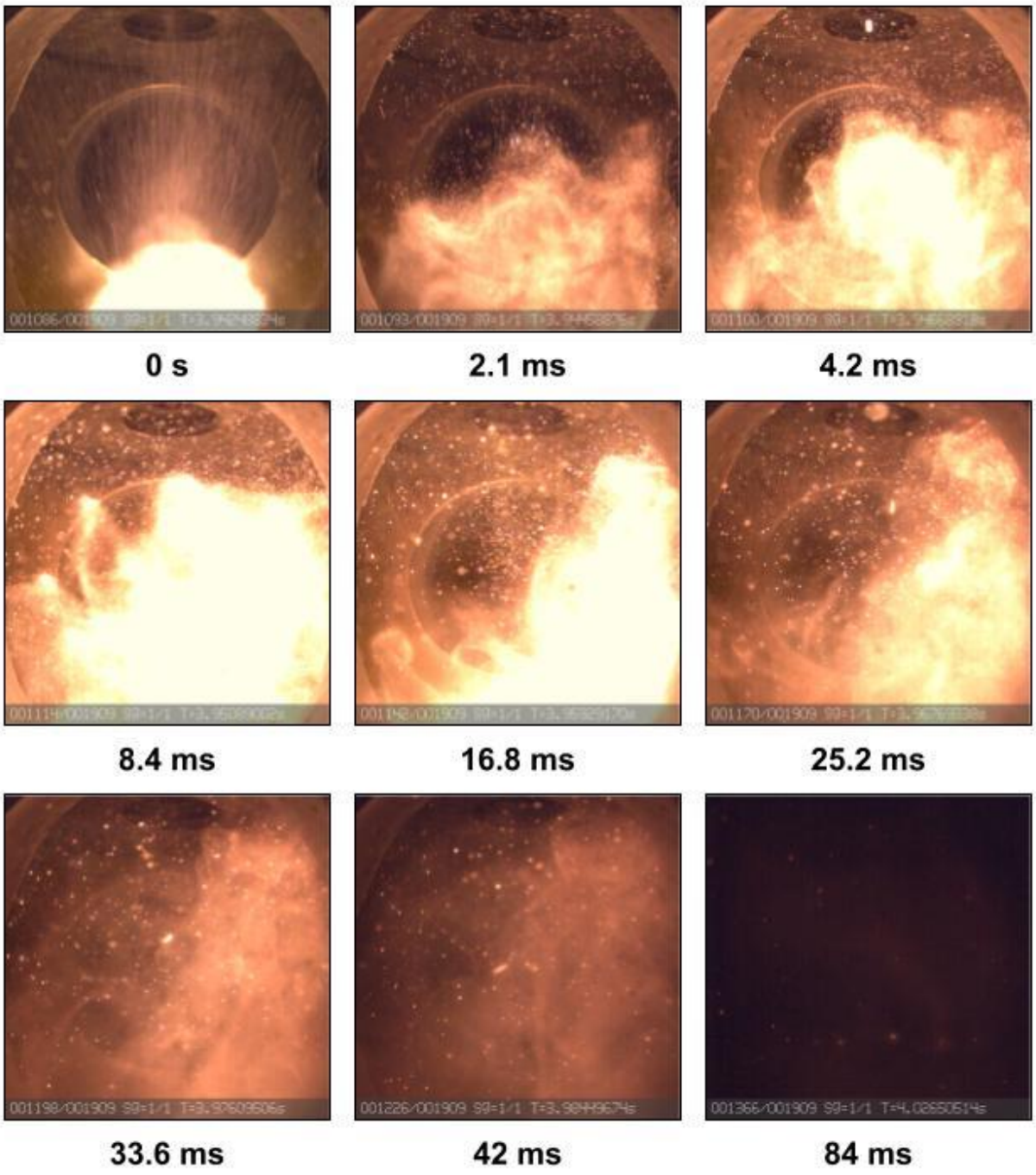

Figure 4.13: Iron dust cloud storyboard (3.3 mg).

Hafnium oxide volatilization temperature is also lower than the metal boiling point, so heterogeneous combustion proceeds (Figure 4.14). Here, exploding particle behavior was observed.

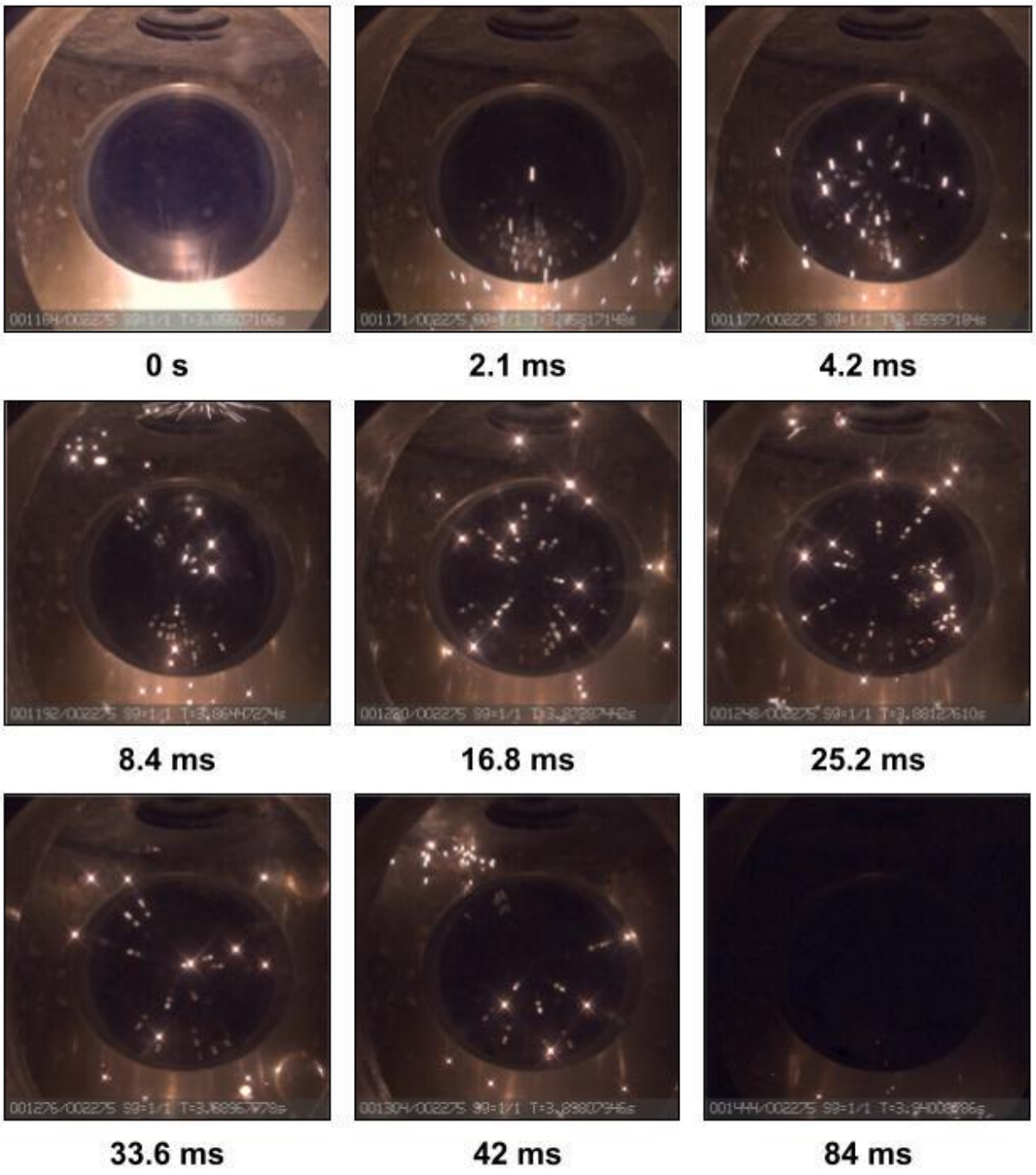

Figure 4.14: Hafnium dust cloud storyboard (3.9 mg).

Due to the fine particle size of Mo (all powders were sifted down, but Mo had among the lowest initial particle sizes), it initially appears to be combusting in a vapor cloud, but Markstein attributes the 'smoke' produced in Mo particle combustion to oxide vapor (Figure 4.15) [71]. Of the materials tested, Mo has the largest discrepancy between its low oxide volatilization temperature

of 900 K and its high metal boiling point of 5833 K [118]. Exploding particle behavior has previously been observed in Mo [60].

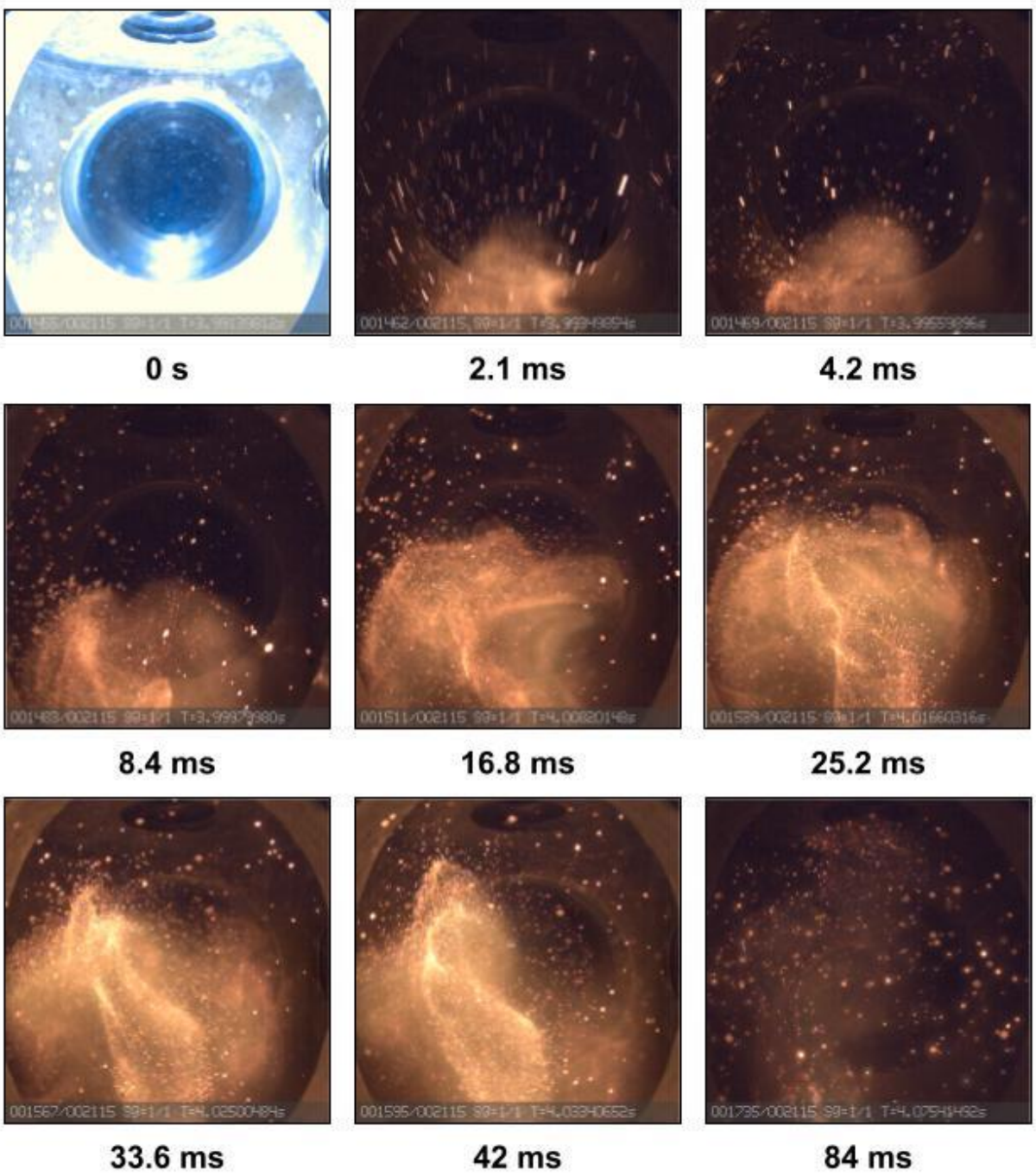

Figure 4.15: Molybdenum dust cloud storyboard (3.4 mg).

Silicon is well known to combust heterogeneously as well and likewise has also exhibited exploding particle behavior in the literature (Figure 4.16) [134]. Of the species tested in this work,

Si most strongly showed this behavior, which was the cause for the numerous spikes in the corresponding photodiode burn time measurements (Figure 4.9). Si does, however, have relatively low oxide and metal volatilization temperatures (2633 and 3177 K, respectively), which could have led to vaporization of the powder.

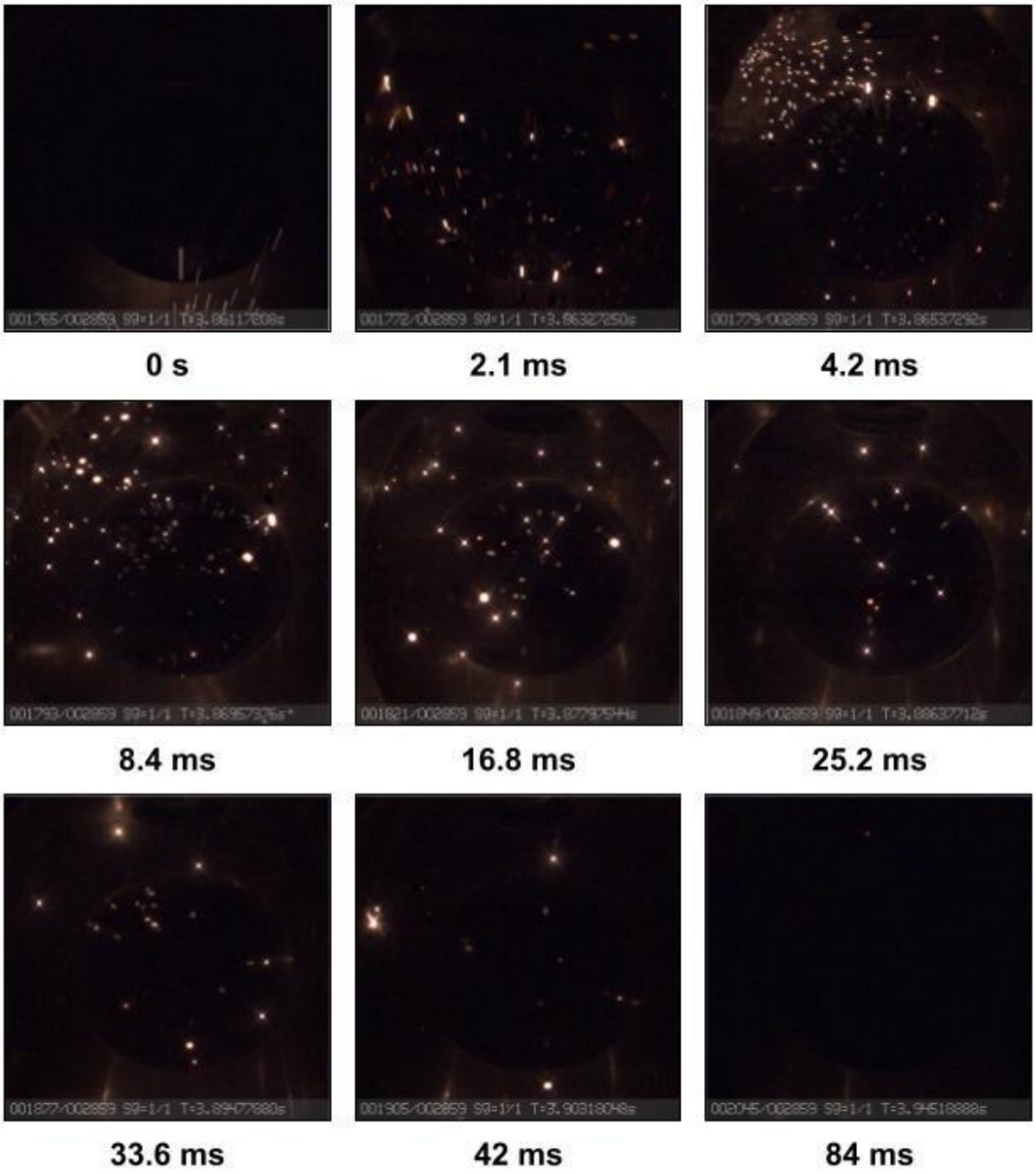

Figure 4.16: Silicon dust cloud storyboard (2.6 mg).

Tantalum is also expected to burn heterogeneously (Figure 4.17). Of all the species tested, it had the longest burn time on average.

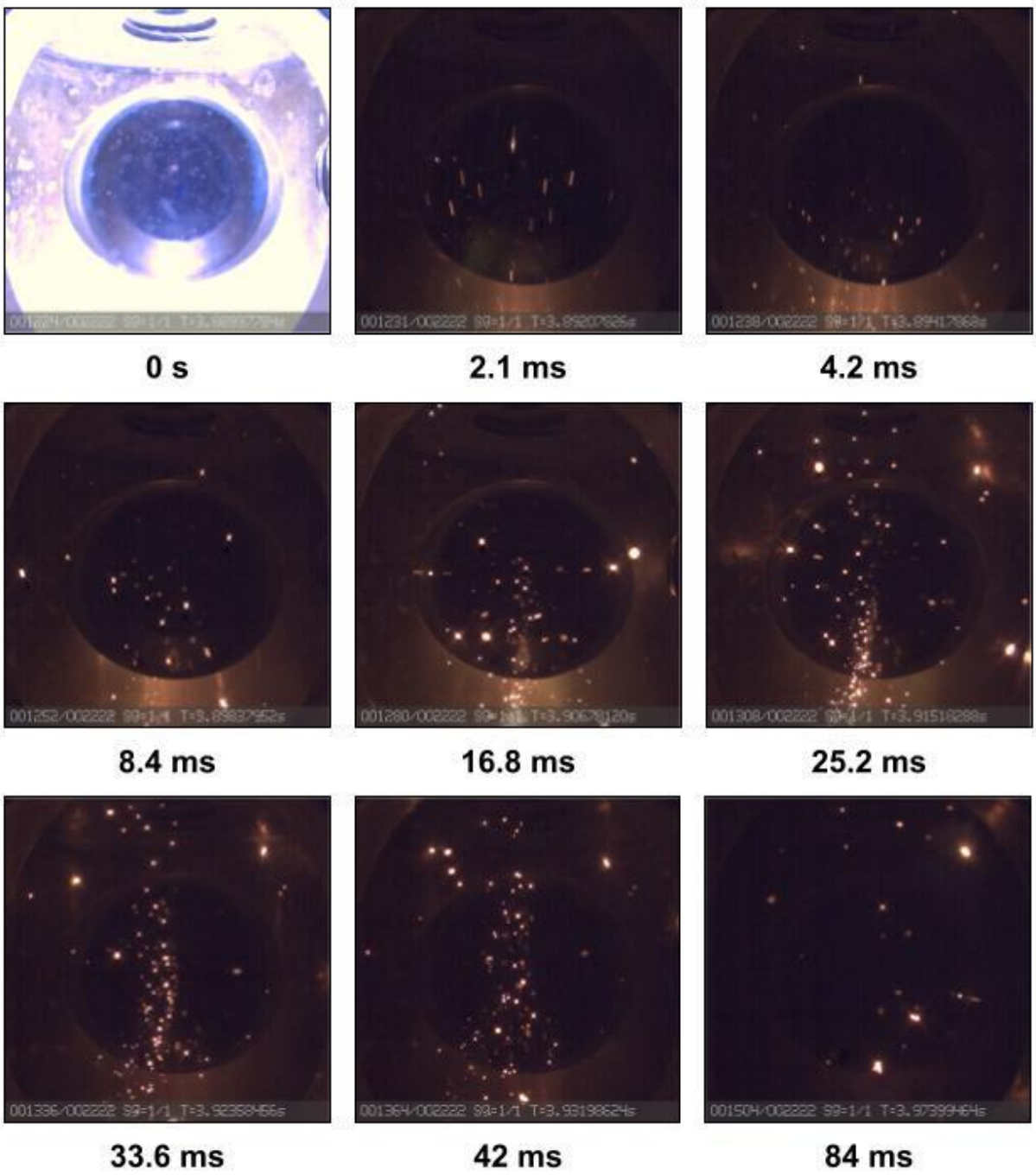

Figure 4.17: Tantalum dust cloud storyboard 2 (shot 1, 2.2 mg).

Titanium (Figure 4.18) and Zirconium (Figure 4.20) combustion have been thoroughly studied, and both metals combust heterogeneously under these conditions. As mentioned previously, it

shows exploding behavior as does Zirconium. There do appear to be vapors present at the later time images in the Titanium storyboard. Titanium does have relatively low volatilization temperatures and may have partially vaporized in this process.

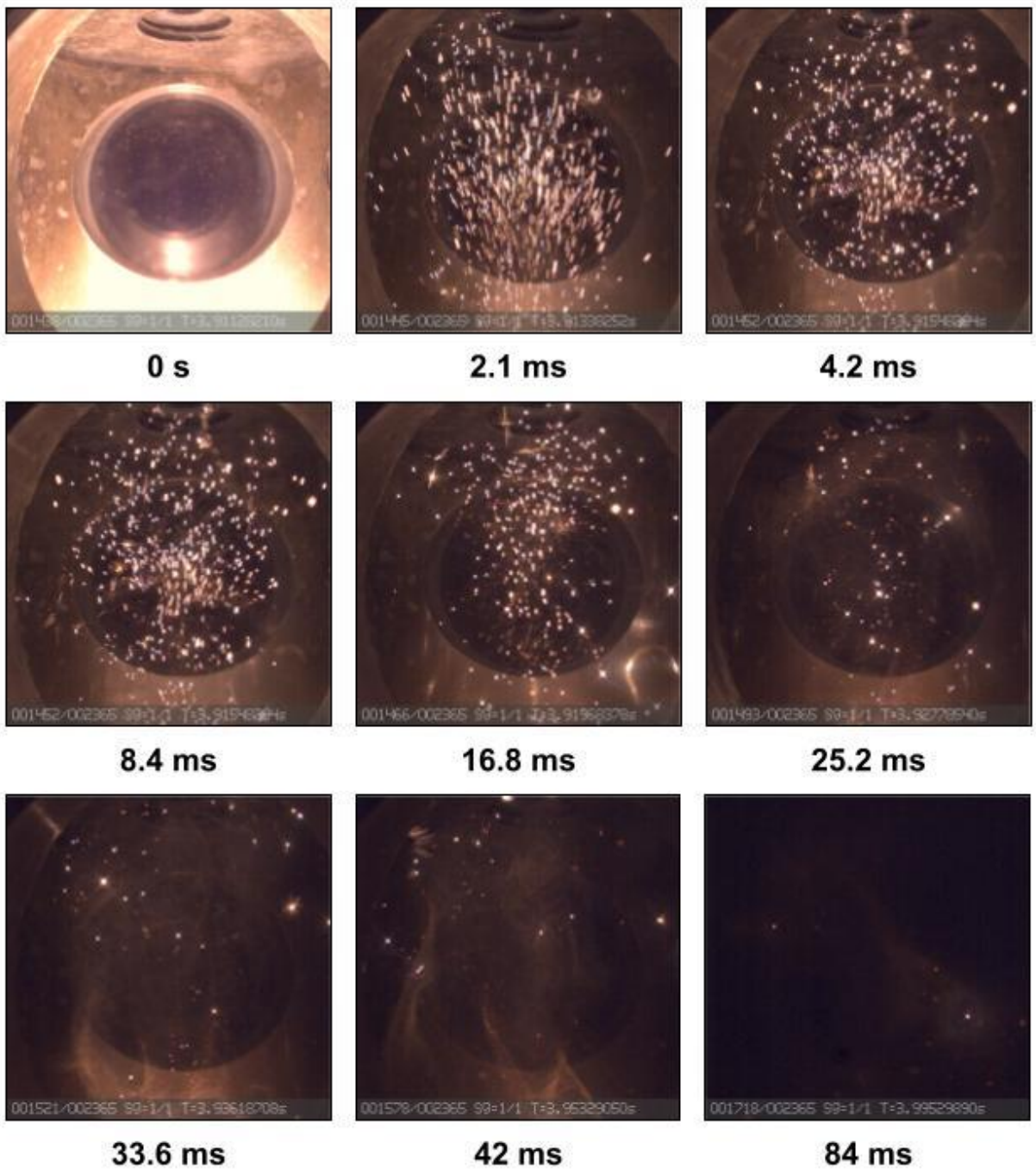

Figure 4.18: Titanium dust cloud storyboard (3.0 mg).

Tungsten is expected to combust heterogeneously. It has the highest metal boiling point of all the elements is frequently used in applications that take advantages of its bright, broadband emission in the visible region of the electromagnetic spectrum when excited (i.e. lightbulbs). Here, similar phenomena are observed. In later frames it is apparent that the particles are still present. Dreizin et al. also observed ‘smoke’ in tungsten particle combustion of a larger diameter, and this is thought to be due to the vaporization of tungsten oxide [60], [71].

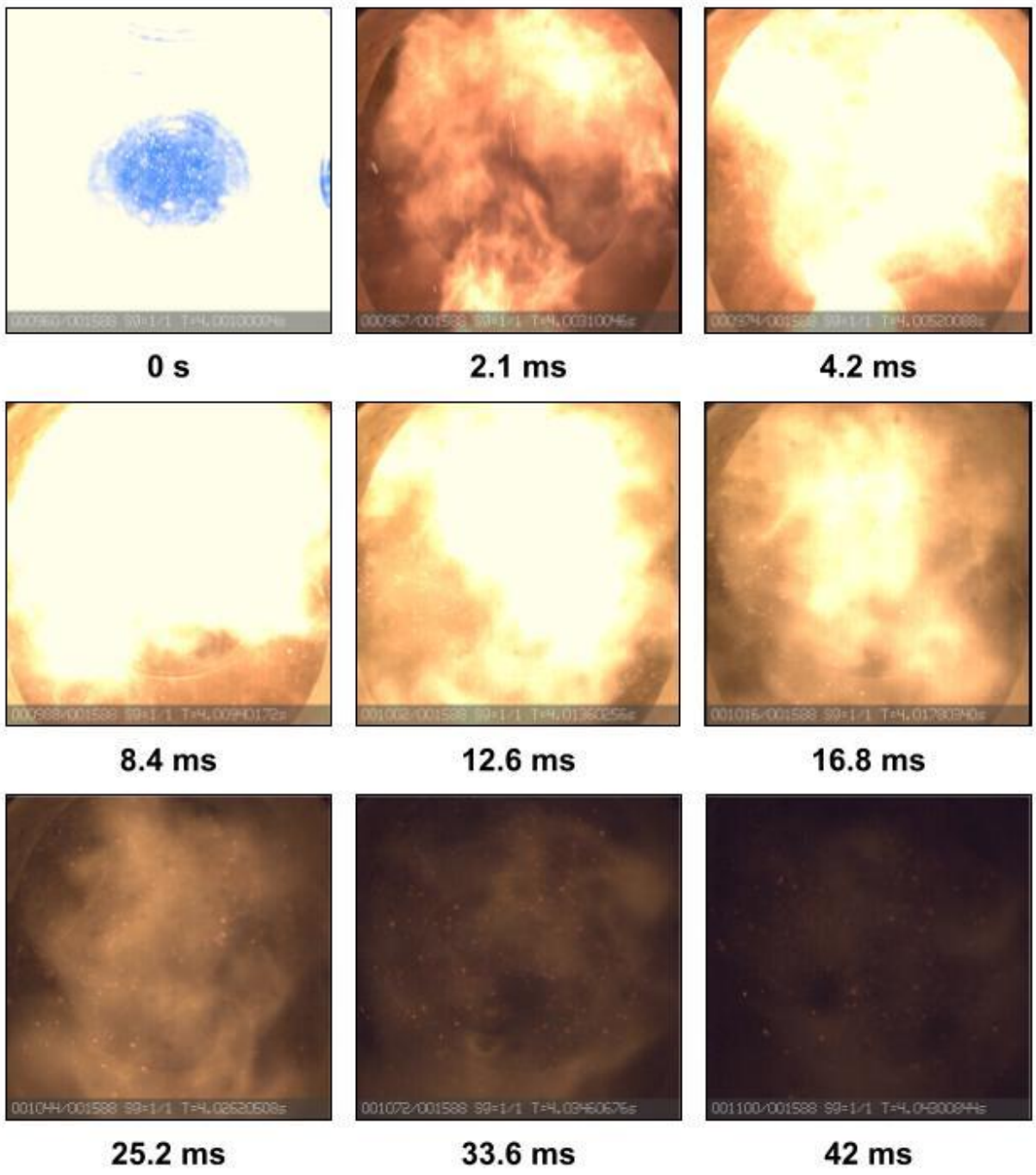

Figure 4.19: Tungsten dust cloud storyboard (3.0 mg).

Some vapor similarly accompanies the combustion of Zirconium. While it is possible that some Zirconium is vaporizing—its volatilization temperatures are slightly higher than this setup is expected to reach—it does still appear to be combusting heterogeneously, with hot particles present after initial combustion.

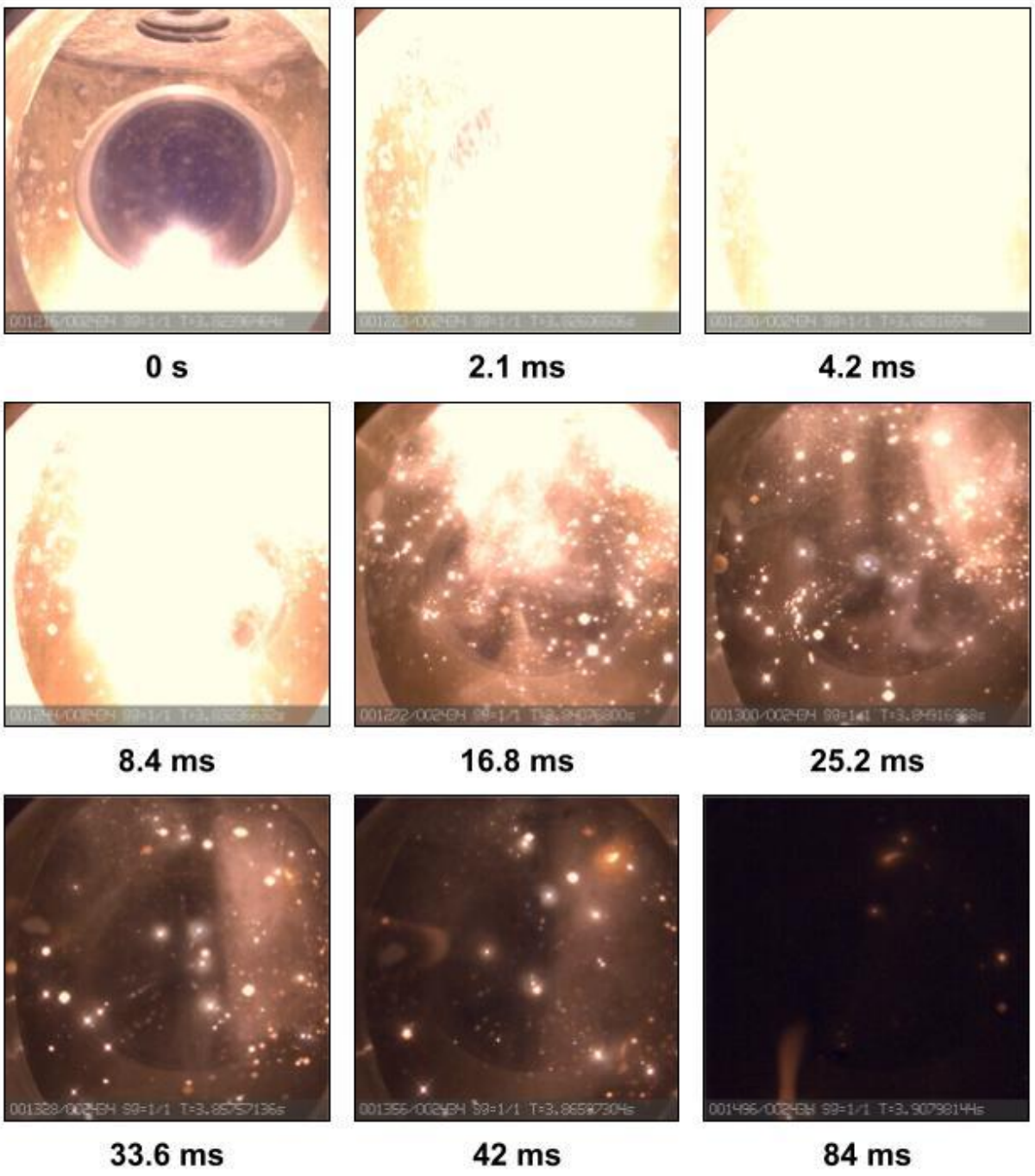

Figure 4.20: Zirconium dust cloud storyboard (3.7 mg).

Rather interestingly, powders that produced more robust clouds tended to have higher ignition temperatures in dust cloud environments, but all ignition temperatures were still much lower than those reached by the system. W, Fe, and Mo were considered weakly explosible in comparison to

other materials tested as determined by rate of pressure rise after ignition of the powder dust clouds, whereas Al, U, Ti, and Zr were considered severely explosible [54].

4.2.3. Spectral Measurements

Spectral measurements were taken from uranium combustion to determine what emission or absorption features would appear in these excitation conditions. Emission from a uranium dust explosion in a 1 atm air environment is shown in Figure 4.21. Continuum emission was subtracted out.

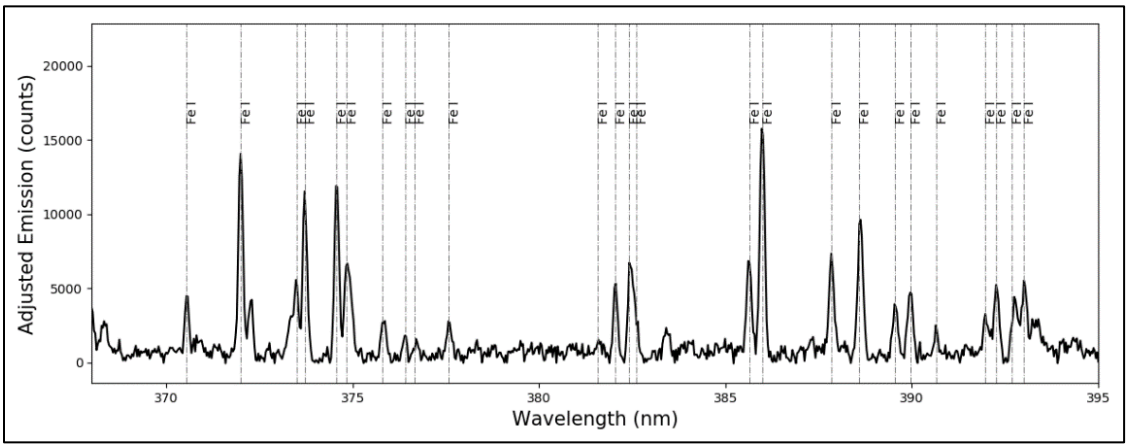

Figure 4.21: Emission from uranium dust cloud combustion in 1 atm air environment.

Fe I signatures from trace amounts of particulate present dominate the spectrum, indicating that the temperature of combustion is insufficient to excite uranium transitions. This further corroborates the conclusion that uranium is not burning in the vapor phase at this temperature. Figure 4.22 shows the absorbance spectrum from combustion of uranium at a 1 ms delay from initial combustion with an overlaid model at a Boltzmann method calculated temperature of 3428 K.

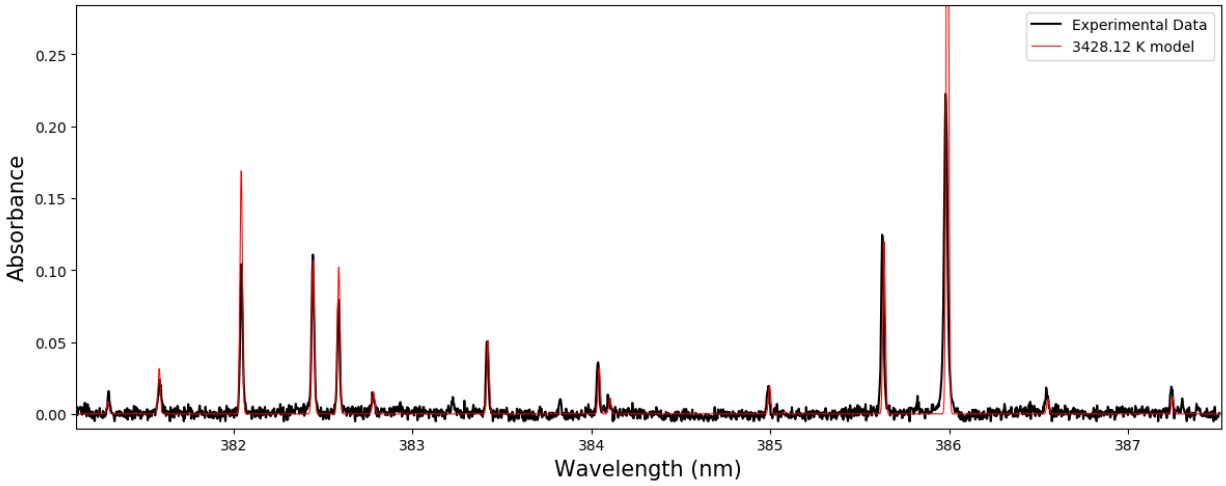

Figure 4.22: Absorbance at 1 ms delay from spark in 1 atm air. The red peaks are labeled Fe I transitions.

Attempts were made to obtain higher temperature spectra at different delay times, but these were unsuccessful. The concentration of iron in the chamber should be much lower than that of the uranium present, but iron transitions are excited at much lower temperatures than that of uranium. The iron concentration along the path measured was determined to be 1.967E+17 m^{-3} which corresponds to about 18.24 μg. The total amount of uranium powder used in this test was 25 mg. Using the Beer-Lambert Law, and with the assumption of constant attenuation coefficient at a given moment along the optical path through the dust cloud, the detection limit of uranium was determined to be 2.781E+16 m^{-3} along the path from correlation to the ground state Fe I transition at 385.9911 nm.

Table 4.2 shows the adiabatic flame temperatures as calculated in NASA CEA in Air and O_2 for all powders tested with the exception of Hf, which was found in a Hertzberg et al. [55], [67].

Table 4.2: Calculated Adiabatic Flame Temperatures in Air and O_2 at 1 atm and 300 K [67].

Element	Air (K)	O_2 (K)
Al	3668.93	3968.53
B	4058.79	5543
Fe	3014.59	3383.55
Hf	4120 [55]	-
Mo	3191.98	4109.48
Si	3072.56	4899.67
Ta	3778.5	5062.85
Ti	3595.08	4461.72
W	3494.22	4374.91
Zr	4000.69	5118.31
U	3773.32	4843.2

Of these elements, Fe had the lowest adiabatic flame temperature in Air, which corroborates its appearance in the vapor phase. Since vapor phase uranium signatures were not detected, it is likely that temperature in the system did not exceed ~3773 K, which is supported by temperatures gleaned from emission and absorption measurements of the uranium dust cloud—consistently lower than that in Figure 4.22. The amount of uranium and oxygen present in the system would constitute a fuel lean mixture and thus would burn at a lower maximum temperature, certainly lower than the volatilization temperature of uranium oxide and the boiling point of uranium. Badiola and Dreizin note that NASA CEA code does not take into account nitride formation [57]. The observed temperature is somewhat higher than theorized by Mouradian and Baker for uranium and zirconium spheres of this size regime burning in air [68].

Not much information was found dealing primarily with the burning of uranium, but similarities can be drawn from work on Zr. Like uranium, Zr behaves refractorily, burns heterogeneously, and exhibits the exploding particle effect described earlier. Combustion of micron regime Zr and Ti yields spectra reminiscent of blackbodies with no unique, discernible atomic transitions (aside from the iron impurity). Similarly, uranium transitions in are absent from Figure 4.21 and Figure 4.22. Uranium has a relatively thick, protective oxide layer that further prevents the particle from entering the vapor phase and oxidizes readily [21], [135], [136]. This oxide layer builds quickly, and that increased oxide layer thickness leads to increased emissivity [137].

4.3. Shock tube series 1

Controlled shock heating of uranium particles was performed to determine the point at which uranium signatures begin to appear. This may correspond to the temperature at which the entire uranium particle begins to vaporize, as opposed to the surface burning that would occur at lower temperatures. Recall that initially and at lower temperatures of combustion, the uranium particle is protected by an oxide coating, whereas a pure metal particle surface will have less of a barrier to vaporization—granted exposed uranium metal will readily start to oxidize. Although it varies with shock speed, generally the test duration for shock tube experiments discussed in this document was around 2 ms long. Figure 4.23 shows the storyboard for the highest temperature shot performed in the initial shock tube series at 9138 K. As mentioned previously, the uranium powder was loaded onto a knife blade mounted on the end of the shock tube (left side of image). When the incident shock travels down the tube, it begins to displace the powder, which begins to heat up, trailing behind the shock wave (T = 1 ms, the incident shock had a calculated temperature of about 4392 K).

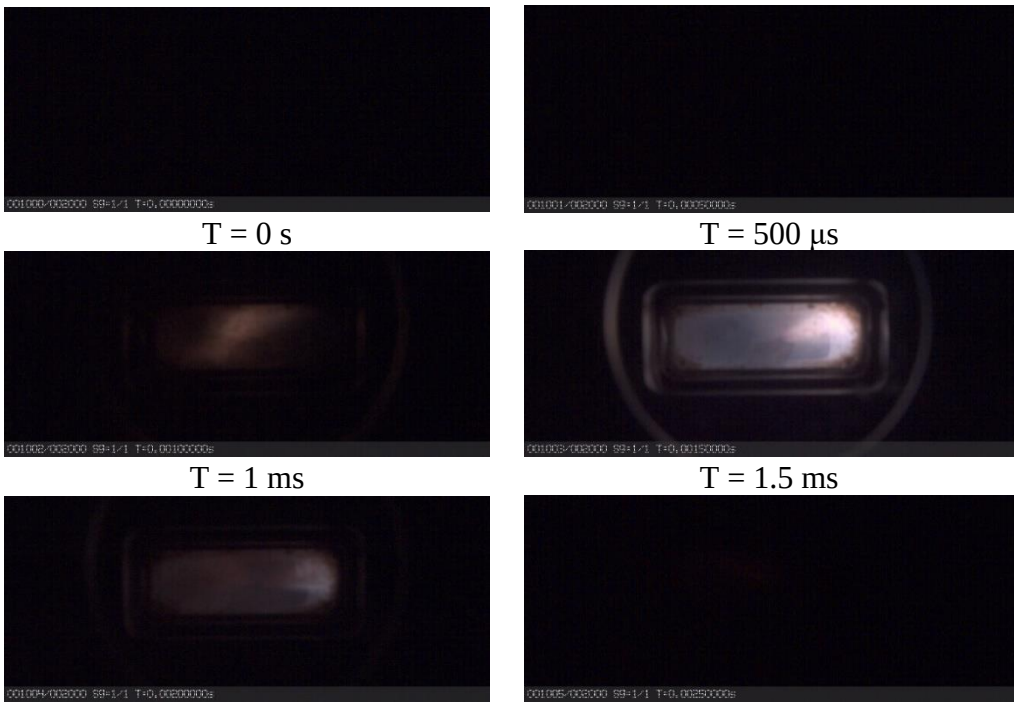

Figure 4.23: Storyboard of 9138 K shot in Argon environment. Each frame was taken 500 µs apart. The left side of the image is the end of the shock tube. Here powder entrainment and combustion in the reflected shock can be observed.

Once the shock reflects off of the end wall, the luminous jet-like particle heating can be observed (T = 1.5 ms). This phenomenon was seen in most of the tests performed in this series, although it did not always appear as strongly. Depending on the temperature (increased temperature → increased vapor pressure) and its oxide layer (which will hinder phase transition), the particle may undergo phase transition, continue to heat up, and produce atomic and ionic emission signatures. Here it is important to note a few things: the particles are not evenly dispersed. This will affect the ability of the particles to reach the ideal calculated shock temperatures. Prior shock tube powder testing has involved the use of an injection apparatuses upstream in the shock tube. This would create a more evenly dispersed cloud of powder, which would be more likely to attain the desired temperatures, but there would be a tradeoff in intensity of spectral measurement.

Emission spectra were obtained for the 100% Argon environment series. Selected spectra spanning the temperatures tested are shown in Figure 4.24. Due to a small leak of air into the chamber in between gas fill of the test section and triggering the shock wave, the O_2 content was 0.4% on average for this series.

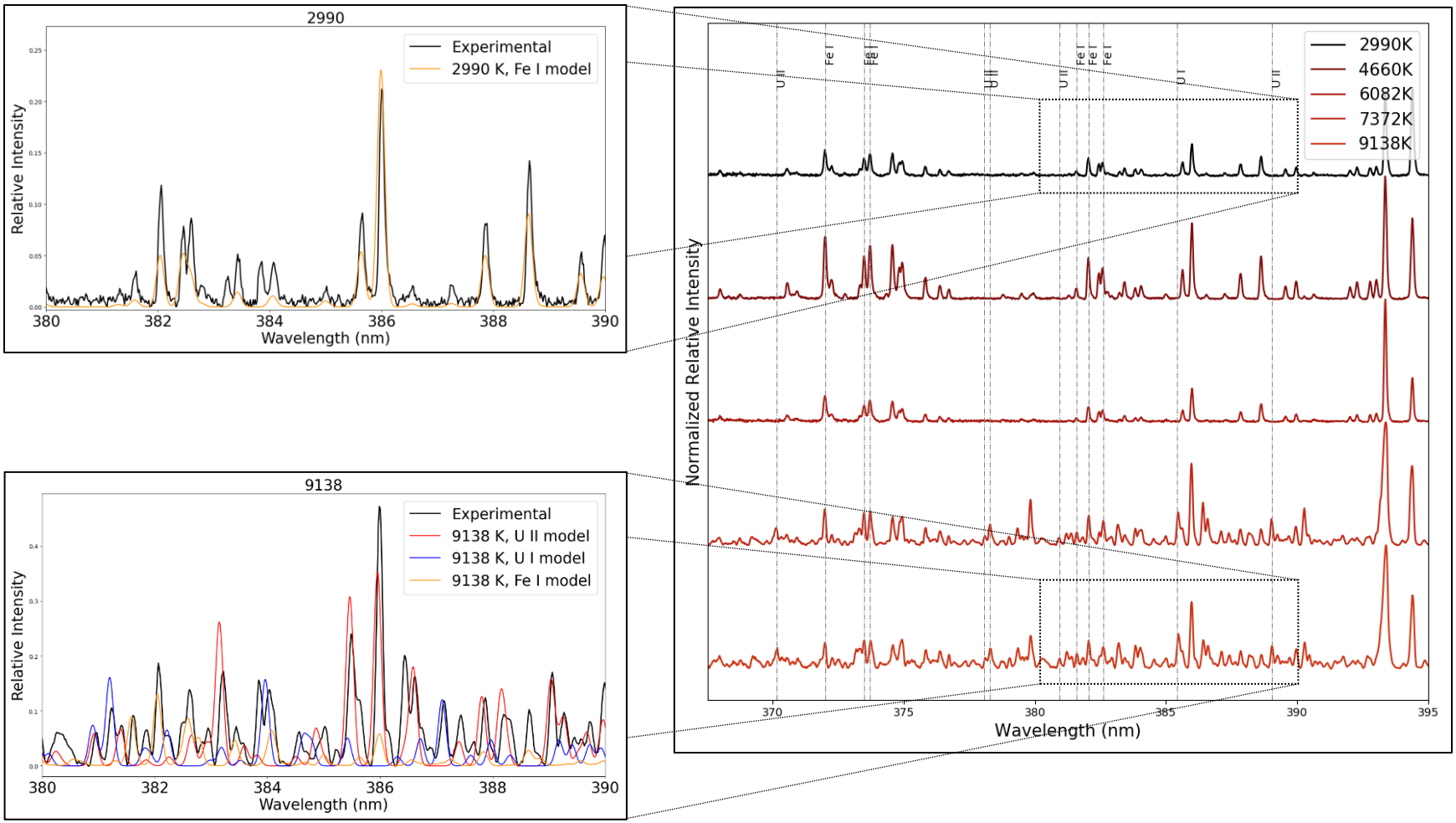

Figure 4.24: Emission spectra from shock tube combustion of uranium powder at various temperatures of combustion for 100% Argon environment.

Although there are a multitude of iron and uranium signatures in this region, labeled Fe I, U I, and U II transitions correspond to transitions that are free from interference from other species. In Figure 4.25, U I and U II peaks found to free from interference of Fe I peaks in the same region were tracked over the various temperatures tested.

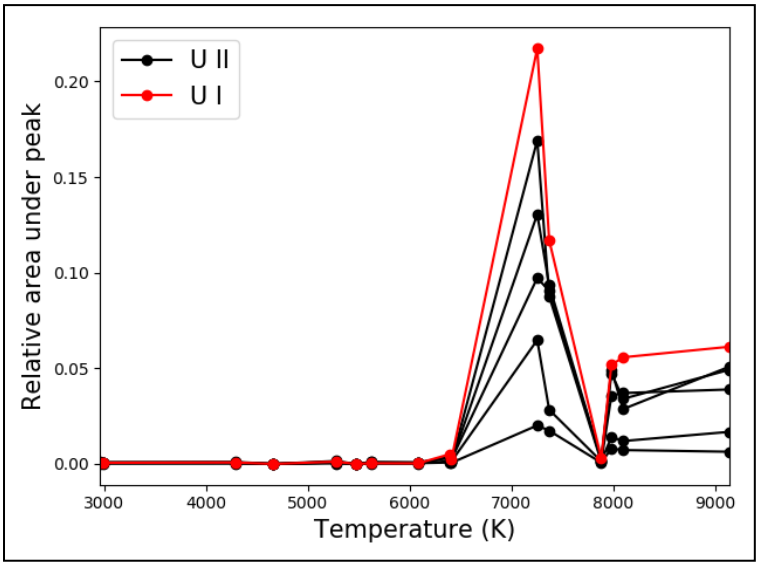

Figure 4.25: Emission peak areas of U I and U II transitions free from interference from Fe impurities tracked over temperature for 100% Argon tests.

Signatures from uranium begin to show up after 6000 K, with some fluctuation thereafter, an initial indication that the threshold for uranium vaporization is around this temperature.

Temperature-sensitive Fe I transitions were used to spectrally confirm temperatures reached by the vapor phase products. The temperatures yielded in these measurements were compared to those calculated using the NASA CEA program (Figure 4.26). Here, it is apparent that there is considerable scatter in these results.

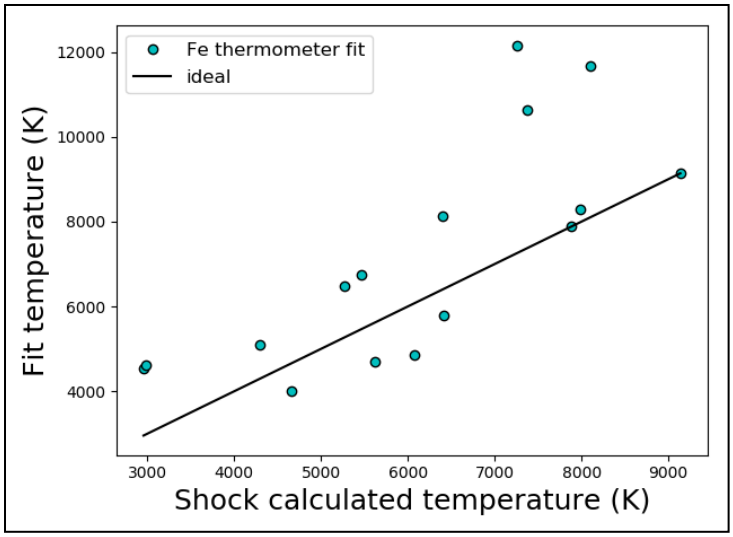

Figure 4.26: Fe I Fit Temperature vs. Calculated Shock Temperature for the 100% Ar tests.

This is likely due to the long spectral acquisition times. Although higher temperatures are favored in spectral emission measurements, the long acquisitions would lead to the effective convolution of spectra of different temperatures.

For this series, spectra were not gated, and one spectrum would be produced from the entire duration of one test. This allowed for the interference of lower temperature Fe I signatures, which begin to show up at much lower temperatures due to Fe's lower volatilization temperatures. Recall that Fe I showed up in the lower temperature dust cloud spectra when U signatures did not.

Testing was also performed in 1% O_2/99% Argon environments, with otherwise similar conditions, and there was little difference in the results. This corroborates laser ablation data in which the introduction of a minute amount of O_2 was sufficient to oxidize uranium as well as previous vapor pressure study [15], [21], [34]. Attempts were made to capture absorption spectra of shock combustion products, but this proved largely unsuccessful with the current setup due to timing issues. In general, these results well supplement testing completed with the absorption LIBS setup in previous years looking at changes in spectra with environment composition and ambient pressure. Similar work can be completed in the future on other actinides and fission products to better characterize resulting signatures.

4.4. Shock tube series 2

From previous test results, it was determined that a more focused study on the temperature region at where uranium signatures begin to appear would be beneficial. This study would be completed with gated measurements to better isolate the high-temperature early time uranium signatures from the later time iron signatures. Additional diagnostics would be fielded to determine the agreement of experimental shock conditions with the ideal calculated temperatures with NASA CEA.

4.4.1. Pyrometer Data

As mentioned previously, when the measured phenomena do not follow ideal blackbody or graybody behavior, emissivity of the material in question at each wavelength measured needs to be considered. Unfortunately, emissivity information in temperature regimes and wavelengths appropriate to this work is not available for uranium. Thus, assumptions needed to be made about emissivity. These are typically taken to be wavelength-dependent and can follow a power-law (λ^x). Lynch et al. discusses this further in their work, finding polynomial fits to alumina emissivity curves obtained from shock tube testing [89]. Relations of the form shown in Equation 33 were obtained for alumina particles at various temperatures between 2000 and 4000 K.

$$\varepsilon_\lambda(T) \sim C\left(\frac{\lambda}{\lambda_0}\right)^n \qquad \textit{Equation 33}$$

At lower temperatures, power law dependences of -1 and -2 were found to be appropriate alternatives to the black body assumption, whereas increased powers were deemed appropriate for the higher temperatures. Although these findings were specific to work on alumina, temperatures at various power laws were taken to determine which would provide the most plausible temperatures, given known information about the test conditions to find ‘best guesses’ absent of other potential sources of discrepancy such as inhomogeneity of particle burning. Powers ranging from -1 to 4 were tested and the resulting temperatures for cases that did not follow reasonable trends are shown in Figure 4.27.

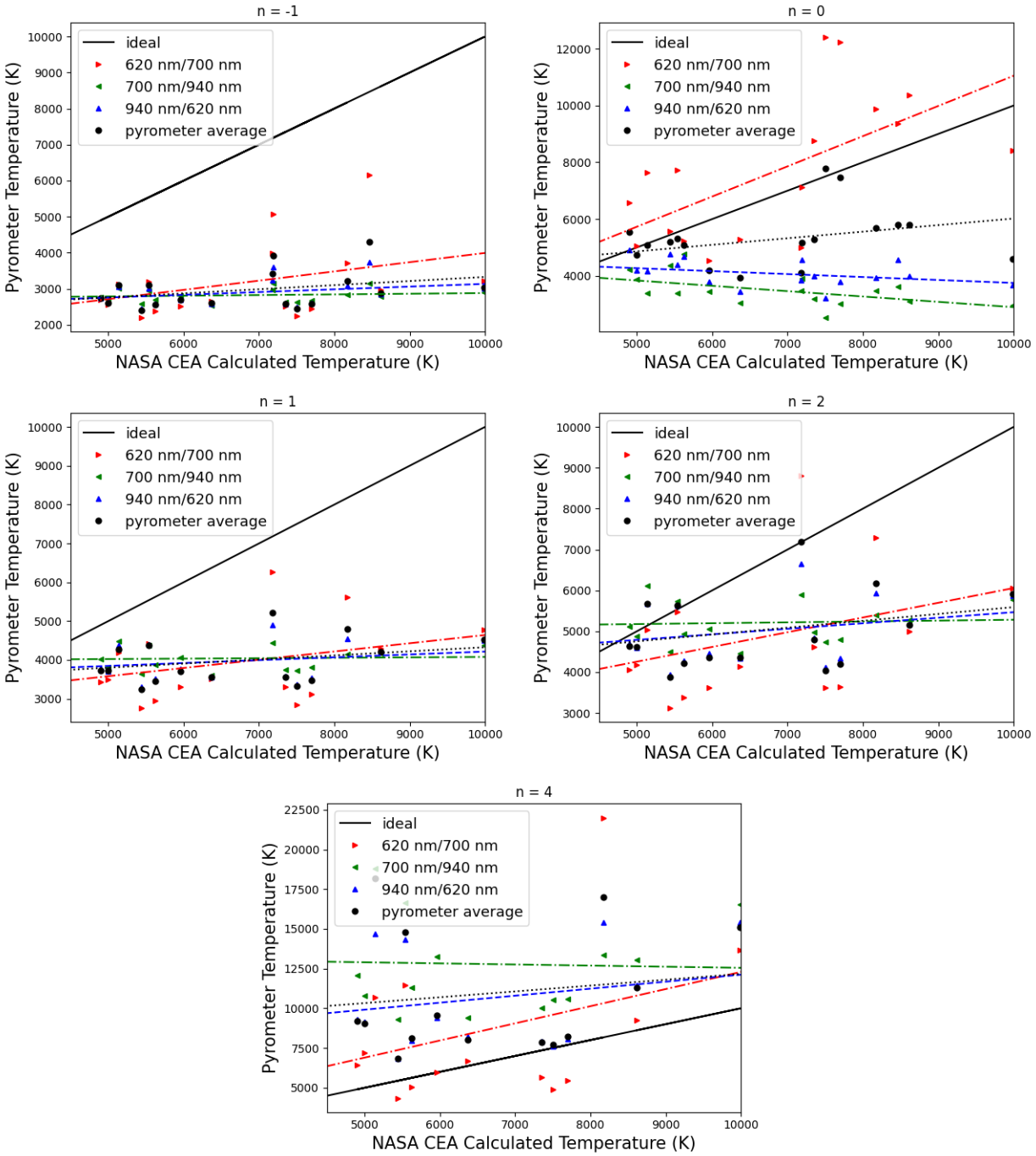

Figure 4.27: Temperatures summaries for implausible cases with different emissivity wavelength dependences.

Pyrometer data following $\varepsilon \sim \lambda^3$ is shown in the Appendix as the best approximation of shock temperature in comparison to those yielded by employing other emissivity wavelength dependences. Figure 4.28 shows a summary of temperatures yielded by each wavelength ratio as well as an average temperature from the three ratios.

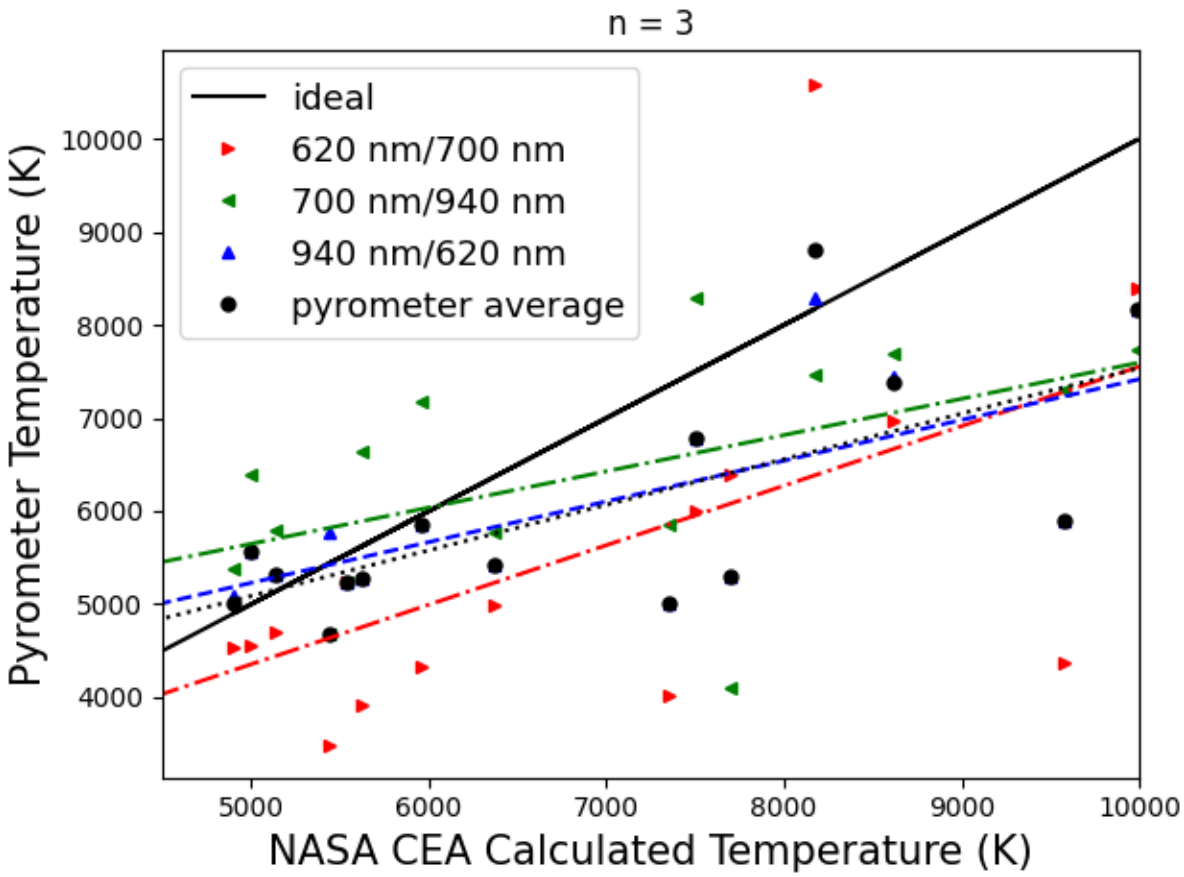

Figure 4.28: Summary of pyrometer temperatures for n = 3 dependence.

It is important to note that emissivity-wavelength dependence cannot be the only factor at play. The n = 3 emissivity dependence producing the most plausible temperatures when compared to those calculated in CEA demonstrates that—an impossible result. Uranium produces many emission signatures across the visible and NIR region, and it is possible that these signatures interfered with the acquisition of what should be a measure of blackbody emission. A brief search of the Kurucz database yields several transitions falling within the 10 nm bandpass for the 620 nm and 700 nm filtered photodiodes [17]. It is therefore important to consider the effects that the knife blade powder loading method will have on powder dispersal, temperature distribution, and resulting optical measurements which will be discussed later.

4.4.2. NIR Spectra

Near Infrared spectra were obtained spanning the region from about 1000-1500 nm. Here, a few uranium transitions were identified amongst Argon signatures that appeared at higher temperatures (~> 8000 K) [138]. Acquired spectra were not gated as desired (ideally ~1 ms) due to experimental difficulties; thus, some blackbody fits of the resulting spectra do not accurately reflect reflected shock temperatures. Figure 4.29 is an illustration of this discrepancy. While some of the blackbody temperatures appeared to match the calculated shock temperature via NASA CEA (possibly due to T^4 dependence of emission on temperature), many temperatures lay somewhere in between the reflected and incident shock temperatures. Additionally, this metric is highly dependent on an accurate blackbody calibration using a source of known temperature. Here the 3400 K QTH lamp discussed in 3.4.2.1 was used.

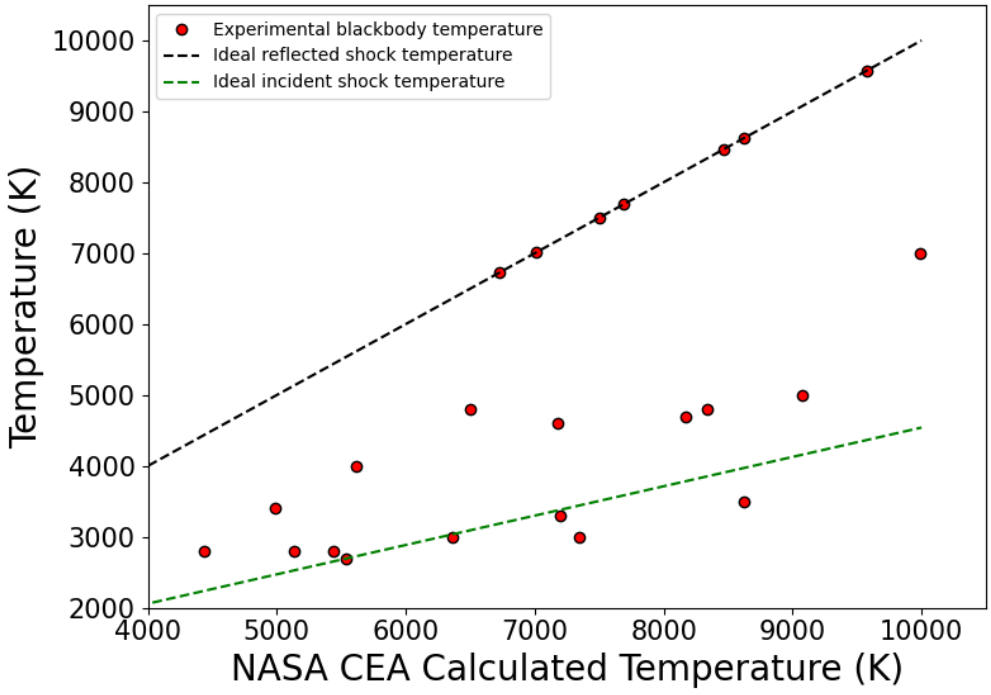

Figure 4.29: Blackbody temperatures for NIR spectra collected from shock tube testing of uranium powder.

Unfortunately, this technique was fruitless in terms of confirming shock temperature for this series, but a few different uranium transitions were observed.

Temperature variance of argon signatures was also investigated to correlate shock temperatures, but those in this region proved to be insufficiently variant for temperature measurement from

spectra and would be beholden to the same issue with temporal gating as the blackbody measurements.

Figure 4.30 shows a sample blackbody-subtracted NIR spectrum with Ar I (red) simulated at 7000 K and U I transitions labeled in blue at intensities seen in spectra for ease of observation.

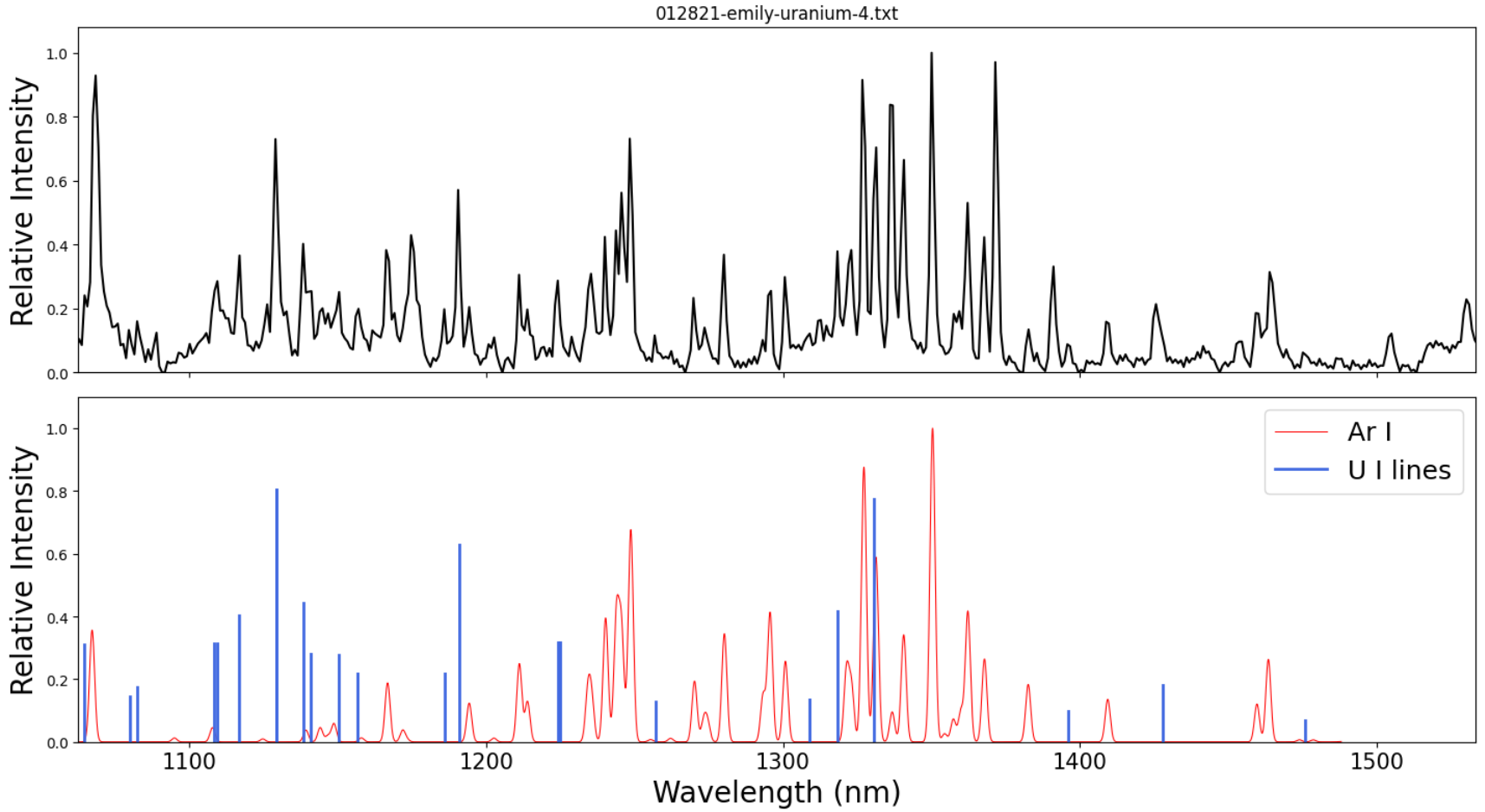

Figure 4.30: Sample NIR spectrum, NASA CEA calculated 9080 K. Ar model overlay at 7000 K, U I lines from NIST scaled to height of corresponding peak [18].

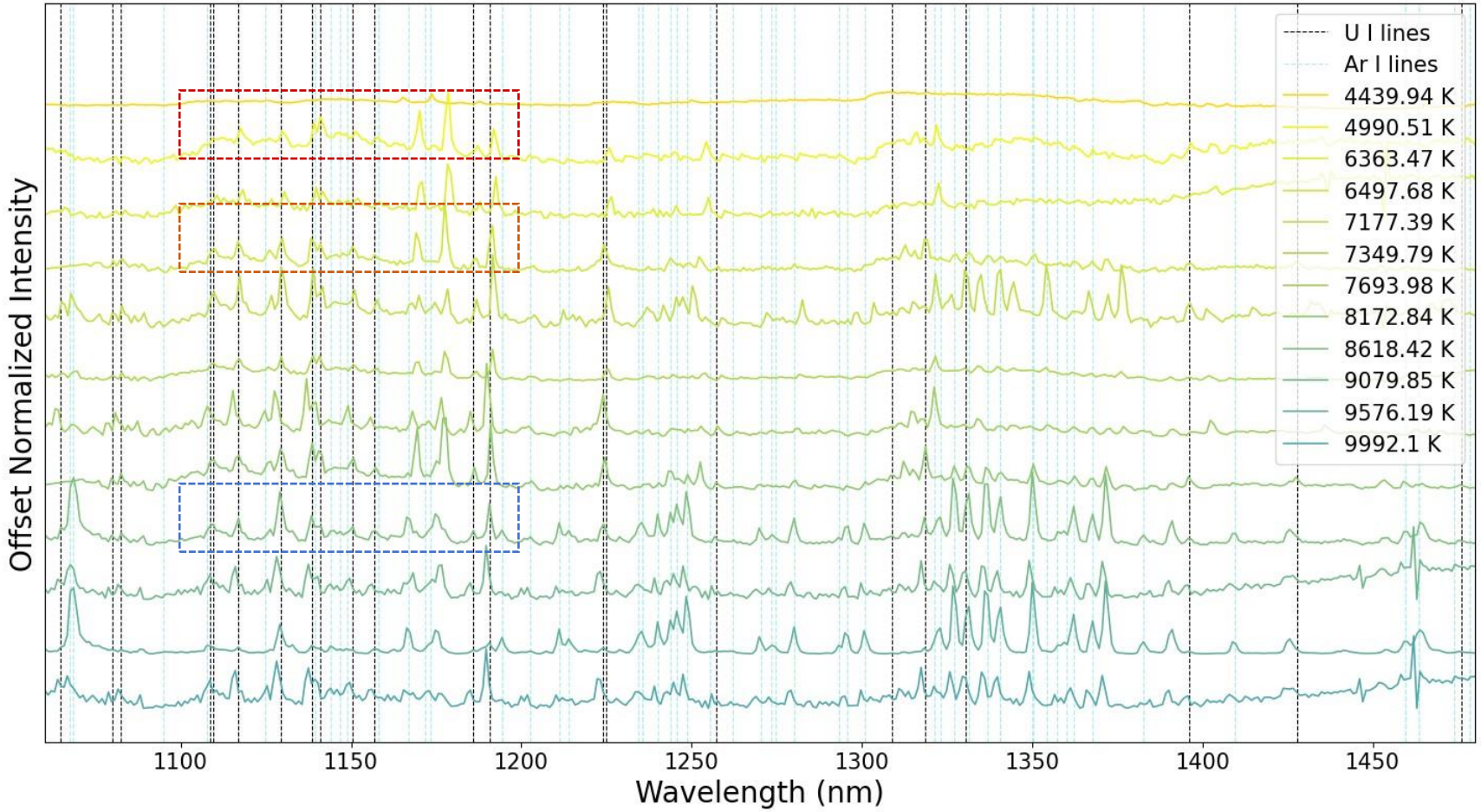

Figure 4.31: Emission spectra from shock tube combustion of uranium powder at various temperatures of combustion for 100% Argon environment in the NIR region with selected regions of interest.

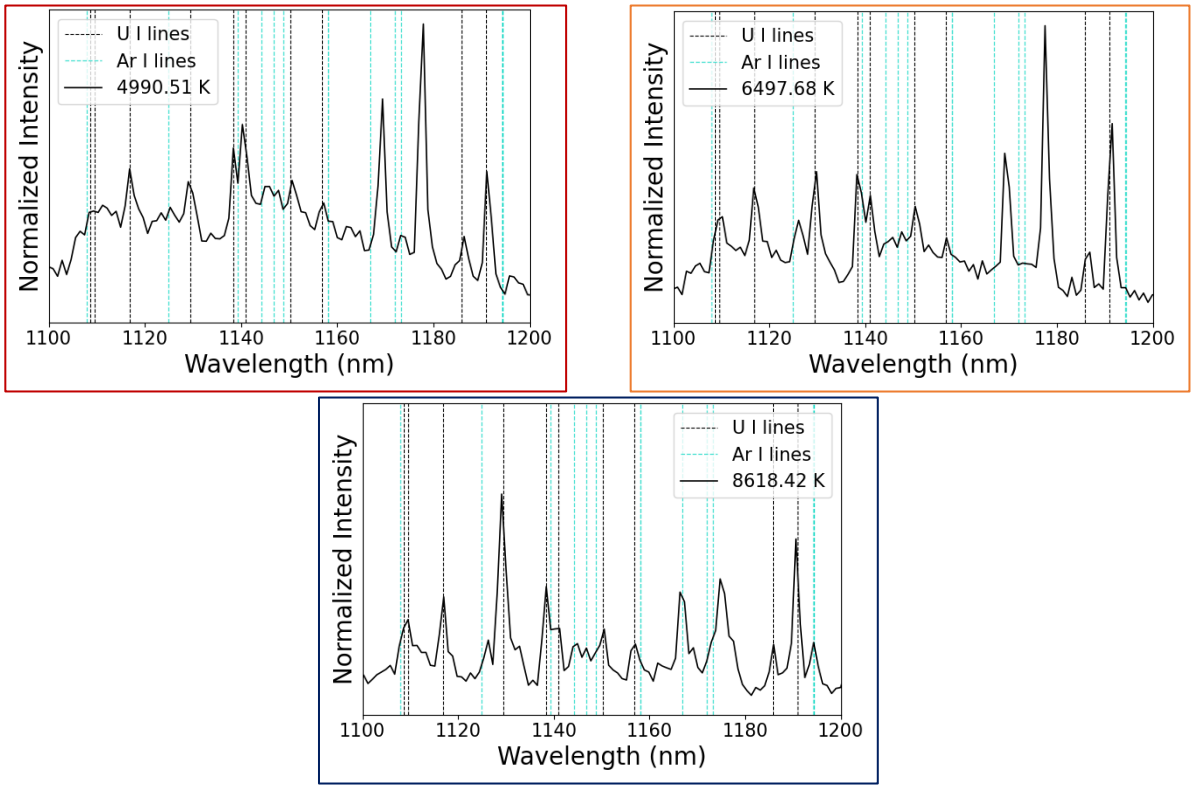

Figure 4.32: Close up of U I transitions for selected regions of interest at different temperatures.

Tracking the appearance of U I peaks over the range of temperatures tested indicated that they began to appear between 4400 K and 4900 K calculated reflected temperatures, which is close to the boiling point of uranium (4404 K). Tracked similarly, Ar I signatures started appearing around calculated reflected temperatures of 6500 K, which is a little lower of a threshold than that reported in the literature in atmospheric conditions [138]. These spectra were taken of phenomena occurring at lower pressures than atmospheric which might lead to lower excitation temperatures.

It is additionally likely that other unidentified peaks also belong to uranium. Work by Redman et al. indicates that there are a plethora of U I and U II transitions in this region that have not yet been further characterized [20]. Insufficient information was available to simulate the U I spectra. Although these signatures have been identified as U I, and energy levels are known, Einstein coefficients were not found. Some of these transitions do appear to vary with temperature and may prove useful in future work. Although there should be weak U II signatures in this region, not enough information was available to definitively identify a signature as such.

4.4.3. Visible Spectra

Time-resolved spectra were obtained for most test conditions. Since the spectrometer trained at the visible region took in light from a window located at the end of the shock tube, spectra prior to the shock heating of the uranium powder could sometimes be captured as well. The prior test series yielded one spectrum for the entire duration of the shock, whereas these spectra could be obtained in increments of 360 μs. This ideally would allow for more accurate determination of high-temperature uranium signatures, and potential Boltzmann temperature measurements of species.

Figure 4.33 shows spectra for a few temperatures spanning the region tested with overlaid U I and U II lines as identified in the Kurucz Spectral Database [17]. From all results, it appears that U signatures are present at temperatures < 6000 K in contrast to previous results, but that transitions become much more populated at temperatures higher than around ~5500 K.

Figure 4.35 shows an example spectrum produced from a reflected shock calculated to be 7506 K. Here, emissions from U I and U II are evident and relatively free from interference from iron signatures as in the previous series. The strong Al I and Ca II impurities are present, as is the CN B-X 0-0 bands, which was not seen in the previous series. The CN band appeared throughout testing and is attributed to a combination of carbon impurity in the shock tube and a minute leak of air into the shock tube in between test section preparation and firing the shock as discussed in Section 3.4. This signature was likely present in previous testing but could not be differentiated from overlapping U I and U II signals due to the much longer acquisition times.

U II signatures that were free from interference from U I and Fe I signatures were selected for Boltzmann temperature measurement. These are listed in Table 4.3 and were obtained from the Kurucz Spectral Database [17].

Table 4.3: Selected U II transitions [17].				
Wavelength (nm)	**Einstein A_{ul} (s^{-1})**	**Upper state energy (cm^{-1})**	**Lower state J**	**Upper state J**
366.2329	6.94E+06	31961.06	3.5	3.5
369.1918	2.25E+07	31784.76	2.5	3.5
369.3696	2.44E+07	34612.82	3.5	4.5
370.1516	3.24E+07	32535.02	6.5	6.5
372.4983	3.98E+06	28587.25	6.5	5.5
375.5482	1.01E+07	32410.82	5.5	6.5
376.0887	1.87E+06	26581.92	4.5	4.5
376.8795	6.77E+06	32316.79	5.5	6.5
378.2841	1.11E+07	26716.69	5.5	6.5
379.0209	3.81E+06	32166.92	5.5	5.5
381.379	4.32E+06	28507.89	5.5	5.5
387.4037	3.11E+06	26094.59	5.5	6.5
389.0361	1.07E+07	25986.31	5.5	6.5

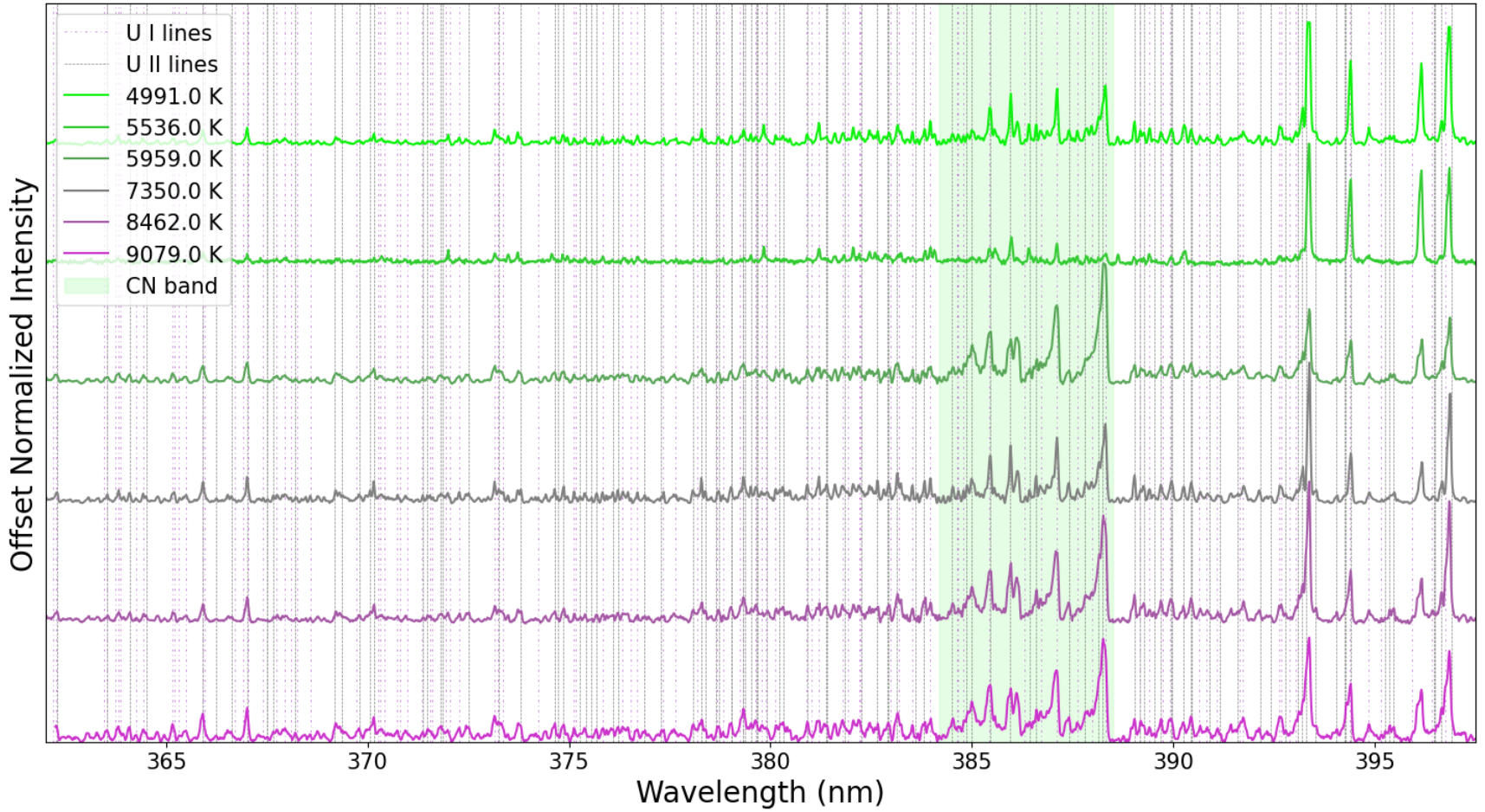

Figure 4.33: Gated emission spectra (360 µs) from shock tube combustion of uranium powder at various temperatures of combustion for 100% Argon environment. Vertical lines correspond to U I and U II signatures as reported in the Kurucz Spectral Database [17].

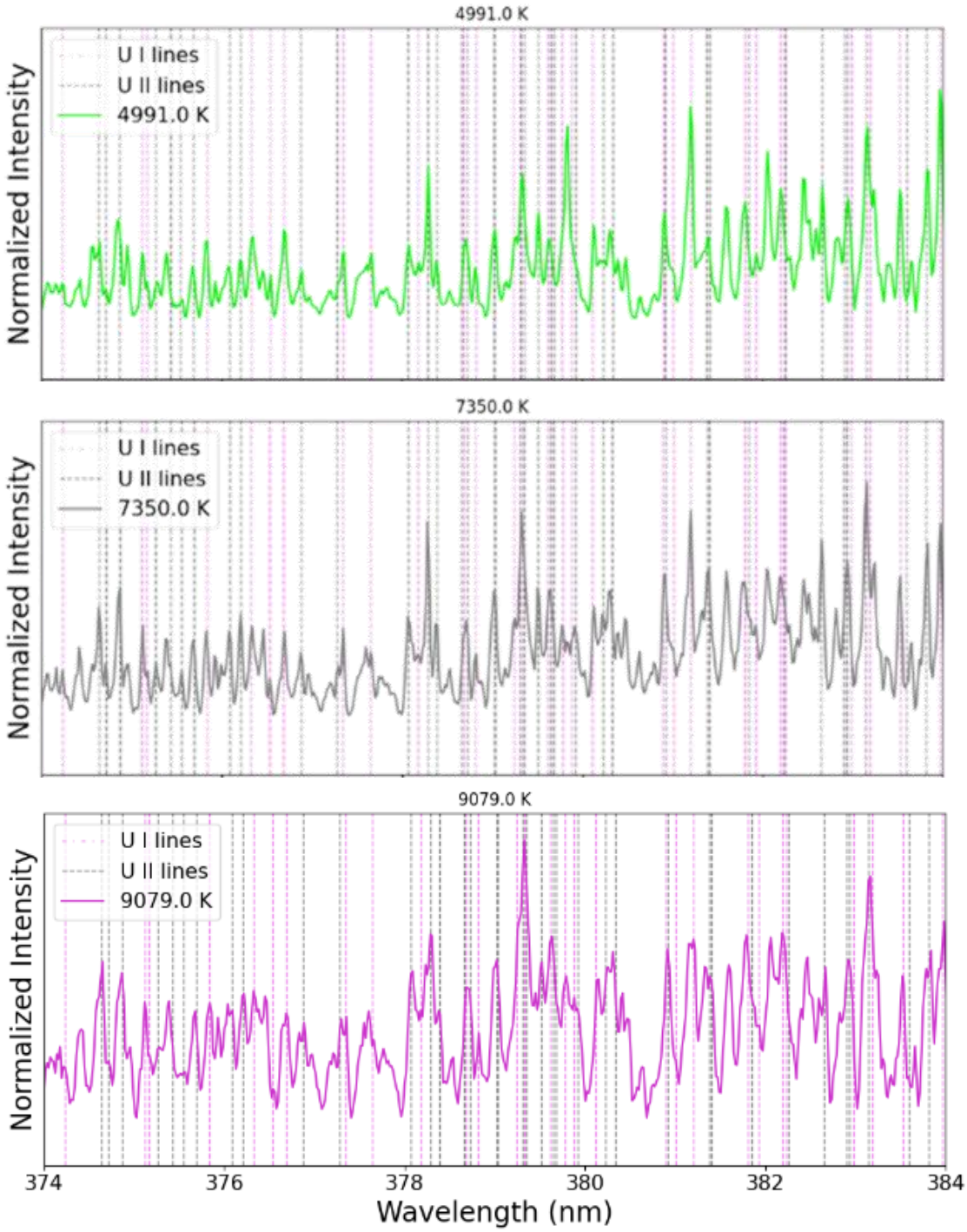

Figure 4.34: Close up of region populous with U I and U II transitions and relatively free from interference from other signatures.

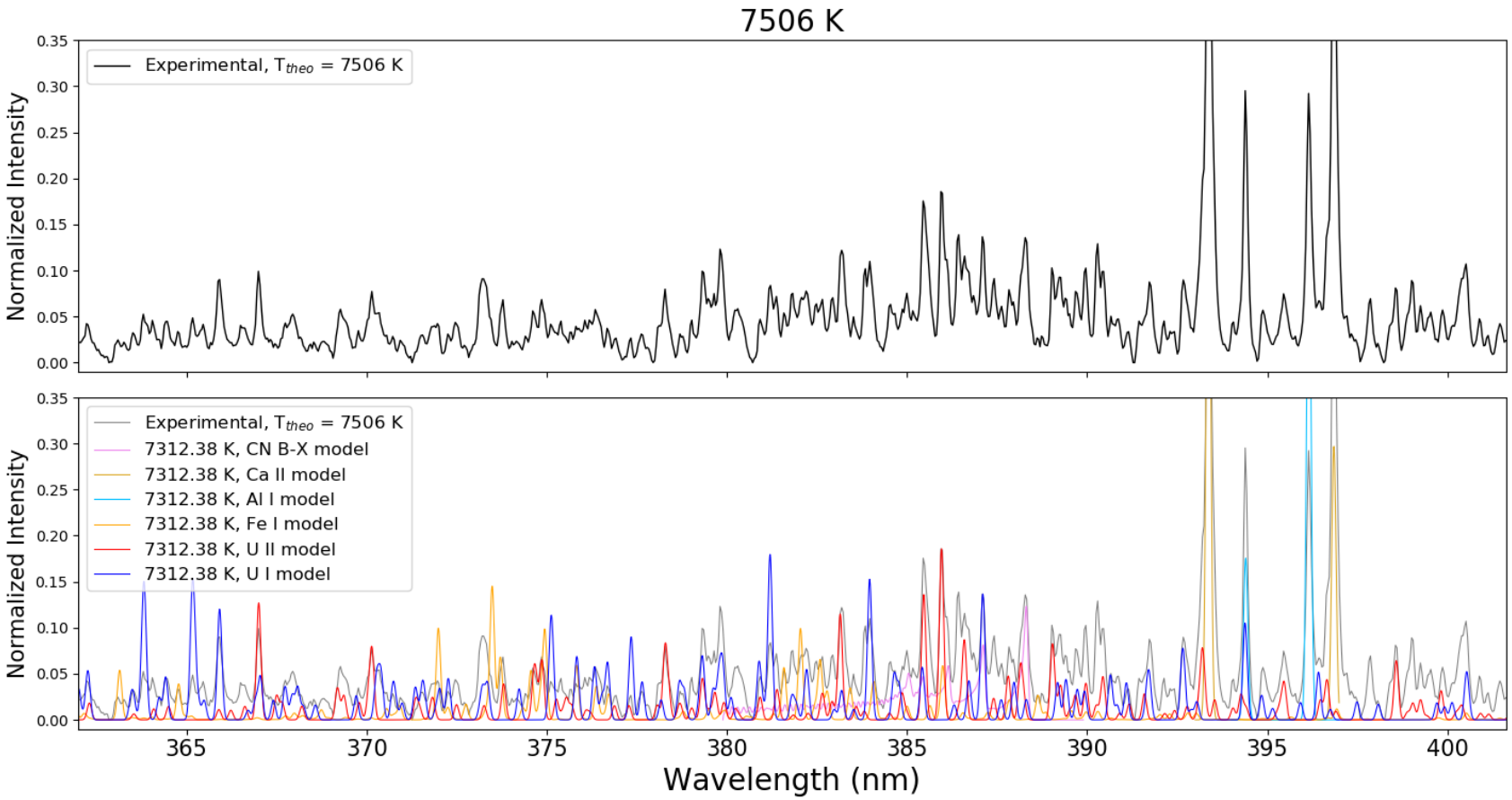

Figure 4.35: Emission spectrum with overlaid models (at U II Boltzmann temperature of 7312.38 K) of species observed for 7506 K shot.

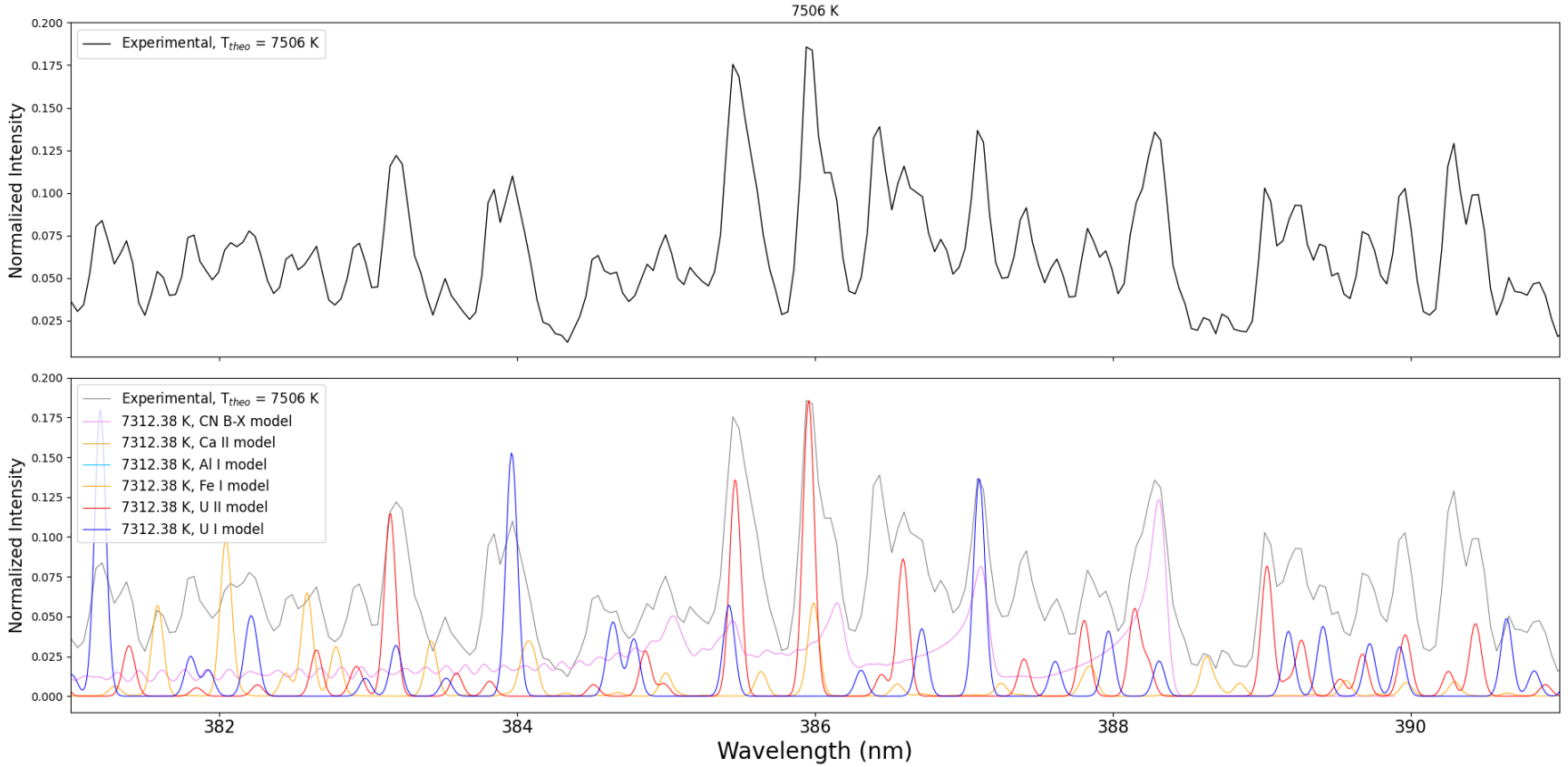

Figure 4.36: Emission spectrum with overlaid models (at U II Boltzmann temperature of 7312.38 K) of species observed for 7506 K shot focused in on U I and U II transitions in the range.

Generally, there was more scatter than would be ideal in the resulting Boltzmann plots. This was likely due to the length of acquisition time. Although considerably shorter than the previous test series, the 360 μs period was still relatively long when considering shock speed for these tests. At an average shock speed of 1832.84 m/s incident for this series; in 360 μs, the shock wave can travel ~0.66 m, presumably faster after the shock reflection—which is a long way to say that this is not a system at equilibrium, and Boltzmann measurements assume local thermodynamic equilibrium. Scatter in this measurement is to be expected. Furthermore, there is some uncertainty in the spectral information, such as Einstein coefficients, currently available for U I and U II in databases. Additionally, although many electronic transitions have been determined to be from uranium, for many transitions, further characterization has not been performed [41].

Additionally, although some spatial filtering is employed in the optical setup, a measurement is being made of a medium that is at a distribution of temperatures due to the irregular dispersal of powder resulting from sting loading, an issue that propagates into all measurement techniques.

Figure 4.37 shows the temperatures obtained from the Boltzmann regressions for each of the shots during the frame where particles were first excited by the reflected shock wave as compared to the NASA CEA calculated temperatures.

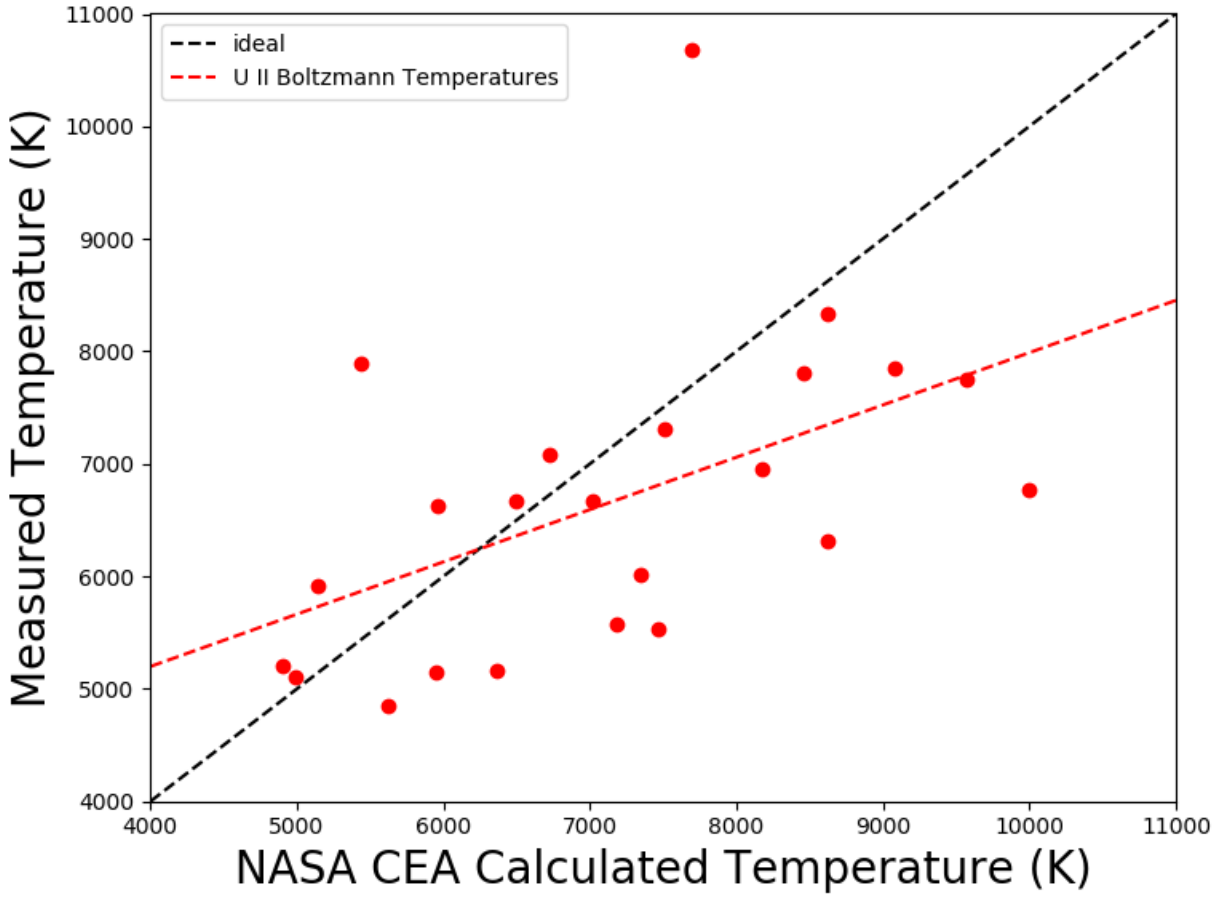

Figure 4.37: U II Boltzmann temperatures versus NASA CEA Calculated Temperatures in Kelvin.

This yields better agreement with the ideal at lower temperatures and increasing deviation at higher temperature. These various temperatures are shown overlaid in Figure 4.38.

These results underscore a need to better characterize the performance of the heterogeneous shock tube setup at high temperatures > 6000 K. This document details the first test series performed in this temperature regime in this setup, and reliable validation techniques are necessary to characterize the peak temperatures reached in a given high temperature shot.

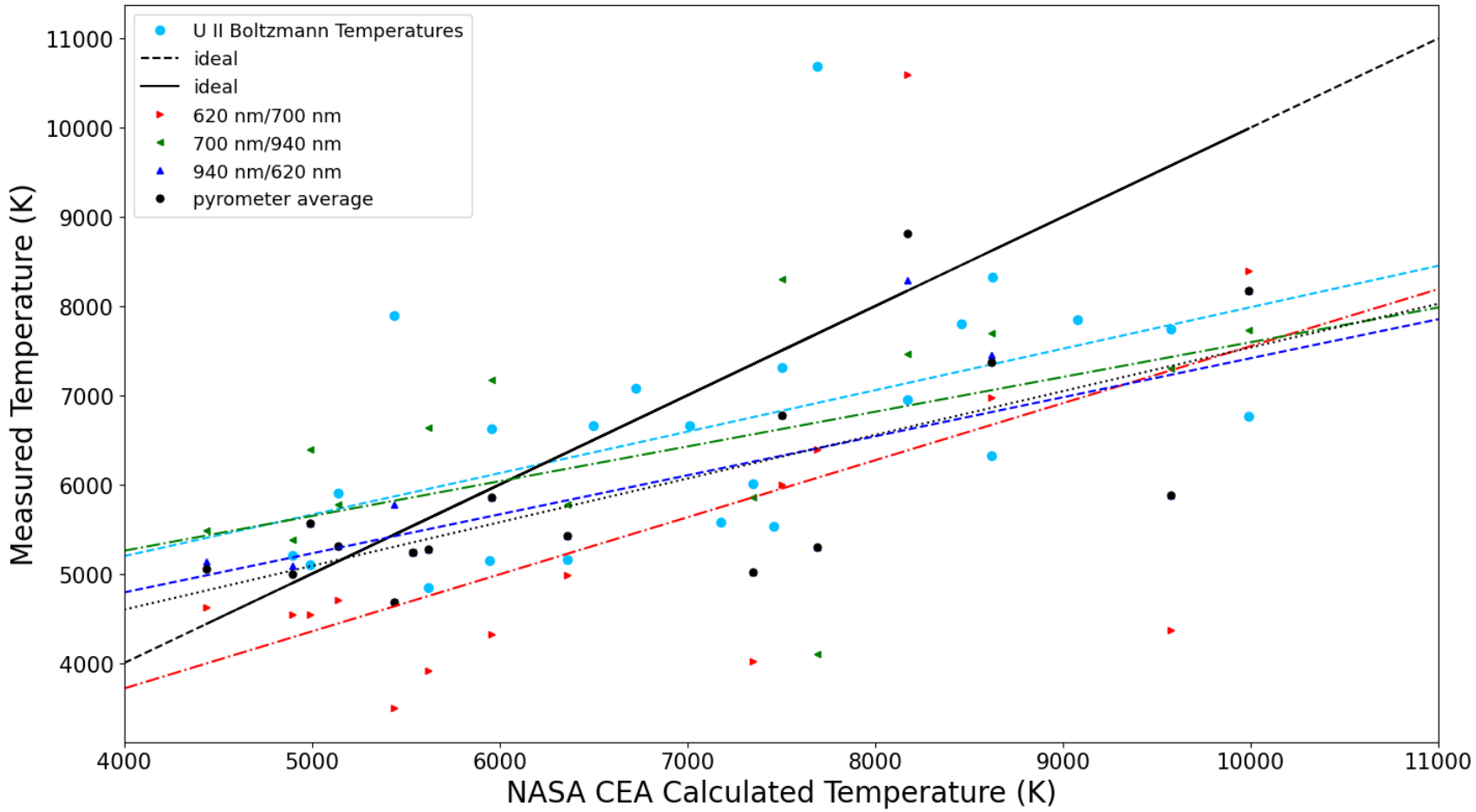

Figure 4.38: Comparison between U II temperatures and questionable pyrometer-calculated temperatures.

A separate set of iron transitions than that discussed previously (Figure 3.12) was used to determine temperature for spectra where the uranium signatures ceased to exist, after the initial shock. The necessary information is summarized in Table 4.4. The targeted transitions are shown in Figure 4.39.

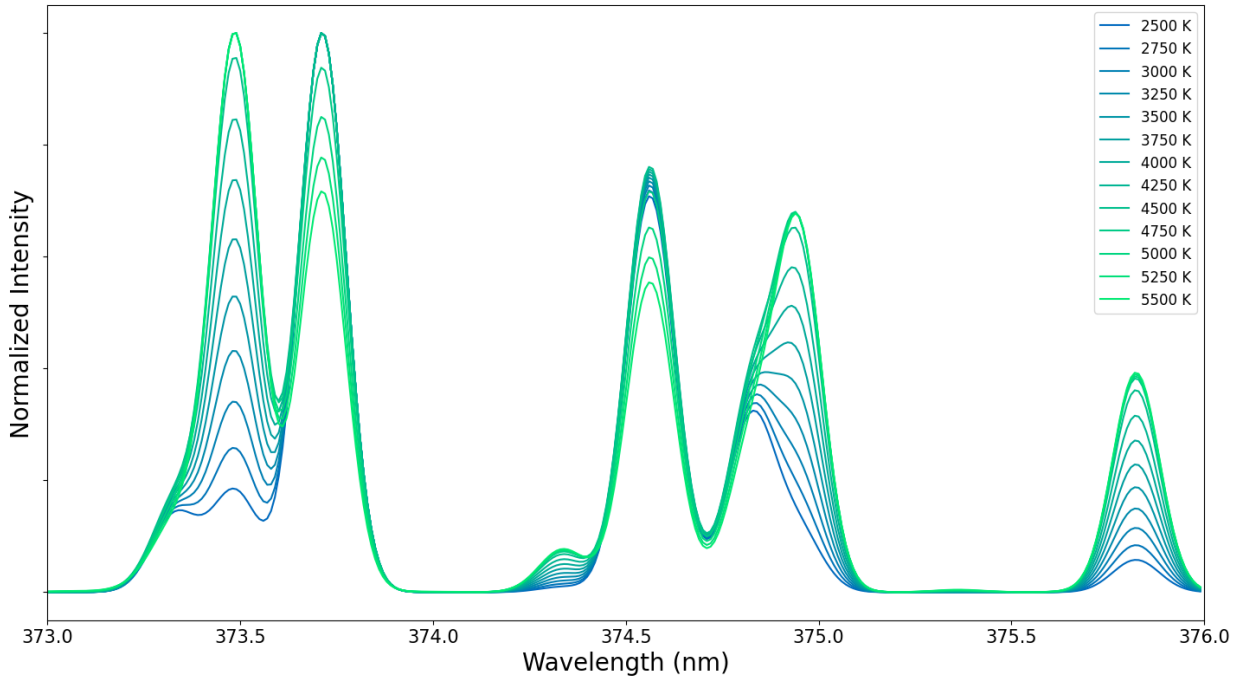

Figure 4.39: Modeled temperature variant Fe I transitions.

Figure 4.40 shows the resulting temperatures. Temperatures were obtained for both the last frame with uranium signatures in it as well as the first frame with no uranium signatures as available for all shots (i.e. shots > 9000 K were too fast to obtain this metric, since only a few usable frames existed at all).

Table 4.4: Selected Fe I transitions for temperature fitting.			
Wavelength (nm)	**A_{ul} (s^{-1})**	**Upper state energy (cm^{-1})**	**Upper state J**
373.0386	9.73E+06	51373.91	5
373.046	3.09E+06	50979.58	4
373.0946	3.50E+06	47834.22	3
373.1373	3.37E+06	47831.15	2
373.2396	2.69E+07	44511.81	2
373.3317	6.48E+06	27666.35	1
373.4864	9.01E+07	33695.4	5
373.5324	2.70E+07	50475.29	4
373.7131	1.41E+07	27166.82	4
373.8305	3.44E+07	53093.53	6
373.9116	4.51E+05	44664.08	2
373.9314	5.30E+05	44285.45	2
374.0239	1.30E+07	52953.63	4
374.2616	6.75E+06	50423.14	4
374.3362	2.60E+07	34692.15	1
374.3468	6.05E+07	55525.56	5
374.3776	3.55E+05	48702.54	4
374.4102	3.17E+07	51208	1
374.5561	1.15E+07	27394.69	3
374.5899	7.32E+06	27666.35	1
374.6474	6.10E+05	44411.16	1
374.6927	2.33E+07	50861.82	3
374.8262	9.15E+06	27559.58	2
374.8964	1.48E+07	50377.91	5
374.9485	7.63E+07	34039.52	4
375.1821	4.74E+05	48361.88	4
375.3138	1.14E+05	46026.97	6
375.3611	1.22E+07	44183.63	2
375.45	2.42E+06	50808	4
375.6068	5.13E+05	44166.21	3
375.6937	2.20E+07	55429.82	5
375.7454	8.26E+06	53229.94	1
375.8233	6.34E+07	34328.75	3
375.9155	4.55E+06	55907.18	5

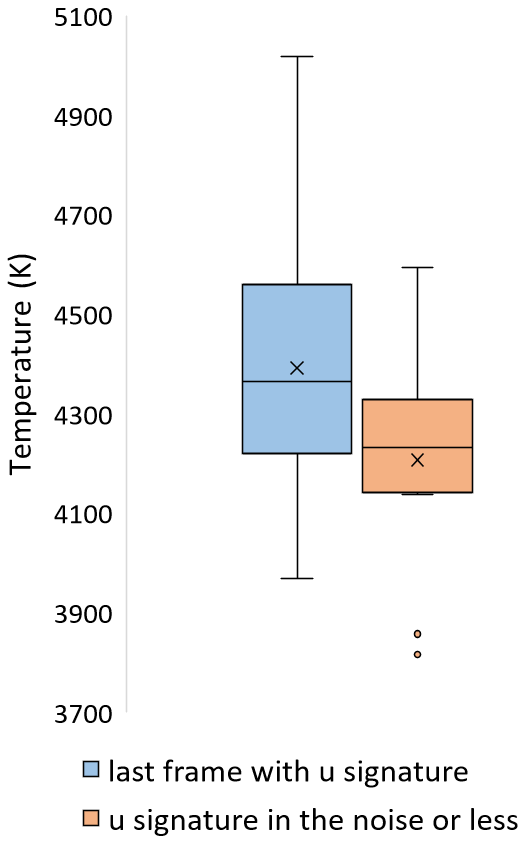

Figure 4.40: Box and whisker plot for temperatures obtained from tracking persistence of uranium signatures.

The most interesting result from these data is that these temperatures are extremely close to the boiling point of uranium, 4404 K. This makes sense because after the materials is heated enough to burn in the vapor phase, it should continue to emit so long as it remains in that phase. Once uranium cools and condenses, it should no longer emit electronic signatures.

4.4.4. Uncertainty in Temperature Measurement

It is evident from the various measurement techniques previously discussed that temperature is difficult to measure in a rapidly changing system. Deviations from what would be considered ideal, the temperatures calculated using NASA's CEA program, are expected and can arise from various facets of the experiment.

Perhaps a large contributor to the deviations in measurement is the use of knife blade or 'sting' loading. This technique has been used for measurements in this setup in the past to bolster signal for such applications as spectral absorption measurements of the excitation of aluminum powder. Lynch notes that this loading method may lead to effects from the optical thickness of burning

particles due to their inhomogeneous dispersal in a relatively small volume. This may also lead to entrainment of particles in the flow and extended burn times [139]. There may additionally be some effect due to oblique shocks created from the edge of the knife blade [107]. Bazyn notes that this technique may lend itself well to stronger shocks, such as that employed in this study, where the reflected shock occurs before the particles impact the end wall, potentially deforming them and affecting burn behavior [88]. The images in Figure 4.23, which were fairly typical of those observed for other test temperatures albeit not always so bright, show that while a small amount of powder is entrained after the initial shock, the bulk motion of particles does not occur until the reflected shock excites the particles whilst it travels in the direction opposite the end wall.

Simple calculations of heat capacity of a cubic centimeter of volume indicate that if 1 mg of U particles are present alongside Ar, O_2, and N_2 in proportions mirroring test conditions, the amount of energy necessary to raise the temperature the same number of degrees Kelvin increases six-fold, indicating that uranium that is not sufficiently dispersed serves as a heat sink. Mixture-averaged heat capacity decreases from 0.32 kJ/(kg*K) to 0.19 kJ/(kg*K), since the heat capacity of uranium is 0.184 kJ/(kg*K) [135], but the mass present in the system increases by three orders of magnitude due to the significantly higher density of uranium. If volume is increased, this discrepancy is removed (uranium is sufficiently dispersed). The same would hold likely hold true for almost any metal introduced to the system in this way. This may be a reason for the consistent measurement of temperatures below what would be ideal with this system.

Another potential contributor to lower experimental temperatures is the amount of oxygen present in the system. In these types of conditions, the reflected shock temperature, T5, is somewhat sensitive to oxygen concentration, which would increase with time since it would be due to a leak into the shock tube (driven pressure would increase slightly as well). Since the leak rate was so small, the pressure change alone would not have much effect on T5 (< 1 K variation for pressure range in this series), but change in the percentage of O_2 in the system can make a large difference when all else is equal (Figure 4.41).

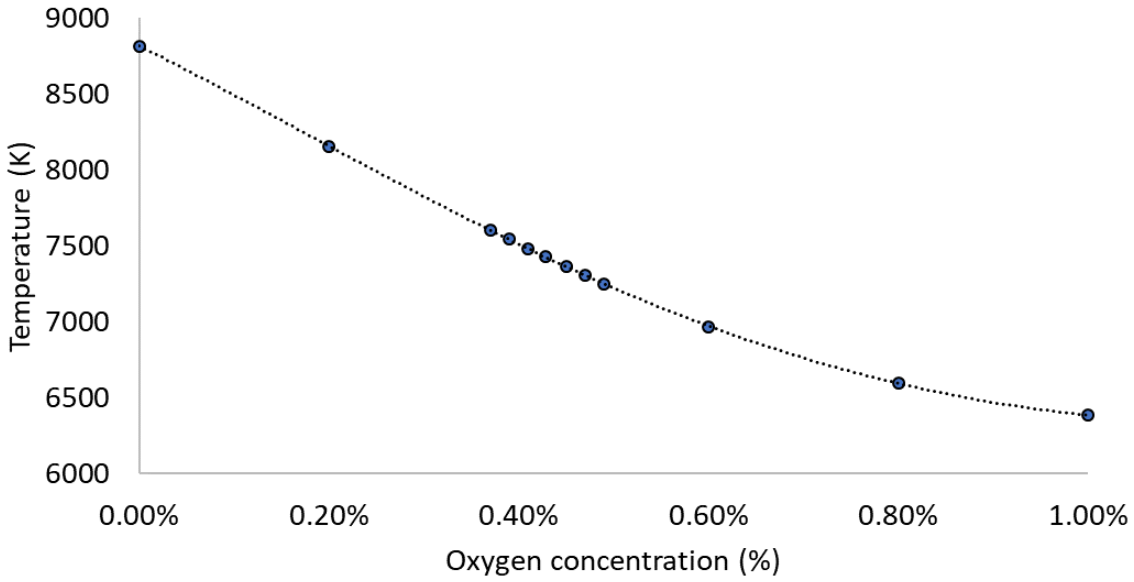

Figure 4.41: Theoretical temperature variation with oxygen concentration at constant driven pressure of 2.04 torr and shock speed of 2000 m/s, $[N_2] = 4*[O_2]$, and $[Ar] = 1-[N_2]-[O_2]$, mirroring shot conditions. Trace species were not considered. The dotted line is a polynomial fit to NASA CEA calculated values for temperature [67].

4.5. Flash powder testing – Cs and Sr mixtures

Flash powders doped with small amounts of Sr and Cs carbonates were set off in order to determine whether signatures from these materials would appear when energized. Figure 4.42 shows emission near 460 nm where strong Sr I and Cs I signatures exists. The strontium signature at 460.7 nm exhibits self-reversal at early times. As an aside, self-absorption occurs when one portion of a fireball in the optical path acts as an absorption source for species closer to the detector. Self-reversal occurs when a brighter (hotter) spectral line is partially absorbed by cooler gas nearer the detector, weakening the center.

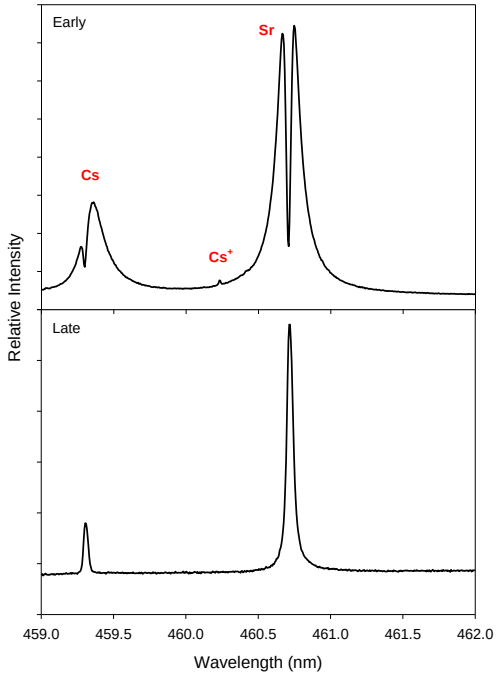

Figure 4.42: Visible emission from combustion of Mg flash powder (stoichiometric Mg and $Sr(NO_3)_2$) doped with Cs_2CO_3 (courtesy of Dr. Glumac).

Even Cs II appeared in these spectra at early times. It was uncertain that the energy attained in this experiment would be sufficient to ionize Cs. Figure 4.43 shows signatures in the higher end of the visible spectrum and near-IR.

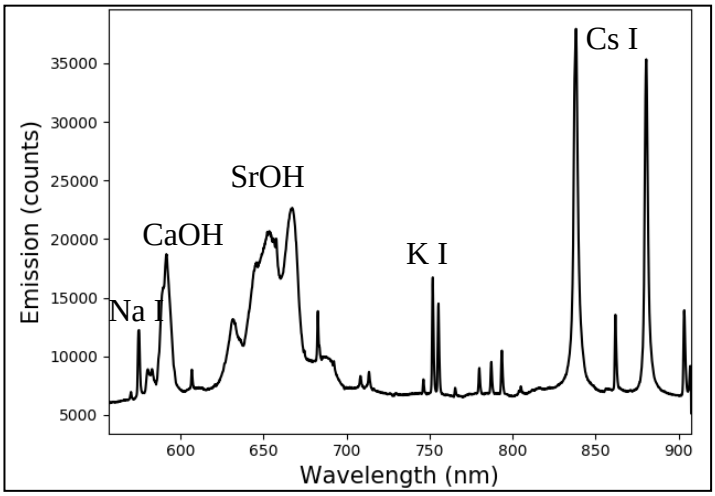

Figure 4.43: Near-IR emission 720 μs after ignition from combustion of Al Flash powder (stoichiometric Al and $Sr(NO_3)_2$) doped with Cs_2CO_3.

These included molecular signatures, SrOH and CaOH, which arose from a Ca impurity. Na and K impurities also appeared. N I signatures appeared near 775 nm. Strong Cs I signatures show up between 825 and 900 nm as well.

4.6. Small-scale high explosive testing

High explosive testing was performed to determine the appearance of the previously studied signatures in conditions of higher energy input. Here, only one of the regions was probed, the red-NIR (Figure 4.44).

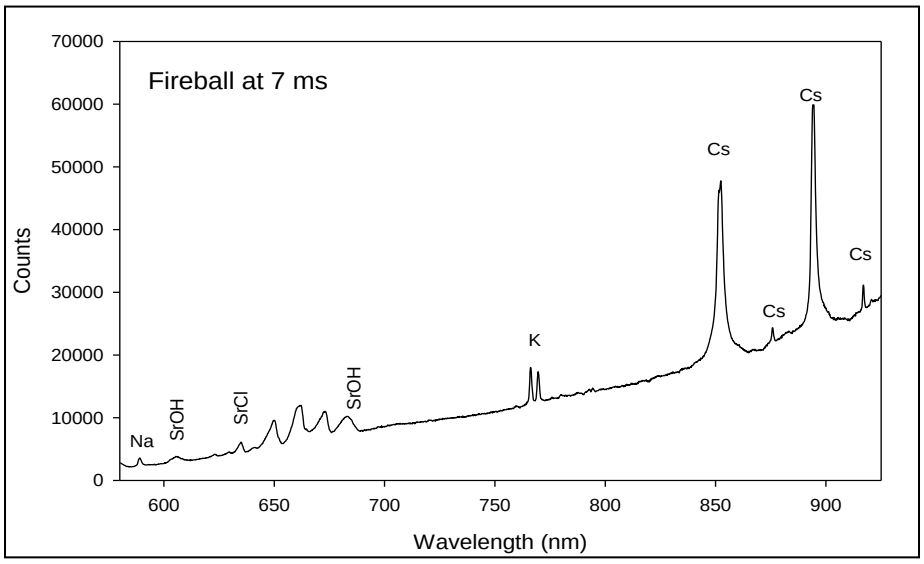

Figure 4.44: Near-IR spectrum from high explosive test article (courtesy of Dr. Glumac).

In this test, chlorides instead of carbonates were used to introduce cesium and strontium to the system. Molecular strontium signatures (SrOH and SrCl) were observed almost superimposed as well as strong atomic Cesium signatures. Na and K impurities were also present.

Figure 4.45 shows the persistence of the Cs and SrOH signals, which appeared shorter after initial continuum and lasted longer than 16 ms from detonation of the charge.

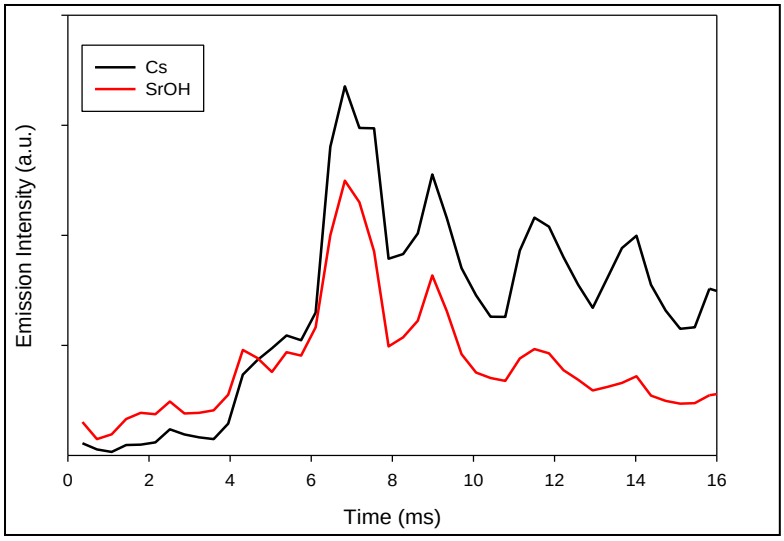

Figure 4.45: Cs and SrOH signal intensities from high explosive test article over time (courtesy of Dr. Glumac).

The 'waves' in emission intensity are due to shock reflections off of the chamber wall.

4.7. Field-scale high explosive testing

After the preliminary lab-scale testing was completed, a series of field tests were conducted at the Naval Surface Warfare Center's Blossom Point Facility in conjunction with researchers there, as well as collaborators from Craft Tech and Sandia. Several cases were tested to evaluate whether spectral signatures were sensitive to change in proportion and amount of Cs and Sr present in an explosion, as well as if these signatures would appear differently in the presence of differently oxidizing materials. Different explosives were also tested to gauge their effect on resulting spectra. Figure 4.46 and Figure 4.47 show images and spectra in both regions acquired for the base cases of charges containing equivalent masses of Mg (magnesium) or Cu (copper) with Octol explosive.

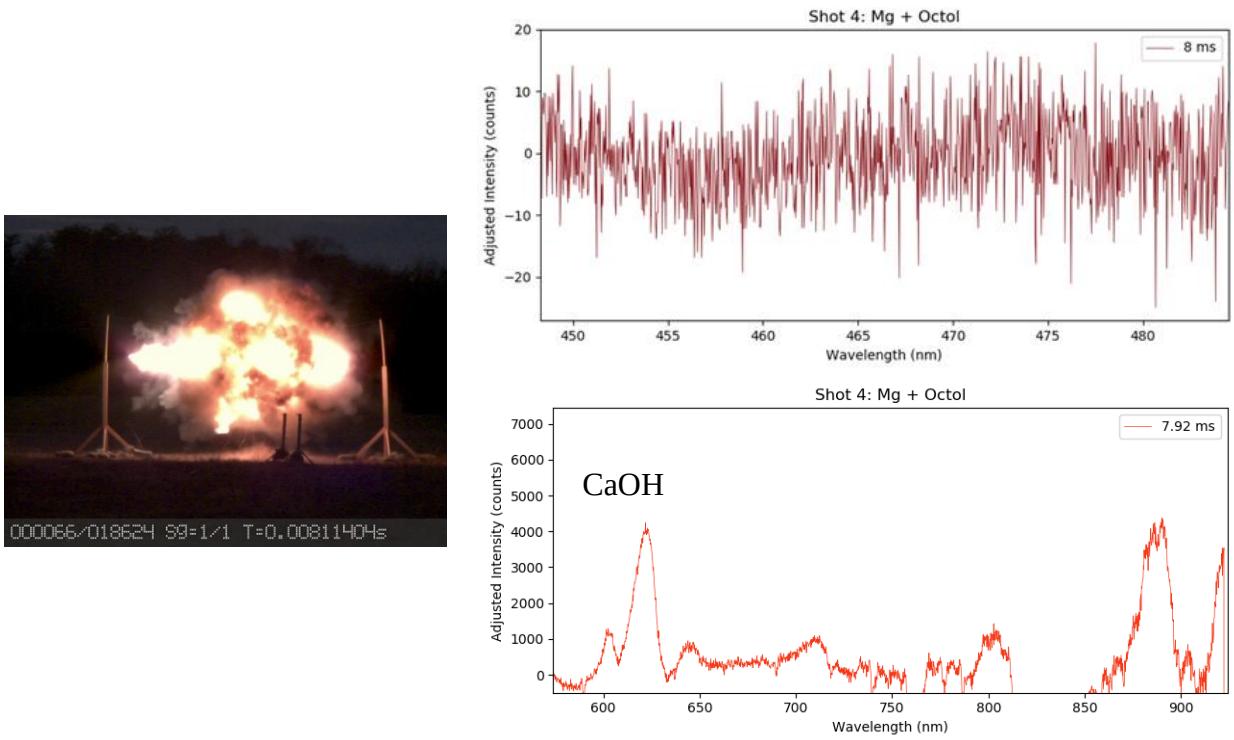

Figure 4.46: Base case of Mg + Octol explosive. Spectra are from ~8 ms after initial detonation.

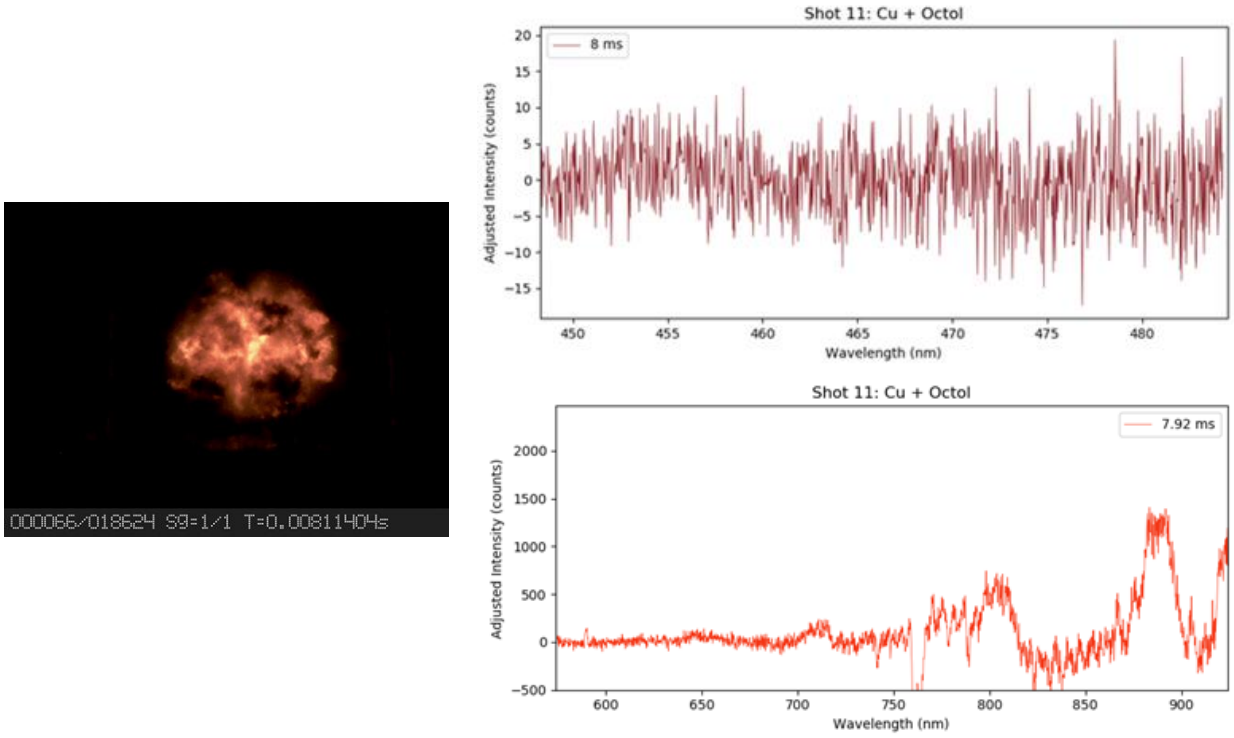

Figure 4.47: Base case of Cu + Octol explosive. Spectra are from ~8 ms after initial detonation.

Here, no significant features appear, save for CaOH around 625 nm in the Mg + Octol case. Emission for the 580-920 nm spectra has been adjusted for instrument responsivity, and continuum emission from the explosive and background emission from sunlight (due to outdoor testing) have been subtracted out. For the 450-485 nm region, emission spectra have also been adjusted for instrument responsivity. The test containing Mg appears to be much more luminous in general.

Figure 4.48 and Figure 4.49 show the Mg and Octol charges containing different ratios of Cs and Sr.

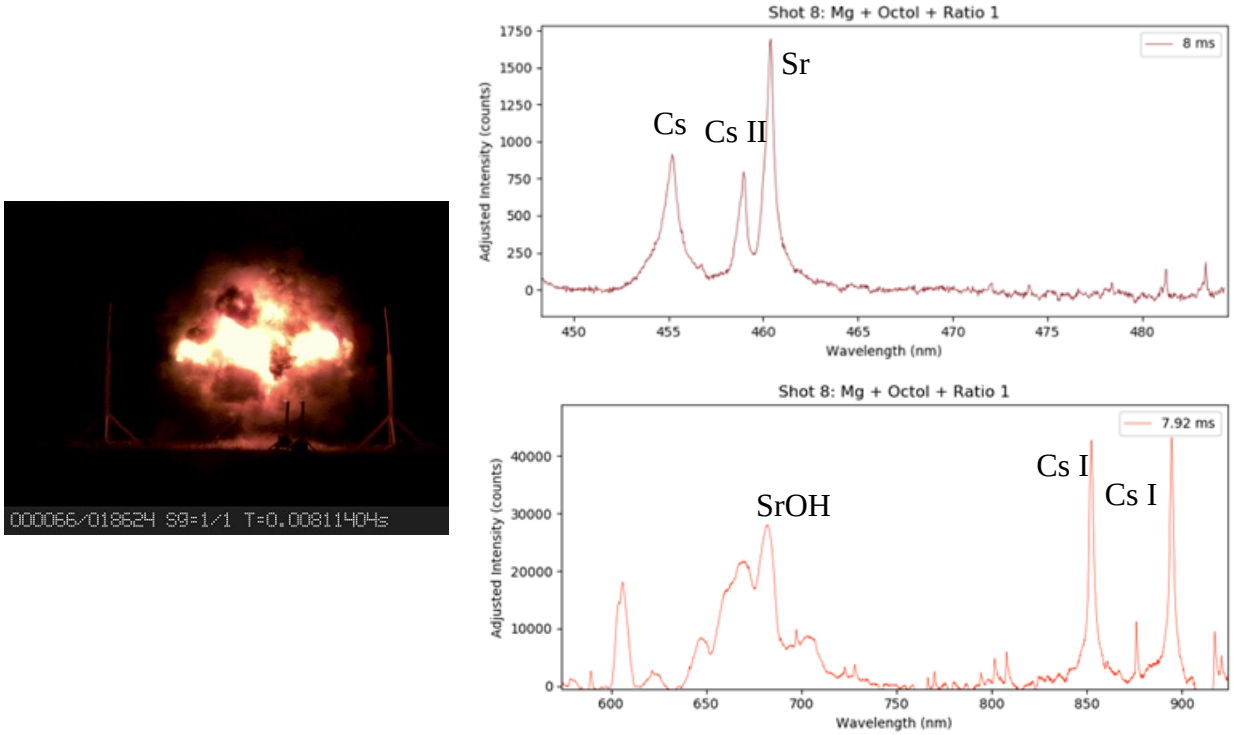

Figure 4.48: Mg + Octol + Ratio 1 (6.1 Cs/5.8 Sr) Case. Spectra are from ~8 ms after initial detonation.

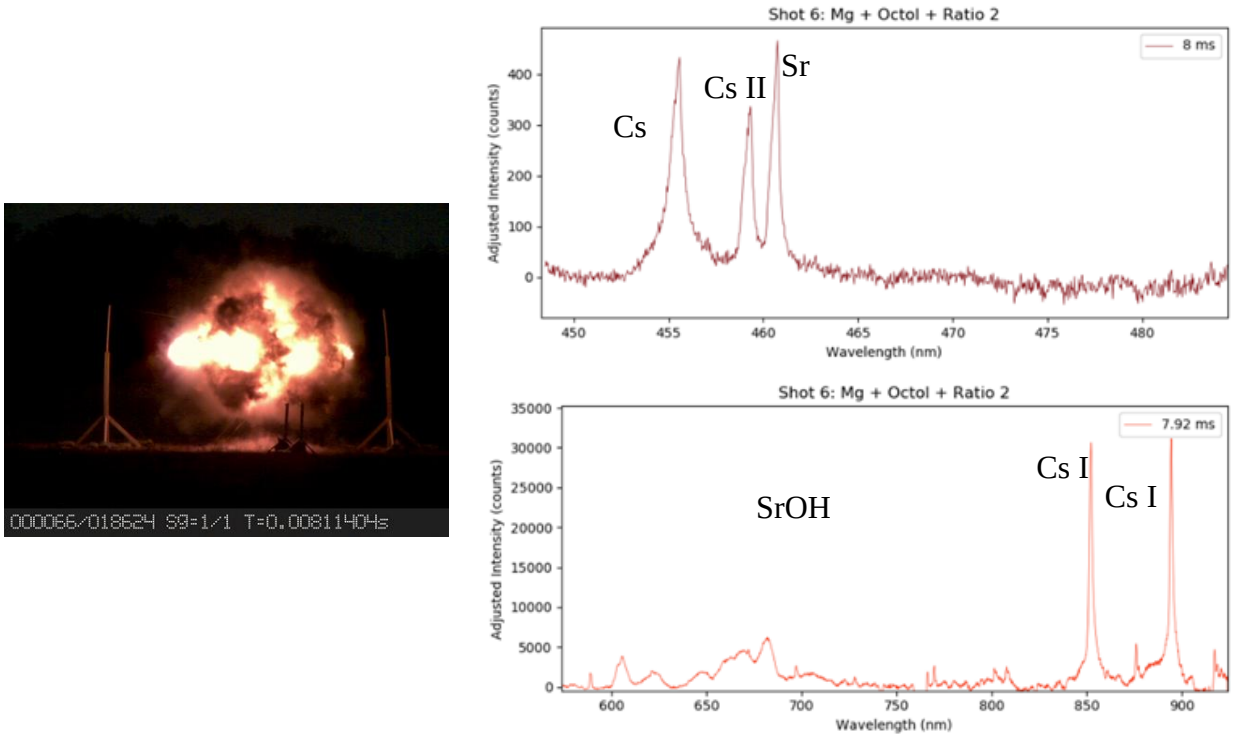

Figure 4.49: Mg + Octol + Ratio 2 (6.6 Cs/2.0 Sr) Case. Spectra are from ~8 ms after initial detonation.

To the eye, these events appear very similar. However, in the blue region, there is a clear difference in the relative intensities of Cs I, Cs II, and Sr I between the two cases, which could be used to differentiate between signatures from hypothetical devices containing different proportions of Cs and Sr—and therefore different fissionable materials. There is also a clear difference in the relative intensity of SrOH and Cs I signatures in the near-IR region between both cases.

There were some changes in relative intensity of spectral signatures over time (as the fireball cooled) for the various cases, but there were still differences in the signatures resulting from different coatings which is promising for future application of these signals to the development of remote sensing diagnostics for identification of fissionable materials from a fireball.

Figure 4.50 and Figure 4.51 also show a comparison between the signatures of different coatings but for Cu charges. Cu and Mg were both tested since varying metal oxidation behavior could affect the appearance of resulting spectral signatures.

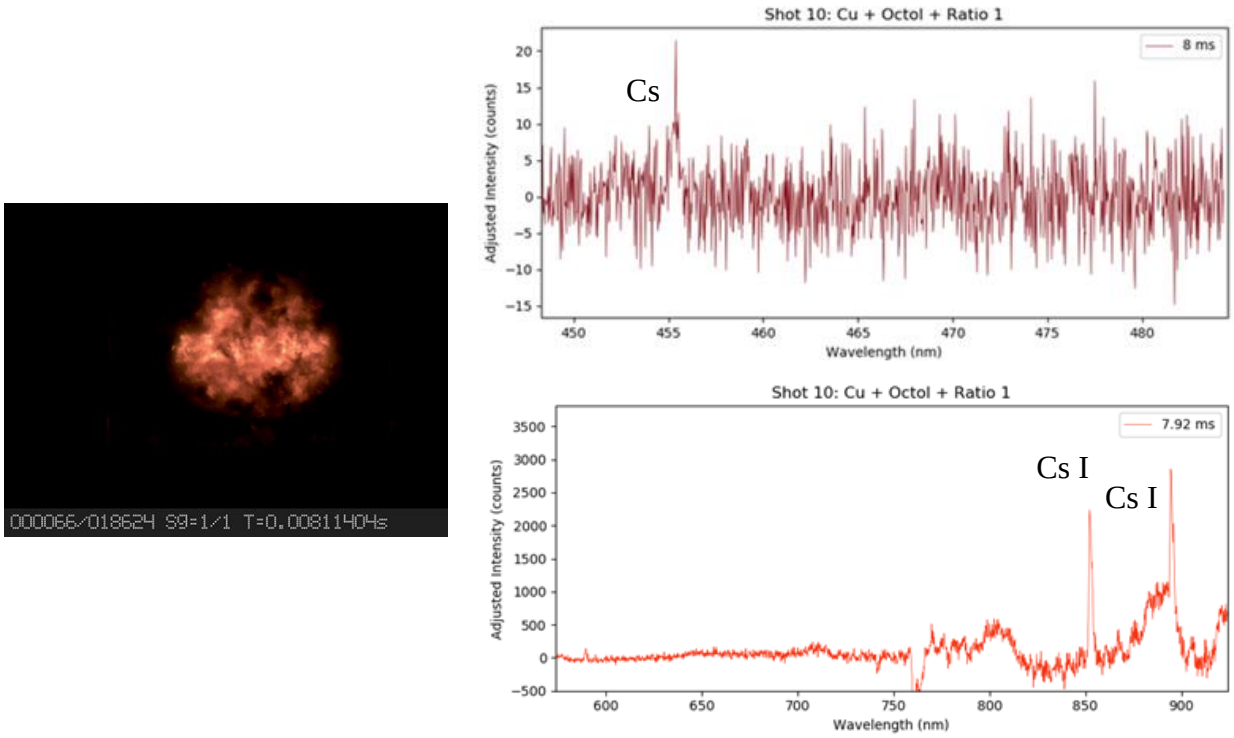

Figure 4.50: Cu + Octol + Ratio 1 (6.1 Cs/5.8 Sr) Case. Spectra are from ~8 ms after initial detonation.

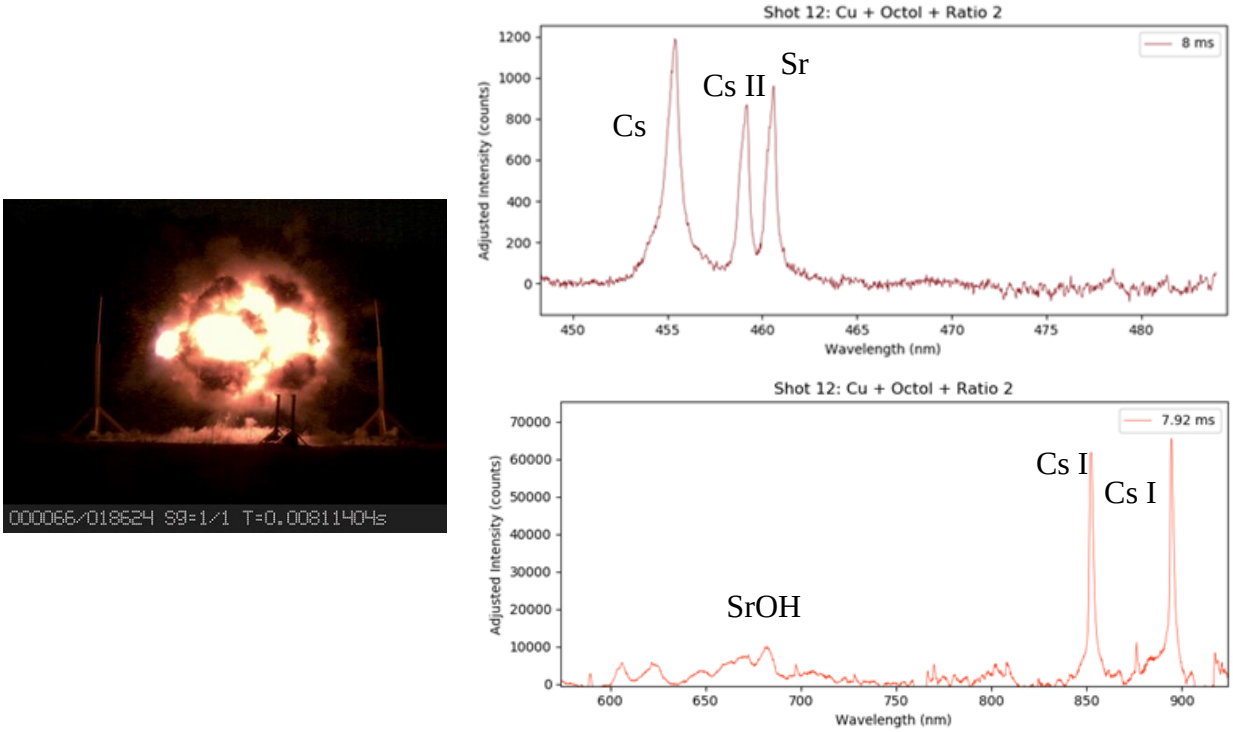

Figure 4.51: Cu + Octol + Ratio 2 (6.6 Cs/2.0 Sr) Case. Spectra are from ~8 ms after initial detonation.

Here there is a clear difference in the appearance of the two events. For the Ratio 1 coating and Cu, the signal was much weaker in both the near-IR and blue region. In general, the Sr signatures were attenuated as compared to the tests with Mg.

Figure 4.52, when compared with Figure 4.48, shows spectral dependence on mass of Ratio 1.

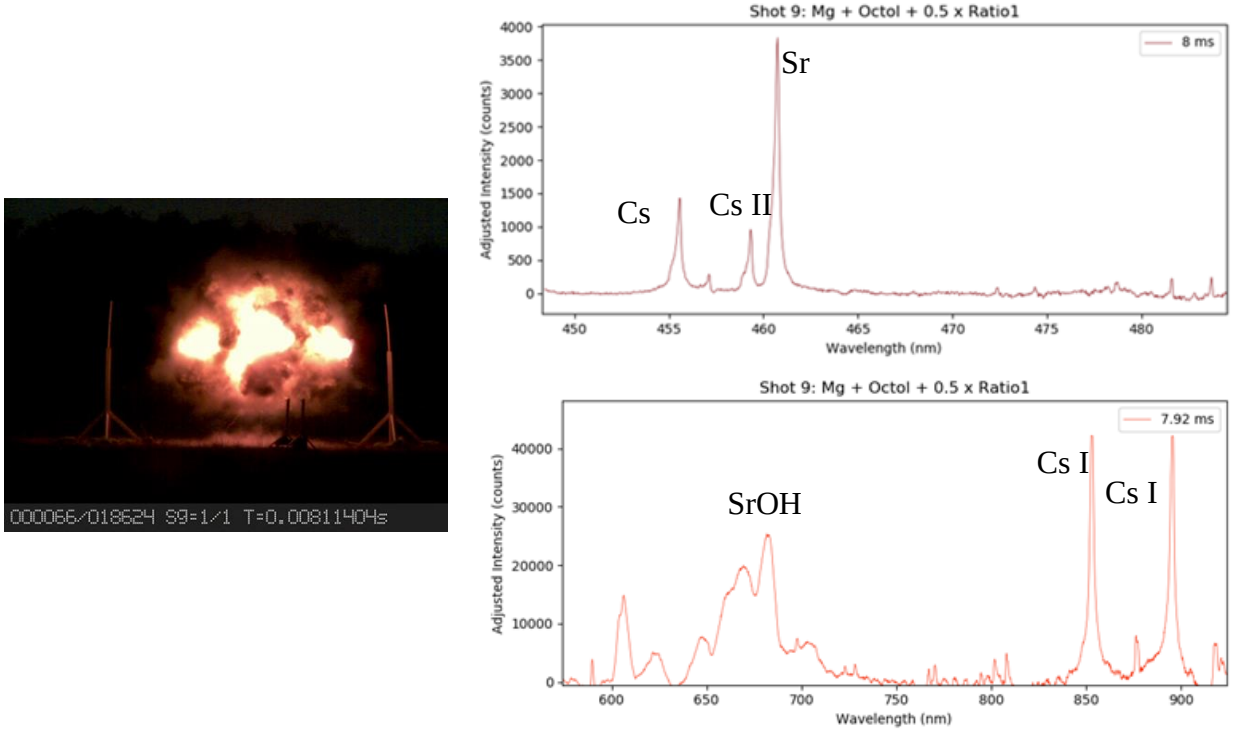

Figure 4.52: Mg + Octol + Ratio 1 (6.1 Cs/5.8 Sr) Case, half mass.

Relative intensities were fairly similar for both tests and spectral output did not greatly vary.

Figure 4.53 tracks the Cs I, Cs II, and Sr I peak areas in the blue region for all tests. Note that the first three shots had shorter acquisition times and therefore fewer points. In general, these peaks would be visible for up to 80 ms after detonation. Peak areas were lower overall for Cu cases, and as expected, cases that did not contain strontium carbonate or cesium carbonate did not have populated transitions but are included for comparison.

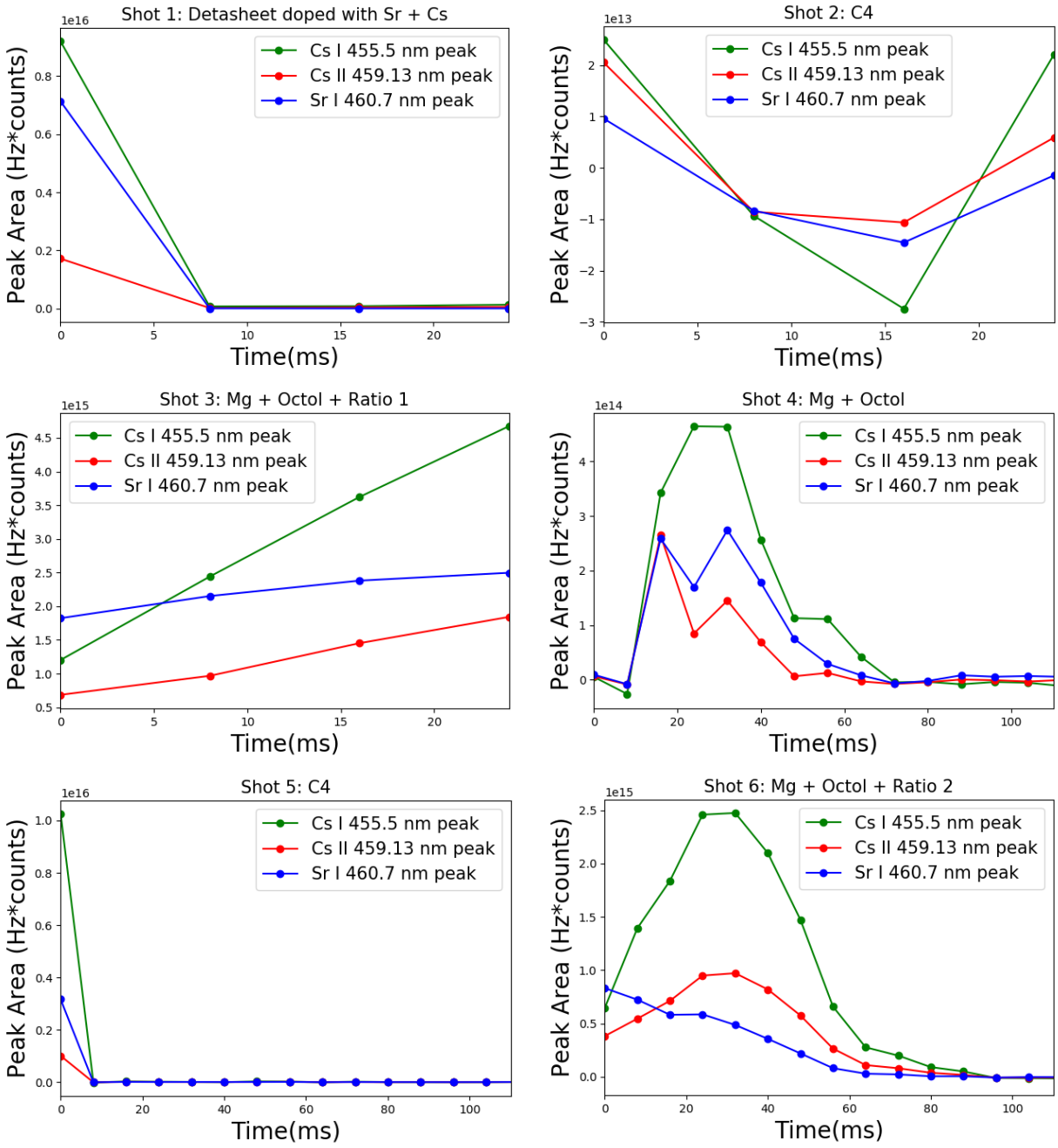

Figure 4.53: Time-resolved Cs I, Cs II, Sr I signatures for all tests in series.

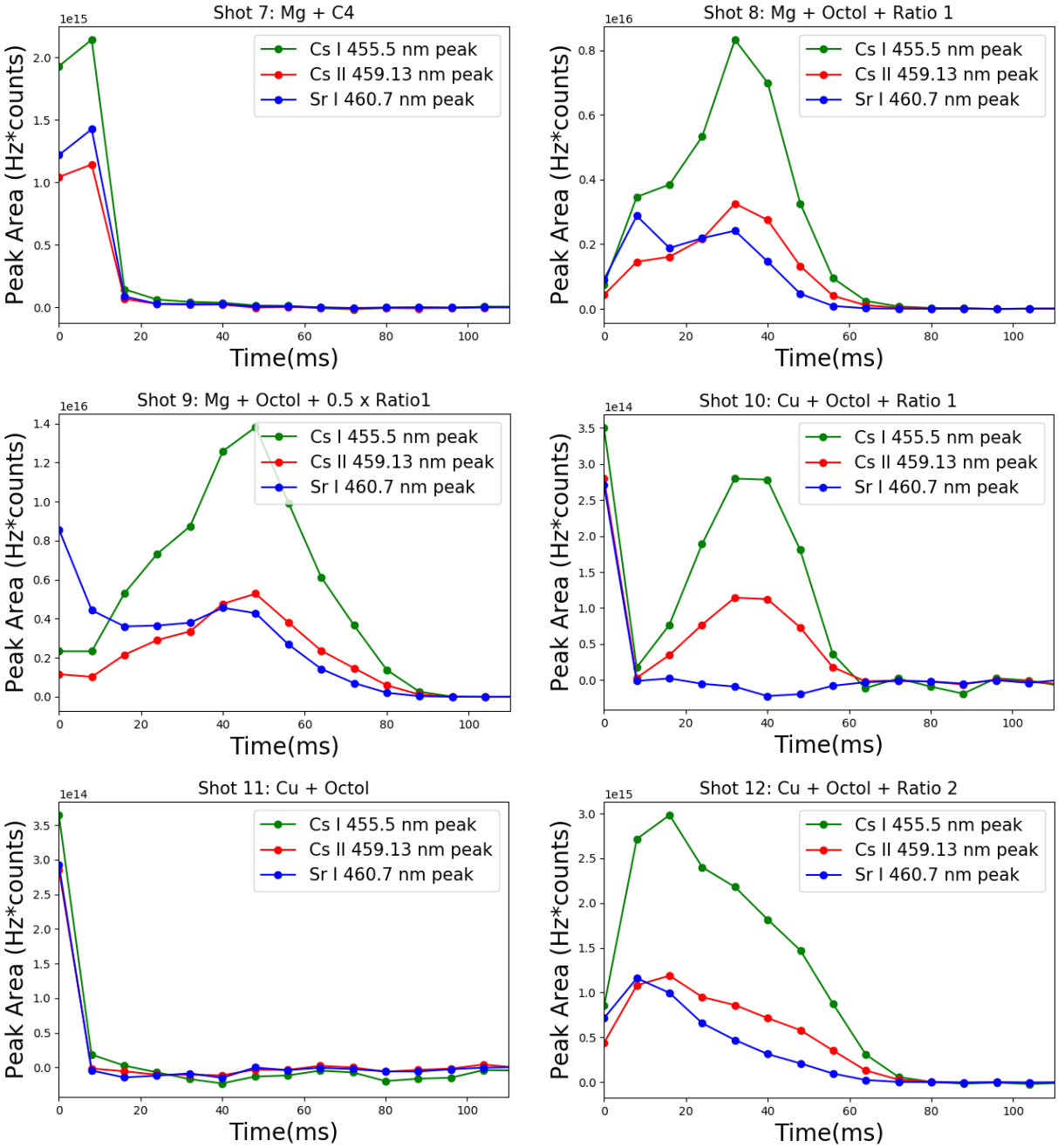

Figure 4.53: Time-resolved Cs I, Cs II, Sr I signatures for all tests in series (continued).

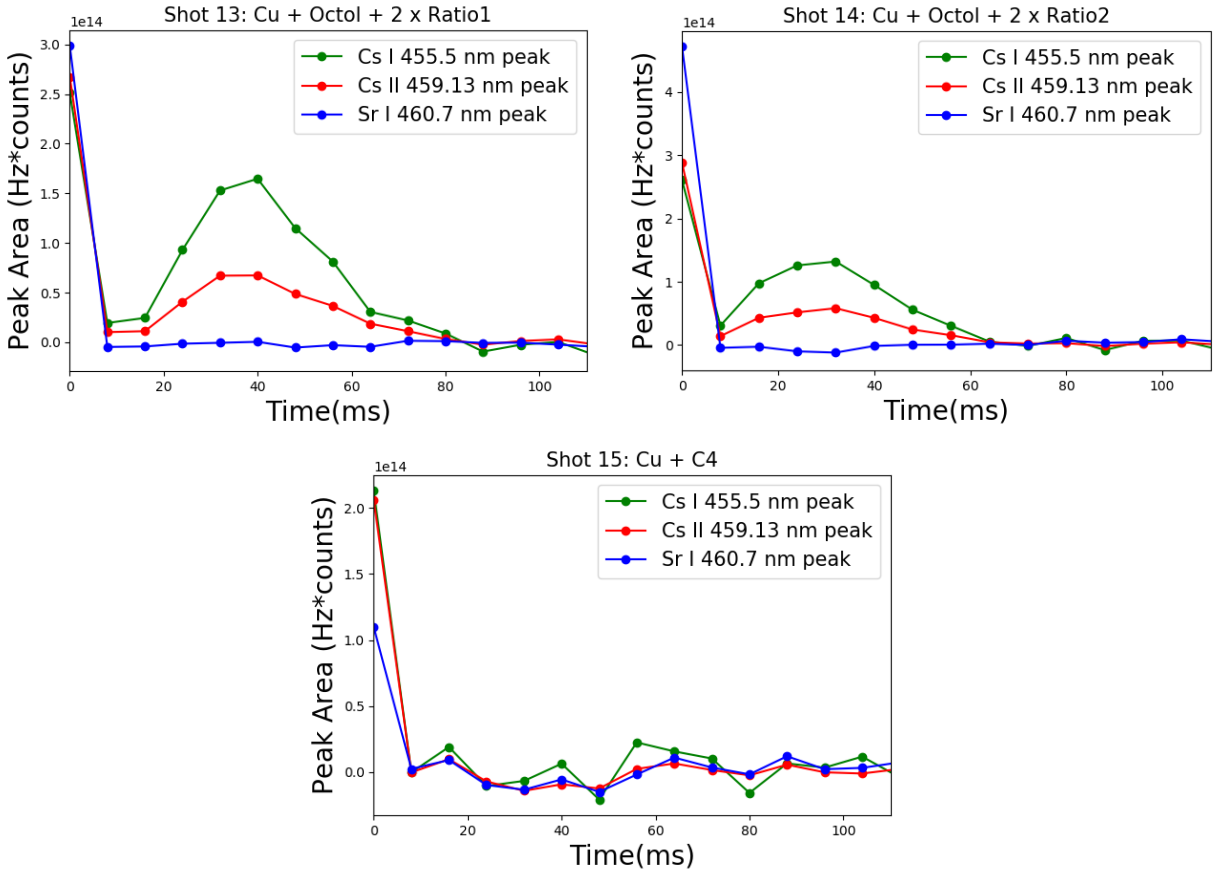

Figure 4.53: Time-resolved Cs I, Cs II, Sr I signatures for all tests in series (continued).

4.8. Flash powder testing – Fission product mixtures

After field testing was completed, and the utility of the Cs and Sr signatures confirmed, additional flash powder testing was performed to determine if other potential fission product signatures were worth further exploration. Based on the figures of merit detailed in Section 2.4.5 as well as material costs, metal, carbonate, and nitrate powders were obtained and mixed in the quantities listed in Table 3.3. These mixtures were combusted as in the previous tabletop flash powder testing with a similar setup, albeit different spectrometer (SPEX 270M) and detector (ZWO ASI174mm). It was uncertain how these signatures would appear when mixed together. Interference between atomic, ionic, and molecular species for each of the elements tested was to be expected. The ionization energies in Table 4.5 lend some insight as to which are more likely to appear when energized—transitions of lower ionization energy are more likely to appear. These are arranged in ascending order by 1st ionization energy.

Table 4.5: Ionization energies of fission products in mixtures [18].		
Element	**1st ionization energy**	**2nd ionization energy**
Cs	3.894	23.157
Rb	4.177	27.290
Ba	5.212	10.004
Nd	5.525	10.783
Ce	5.539	10.956
La	5.577	11.185
Sm	5.644	11.078
Eu	5.670	11.240
Sr	5.695	11.030
Y	6.217	12.224
Zr	6.634	13.130
Nb	6.759	14.320
Mo	7.092	16.160
Ru	7.361	16.760
Sb	8.608	16.626

The same blue region (~445-480 nm) as in the previous tests was probed as were three larger regions spanning the visible and some of the near infrared region of the electromagnetic spectrum. These spectra were then overlaid with simulated spectra from the species of interest and potential impurities to determine which were present and if their appearance differed for the two mixture ratios.

All overlays were modeled at 2000 K since due to the significant overlap of various species, temperature could not be determined. They are each scaled to the tallest peak observed in the range for the species for ease of observation. Figure 4.54 and Figure 4.55 show the fission powder mixtures in the same range around 460 nm as tested for the previous flash powder and explosive experiments.

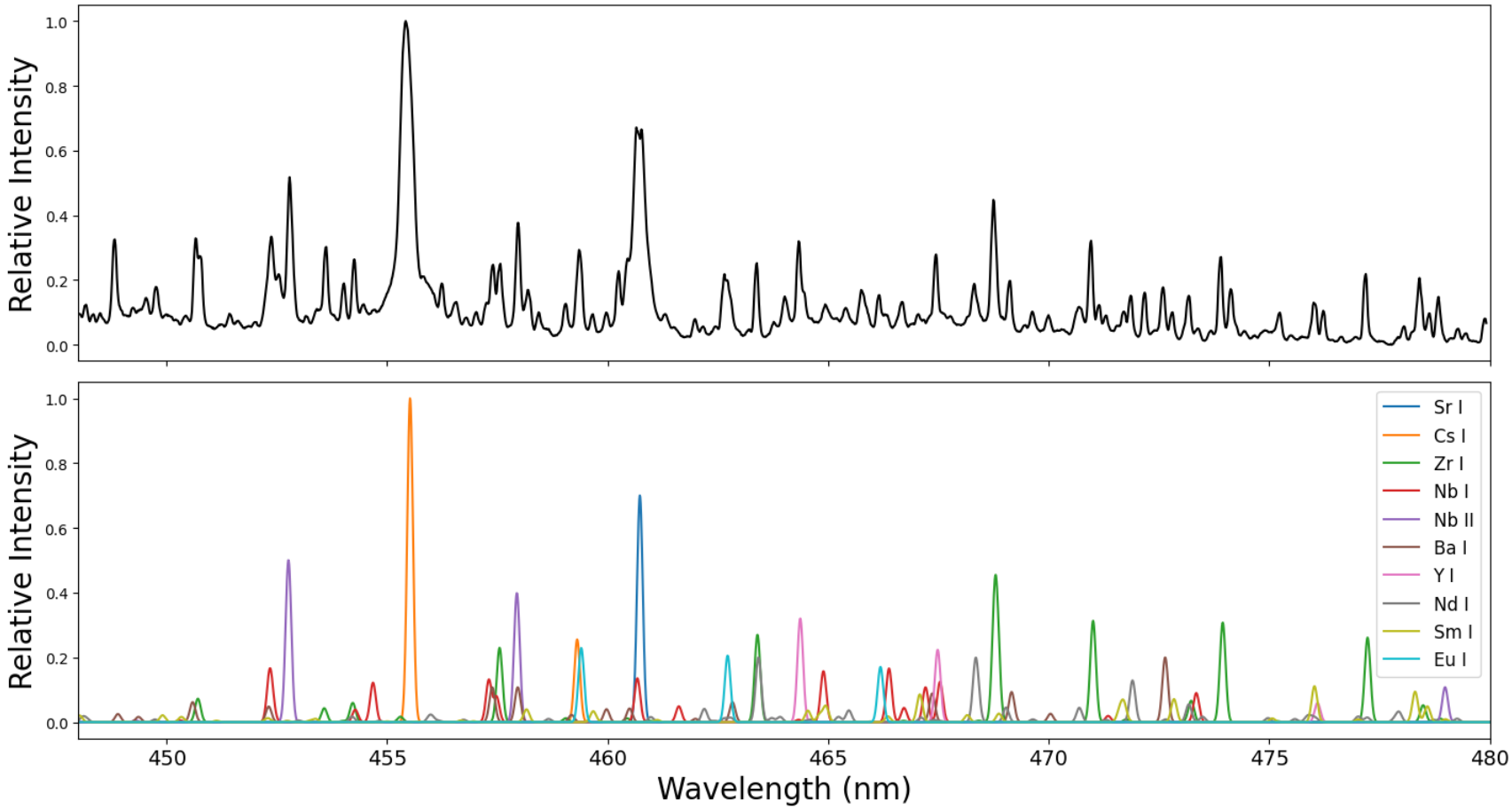

Figure 4.54: Pu^{239} fission product mixture spectrum in 445-480 nm range with tentative line assignments.

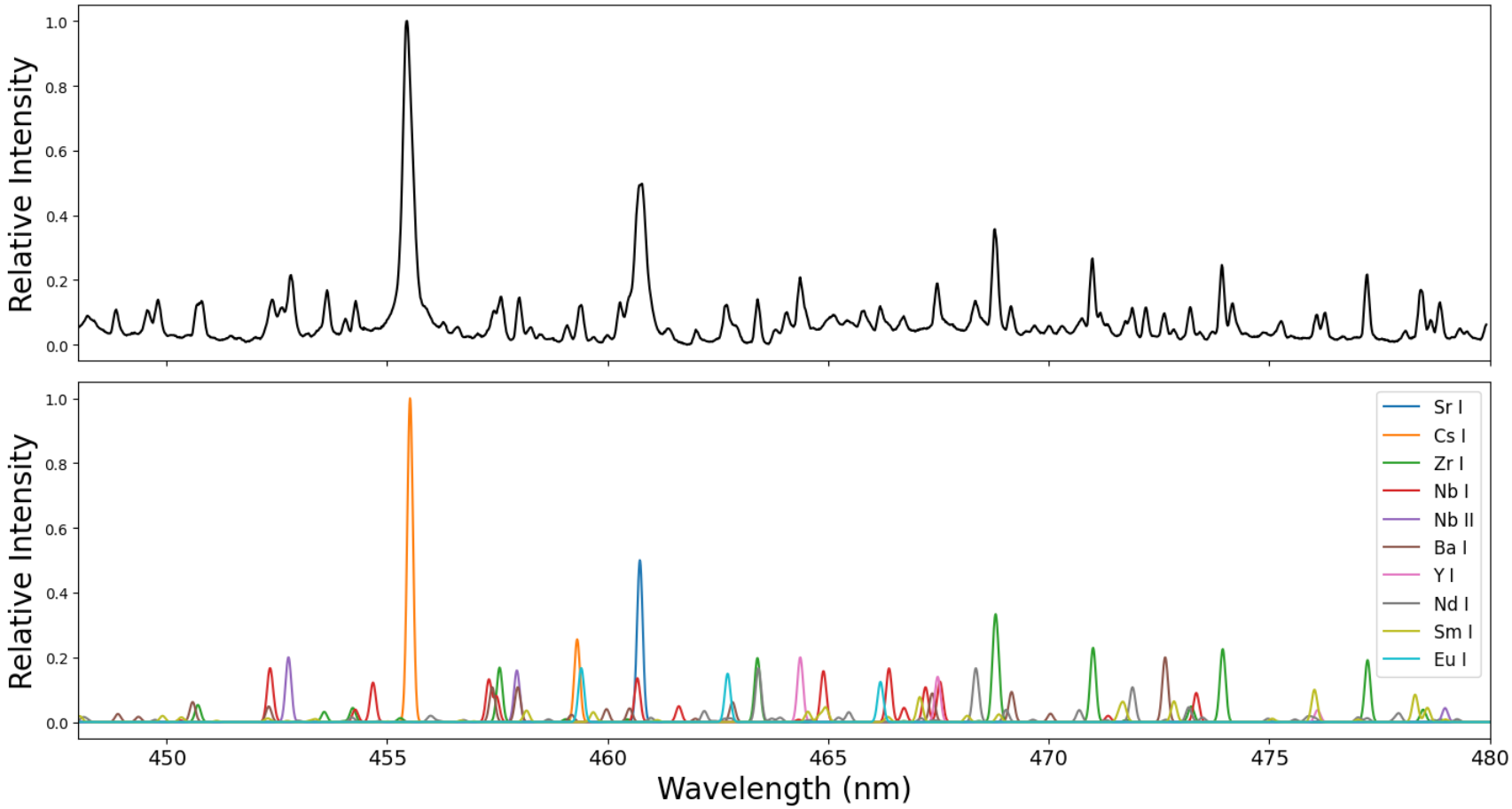

Figure 4.55: U^{235} fission product mixture spectrum in 445-480 nm range with tentative line assignments.

The spectrum for the Pu^{239} product mixture appeared to have a higher amount of Sr relative to Cs contrary to the actual makeup of the mixture. This indicates that emissions may also be due to other factors such as the temperatures that the mixtures achieved when combusted. Cs has a lower ionization energy, and this particular transition is fairly strong, so it is not unexpected that the Cs signatures was stronger than the Sr signature despite there being less Cs present in the mixture.

It also seems from these signatures that Nb II may be a potential indicator of fissionable material in a fireball environment. That having been said, many species appear to emit more strongly in the Pu^{239} product mixture than the U^{235} one. This may be due in part to that these mixtures are not true flash powders with stoichiometrically determined products, but instead are mixed to emulate fission product distributions. Therefore, one of these mixtures (Pu^{239}) may be slightly more energetic than the other, although neither react to completion.

Spectra for each mixture were also observed in larger regions. The first spanned 400 nm to 530 nm (Figure 4.56 and Figure 4.57).

Here, the spectra from the two mixtures appear quite similar save for the strong Sr I peak at 460.7 nm probed in the previous range. There may also be some band formation that is not fully accounted for in this region. Another pair of peaks seem to vary between the two mixtures, a Zr I and Nd II peak near 490 nm. Aside from these peaks, the two spectra are nearly identical.

The next region observed spanned 520 nm to 600 nm, and the corresponding spectra are shown in Figure 4.58 and Figure 4.59.

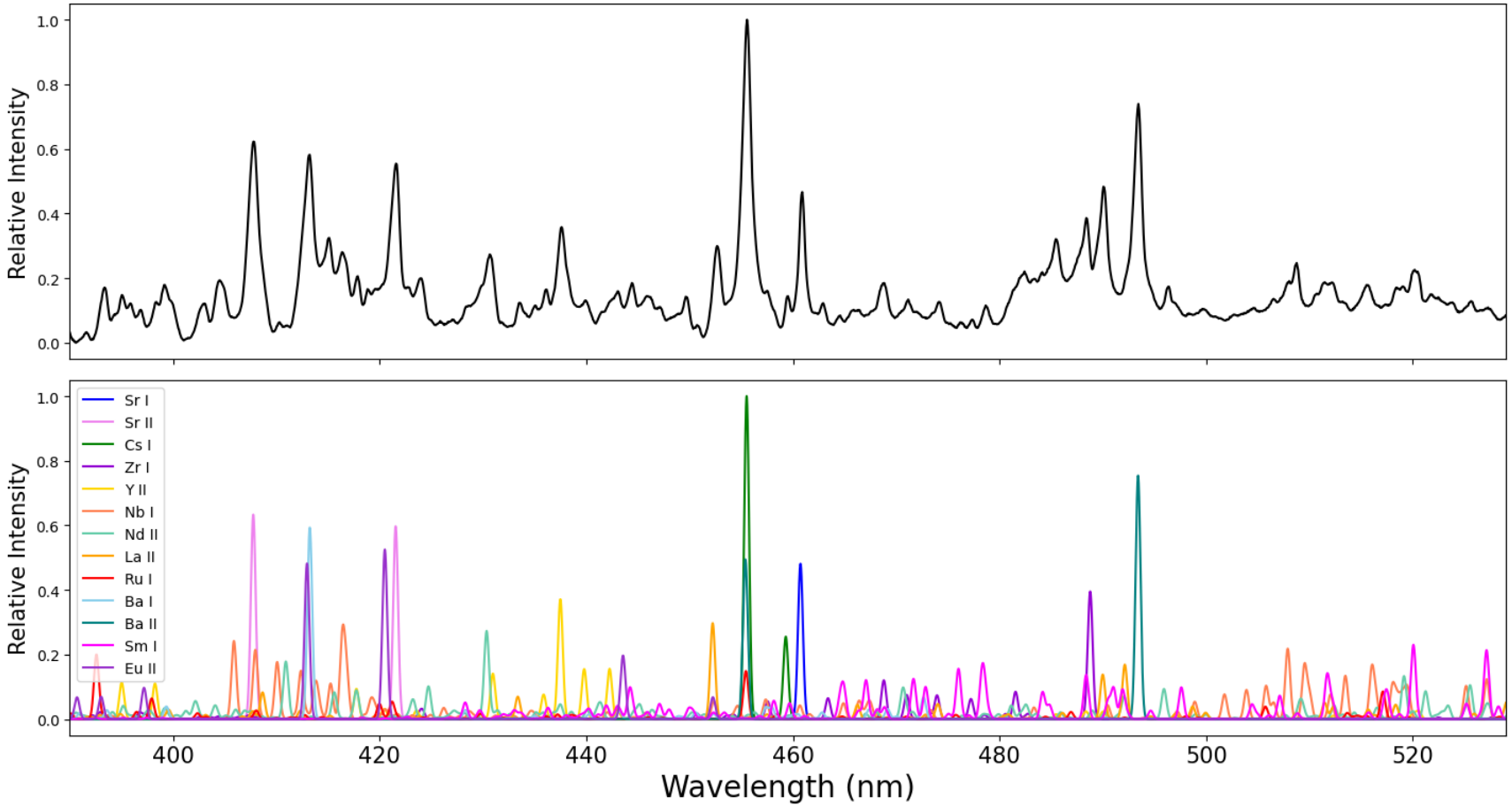

Figure 4.56: Pu^{295} fission product mixture spectrum in 400-530 nm range with tentative line assignments.

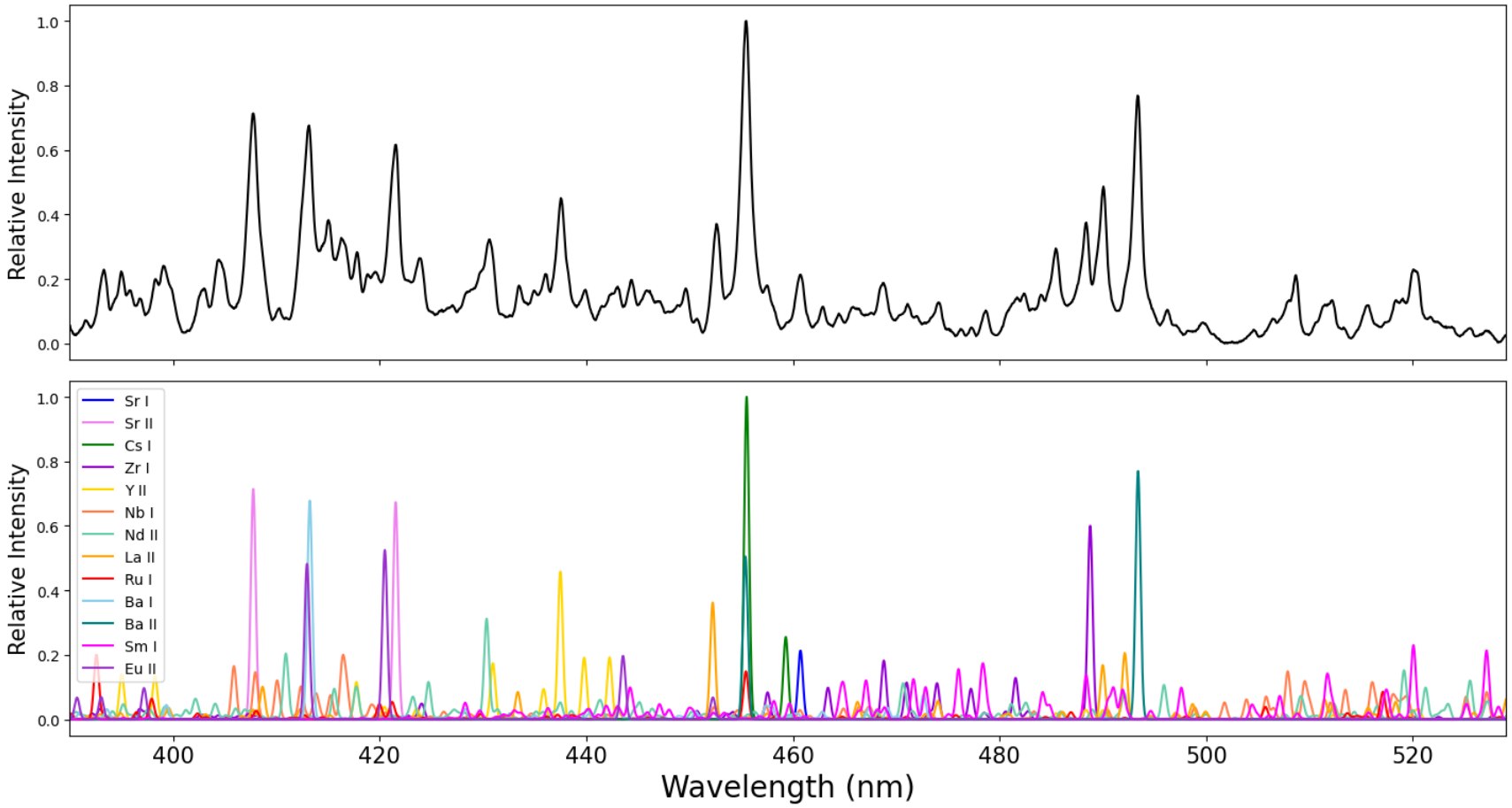

Figure 4.57: U^{235} fission product mixture spectrum in 400-530 nm range with tentative line assignments.

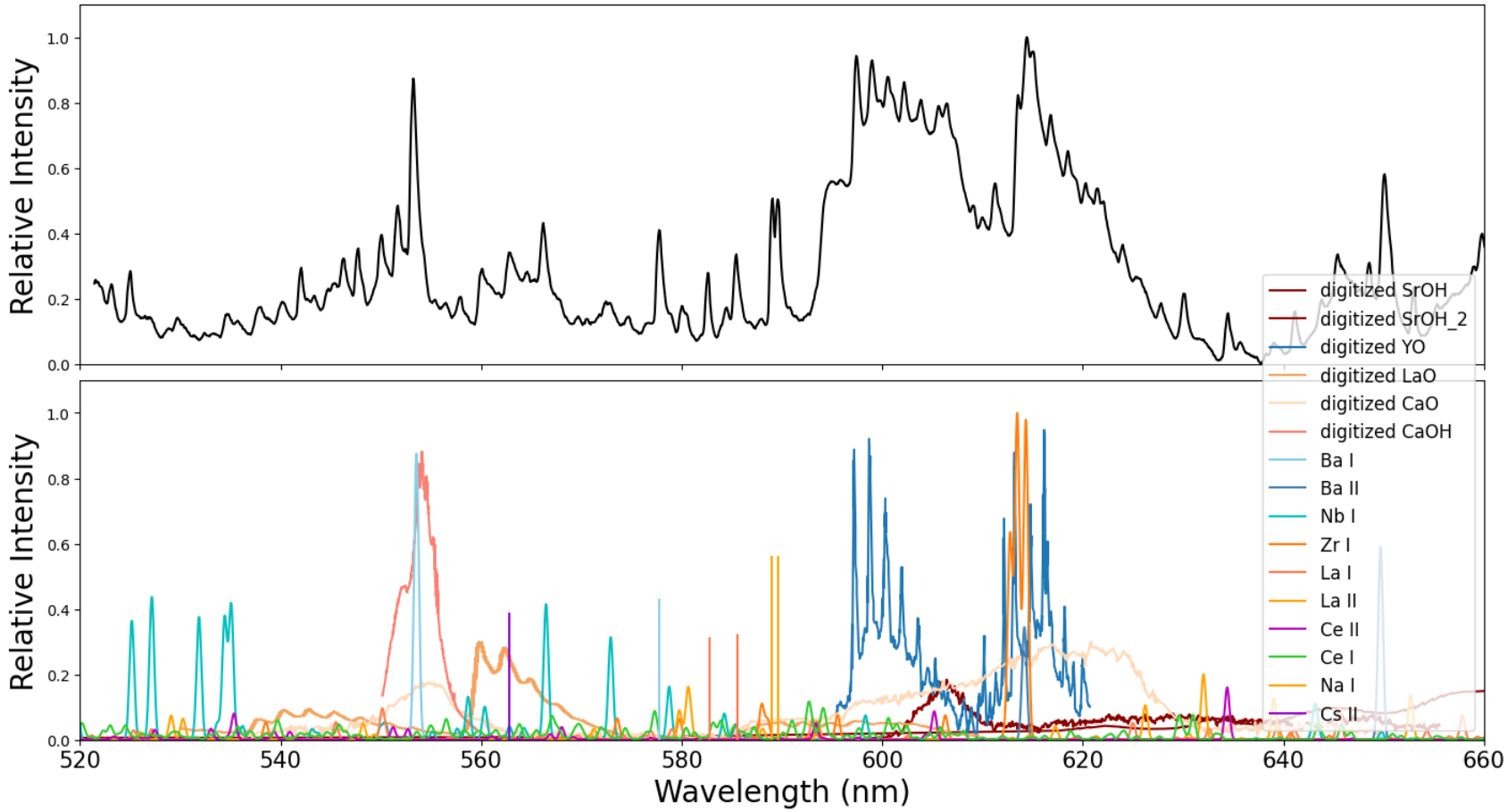

Figure 4.58: U^{235} fission product mixture spectrum in 520-660 nm range with tentative line assignments and digitized SrOH, YO, LaO, CaO, and CaOH bands [17], [18], [140]–[144].

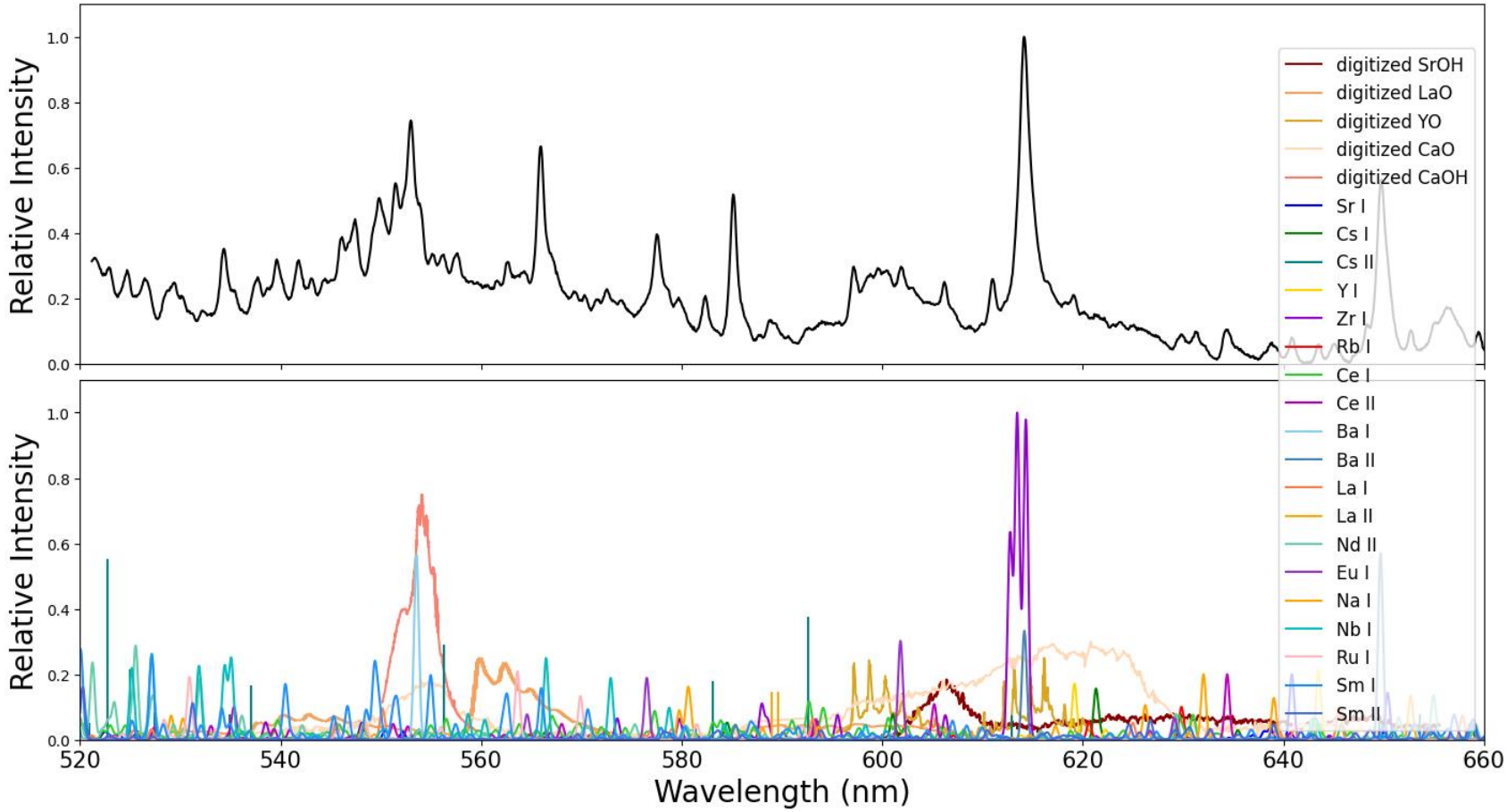

Figure 4.59: Pu^{239} fission product mixture spectrum in 520-660 nm range with tentative line assignments and digitized SrOH, YO, LaO, CaO, and CaOH bands [17], [18], [140]–[144].

These two spectra look quite different with a molecular formation centered around 610 nm dominating a portion of the U^{235} product spectrum. This signature is thought to belong to YO, a digitized spectrum of which is shown overlaid from Gaft et al. [143]. Another molecular formation appeared around 555 nm in both spectra. This is tentatively characterized as CaOH and is shown digitized from Koirtyohann and Pickett [142]. Nearby, appears to be LaO, also digitized from Gaft et al. [143].

More broadband CaO and SrOH signatures seem to appear, and have been digitized from Bezverkhnii et al., Weeks et al., and Juknelevicius and Alenfelt [140], [141], [144]. The 640-660 nm broader signature may also be attributable to SrO [142].

Aside from these molecular signatures, there are a number of atomic signatures present, ranging from impurities like Na II to what appears to be Nb I. A strong Zr I signature appears in both spectra but is somewhat obscured in the U^{235} product signatures. The Na I impurity appears more strongly, and two lines between 580 and 590 appear in U^{235} product spectrum from La I.

The third region, 650 nm to 790 nm, is less populated than this previous one, which simplified identification of the signatures present greatly. Here, the Pu^{239} product mixture appeared to have more species/transitions present (Figure 4.60, Figure 4.61).

Notably, the Y I and Eu I appear much more prominently in the Pu^{239} product mixture spectrum in this region. Both spectra feature regions from Cs I, Ba I, Rb I, potentially Sr I, and K I—all s-block elements. A feature that appears to be a weak band formation appears near 740 nm and remains unidentified. As in prior testing, the molecular Sr signature appears prominently. The strong Rb I signature could also be useful to study in future testing.

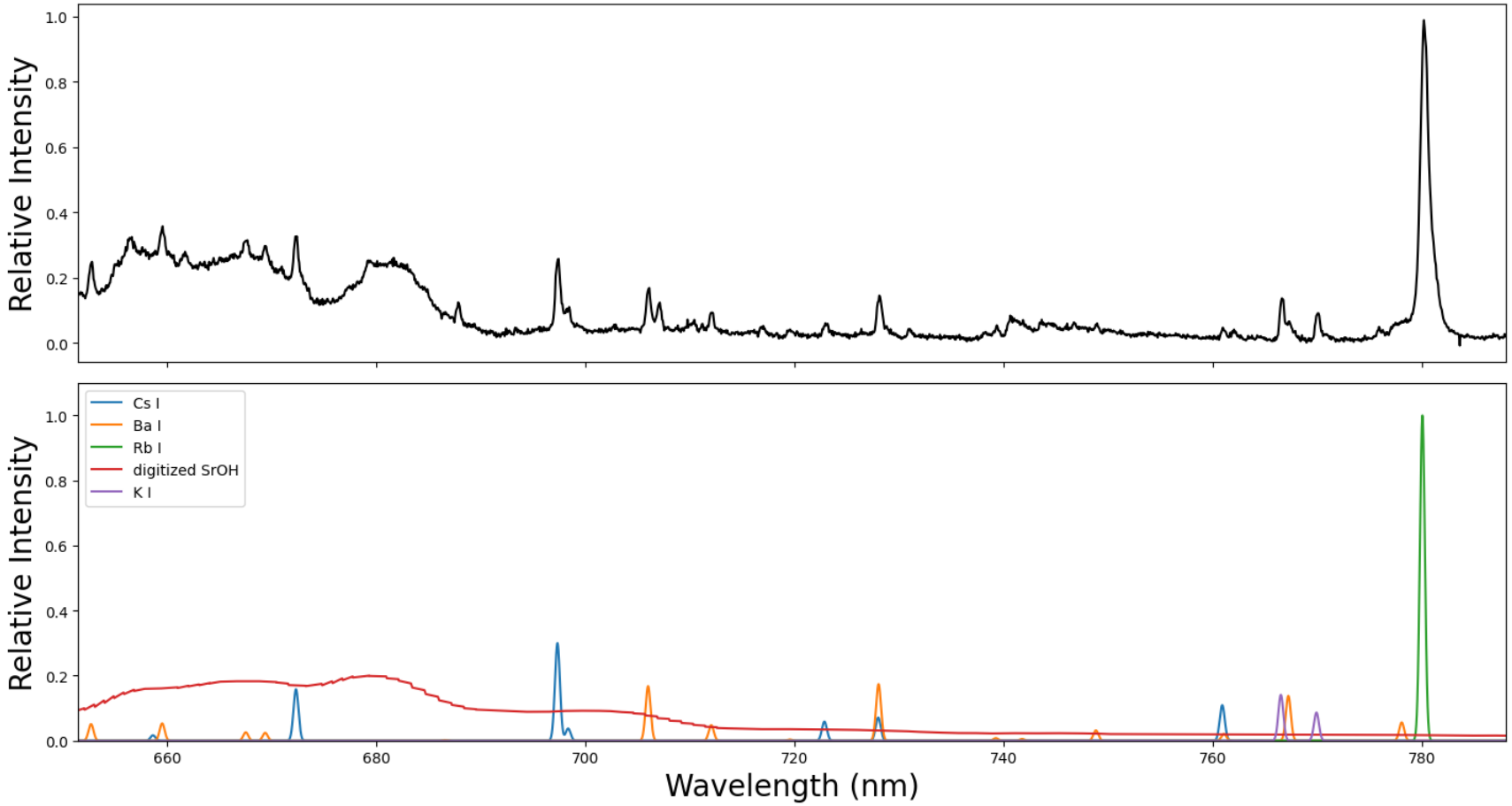

Figure 4.60: U^{235} fission product mixture spectrum in 650-790 nm range with tentative line assignments and digitized SrOH band from Juknelevicius and Alenfelt [144].

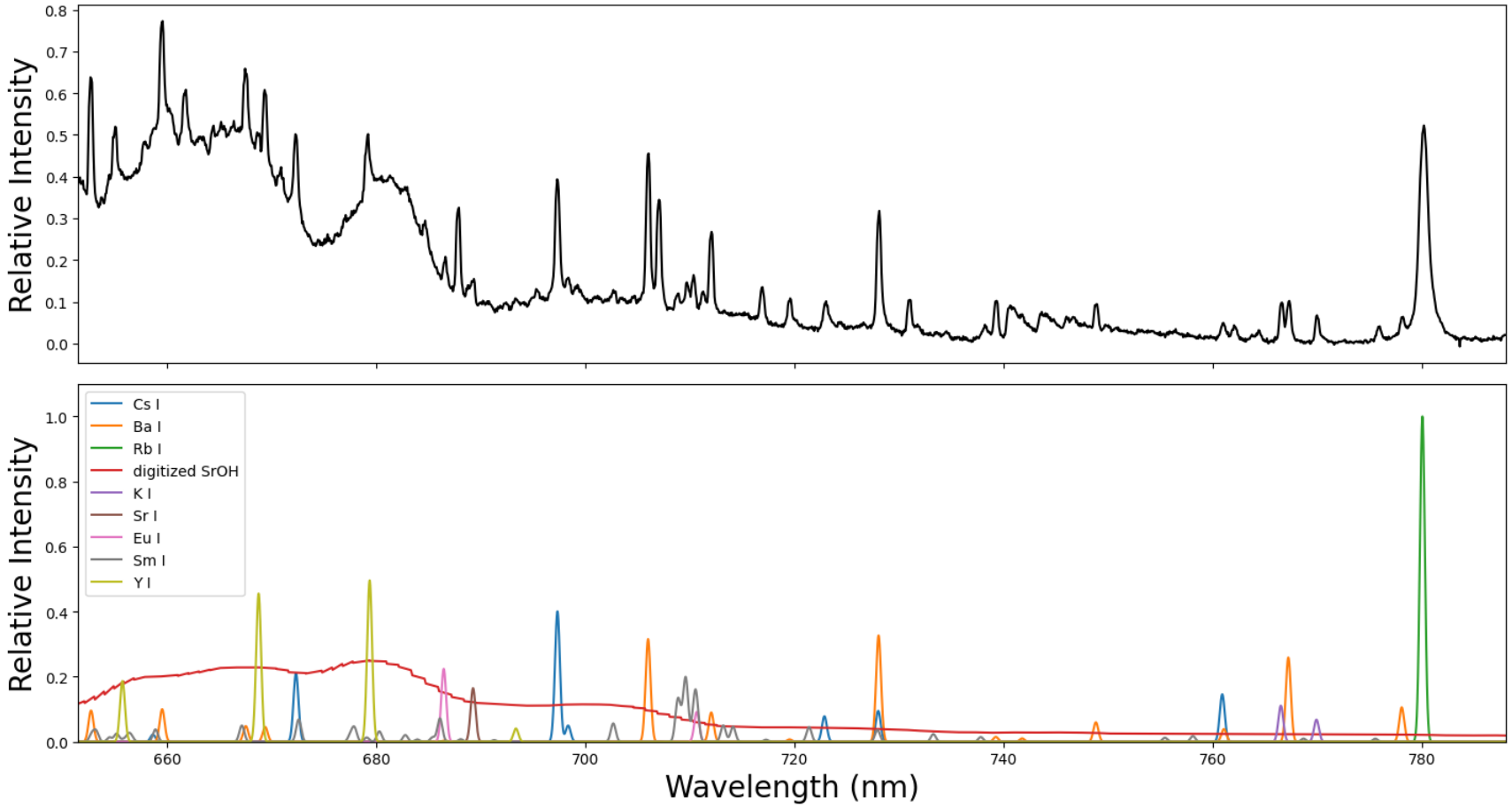

Figure 4.61: Pu^{239} fission product mixture spectrum in 650-790 nm range with tentative line assignments and digitized SrOH band from Juknelevicius and Alenfelt [144].

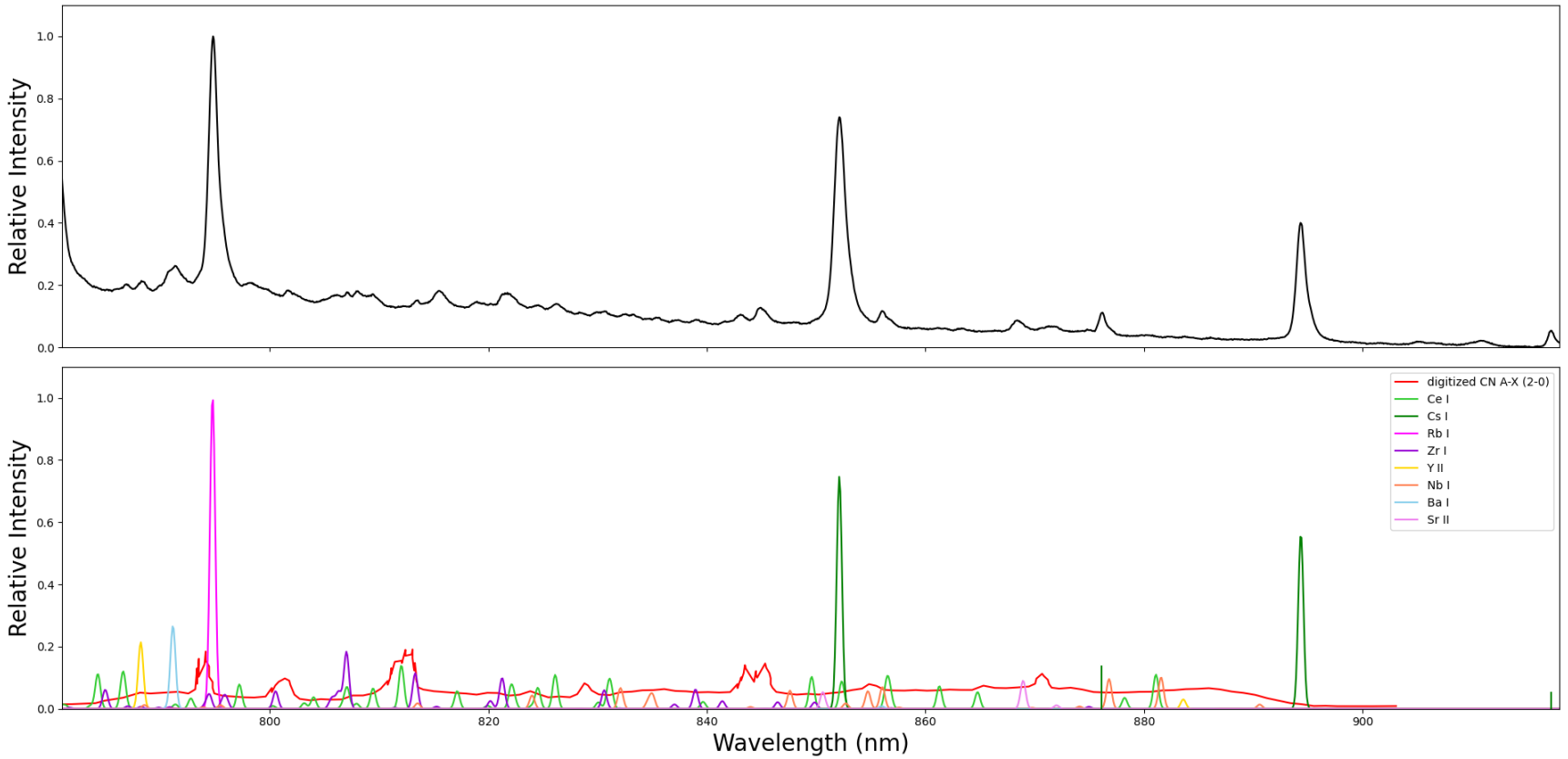

Figure 4.62: U^{235} fission product mixture spectrum in 780-920 nm range with tentative line assignments and digitized CN A-X band from Herzberg and Phillips [17], [18], [145].

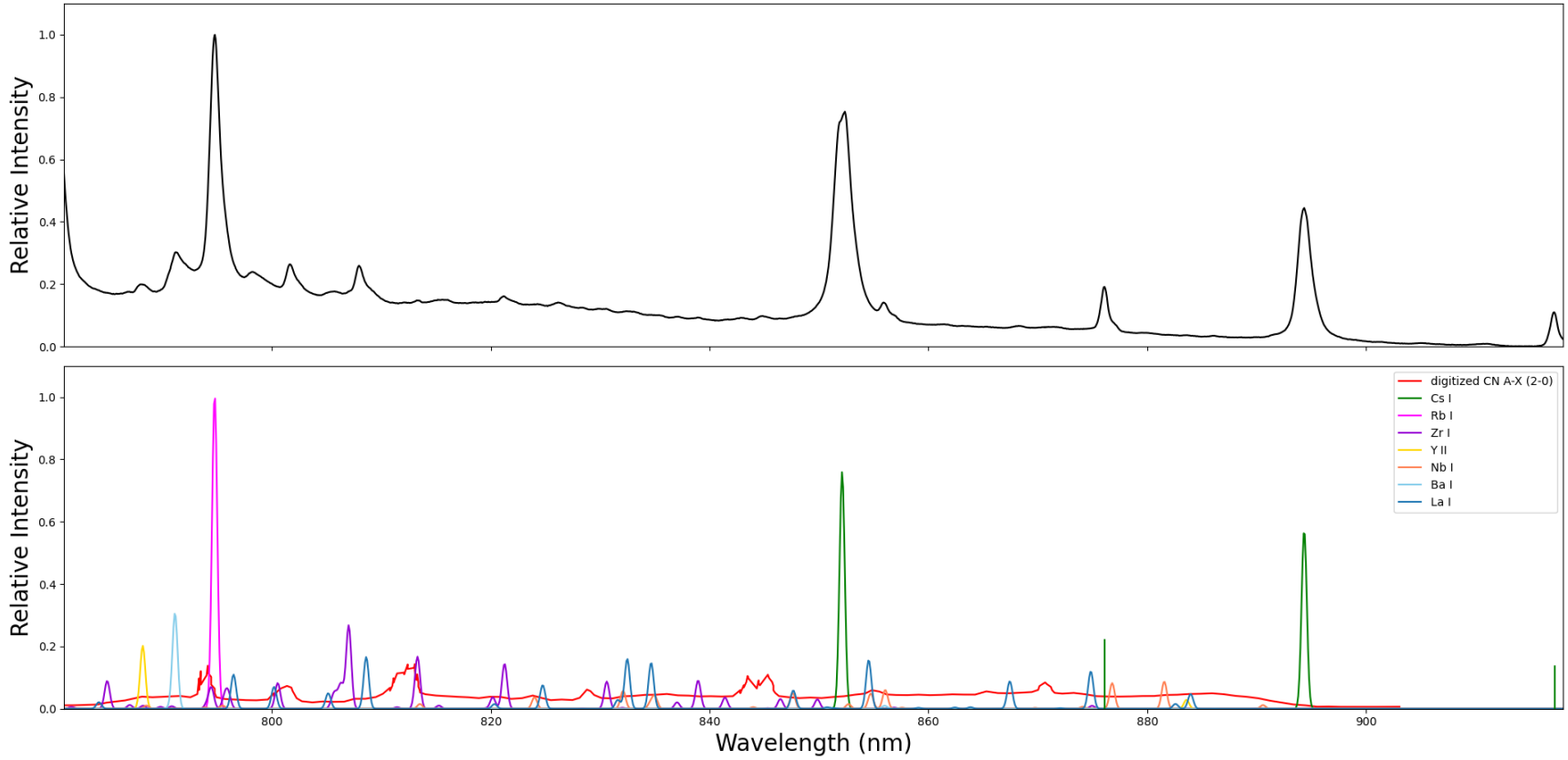

Figure 4.63: Pu^{259} fission product mixture spectrum in 780-920 nm range with tentative line assignments and digitized CN A-X band from Herzberg and Phillips [17], [18], [145].

Here, there are not nearly as many signatures present. This could be due in part to decreased quantum efficiency of the detector used to make these measurements as wavelengths increased. The strong Cs I and Rb I signatures are unobstructed in this region and would be excellent candidates for future testing in this vein.

Overall there are a number of signatures that merit further study under other conditions, particularly Cs, Rb, Ba, and Sr, perhaps in different temperature regimes if achievable. It is additionally interesting that these signatures are from the s-block of elements as opposed to the rare-earth elements that were also studied. Cs, Ba, and Rb had lower (although comparable) ionization energies than the majority of element tested.

These tests are preliminary to future testing in determining the utility of using fission product signatures in remote sensing applications. More tests should be performed in controlled conditions at different temperature regimes, to determine if these signatures are still viable in the present of explosive signatures, such as in field testing. It is additionally necessary to determine which signatures appear differently when different amounts of fission product are present. It is important to note that many of these products were initially in larger molecules (carbonates and carbonate hydrates), and that this may additionally affect their appearance. When carbonates (hygroscopic) are exposed to air during the mixture preparation, they begin to form precipitates with gaseous H_2O almost immediately. Thus, mixtures need to be prepared quickly to minimize this product formation. $Sr(NO_3)_2$, if added first, seemed to mitigate this occurrence. Measures were taken to ensure that mixture was as homogeneous as possible and repeat tests were done to determine any major variations in signatures produced.

It would also be worth comparing these signatures to the appearance of that from engineering steels subjected to high-temperature conditions. If these fission products are among the components in an alloy that may affect the appearance of a targeted signature (i.e. Molybdenum is commonly used in steel alloys). Much work has additionally been done in characterizing the signatures produced from high explosives in plasma environments that merit further consideration as signatures to avoid when selecting candidates for remote detection [146]–[149].

CHAPTER 5: CONCLUSIONS AND FUTURE WORK

5.1. Conclusions

5.1.1. Uranium monoxide estimation

Insufficient data exists in the literature for the absolute quantification of uranium monoxide in absorption measurements of the 593.55 nm band due to unknown transition strength, incomplete energy level information (propagating into incorrect partition functions), and other considerations previously outlined. With higher resolution spectral measurements, some of these unknowns can be quantified, leading to greater accuracy in estimation and eventual calculation of the amounts of UO present in absorption spectra. Largely, Einstein coefficients, transition dipole moment, or oscillator strength must be accurately quantified—with one, the others can be calculated. Tyagi et al. tentatively determined a value for the oscillator strength of UO [47], which was used to determine the Einstein absorption coefficient and evaluate data from previously acquired laser ablation absorption measurements. These findings are subject to the uncertainties in the oscillator strength and other values obtained from the literature. A tentative transition moment was also calculated from the oscillator strength using a relation from Hilborn [124]. To the author's knowledge, this is the first estimation of uranium monoxide based on an absorption measurement of the 593.55 nm band.

5.1.2. How does uranium burn?

From this research several conclusions can be drawn about the combustion of uranium powder. In the dust cloud experiments, which were < 4000 K, uranium burns heterogeneously, exhibiting an exploding particle effect similar to that seen in zirconium and titanium. Relative burn times correlate with previous work comparing the burning of particles of different species. The temperatures attained were not high enough to elicit atomic or ionic uranium spectral emissions (as indicated by the iron impurity signatures which were present), which further confirms that uranium burns heterogeneously in this temperature regime. Although these emissions did not appear, lower temperature U signatures are possible when the metal has already entered the vapor phase, such as in the laser ablation plasma. Since U readily oxidizes, there is barrier to vapor formation when a particle is heated in a dust cloud or shock conditions.

Imaging indicates that uranium powder particles are coated with an oxide layer that is 43.3 nm thick on average and has been found to behave refractorily in previous experimentation [22]. This thickness—and the oxide content of uranium particles in general—should be confirmed with other methods like X-ray diffraction. This thick oxide layer forms a protective coating that inhibits formation of U vapor, and in part explains why uranium ionic and atomic signatures do not always appear in high-temperature conditions despite its abundance in a given system. At lower temperatures, this oxide layer may even increase during the burning process. The exploding effect indicates the transient formation of $U_xO_yN_z$ species, followed by U_xO_y precipitates alongside N_2 containing voids. During this process, as the N_2 escapes and the particle continues to burn, new U is exposed and quickly re-oxidizes. This process likely does not allow for vapor phase emissions since U oxides form readily prior to the vaporization/escape of U from the particle. Only when the particle is heated to higher temperatures, does it begin to vaporize.

Controlled temperature testing of the same powder in the heterogeneous shock tube apparatus indicates that uranium emissions show up between 4400 and 4900 K calculated reflected shock temperature. When time-resolved uranium emissions are tracked over the duration of the burn event, they disappear around 4400 K as the vapor condenses. These results are expected since the oxide volatilization temperature is ~3800 K and the metal boiling temperature is 4404 K (Table 3.2).

It is important to evaluate shock tube results with the knowledge that real temperatures do not reach the ideal calculated shock conditions due to the heat sink provided by insufficiently dispersed uranium powder and other factors associated with knife blade loading of powder for shock tube testing. This discrepancy increases with desired reflected shock temperature. That having been said, uranium vapor phase signatures did appear in these high-temperature conditions and rapidly disappeared as the system cooled. Their short-lived appearance might render the use of uranium signatures challenging for remote detection. These signatures often did not persist longer than 2 ms from the reflected shock. It is additionally important to note that there are significant differences in the thermal environments of the shock/dust explosion experiments and that of laser ablation. The thermal history of uranium is relevant to its potential oxidation and entrance into the vapor phase. In shock heating or a dust explosion, uranium powder with an existing oxide layer is heated from room temperature to temperatures in the 1000s of Kelvin on a time-scale on the order

of microseconds, and the oxide presents a barrier to vapor phase uranium formation. In laser ablation, the high-energy laser pulse produces an almost instantaneous (in comparison) plasma environment. Here, uranium is initially atomized, ionized, and free from oxygen—more similar to the conditions that would be present in a nuclear fireball. Atomic and ionic uranium signatures were short-lived in the laser ablation plume, as were that of UO. However, the nuclear fireball is also significantly larger in scale, species may be more abundant, and time scales may be correspondingly longer. Any bulk uranium contained in the original charge may undergo vaporization, ionization, and later, condensation and oxidation at surfaces. Any vapor phase uranium (or uranium oxides) produced in the early time fireball may be fleeting or obscured by other emissions. It is thus desirable to seek additional, strong, persistent signatures for further study. While much study has been performed on the debris resulting from a nuclear event (after all processes have occurred), models are under development to better simulate the processes that actinide materials can undergo in such a complex environment, and the spectra that may result from these processes, and testing such as that completed here is used to inform their creation.

5.1.3. Viable signatures for remote detection

Flash powder excitation of fission product mixtures indicate that emission signatures from a multitude atomic, ionic, and molecular species appear. In particular, Cs, Sr, Ba, and Rb (s-block fission products) are excellent candidates for further study, since these produce stronger signatures which are sensitive to the amount of product present. These species were selected using a figure of merit approach that did suggest that they would appear most strongly of those considered. Other fission product signatures appeared less strongly, these included Zr, YO, and Nb among others. Signatures from impurities such as Ca, Na, and K were present as well. Signatures from Sb and Ce were either conspicuously weak or absent, when these were expected to be comparable in strength to Zr, Ru, Nd, and Eu. Signatures from species like La, Nb, and Zr were moderately strong and plentiful, but often clustered with other features that may preclude their utility. LaO and YO were prominent in the 520-660 region nm and may prove useful for future study in addition to the s-block fission products, which all had prominent signatures from 650 to 920 nm. Signatures between 560 and 790 nm showed the most variation between U^{235} and Pu^{239} fission product mixtures.

This approach proved fruitful for identifying strong emitters, but did not necessarily take all relevant factors into account. As an example, YO should have appeared similarly in intensity for both mixtures but is significantly stronger in the U^{235} product mixture. Different temperatures may favor the development of different species as shown in the figures of merit considering both flame and plasma detection limits.

Cs and Sr signatures were studied further by way of conventional explosive excitation on small and field scales. These tests reached higher temperatures and different proportions of Cs and Sr could be distinguished between. Signatures from explosives were minimal in the regions chosen for testing, a result which may prove promising in achieving the goal of remotely distinguishing nuclear and non-nuclear fireballs. In some tests, a CaOH signature appeared in the NIR region tested but did not obscure the nearby SrOH signature, which sometimes caused the fireball to appear red. Metals in the explosive field charges also affected the physical appearance of the fireball and resulting signatures to some extent. Magnesium containing shots appeared bright white and fireballs from copper containing shots appeared green tinged at later times. Emission signatures appeared more strongly in the magnesium containing shots, and different amounts of the same proportion of Cs and Sr could not be distinguished between, exhibiting similarly proportioned signatures and producing similar magnitudes of light. Thus, these signatures could potentially be used for time-resolved detection of fissionable material in a fireball at a distance, free from the interference of signatures produced by high explosive and other engineering materials, but not necessarily the amount of material present.

5.2. Future Work

There still remains much work to be done pursuant to the goals of this study:

5.2.1. Laser ablation and uranium signature elucidation

Further high-resolution laser ablation experimentation could be used to observe fine structure of uranium monoxide bands, in order to determine quantities for modeling these spectra. Experimental validation of the oscillator strength parameter determined by Tyagi et al. or determination of transition moment would be ideal for use in quantifying absolute number density from absorption measurements of this transition.

Time-resolved laser ablation techniques can be applied to study uranium containing systems such as U-Fe-O similarly to the U-Si-O study previously discussed. Higher oxide uranium signatures may also be observed to further corroborate the uranium plasma kinetic model developed by Finko et al. Perhaps some of these signatures could be leveraged to observe late-time fireball behavior. Other researchers have already begun to explore the condensation of uranium from plasma to higher oxides and their relevant properties [150], [151].

Other uranium monoxide and uranium diatomic species such as UH and UN merit further study and cataloguing, as well as any higher oxides that can be probed similarly.

5.2.2. Shock Tube Testing

Higher resolution uranium signatures can be obtained under these shock conditions free from interference of CN and Fe I signatures. At the temporal resolution from the second round of testing (360 μs), sufficient signal should be available for further characterization of these signatures and their variation with temperature as well as over the duration of the shock event. Nearby Fe I signatures can be leveraged to confirm temperatures reached via fitting modeled spectra as well as fitting blackbody curves from appropriately gated NIR spectra in the region previously studied (1000-1500 nm). It may additionally be worth observing the 593.55 nm UO transition in controlled shock conditions to confirm its appearance in the temperature range > 3000 K from previous testing as well as to observe its variation in band structure over temperature [152]. Similar study could be completed on higher uranium oxides. For these studies, rigorous quantification of temperature would be ideal, especially for higher temperature tests that deviate more from

calculated conditions. There are several ways to do this—using high-resolution, well characterized spectral transitions may be a more accurate way to achieve this validation than previously attempted techniques like multi-color pyrometry, which has its failings. Tests on particles of deliberately varied oxidation may also prove informative. Information on oxidation of uranium at these very high temperatures is sparse in currently available literature.

Absorption measurements of controlled high temperature uranium signatures may also be worthwhile. However, there is some difficulty in accurately timing a flash absorption source to occur simultaneously with the combustion event in the windowed end section of the shock tube, especially at the high speeds required to obtain the high temperatures achieved in this test series.

Blast testing in which bulk uranium is present as a case material may also prove fruitful for characterization of oxide formation and any other morphological variations that may occur when it is subjected to extreme conditions.

5.2.3. Explosive Excitation of Fission Products of Interest

In the vein of understanding the real-time fireball, it would be desirable to identify a number of potentially strong signatures in different temperature regimes from the actinide, fission products, their associated oxides, and potential compounds with the surrounding environment and track all of these spectroscopically. Efforts are ongoing to further identify and characterize these signatures.

Particular to this work, further studying the fission products of interest in different, potentially controlled temperature conditions would be worthwhile in determining which signatures can be leveraged for detection and differentiation between the fissionable materials in a nuclear fireball. Results from the flash powder survey indicate that some oxides of fission products (SrOH, YO) may also be viable signatures for detection in addition to atomic and ionic signatures from strong emitters like Ba and Rb. It may be worth probing these and other strongly emitting signatures that fission products may form with the surrounding environment of a fireball. Time-resolved spectral acquisition from flash powder and conventional explosive excitation will allow for the identification of persistent species as well as some insight into when some species develop in the fireball produced.

Extensive work has been performed in the past regarding the emission signatures of explosives and must be considered when developing diagnostics to observe these signatures. There must also

be some consideration of signatures that may result from engineering materials used in the construction of devices, as the nuclear fireball reaches incredibly high temperatures that might elicit emissions from almost any species.

Excitation of the fission product mixtures by conventional explosives may lend some insight as to how these signatures may appear in different spectral regions and if there is indeed interference from explosive and other material signatures. Laser ablation of these mixtures would provide the most analogous environment to nuclear fireball conditions and would allow for the time-resolved observation of chemical pathways and further identification of signatures of interest and persistence thereof.

REFERENCES

[1] B. C. Reed, *The History and Science of the Manhattan Project*. Berlin, Germany: Springer-Verlag Berlin Heidelberg, 2014.

[2] "Atomic Timeline," *Atomic Heritage Foundation*, 2019. .

[3] "The Manhattan Project," *Atomic Heritage Foundation*. [Online]. Available: https://www.atomicheritage.org/history/manhattan-project.

[4] "Trinity Test-1945," *Atomic Heritage Foundation*. [Online]. Available: https://www.atomicheritage.org/history/trinity-test-1945.

[5] "Nuclear Test Ban Treaty," *JFK Presdential Library and Museum*. [Online]. Available: https://www.jfklibrary.org/learn/about-jfk/jfk-in-history/nuclear-test-ban-treaty.

[6] "Treaty on the Non-Proliferation of Nuclear Weapons (NPT)," *United Nationals Office for Disarmament Affairs*. [Online]. Available: https://www.un.org/disarmament/wmd/nuclear/npt/.

[7] "Comprehensive Nuclear-Test-Ban Treaty (CTBT)," *United Nations Office for Disarmament Affairs*. [Online]. Available: https://www.un.org/disarmament/wmd/nuclear/ctbt/. [Accessed: 03-Apr-2021].

[8] L. R. Morss, N. M. Edelstein, and J. Fuger, Eds., *The Chemistry of the Actinide and Transactinide Elements*, 3rd ed. Springer, 2006.

[9] H. L. Brode, "REVIEW OF NUCLEAR WEAPONS EFFECTS," *Annu. Rev. Anal. Chem.*, vol. 18, no. March, pp. 153–202, 1968.

[10] S. Glasstone and P. J. Dolan, Eds., *The Effects of Nuclear Weapons*, 3rd ed. United States Department of Defense, United States Department of Energy, 1977.

[11] H. L. Brode, "Thermal Radiation From Nuclear Explosions." The RAND Corporation, p. 25, 1963.

[12] G. Walker, "Scientific Aspects of Nuclear Explosion Phenomena," *Trinity Atomic Website*, 2003. [Online]. Available: https://www.abomb1.org/nukeffct/enw77b3.html#foot_7.

[13] I. Ogawa, "Detection of Nuclear Warheads by Radiation: A Brief Review," Tsukuba, Ibaraki.

[14] R. LATTER, R. F. HERBST, and K. M. WATSON, "Detection of nuclear explosions.," *Annu. Rev. Nucl. Sci.*, vol. 11, no. June, pp. 371–418, 1961.

[15] E. N. Weerakkody, "Use of Absorption Laser-Induced Breakdown Spectroscopy in Characterization of Actinide Species and Oxides," Mechanical Science and Engineering, University of Illinois at Urbana-Champaign, 2018.

[16] N. M. Laurendeau, *Statistical Thermodynamics, Fundamentals and Applications*. 2005.

[17] P. L. Smith, C. Heise, J. R. Esmon, and R. L. Kurucz, "Division of Plasmaphysics - Atomic spectral line database," *Hannover University*, 2018. [Online]. Available: http://www.pmp.uni-hannover.de/cgi-bin/ssi/test/kurucz/sekur.html.

[18] A. Kramida, Y. Ralchenko, J. Reader, and N. A. Team, "NIST Atomic Spectra Database Lines Form," *National Institute of Standards and Technology*, 2018. [Online]. Available: http://physics.nist.gov/asd. [Accessed: 18-Sep-2018].

[19] B. Palmer, R. Keller, and R. Engleman, “An Atlas of Uranium Emission Intensities in A Hollow Cathode Discharge,” 1980.

[20] Redman, S.L., J. E. Lawler, G. Nave, L. W. Ramsey, and S. Mahadevan, “The Infrared Spectrum of Uranium Hollow Cathode Lamps from 850 nm to 4000 nm: Wavenumbers & Line Identifications from Fourier Transform Spectra,” 2011. [Online]. Available: https://cfn-live-content-bucket-iop-org.s3.amazonaws.com/journals/0067-0049/195/2/24/1/apjs398971t2_mrt.txt?AWSAccessKeyId=AKIAYDKQL6LTV7YY2HIK&Expires=1616599234&Signature=oWQLBsZu1WCC3lmJS%2BIddZdwcUk%3D. [Accessed: 17-Mar-2021].

[21] E. G. Rauh and R. J. Thorn, “Vapor pressure of uranium,” *J. Chem. Phys.*, pp. 1414–1420, 1954.

[22] M. Radu and H. Boiteux, *Flame Spectroscopy*. New York: John Wiley and Sons, Inc., 1965.

[23] M. S. Finko *et al.*, “A model of early formation of uranium molecular oxides in laser-ablated plasmas,” *J. Phys. D. Appl. Phys.*, vol. 50, no. 48, 2017.

[24] D. W. Hahn and N. Omenetto, “Laser-induced breakdown spectroscopy (LIBS), part II: Review of instrumental and methodological approaches to material analysis and applications to different fields,” *Appl. Spectrosc.*, vol. 66, no. 4, pp. 347–419, 2012.

[25] E. J. Judge *et al.*, “Laser-induced breakdown spectroscopy measurements of uranium and thorium powders and uranium ore,” *Spectrochim. Acta - Part B At. Spectrosc.*, 2013.

[26] R. C. Chinni, D. A. Cremers, L. J. Radziemski, M. Bostian, and C. Navarro-Northrup, “Detection of Uranium Using Laser-Induced Breakdown Spectroscopy,” *Appl. Spectrosc.*, vol. 63, no. 11, pp. 1238–1250, 2009.

[27] P. J. Skrodzki *et al.*, “Significance of ambient conditions in uranium absorption and emission features of laser ablation plasmas,” *Spectrochim. Acta - Part B At. Spectrosc.*, 2016.

[28] S. S. Harilal, P. K. Diwakar, N. L. Lahaye, and M. C. Phillips, “Spatio-temporal evolution of uranium emission in laser-produced plasmas,” *Spectrochim. Acta - Part B At. Spectrosc.*, vol. 111, pp. 1–7, 2015.

[29] M. C. Phillips, B. E. Brumfield, N. Lahaye, S. S. Harilal, K. C. Hartig, and I. Jovanovic, “Two-dimensional fluorescence spectroscopy of uranium isotopes in femtosecond laser ablation plumes,” *Sci. Rep.*, 2017.

[30] D. G. Weisz *et al.*, “Formation of ^{238}U ^{16}O and ^{238}U ^{18}O observed by time-resolved emission spectroscopy subsequent to laser ablation,” *Appl. Phys. Lett.*, vol. 111, no. 3, p. 034101, 2017.

[31] X. Mao, G. C. Y. Chan, I. Choi, V. Zorba, and R. E. Russo, “Combination of atomic lines and molecular bands for uranium optical isotopic analysis in laser induced plasma spectrometry,” *J. Radioanal. Nucl. Chem.*, vol. 312, no. 1, pp. 121–131, 2017.

[32] S. S. Harilal *et al.*, “Physical conditions for UO formation in laser-produced uranium plumes,” *Phys. Chem. Chem. Phys.*, vol. 21, no. 29, pp. 16161–16169, 2019.

[33] Zhang, D. Zhang, X. Ma, S. Wang, X. Zhu, and Zhang, “Influence of Ambient Gas on Laser-Induced Breakdown Spectroscopy of Uranium Metal,” *Plasma Sci. Technol*, vol. 17,

2015.

[34] K. C. Hartig, S. S. Harilal, M. C. Phillips, B. E. Brumfield, and I. Jovanovic, “Evolution of uranium monoxide in femtosecond laser-induced uranium plasmas,” *Opt. Express*, vol. 25, no. 10, p. 11477, 2017.

[35] E. N. Weerakkody and N. G. Glumac, “Quantitative absorption spectroscopy of laser-produced plasmas,” *J. Phys. D. Appl. Phys.*, vol. 54, pp. 1–13, 2021.

[36] E. N. Weerakkody and N. G. Glumac, “Quantitative absorption spectroscopy of laser-produced plasmas,” *J. Phys. D. Appl. Phys.*, vol. 54, no. 12, 2021.

[37] E. N. Weerakkody *et al.*, “Time-resolved formation of uranium and silicon oxides subsequent to the laser ablation of U 3 Si 2,” *Spectrochim. Acta Part B*, vol. 170, no. July, 2020.

[38] S. S. Harilal, B. E. Brumfield, N. G. Glumac, and M. C. Phillips, “Elucidating uranium monoxide spectral features from a laser-produced plasma,” *Opt. Express*, vol. 26, no. 16, pp. 54–62, 2018.

[39] L. A. Kaledin and M. C. Heaven, “Electronic Spectroscopy of UO,” *J. Mol. Spectrosc.*, vol. 1–7, no. 185, p. 22, 1997.

[40] L. A. Kaledin, J. E. McCord, and M. C. Heaven, “Laser spectroscopy of UO: Characterization and assignment of states in the 0- to 3-ev range, with a comparison to the electronic structure of ThO,” *Journal of Molecular Spectroscopy*, vol. 164, no. 1. pp. 27–65, 1994.

[41] G. R. Harrison, *Massachusetts Institute of Technology Wavelength Table, vol. 2*. Massachusetts Institute of Technology: The Technology Press, John Wiley and Sons, 1939.

[42] M. C. Heaven, J. P. Nicolai, S. J. Riley, and E. K. Parks, “Rotationally resolved electronic spectra for uranium monoxide,” *Chem. Phys. Lett.*, vol. 119, no. 2–3, pp. 229–233, 1985.

[43] G. Herzberg, *Molecular Spectra and Molecular Structure I. Diatomic Molecules*, 1st ed. New York: Prentice-Hall, Inc., 1939.

[44] M. C. Heaven, J. P. Nicolai, S. J. Riley, and E. K. Parks, “Rotationally resolved electronic spectra for uranium monoxide,” *Chem. Phys. Lett.*, vol. 119, no. 2–3, pp. 229–233, 1985.

[45] L. A. Kaledin, A. N. Kulikov, and L. V. Gurvich, “Vibrational Structure of the low-lying electronic states of the UO molecule,” *Russ. J. Phys. Chem.*, vol. 63, 1989.

[46] L. A. Kaledin, A. N. Kulikov, A. I. Kobyliansky, E. A. Shenyavskaya, and L. V. Gurvich, “The Relative Positions of the Low-Lying States of the Uranium Monoxide (UO) Molecule,” *Russ. J. Phys. Chem.*, vol. 61, no. 5, 1987.

[47] R. Tyagi, Z. Zhang, and R. M. Pitzer, “Electronic Spectrum of the UO and UO^+ Molecules,” *J. Phys. Chem. A*, vol. 118, no. 50, pp. 11758–11767, 2014.

[48] P. R. Amyotte, M. P. Clouthier, and F. I. Khan, *Dust explosions : An overview*, 1st ed., vol. 3. Elsevier Inc., 2019.

[49] R. A. Ogle, *Dust Explosion Dynamics*. Oxford, UK: Elsevier Inc., 2017.

[50] L. Türker, “Thermobaric and enhanced blast explosives (TBX and EBX),” *Def. Technol.*, vol. 12, no. 6, pp. 423–445, 2016.

[51] J. E. Geddie, “A Guide to Combustible Dusts,” Raleigh, NC, NC, 2012.

[52] C. Mitsakou, K. Eleftheriadis, C. Housiadas, and M. Lazaridis, “MODELING OF THE DISPERSION OF DEPLETED URANIUM AEROSOL,” *Health Phys.*, vol. 84, no. 4, 2003.

[53] A. V. Grosse and J. B. Conway, “Combustion of Metals in Oxygen,” *Ind. Eng. Chem.*, vol. 50, no. 4, pp. 663–672, 1958.

[54] M. Jacobson, A. R. Cooper, and J. Nagy, “Explosibility of Metal Powders,” *Bur. Mines Rep. Investig. 6516*, p. 20, 1964.

[55] M. Hertzberg, I. A. Zlochower, and K. L. Cashdollar, “Metal dust combustion: Explosion limits, pressures, and temperatures,” *Symp. Combust.*, vol. 24, no. 1, pp. 1827–1835, 1992.

[56] A. Bleise, P. R. Danesi, and W. Burkart, “Properties , use and health effects of depleted uranium (DU): a general overview,” *J. Environ. Radioact.*, vol. 64, pp. 93–112, 2003.

[57] C. Badiola and E. L. Dreizin, “Combustion of micron-sized particles of titanium and zirconium,” *Proc. Combust. Inst.*, vol. 34, no. 2, pp. 2237–2243, 2013.

[58] E. L. Dreizin, “Effect of Phase Changes on Metal-Particle Combustion Processes,” *Combust. Explos. Shock Waves*, vol. 39, no. 6, pp. 681–693, 2003.

[59] I. E. Molodetsky, E. L. Dreizin, and C. K. Law, “Evolution of particle temperature and internal composition for zirconium burning in air,” *Symp. Combust.*, vol. 26, no. 2, pp. 1919–1927, 1996.

[60] E. L. Dreizin, A. V. Suslov, and M. A. Trunov, “General Trends in Metal Particles Heterogeneous Combustion,” *Combust. Sci. Technol.*, vol. 90, no. 1–4, pp. 79–99, 1993.

[61] J. Kalman, N. G. Glumac, and H. Krier, “Experimental study of constant volume sulfur dust explosions,” *J. Combust.*, vol. 2015, 2015.

[62] R. Hrach, M. Vicher, and V. Hrachová, “Study of plasma oxidation of metals,” *Vacuum*, 1998.

[63] D. Cubicciotti, “The Reaction between Uranium and Oxygen,” vol. 345, no. 4, pp. 1947–1949, 1952.

[64] L. Baker and J. D. Bingle, “THE KINETICS OF OXIDATION OF URANIUM 300 AND 625 C,” *J. Nucl. Mater.*, vol. 20, pp. 11–21, 1966.

[65] F. Le Guyadec, X. Génin, J. P. Bayle, O. Dugne, A. Duhart-Barone, and C. Ablitzer, “Pyrophoric behaviour of uranium hydride and uranium powders,” *J. Nucl. Mater.*, vol. 396, no. 2–3, pp. 294–302, 2010.

[66] C. Ablitzer, F. Le Guyadec, J. Raynal, X. Génin, and A. Duhart-Barone, “Influence of superficial oxidation on the pyrophoric behaviour of uranium hydride and uranium powders in air,” *J. Nucl. Mater.*, vol. 432, no. 1–3, pp. 135–145, 2013.

[67] C. Snyder, “CEARUN,” *NASA Glenn Research Center*, 2019. [Online]. Available: https://cearun.grc.nasa.gov.

[68] E. M. Mouradian and L. Baker Jr., “Burning Temperatures of Uranium and Zirconium in Air,” *Nucl. Sci. Eng.*, vol. 15, no. September, 1963.

[69] M. Bober and J. Singer, “Vapor Pressure Determination of Liquid UO 2 Using a Boiling

Point Technique," vol. 5639, no. May, 2017.

[70] C. Gueneau, M. Baichi, D. Labroche, C. Chatillon, and B. Sundman, "Thermodynamic assessment of the uranium – oxygen system," *J. Nucl. Mater.*, vol. 304, pp. 161–175, 2002.

[71] G. H. Markstein, "Heterogenous Reaction Processes in Metal Combustion," *Symp. Combust.*, vol. 11, no. 1, 1967.

[72] K. C. Hartig, I. Ghebregziabher, and I. Jovanovic, "Standoff Detection of Uranium and its Isotopes by Femtosecond Filament Laser Ablation Molecular Isotopic Spectrometry," *Sci. Rep.*, vol. 7, no. March, pp. 1–9, 2017.

[73] M. Miyabe *et al.*, "Absorption spectroscopy of uranium plasma for remote isotope analysis of next-generation nuclear fuel," *Appl. Phys. A Mater. Sci. Process.*, vol. 112, no. 1, pp. 87–92, 2013.

[74] X. K. Shen and Y. F. Lu, "Detection of uranium in solids by using laser-induced breakdown spectroscopy combined with laser-induced fluorescence," *Appl. Opt.*, vol. 47, no. 11, p. 1810, 2008.

[75] B. Koroglu *et al.*, "Gas phase chemical evolution of uranium, aluminum, and iron oxides," *Sci. Rep.*, vol. 8, no. 1, pp. 1–15, 2018.

[76] K. Hauffe, *Oxidation of Metals*. New York: Plenum Press, 1965.

[77] P. J. Hayward, D. G. Evans, P. Taylor, I. M. George, and A. M. Duclos, "Oxidation of uranium in argon-25% oxygen at 190-610°C," *J. Nucl. Mater.*, 1992.

[78] L.G. Stonhill, "The determination of atomic ratios in the uranium-oxygen system by a thermogravimetric method'," *Can. J. Chem.*, vol. 37, 1959.

[79] R. K. Hanson, R. M. Spearrin, and C. S. Goldenstein, *Spectroscopy and optical diagnostics for gases*. 2016.

[80] I. Glassman, R. A. Yetter, and N. G. Glumac, *Combustion*, 5th ed. Elsevier, 2015.

[81] I. Glassman, "Metal Combustion Processes," Princeton, New Jersey, 1959.

[82] D. Chitty, "A note on shock tubes," *Ecology*, vol. 40, no. (4), pp. 727–730, 1959.

[83] R. D. Zucker and O. Biblarz, *Fundamentals of Gas Dynamics*, 2nd ed. Hoboken, New Jersey: John Wiley and Sons, Inc., 2002.

[84] R. K. Hanson, "Shock Tube Techniques," *Combustion Summer School, Princeton University*, 2013. [Online]. Available: https://cefrc.princeton.edu/combustion-summer-school/archived-programs/2013-session/lecture-notes.

[85] S. Guo, "Turbulent Interactions with Normal Shocks and Their Effects on Aluminum Particle Burn Time," Mechanical Science and Engineering, University of Illinois at Urbana-Champaign, 2014.

[86] T. A. Roberts, R. L. Burton, and H. Krier, "Ignition and combustion of aluminum magnesium alloy particles in O2 at high pressures," *Combust. Flame*, vol. 92, no. 1–2, pp. 125–143, 1993.

[87] H. Krier, R. L. Burton, M. J. Spalding, and T. J. Rood, "Ignition dynamics of boron particles in a shock tube," *J. Propuls. Power*, vol. 14, no. 2, pp. 166–172, 1998.

[88] T. A. Bazyn, "Spectroscopic Measurements of the Combustion of Aluminum and

Aluminum-based Energetic Material Particles using a Heterogeneous Shock Tube," Mechanical Science and Engineering, University of Illinois at Urbana-Champaign, 2005.

[89] P. Lynch, H. Krier, and N. Glumac, "Emissivity of Aluminum-Oxide Particle Clouds: Application to Pyrometry of Explosive Fireballs," *J. Thermophys. Heat Transf.*, vol. 24, no. 2, pp. 301–308, 2010.

[90] P. Lynch, H. Krier, and N. Glumac, "Micro-alumina particle volatilization temperature measurements in a heterogeneous shock tube," *Combust. Flame*, vol. 159, no. 2, pp. 793–801, 2012.

[91] D. J. Allen, "Optical Combustion Measurements of Novel Energetic Materials in a Heterogeneous Shocktube," Mechanical Science and Engineering, University of Illinois at Urbana-Champaign, 2012.

[92] D. J. Allen, "Dynamics of Nanoparticle Combustion," Mechanical Science and Engineering, University of Illinois at Urbana-Champaign, 2015.

[93] W. Bleam, *Soil and Environmental Chemistry*. Elsevier Inc., 2017.

[94] IAEA, "Chain Fission Yields," *IAEA Handbook of Nuclear Data for Safeguards*. .

[95] P. Fireworks, "Chemistry of Fireworks," 2021. [Online]. Available: https://fireworks.com/education-and-safety/chemistry-compounds.

[96] J. A. Conkling, *Chemistry of Pyrotechnics*. New York, NY: Marcel Denker Inc., 1985.

[97] IAEA, "Compilation and evaluation of fission yield nuclear data," *Sci. Total Environ.*, no. December, 2000.

[98] V. A. Fassel and D. W. Golightly, "Detection Limits of Elements in the Spectra of Premixed, Oxy-Acetylene Flames," *Anal. Chem.*, vol. 39, no. 4, pp. 466–476, 1967.

[99] "Sensitivity vs Detection Limit," in *Atomic Spectroscopy: A Guide to Selecting the Appropriate Technique and System*, Perkin Elmer, 2011, p. 16.

[100] V. A. Fassel and R. N. Knfseley, "Inductively Coupled Plasma: Optical Emission Spectroscopy," *Anal. Chem.*, vol. 46, no. 13, pp. 1110A-1120a, 1974.

[101] J. Gambogi, "Rare Earths Statistics and Information," *National Minerals Information Center*. [Online]. Available: https://www.usgs.gov/centers/nmic/rare-earths-statistics-and-information.

[102] H. M. King, "Rare Earth Elements and their Uses," *Geology.com*, 2021. [Online]. Available: https://geology.com/articles/rare-earth-elements/.

[103] N. C. for B. Information, "PubChem Periodic Table of the Elements," *Pubchem*. [Online]. Available: https://pubchem.ncbi.nlm.nih.gov/periodic-table/.

[104] F. Le Guyadec, X. Génin, J. P. Bayle, O. Dugne, A. Duhart-Barone, and C. Ablitzer, "Pyrophoric behaviour of uranium hydride and uranium powders," *J. Nucl. Mater.*, vol. 396, no. 2–3, pp. 294–302, 2010.

[105] B. A. Read, "A Review of Optical Diagnostic Techniques Used to Identify Uranium Spectral Signatures," Aerospace Engineering Department, University of Illinois at Urbana-Champaign, 2018.

[106] M. J. Spalding, "Boron Particle Ignition and Combustion in a Shock Tube Using Time-

Resolved Spectroscopy," Mechanical Engineering Department, University of Illinois at Urbana-Champaign, 2000.

[107] J. Guadarrama, "Burn Time Measurements of Micron Sized Al-Mg Alloys and Mg in a Heterogeneous Shock Tube in Different Oxidizing Environments By," Mechanical Science and Engineering, University of Illinois at Urbana-Champaign, 2016.

[108] Y. Zhang, J. R. G. Evans, and S. Yang, "Corrected values for boiling points and enthalpies of vaporization of elements in handbooks," *J. Chem. Eng. Data*, vol. 56, no. 2, pp. 328–337, 2011.

[109] R. W. Ohse, "High-temperature vapor-pressure studies of UO2 by the effusion method and its thermodynamic interpretation," *J. Chem. Phys.*, vol. 44, no. 4, pp. 1375–1378, 1966.

[110] J. W. McMurray, "Characterization of urania vaporization with transpiration coupled thermogravimetry," *J. Chem. Thermodyn.*, vol. 95, 2015.

[111] M. B. Panish and L. Reif, "Thermodynamics of the vaporization of Hf and HfO2: Dissociation energy of HfO," *J. Chem. Phys.*, vol. 38, no. 1, pp. 253–256, 1963.

[112] H. Okamoto, "Hf-O (Hafnium-Oxygen)," *J. Phase Equilibria Diffus.*, vol. 29, no. 1, pp. 124–124, 2008.

[113] H. Okamoto, "O-U (Oxygen-Uranium)," *J. Phase Equilibria Diffus.*, vol. 28, no. 5, p. 497, 2007.

[114] S. J. Schneider, "Compilation of the Melting Points of the Metal Oxides," *United States Dep. Commer.*, 1963.

[115] G. L. Humphrey, "Heats of Formation of Tantalum, Niobium and Zirconium Oxides, and Tantalum Carbide," *J. Am. Chem. Soc.*, vol. 76, no. 4, pp. 978–980, 1954.

[116] L. Brewer, "The Thermodynamic Properties of the Oxides and Their Vaporization Processes," *Chem. Rev.*, vol. 52, no. 1, pp. 1–75, 1953.

[117] Q. N. Nguyen, "High Temperature Volatility and Oxidation Measurements of Titanium and Silicon Containing Ceramic Materials," Clinical/Bioanalytical Chemistry, Cleveland State University, 2008.

[118] B. P. E. Blackburn, M. Hoch, and H. L. Johnston, "The Vaporization of Molybdenum and Tungsten Oxides," *J. Phys. Chem.*, vol. 62, no. 7, pp. 769–773, 1958.

[119] C. Murzyn, "Diode laser gas sensing for high-speed temperature and speciation measurements inside explosive fireballs," Mechanical Science and Engineering, University of Illinois at Urbana-Champaign, 2018.

[120] I. Bonefačić and P. Blecich, "Two-color temperature measurement method using BPW34 PIN photodiodes," *Eng. Rev.*, vol. 35, no. 3, pp. 259–266, 2015.

[121] M. C. Heaven, V. Goncharov, T. C. Steimle, T. Ma, and C. Linton, "The permanent electric dipole moments and magnetic g factors of uranium monoxide," *J. Chem. Phys.*, vol. 125, no. 20, 2006.

[122] R. S. Mulliken, "Intensities of Electronic Transitions in Molecular Spectra I. Introduction," *J. Chem. Phys.*, vol. 7, no. 1, pp. 14–20, 1936.

[123] R. Ladenburg and C. C. Van Voorhis, "The Continuous Absorption of Oxygen Between

1750 and 1300A and its Bearing Upon the Dispersion," *Phys. Rev.*, vol. 43, no. 1933, pp. 315–321, 1933.

[124] R. C. Hilborn, "Einstein coefficients, cross sections,f values, dipole moments, and all that (revised)," *Am. J. Phys.*, vol. 50, pp. 982–986, 2002.

[125] R. J. Gill, S. Mohan, and E. L. Dreizin, "Sizing and burn time measurements of micron-sized metal powders," *Rev. Sci. Instrum.*, vol. 80, no. 6, 2009.

[126] K. A. Chintersingh, "Improving boron for combustion applications," Otto H. York Department of Chemical and Materials Engineering, New Jersey Institute of Technology, 2019.

[127] J. H. Sun, R. Dobashi, and T. Hirano, "Combustion Behavior of Iron Particles Suspended in Air," *Combust. Sci. Technol.*, vol. 150, no. 1–6, pp. 99–114, 1990.

[128] S. Wang, S. Mohan, and E. L. Dreizin, "Effect of flow conditions on burn rates of metal particles," *Combust. Flame*, vol. 168, pp. 10–19, 2016.

[129] A. Korotkikh, I. Sorokin, and E. Selikhova, "Ignition and combustion of high-energy materials containing aluminum, boron and aluminum diboride," *MATEC Web Conf.*, vol. 194, pp. 0–5, 2018.

[130] E. T. Zepper, M. L. Pantoya, S. Bhattacharya, J. O. Marston, A. A. Neuber, and R. J. Heaps, "Peering through the flames : imaging techniques for reacting aluminum powders," vol. 56, no. 9, 2017.

[131] P. Lipetzky, "Refractory metals: A primer," *Jom*, vol. 54, no. 3, pp. 47–49, 2002.

[132] E. C. Freiling, "Radionuclide Fractionation in Bomb Debris," *Science (80-.).*, vol. 133, no. 3469, pp. 1991–1998, 1961.

[133] I. E. Molodetsky, E. P. Vicenzi, E. L. Dreizin, and L. C K, "Phases of titanium combustion in air," *Combust. Flame*, vol. 112, no. 4, pp. 522–532, 1998.

[134] S. I. Futko, I. A. Koznacheev, O. S. Rabinovich, O. G. Penyazkov, and P. N. Krivosheyev, "On the Mechanism of Combustion of Thin Nanostructurized Silicon Plates in Oxygen at an Elevated Pressure," *J. Eng. Phys. Thermophys.*, vol. 92, no. 1, pp. 3–13, 2019.

[135] L. Baker, J. G. Schnizlein, and J. D. Bingle, "THE IGNITION OF URANIUM," *J. Nucl. Mater.*, vol. 20, pp. 22–38, 1966.

[136] V. G. Ioffe, "Inflammability of Zirconium Powders and its Alloys in the Suspended State," *Poroshkovaya Metall.*, vol. 3, pp. 100–104, 1968.

[137] C. W. Solbrig, "Heat release rate from the combustion of uranium," Idaho Falls, Idaho, 1995.

[138] R. Miotk, B. Hrycak, M. Jasiński, and J. Mizeraczyk, "Characterization of an atmospheric-pressure argon plasma generated by 915MHz microwaves using optical emission spectroscopy," *J. Spectrosc.*, vol. 2017, pp. 1–7, 2017.

[139] P. T. Lynch, "High Temperature Spectroscopic Measurements of Aluminum Combustion in a Heterogeneous Shock Tube," Mechanical Science and Engineering, University of Illinois at Urbana-Champaign, 2010.

[140] N. O. Bezverkhnii, T. A. Lapushkina, N. A. Monakhov, M. V. Petrenko, and S. A. Ponyaev,

"A Study of the Emission Spectra of CaO Molecule in the Wavelength Range of 540–650 nm in Shock Tube Experiments," *Tech. Phys. Lett.*, vol. 47, no. 1, pp. 68–70, 2021.

[141] S. J. Weeks, H. Haraguchi, and J. D. Winefordner, "Laser-excited molecular fluorescence of CaOH in an air-acetylene flame," *J. Quant. Spectrosc. Radiat. Transf.*, vol. 19, no. 6, pp. 633–640, 1978.

[142] S. R. Koirtyohann and E. E. Pickett, "Spectral Interferences in Atomic Absorption Spectrometry," *Anal. Chem.*, vol. 38, no. 4, pp. 585–587, 1966.

[143] M. Gaft, Y. Raichlin, F. Pelascini, G. Panzer, and V. Motto Ros, "Imaging rare-earth elements in minerals by laser-induced plasma spectroscopy: Molecular emission and plasma-induced luminescence," *Spectrochim. Acta - Part B At. Spectrosc.*, vol. 151, no. September 2018, pp. 12–19, 2019.

[144] D. Juknelevicius, P. Alenfelt, and A. Ramanavicius, "The Performance of Red Flare Pyrotechnic Compositions Modified with Gas Generating Additives," *Propellants, Explos. Pyrotech.*, vol. 45, no. 4, pp. 671–679, 2020.

[145] G. Herzberg and J. G. Phillips, "Infrared CN Bands," *Astrophys. J.*, vol. 108, no. 49, pp. 163–166, 1948.

[146] J. L. Gottfried, "Laser-induced plasma chemistry of the explosive RDX with various metallic nanoparticles," *Appl. Opt.*, vol. 51, no. 7, pp. 13–21, 2012.

[147] J. L. Gottfried, F. C. De Lucia, C. A. Munson, and A. W. Miziolek, "Strategies for residue explosives detection using laser-induced breakdown spectroscopy," *J. Anal. At. Spectrom.*, vol. 23, no. 2, pp. 205–216, 2008.

[148] J. L. Gottfried, F. C. De Lucia, C. A. Munson, and A. W. Miziolek, "Laser-induced breakdown spectroscopy for detection of explosives residues: A review of recent advances, challenges, and future prospects," *Anal. Bioanal. Chem.*, vol. 395, no. 2, pp. 283–300, 2009.

[149] F. C. De Lucia, J. L. Gottfried, C. A. Munson, and A. W. Miziolek, "Double pulse laser-induced breakdown spectroscopy of explosives: Initial study towards improved discrimination," *Spectrochim. Acta - Part B At. Spectrosc.*, vol. 62, no. 12, pp. 1399–1404, 2007.

[150] B. Koroglu *et al.*, "Experimental Investigation of Uranium Volatility during Vapor Condensation," *Anal. Chem.*, vol. 92, no. 9, pp. 6437–6445, 2020.

[151] B. Koroglu *et al.*, "Gas Phase Chemical Evolution of Uranium , Aluminum, and Iron Oxides," *Sci. Rep.*, no. January, pp. 1–15, 2018.

[152] E. N. Weerakkody *et al.*, "Time-resolved formation of uranium and silicon oxides subsequent to the laser ablation of U3Si2," *Spectrochim. Acta - Part B At. Spectrosc.*, vol. 170, 2020.

[153] B. J. McBride and S. Gordon, *Computer Program for Calculation Complex Chemical Equilibrium Compositions and Applications II. Users Manual and Program Description*. NASA, 1996.

[154] S. Gordon and B. J. McBride, *Computer Program for Calculation Complex Chemical Equilibrium Compositions and Applications I. Analysis*. NASA, 1994.

APPENDIX A: ADDITIONAL FIGURES AND CALCULATIONS

A.1. Shock tube series 2 Test Matrix

The test parameters for the second shock tube test series follow.

Date	Shot #	Driver Gas	Powder	Driver Pressure (psi)	Diaphragms (thickness & number) High pressure side	thickness H	M	L	(in)
1/21/2021	1	He	U	80	1 Heavy, 4 Lights	1	4	0	0.017
1/21/2021	2	He	U	180	1 Heavy, 1 Medium	1	1	0	0.008
1/22/2021	3	He	U	180	1 Heavy, 1 Medium, 1 Light	1	1	1	0.009
1/22/2021	4	He	U	190	1 Heavy, 1 Medium, 1 Light	1	1	1	0.009
1/22/2021	5	He	U	180	1 Heavy, 1 Medium, 2 Light	1	1	2	0.01
1/22/2021	6	He	U	200	1 Heavy, 1 Medium, 3 Light	1	1	3	0.011
1/22/2021	7	He	U	260	3 Heavies, 2 Lights	3	0	2	0.017
1/24/2021	8	He	U	200	1 Heavy, 1 Medium, 3 Light	1	1	3	0.011
1/24/2021	9	He	U	200	1 Heavy, 1 Medium, 3 Light	1	1	3	0.011
1/24/2021	10	He	U	190	1 Heavy, 1 Medium, 1 Light	1	1	1	0.009
1/24/2021	11	He	U	200	2 Mediums	0	2	0	0.006
1/24/2021	12	He	U	120	1 Heavy, 2 Lights	1	0	2	0.007
1/24/2021	13	He	U	100	1 Heavy, 1 Lights	1	0	1	0.006
1/24/2021	14	He	U	100	1 Heavy, 1 Lights	1	0	1	0.006
1/24/2021	15	He	U	90	1 Heavy	1	0	0	0.005
1/27/2021	16	He	newU	190	1 Heavy, 1 Medium, 2 Light	1	1	2	0.01
1/27/2021	17	He	newU	110	1 Heavy, 2 Lights	1	0	2	0.007
1/27/2021	18	He	newU	120	1 Heavy, 2 Lights	1	0	2	0.007
1/27/2021	19	He	newU	120	1 Heavy, 2 Lights	1	0	2	0.007
1/27/2021	20	He	newU	100	1 Heavy, 1 Lights	1	0	1	0.006
1/27/2021	21	He	newU	110	1 Heavy, 1 Lights	1	0	1	0.006
1/27/2021	22	He	newU	210	2 Heavies, 1 Medium, 1 Light	2	1	1	0.014
1/27/2021	23	He	newU	210	2 Heavies, 1 Medium	2	1	0	0.013
1/28/2021	24	He	none	100	1 Heavy, 1 Lights	1	0	1	0.006
1/28/2021	25	He	newU	300	3 Heavies, 1 Medium, 1 Light	3	1	1	0.019
1/28/2021	26	He	newU	310	3 Heavies, 1 Medium	3	1	0	0.018
1/28/2021	27	He	newU	220	2 Heavies, 1 Medium, 2 Light	2	1	2	0.015
1/28/2021	28	He	newU	230	2 Heavies, 1 Medium, 3 Light	2	1	3	0.016

Shot #	Diaphragms (thickness & number) low pressure side	H	M	L	thickness (in)	Vacuum Time (sec)	a-Value	b-Value	Ar Conc.	N2 Conc.	O2 Conc.
1	1 Medium	0	1	0	0.003	171.21	100.000694	0.026550	0.971482	0.022815	0.005704
2	1 Medium	0	1	0	0.003	162.47	100.000563	0.024500	0.984351	0.012519	0.003130
3	1 Medium	0	1	0	0.003	164.55	100.000417	0.024250	0.974177	0.020659	0.005165
4	1 Medium	0	1	0	0.003	167.11	100.000322	0.023800	0.969399	0.024481	0.006120
5	1 Medium	0	1	0	0.003	165.31	100.000368	0.024100	0.974274	0.020581	0.005145
6	1 Medium, 1 Light	0	1	1	0.004	169.1	100.000278	0.023500	0.994486	0.004411	0.001103
7	1 Heavy, 1 Medium, 3 Lights	1	1	3	0.011	161.57	100.000269	0.024580	0.994613	0.004310	0.001077
8	1 Medium, 2 Light	0	1	2	0.005	164.41	100.000246	0.024100	0.994613	0.004310	0.001077
9	1 Medium, 2 Light	0	1	2	0.005	163.98	100.000249	0.024250	0.994582	0.004334	0.001084
10	1 Medium	0	1	0	0.003	165.31	100.000233	0.024100	0.994554	0.004357	0.001089
11	1 Medium	0	1	0	0.003	162.57	100.000526	0.024500	0.994584	0.004333	0.001083
12	1 Medium	0	1	0	0.003	160.16	100.000210	0.024800	0.994613	0.004310	0.001077
13	1 Medium	0	1	0	0.003	162.32	100.000233	0.024500	0.994609	0.004313	0.001078
14	1 Medium	0	1	0	0.003	158.07	100.000178	0.025200	0.994683	0.004254	0.001063
15	1 Medium	0	1	0	0.003	159	100.000219	0.025000	0.994656	0.004275	0.001069
16	1 Medium	0	1	0	0.003	158.55	100.000344	0.025100	0.994669	0.004265	0.001066
17	1 Medium	0	1	0	0.003	162.04	100.000185	0.024530	0.994596	0.004324	0.001081
18	1 Medium	0	1	0	0.003	157.69	100.000222	0.025200	0.994695	0.004244	0.001061
19	1 Medium	0	1	0	0.003	160.31	100.000338	0.024720	0.994631	0.004296	0.001074
20	1 Medium	0	1	0	0.003	162.87	100.000193	0.024370	0.994591	0.004327	0.001082
21	1 Medium	0	1	0	0.003	161.05	100.000207	0.024580	0.994605	0.004316	0.001079
22	1 Heavy, 2 Lights	1	0	2	0.007	161.26	100.000222	0.024620	0.994618	0.004305	0.001076
23	1 Heavy, 2 Lights	1	0	2	0.007	158.27	100.000251	0.025110	0.994673	0.004261	0.001065
24	1 Medium	0	1	0	0.003	161.44	100.000172	0.024600	0.994623	0.004301	0.001075
25	1 Heavy, 1 Medium, 3 Lights	1	1	3	0.011	169.16	100.000183	0.023420	0.994476	0.004419	0.001105
26	1 Heavy, 1 Medium, 3 Lights	1	1	3	0.011	165.73	100.000153	0.024000	0.994544	0.004365	0.001091
27	1 Heavy, 2 Lights	1	0	2	0.007	165.93	100.000190	0.024000	0.994539	0.004369	0.001092
28	1 Heavy, 2 Lights	1	0	2	0.007	166.16	100.000268	0.023900	0.994546	0.004363	0.001091

Shot #	Driven Section Pressure (Torr)	Shock Velocity (m/s)	Reflected Temperature (K)	Data obtained			
				NIR	VIS	Pyrometer	All
1	2.053234971	1467.52285	4439.94	x		x	
2	2.025277876	1989.289252	7693.98	x		x	
3	2.035069793	1936.53568	6723.49		x	x	
4	2.070846232	2011.204306	7013.5		x		
5	2.044448723	1898.995272	6497.68		x		
6	2.018828403	1887.394267	7505.92	x	x	x	x
7	2.026317147	1966.882958	8172.84	x	x	x	x
8	2.026317147	1847.458602	7194.57			x	
9	2.015890248	1986.337784	8336.54				
10	2.011735404	1845.76057	7177.39	x	x	x	x
11	2.013532768	1867.212924	7349.79	x	x	x	x
12	2.011746108	1737.938122	6363.47	x	x	x	x
13	2.018096534	1613.002008	5535.81	x	x	x	x
14	2.011122043	1544.165706	5139.06	x	x	x	x
15	2.017950131	1517.904384	4990.51	x	x	x	x
16	2.01209774	1880.325375	7460.64		x		
17	2.018284159	1502.010097	4900.02		x	x	
18	2.020509539	1677.683793	5948.24		x		
19	2.016927137	1679.788791	5959.15		x	x	
20	2.016021911	1626.721345	5618.19	x	x	x	x
21	2.012537924	1596.333466	5436.75	x	x	x	x
22	2.014392586	2019.293615	8623.78	x			
23	2.013856595	2000.186753	8461.7	x		x	
24	2.020343596	1715.666382	6205.29	x	x	x	
25	2.013157229	2126.191106	9576.19	x			
26	2.015273285	2169.840627	9992.1	x	x	x	x
27	2.015274032	2019.293615	8618.42	x	x	x	x
28	2.019048607	2071.364105	9079.85	x	x		

A.2. Additional Figures

A.2.1. Pyrometer Traces

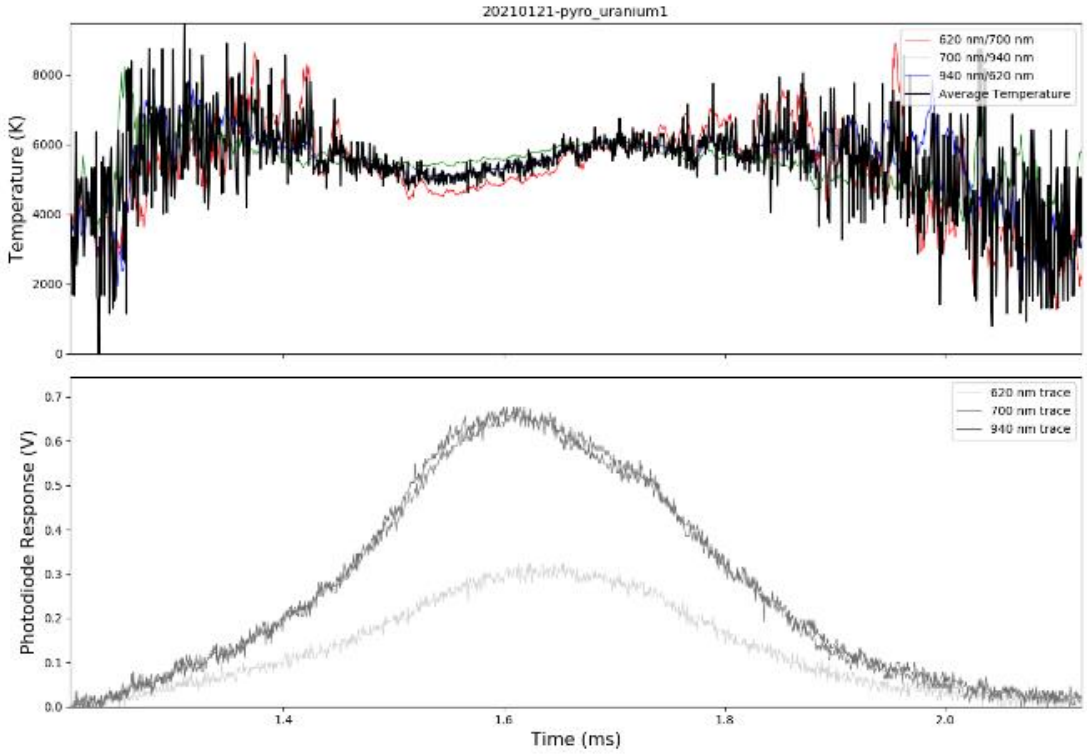

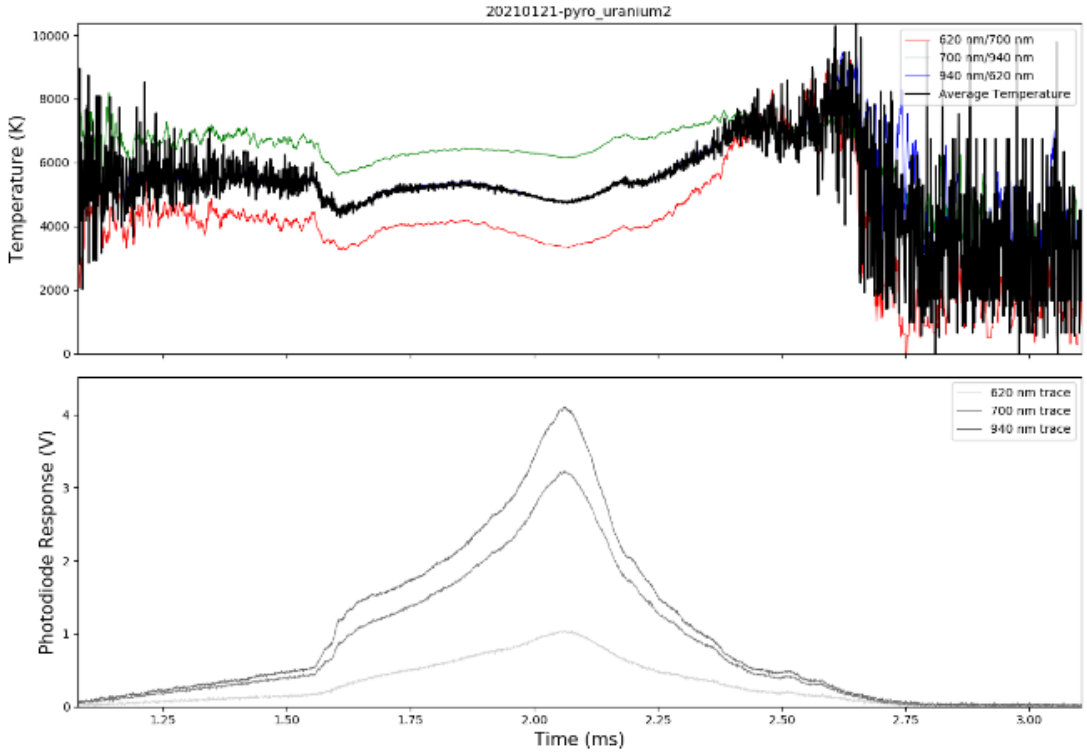
20210121-pyro_uranium2
620 nm/700 nm
700 nm/940 nm
940 nm/620 nm
Average Temperature
Temperature (K)
620 nm trace
700 nm trace
940 nm trace
Photodiode Response (V)
Time (ms)

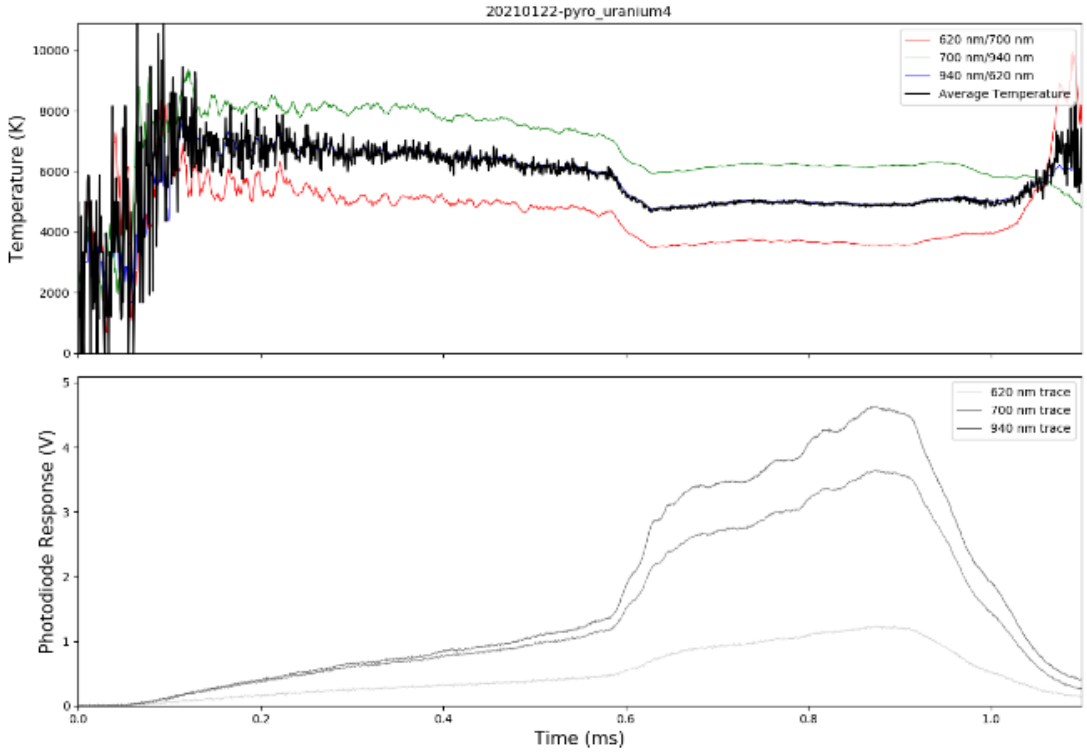
20210122-pyro_uranium4
620 nm/700 nm
700 nm/940 nm
940 nm/620 nm
Average Temperature
Temperature (K)
620 nm trace
700 nm trace
940 nm trace
Photodiode Response (V)
Time (ms)

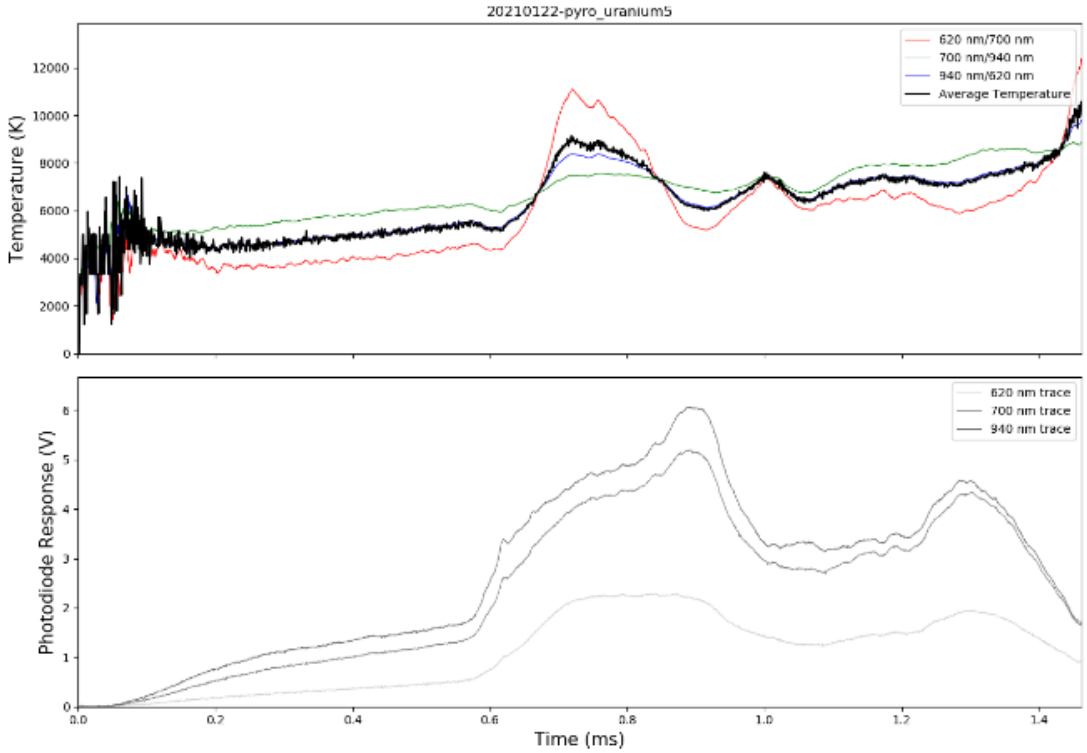
20210122-pyro_uranium5
620 nm/700 nm
700 nm/940 nm
940 nm/620 nm
Average Temperature
Temperature (K)
620 nm trace
700 nm trace
940 nm trace
Photodiode Response (V)
Time (ms)

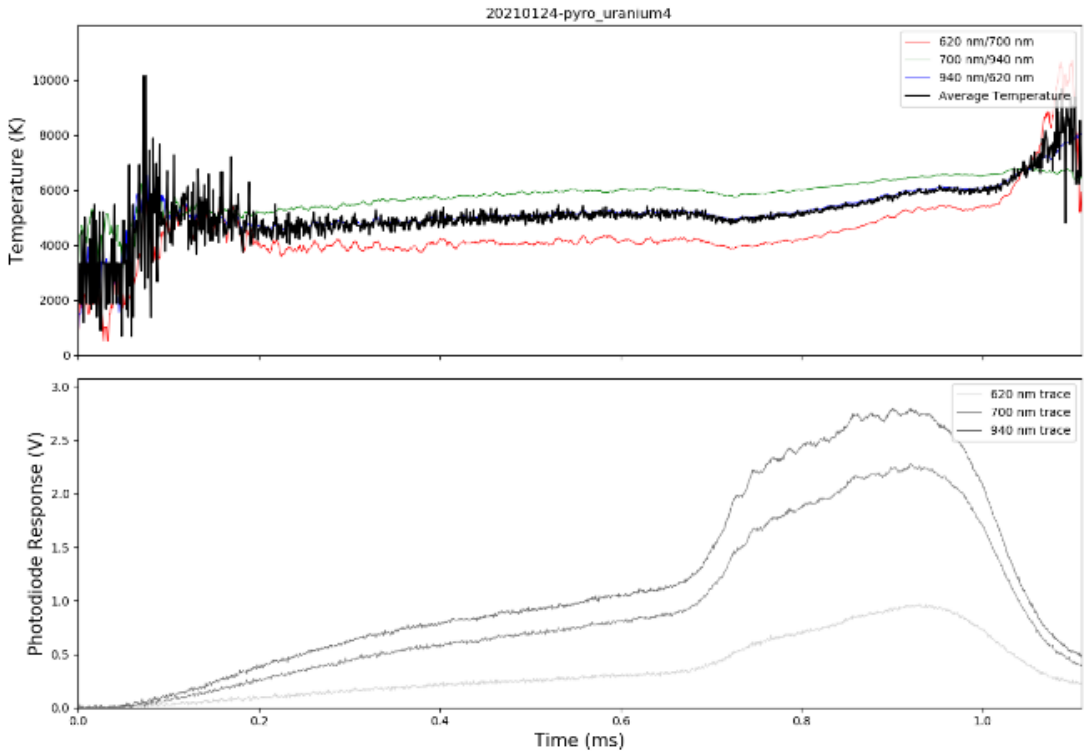
20210124-pyro_uranium4
620 nm/700 nm
700 nm/940 nm
940 nm/620 nm
Average Temperature
Temperature (K)
620 nm trace
700 nm trace
940 nm trace
Photodiode Response (V)
Time (ms)

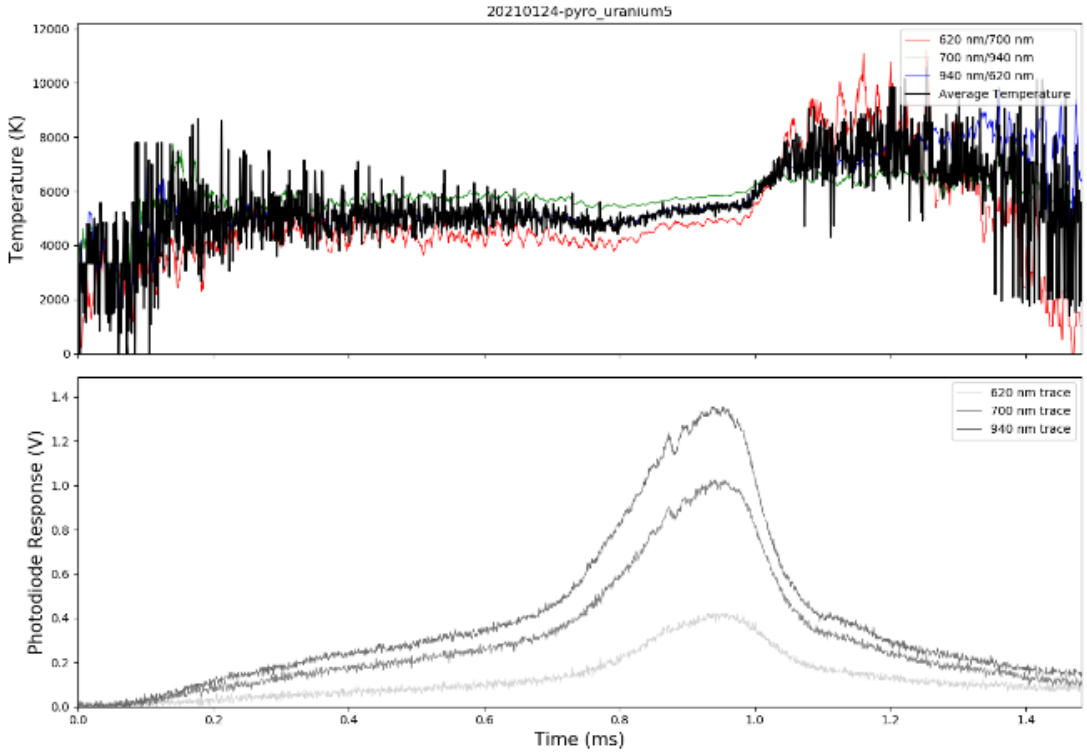
20210124-pyro_uranium5
620 nm/700 nm
700 nm/940 nm
940 nm/620 nm
Average Temperature
Temperature (K)
620 nm trace
700 nm trace
940 nm trace
Photodiode Response (V)
Time (ms)

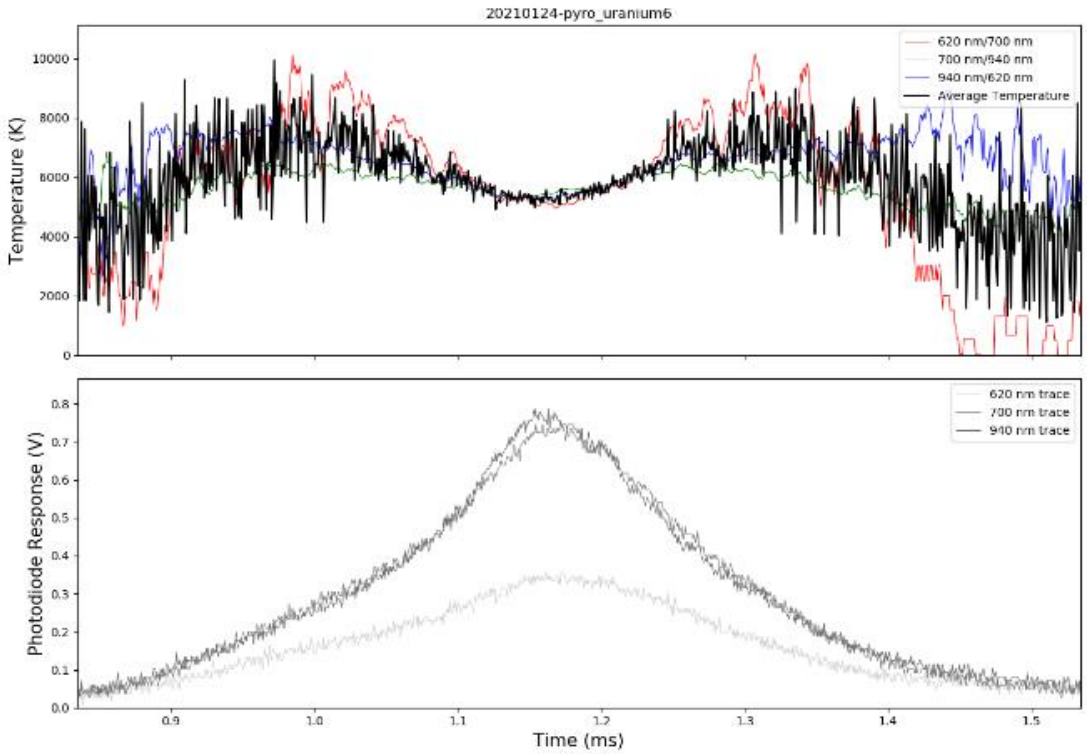
20210124-pyro_uranium6
620 nm/700 nm
700 nm/940 nm
940 nm/620 nm
Average Temperature
Temperature (K)
620 nm trace
700 nm trace
940 nm trace
Photodiode Response (V)
Time (ms)

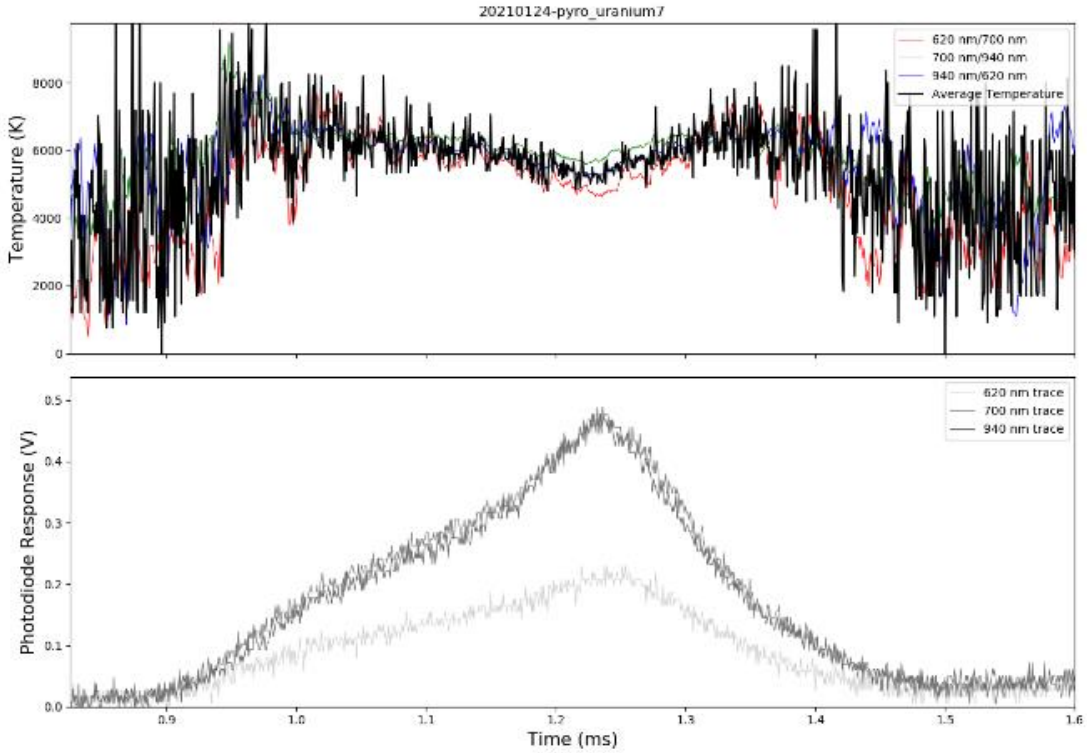
20210124-pyro_uranium7
620 nm/700 nm
700 nm/940 nm
940 nm/620 nm
Average Temperature
Temperature (K)
620 nm trace
700 nm trace
940 nm trace
Photodiode Response (V)
Time (ms)

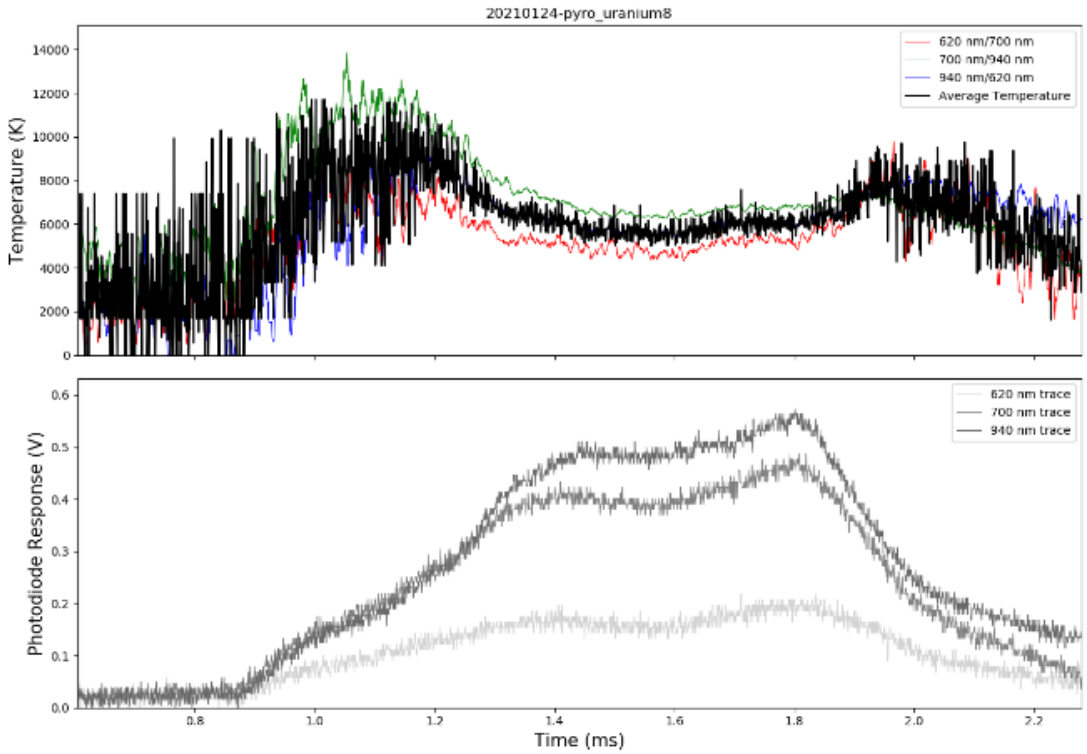
20210124-pyro_uranium8
620 nm/700 nm
700 nm/940 nm
940 nm/620 nm
Average Temperature
Temperature (K)
620 nm trace
700 nm trace
940 nm trace
Photodiode Response (V)
Time (ms)

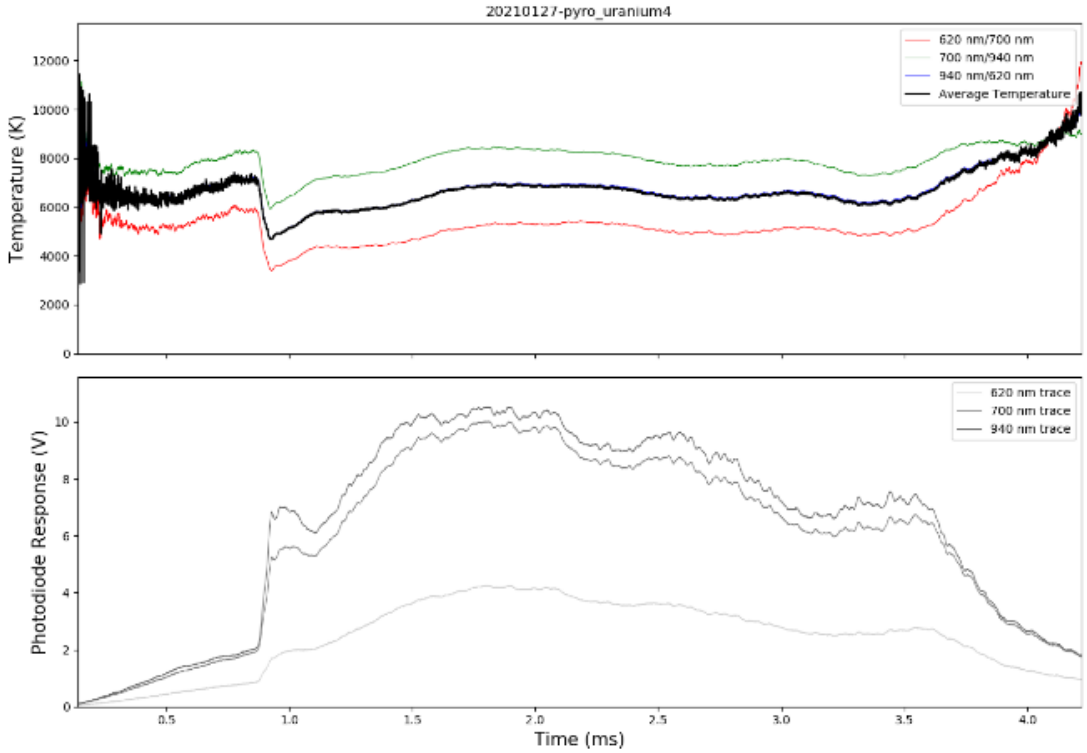
20210127-pyro_uranium4
620 nm/700 nm
700 nm/940 nm
940 nm/620 nm
Average Temperature
Temperature (K)
620 nm trace
700 nm trace
940 nm trace
Photodiode Response (V)
Time (ms)

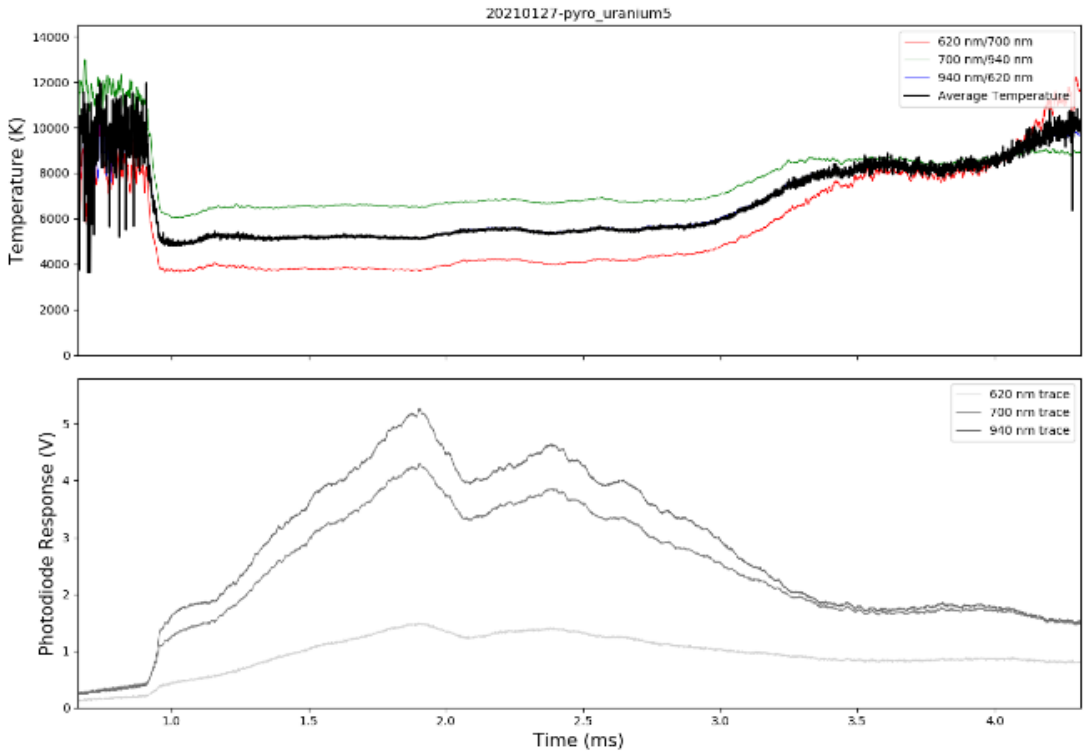
20210127-pyro_uranium5
620 nm/700 nm
700 nm/940 nm
940 nm/620 nm
Average Temperature
Temperature (K)
620 nm trace
700 nm trace
940 nm trace
Photodiode Response (V)
Time (ms)

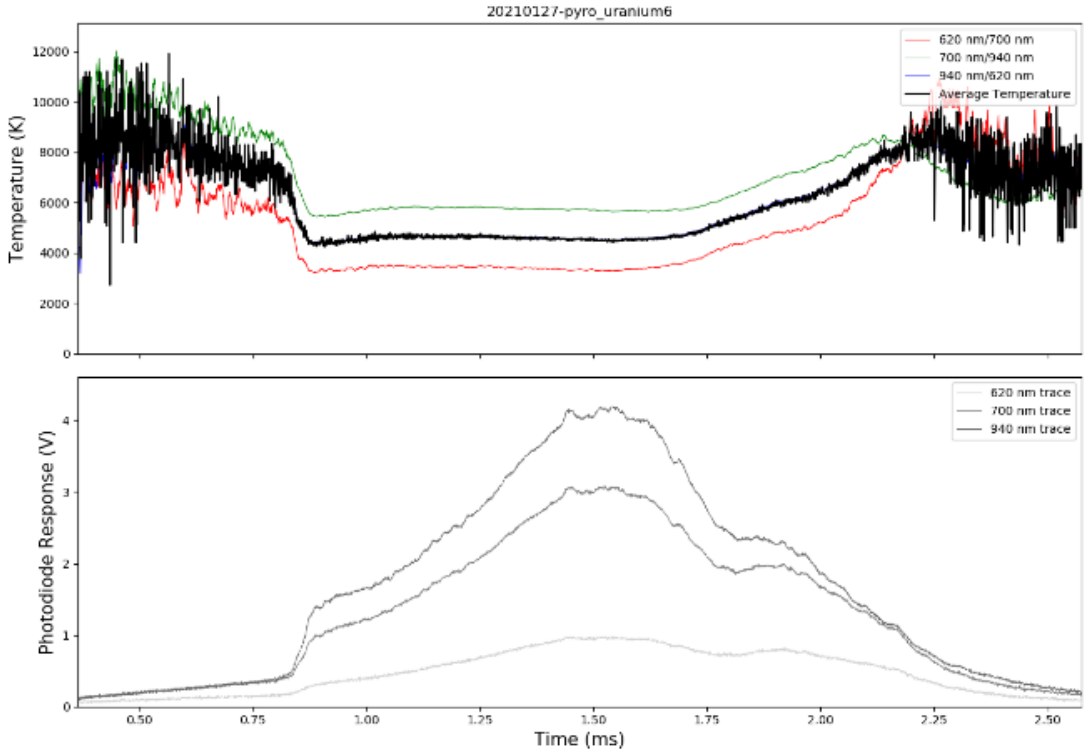
20210127-pyro_uranium6
620 nm/700 nm
700 nm/940 nm
940 nm/620 nm
Average Temperature
Temperature (K)
620 nm trace
700 nm trace
940 nm trace
Photodiode Response (V)
Time (ms)

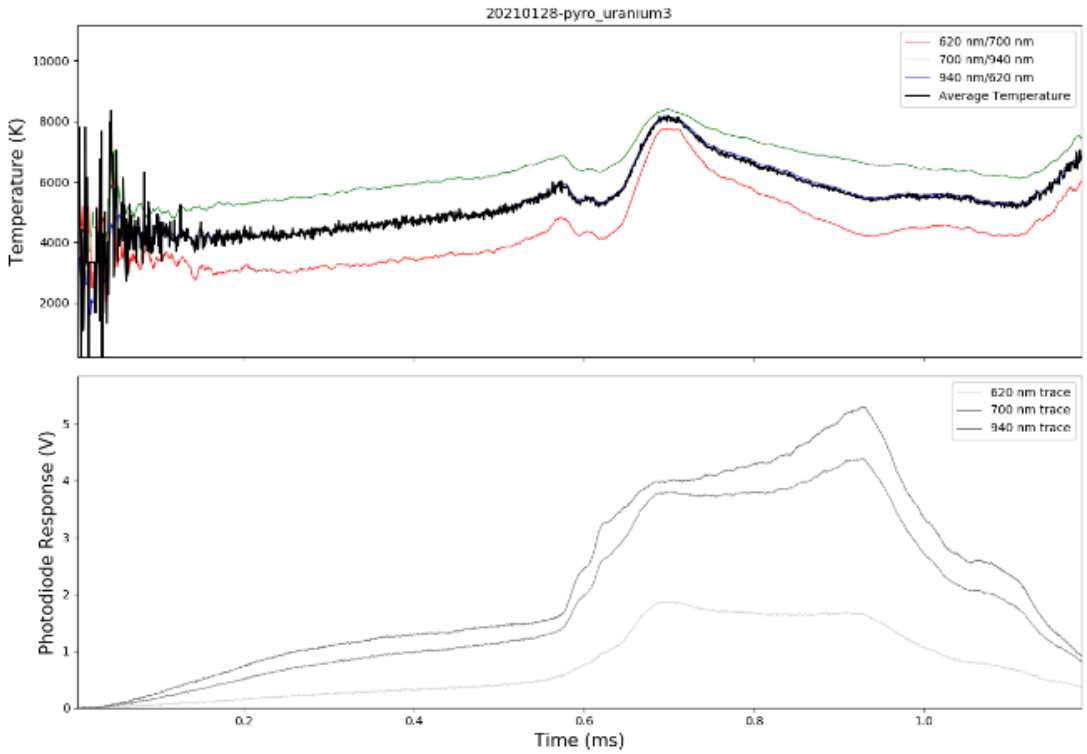
20210128-pyro_uranium3
620 nm/700 nm
700 nm/940 nm
940 nm/620 nm
Average Temperature
Temperature (K)
620 nm trace
700 nm trace
940 nm trace
Photodiode Response (V)
Time (ms)

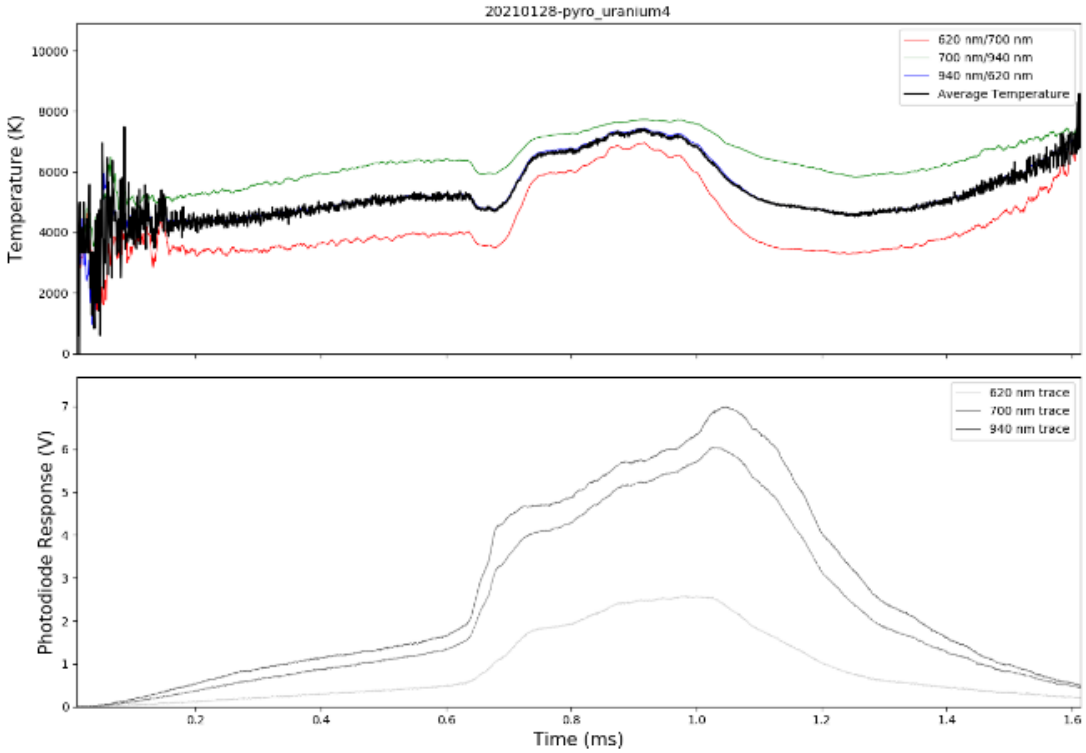
20210128-pyro_uranium4
620 nm/700 nm
700 nm/940 nm
940 nm/620 nm
Average Temperature
Temperature (K)
10000
8000
6000
4000
2000
0
620 nm trace
700 nm trace
940 nm trace
Photodiode Response (V)
0
1
2
3
4
5
6
7
0.2
0.4
0.6
0.8
1.0
1.2
1.4
1.6
Time (ms)

A.2.2. Time-resolved spectra from visible spectrometer, 2nd round of shock tube tests.

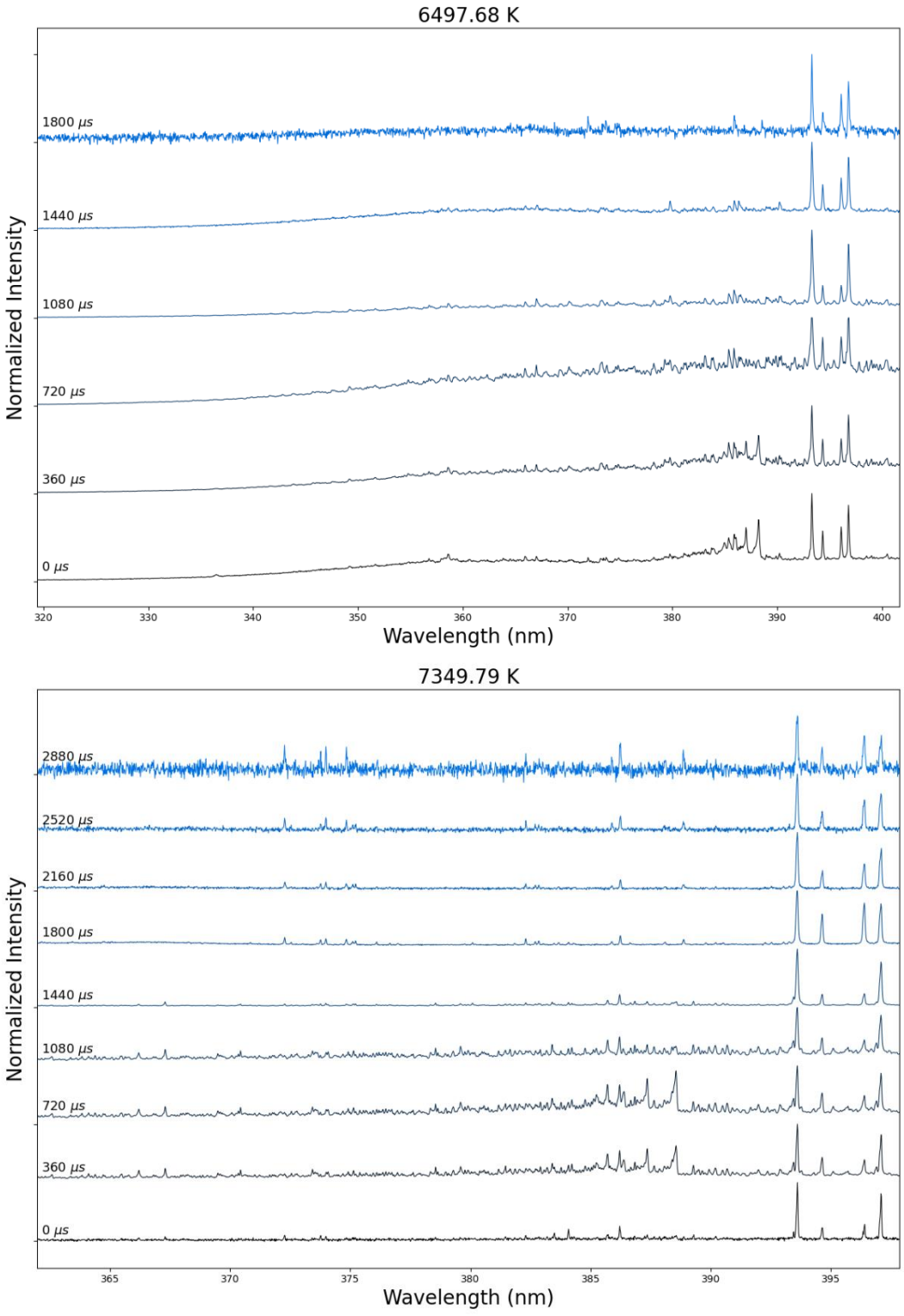

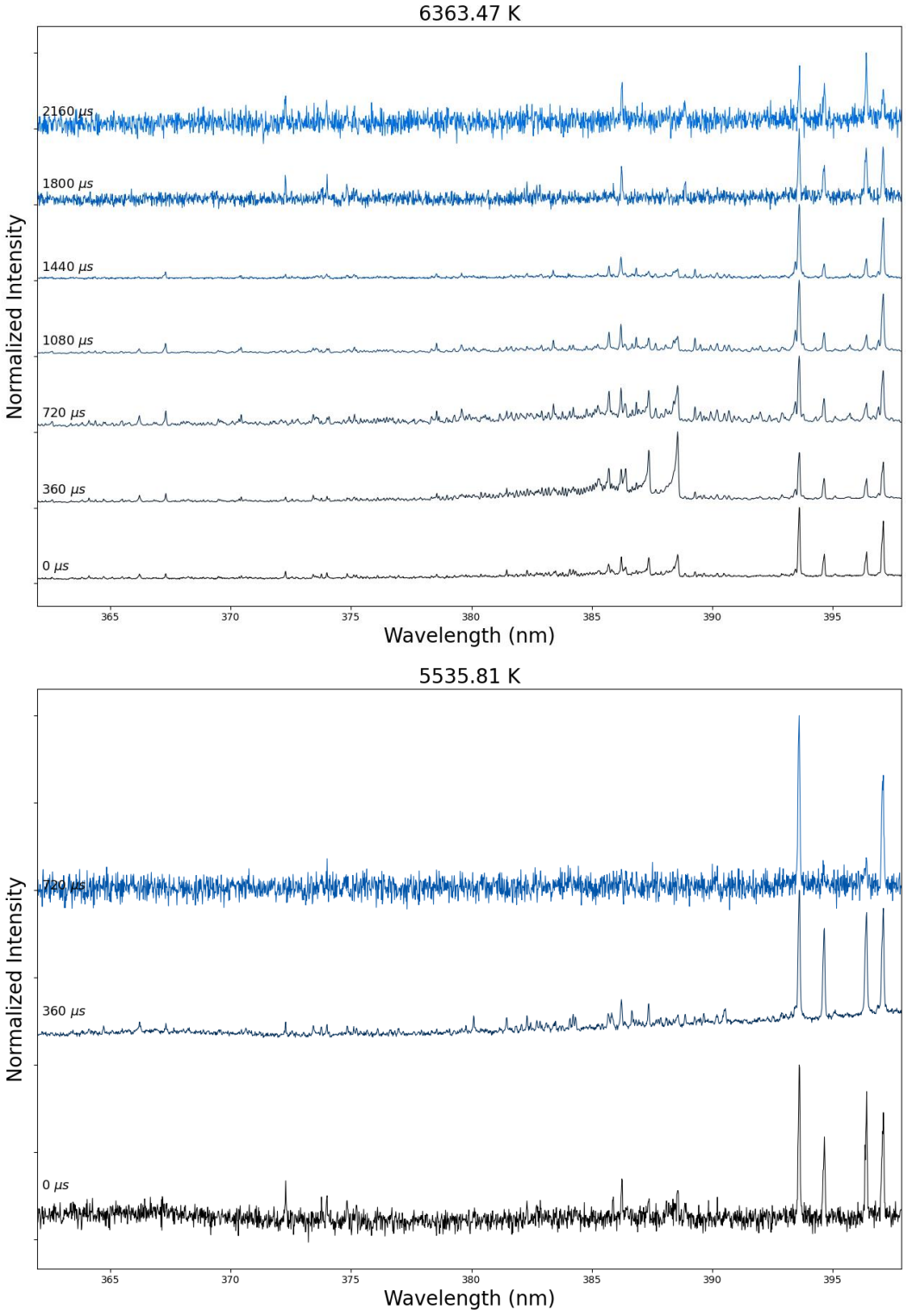
6363.47 K
2160 μs
1800 μs
1440 μs
1080 μs
720 μs
360 μs
0 μs
Normalized Intensity
365
370
375
380
385
390
395
Wavelength (nm)
5535.81 K
720 μs
360 μs
0 μs
Normalized Intensity
365
370
375
380
385
390
395
Wavelength (nm)

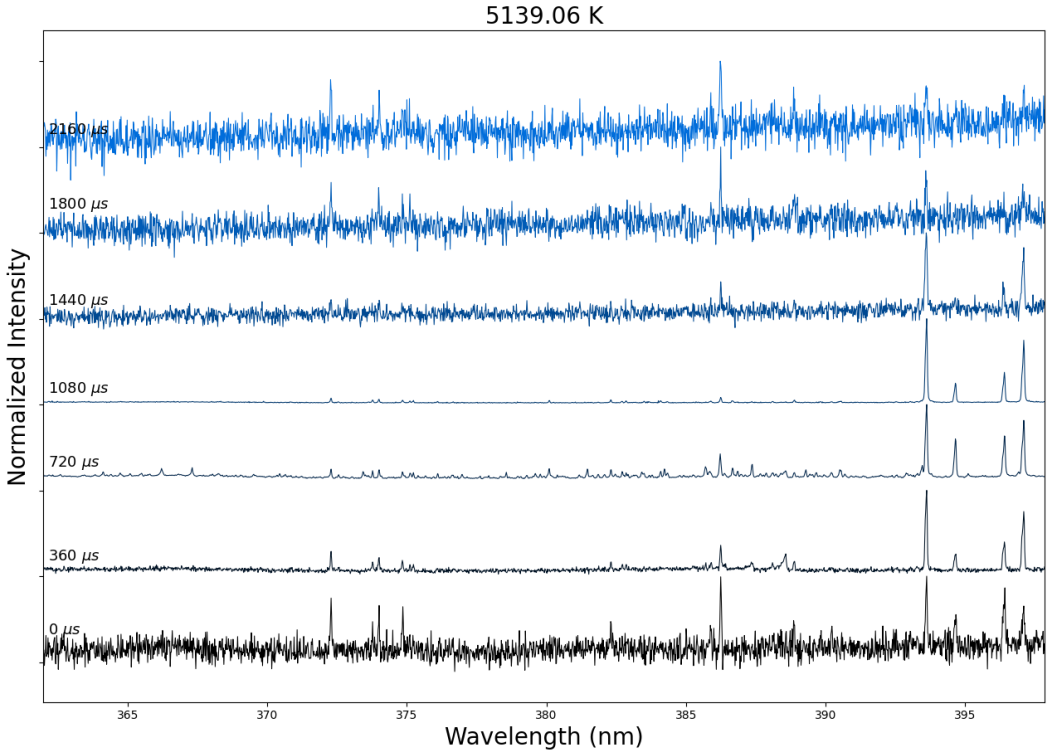
5139.06 K
2160 μs
1800 μs
1440 μs
1080 μs
720 μs
360 μs
0 μs
Normalized Intensity
365
370
375
380
385
390
395
Wavelength (nm)

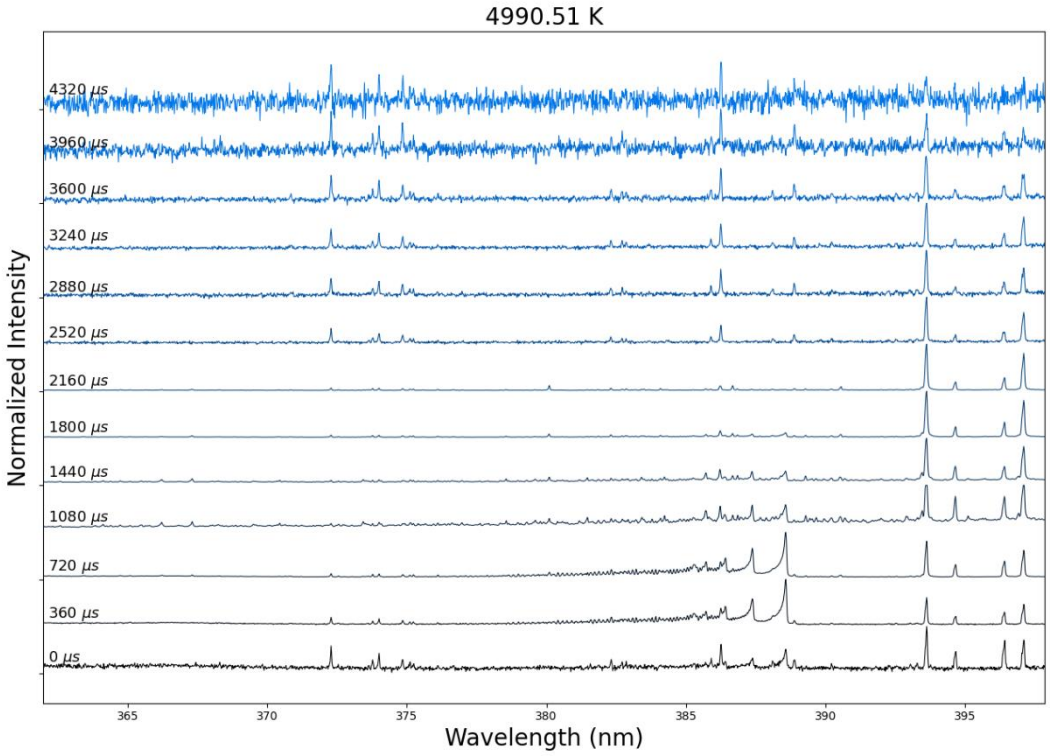
4990.51 K
4320 μs
3960 μs
3600 μs
3240 μs
2880 μs
2520 μs
2160 μs
1800 μs
1440 μs
1080 μs
720 μs
360 μs
0 μs
Normalized Intensity
365
370
375
380
385
390
395
Wavelength (nm)

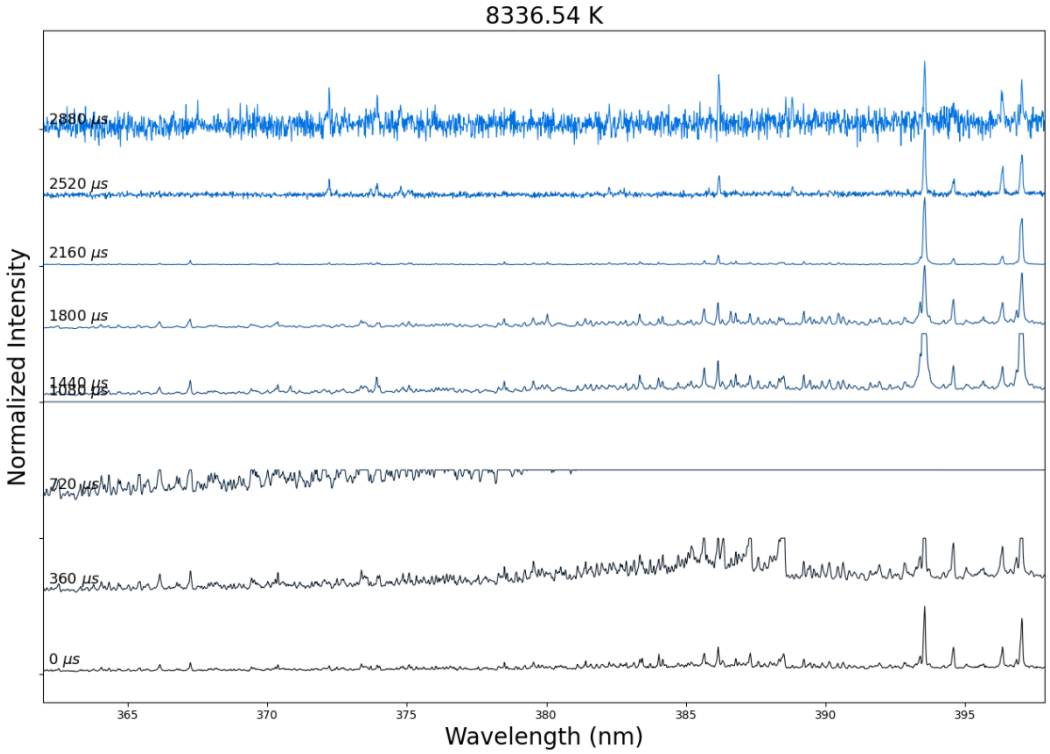
8336.54 K
2880 μs
2520 μs
2160 μs
1800 μs
1440 μs
1080 μs
720 μs
360 μs
0 μs
Normalized Intensity
365
370
375
380
385
390
395
Wavelength (nm)

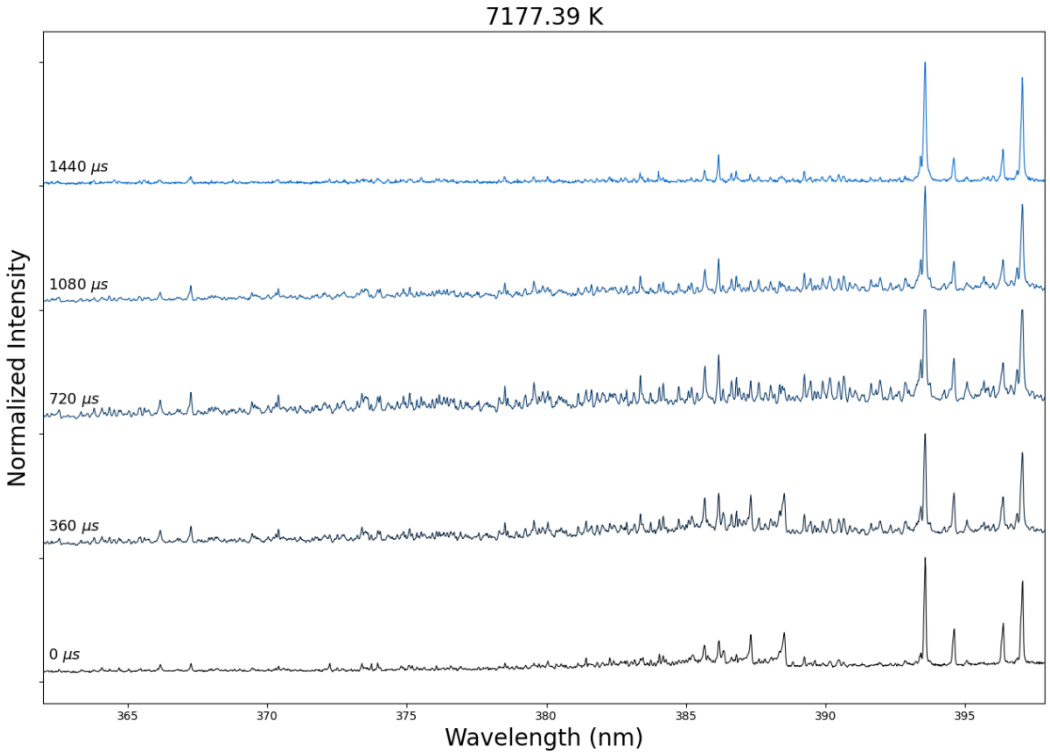
7177.39 K
1440 μs
1080 μs
720 μs
360 μs
0 μs
Normalized Intensity
365
370
375
380
385
390
395
Wavelength (nm)

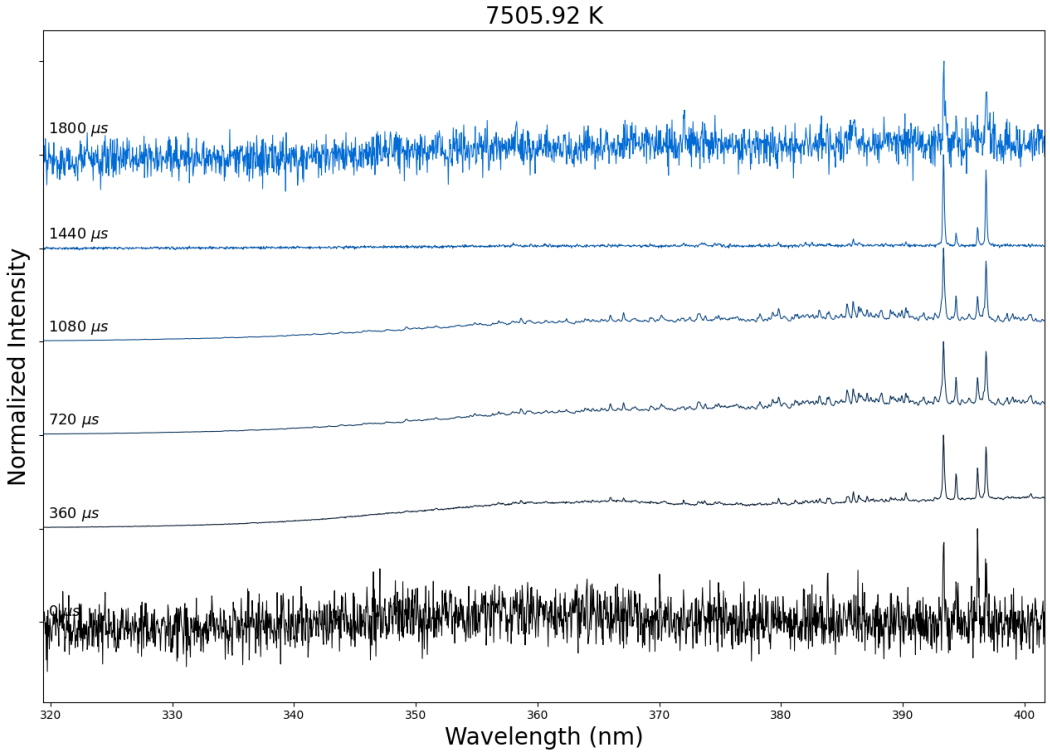
7505.92 K
1800 μs
1440 μs
1080 μs
720 μs
360 μs
0 μs
Normalized Intensity
320
330
340
350
360
370
380
390
400
Wavelength (nm)

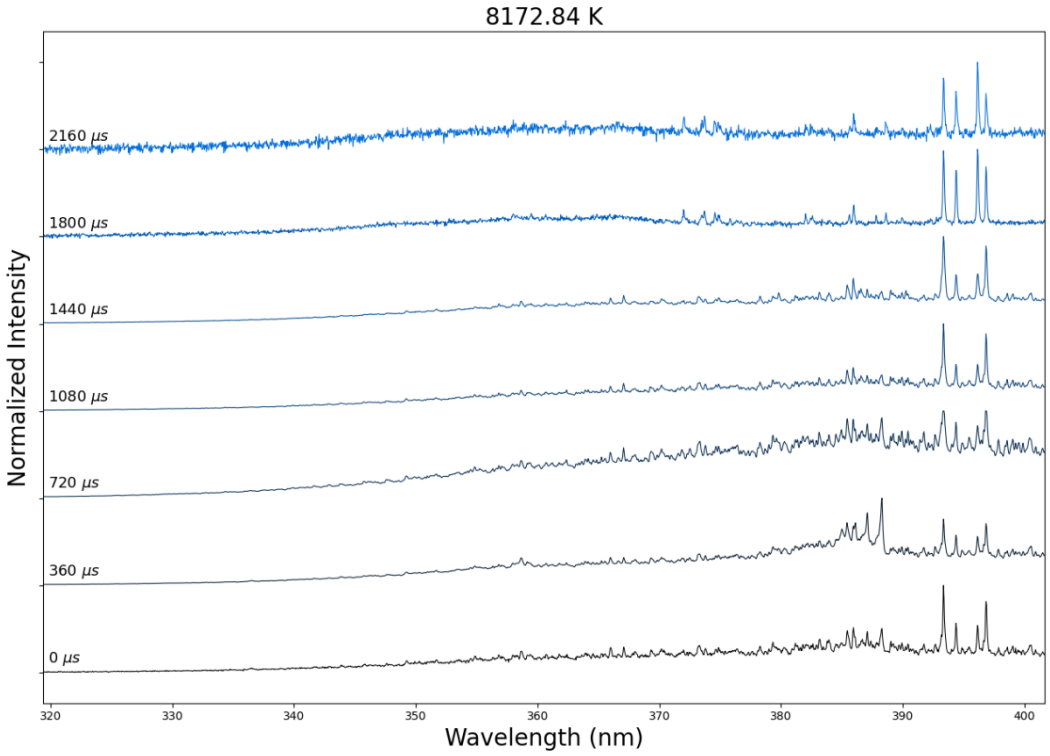
8172.84 K
2160 μs
1800 μs
1440 μs
1080 μs
720 μs
360 μs
0 μs
Normalized Intensity
320
330
340
350
360
370
380
390
400
Wavelength (nm)

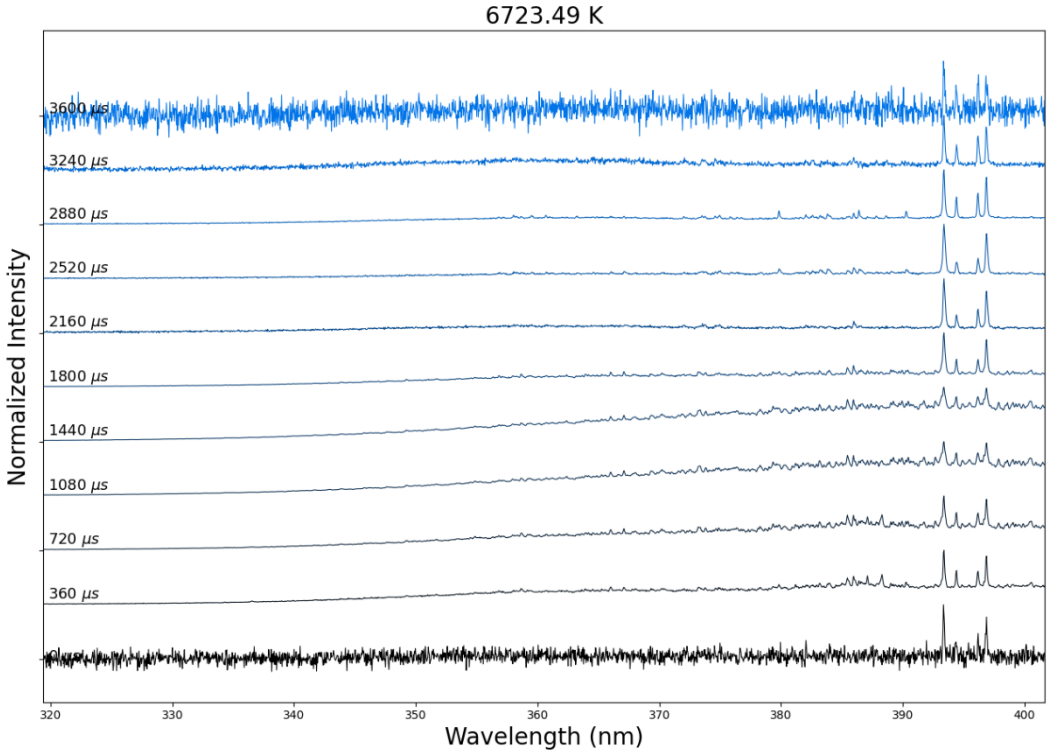
6723.49 K
3600 μs
3240 μs
2880 μs
2520 μs
2160 μs
1800 μs
1440 μs
1080 μs
720 μs
360 μs
Normalized Intensity
320
330
340
350
360
370
380
390
400
Wavelength (nm)

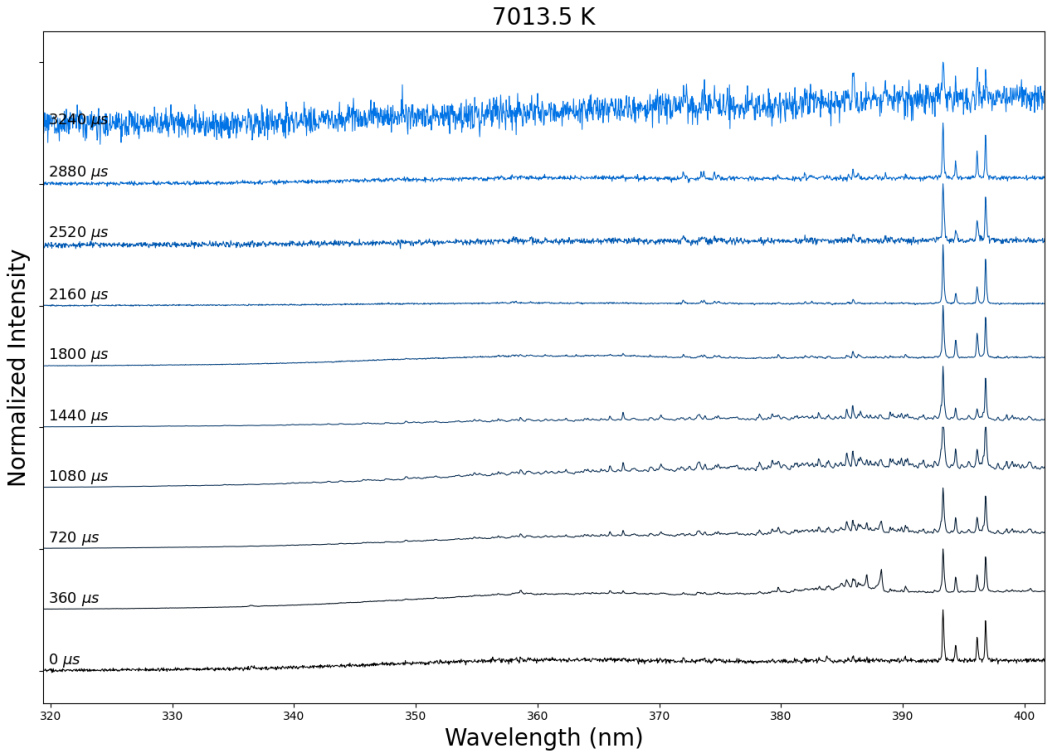
7013.5 K
3240 μs
2880 μs
2520 μs
2160 μs
1800 μs
1440 μs
1080 μs
720 μs
360 μs
0 μs
Normalized Intensity
320
330
340
350
360
370
380
390
400
Wavelength (nm)

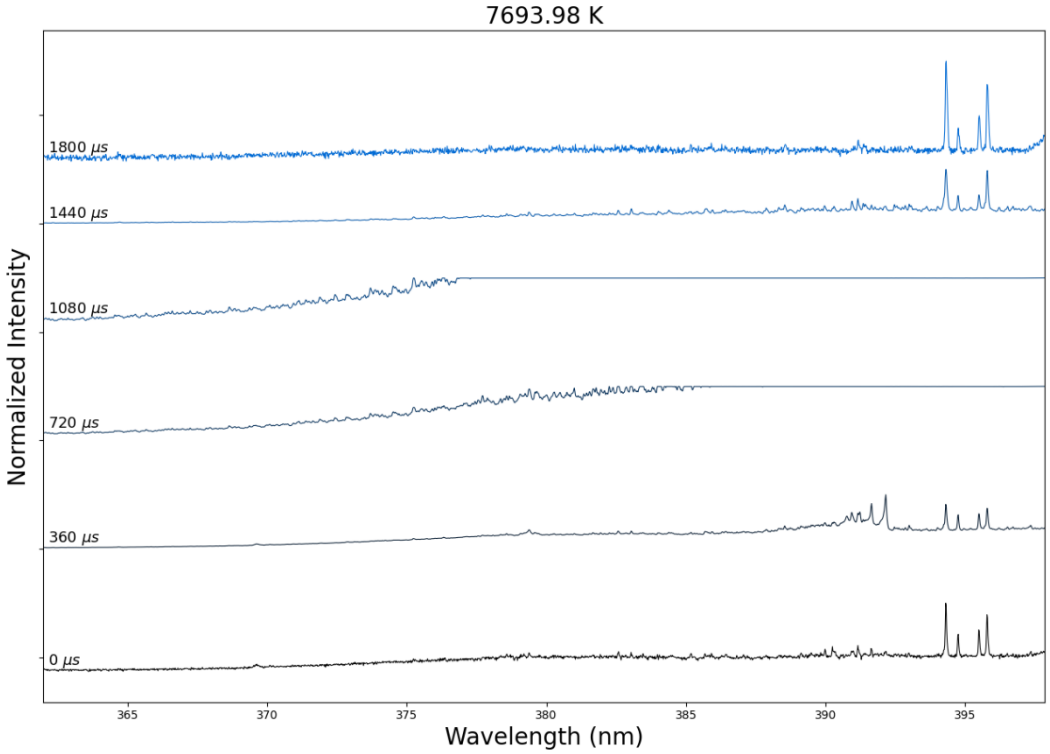
7693.98 K
1800 μs
1440 μs
1080 μs
720 μs
360 μs
0 μs
Normalized Intensity
365
370
375
380
385
390
395
Wavelength (nm)

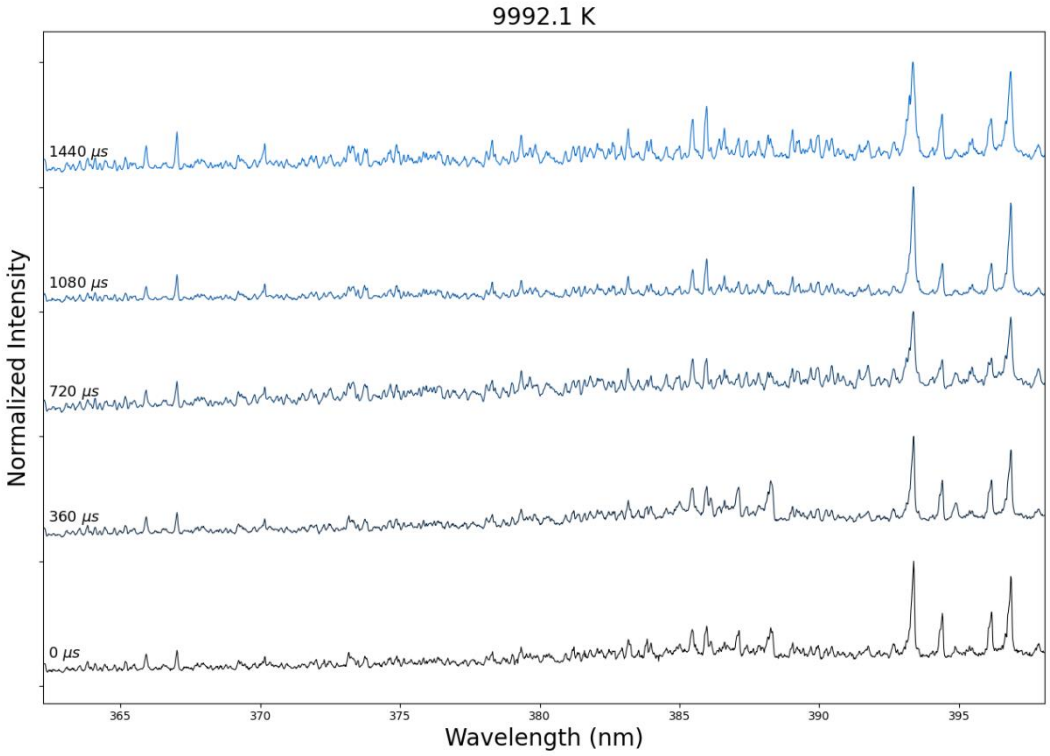
9992.1 K
1440 μs
1080 μs
720 μs
360 μs
0 μs
Normalized Intensity
365
370
375
380
385
390
395
Wavelength (nm)

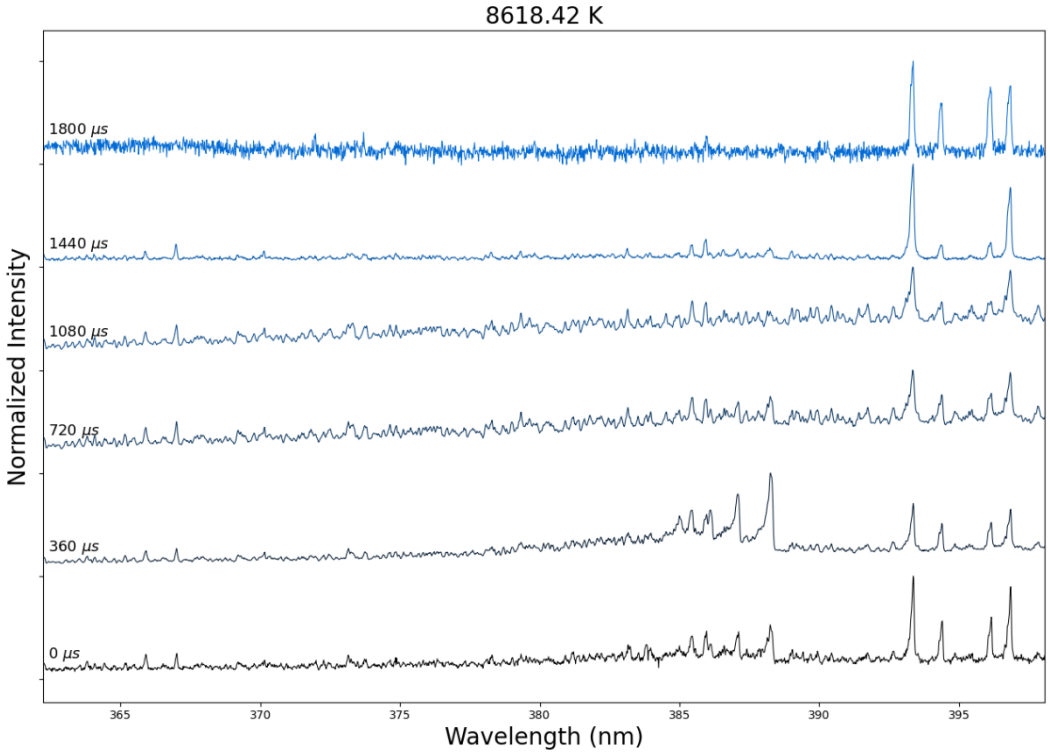
8618.42 K
1800 μs
1440 μs
1080 μs
720 μs
360 μs
0 μs
Normalized Intensity
365
370
375
380
385
390
395
Wavelength (nm)

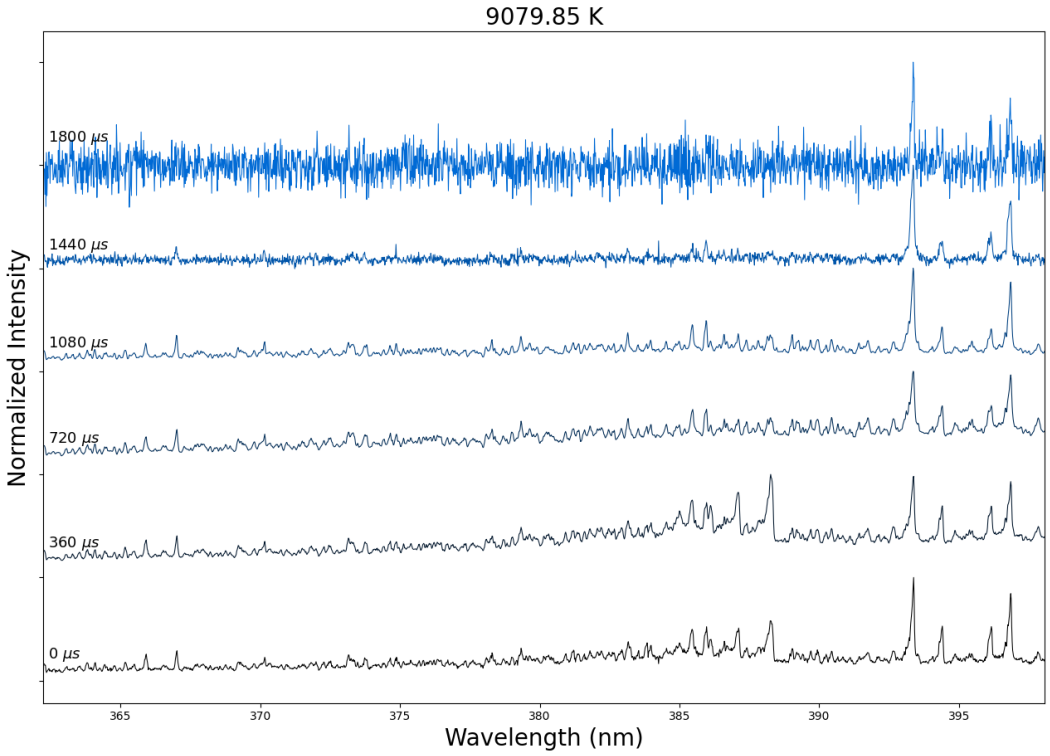
9079.85 K
1800 μs
1440 μs
1080 μs
720 μs
360 μs
0 μs
Normalized Intensity
365
370
375
380
385
390
395
Wavelength (nm)

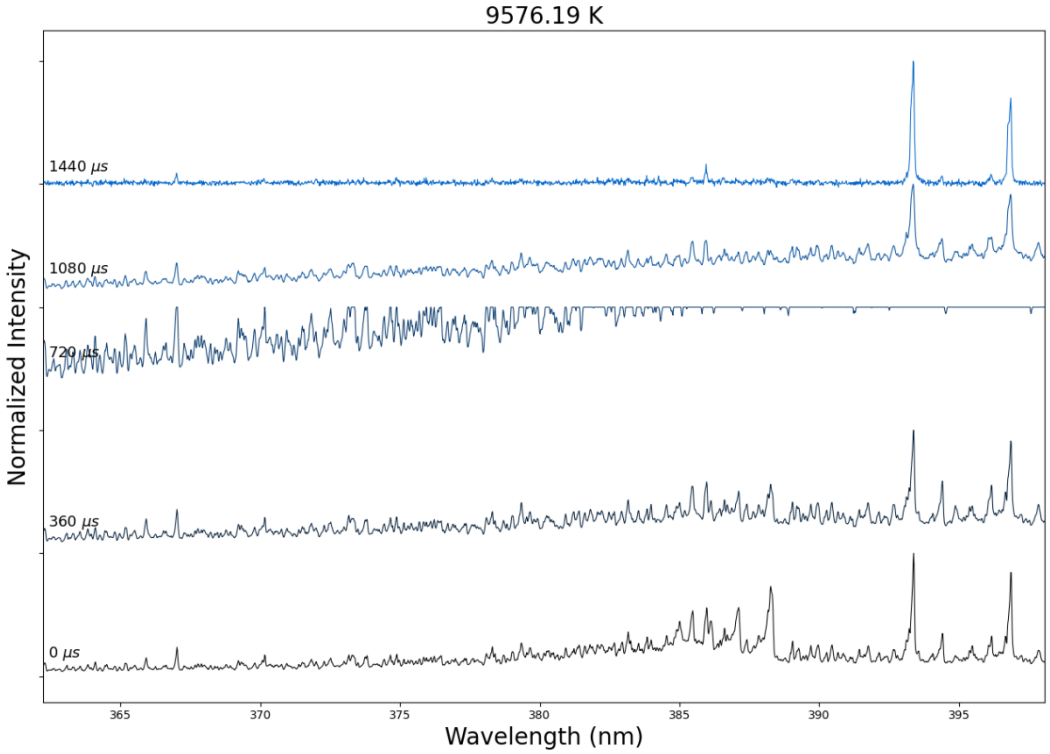
9576.19 K
1440 μs
1080 μs
720 μs
360 μs
0 μs
Normalized Intensity
365
370
375
380
385
390
395
Wavelength (nm)

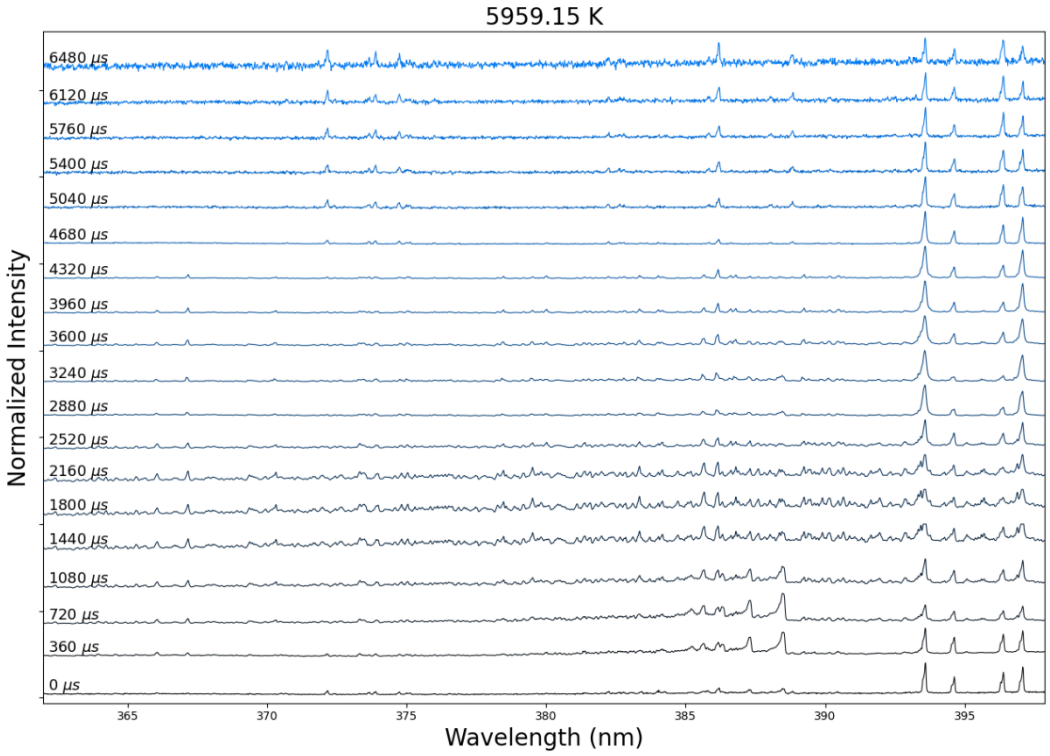
5959.15 K
6480 μs
6120 μs
5760 μs
5400 μs
5040 μs
4680 μs
4320 μs
3960 μs
3600 μs
3240 μs
2880 μs
2520 μs
2160 μs
1800 μs
1440 μs
1080 μs
720 μs
360 μs
0 μs
Normalized Intensity
365
370
375
380
385
390
395
Wavelength (nm)

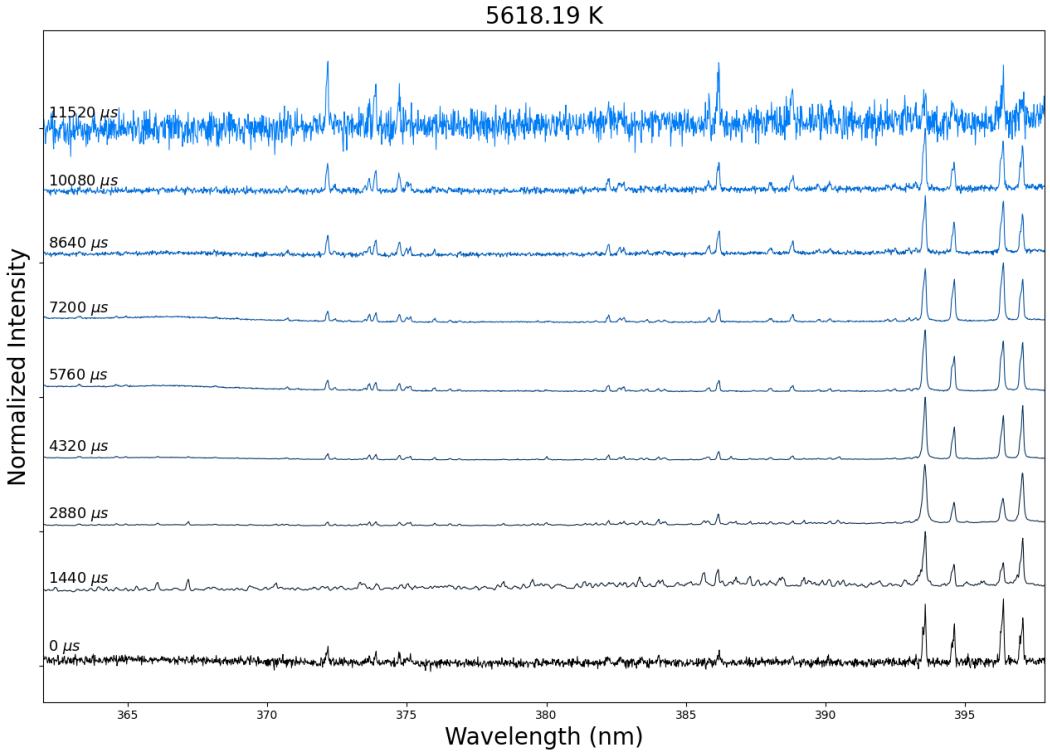
5618.19 K
11520 μs
10080 μs
8640 μs
7200 μs
5760 μs
4320 μs
2880 μs
1440 μs
0 μs
Normalized Intensity
365
370
375
380
385
390
395
Wavelength (nm)

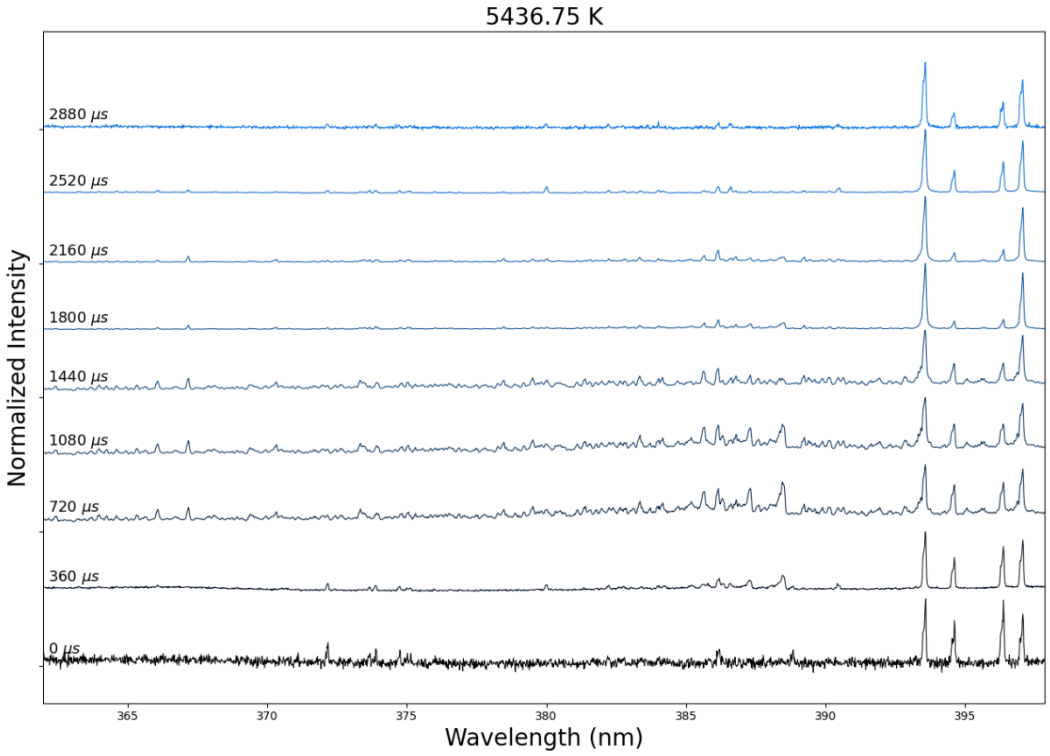
5436.75 K
2880 μs
2520 μs
2160 μs
1800 μs
1440 μs
1080 μs
720 μs
360 μs
0 μs
Normalized Intensity
365
370
375
380
385
390
395
Wavelength (nm)

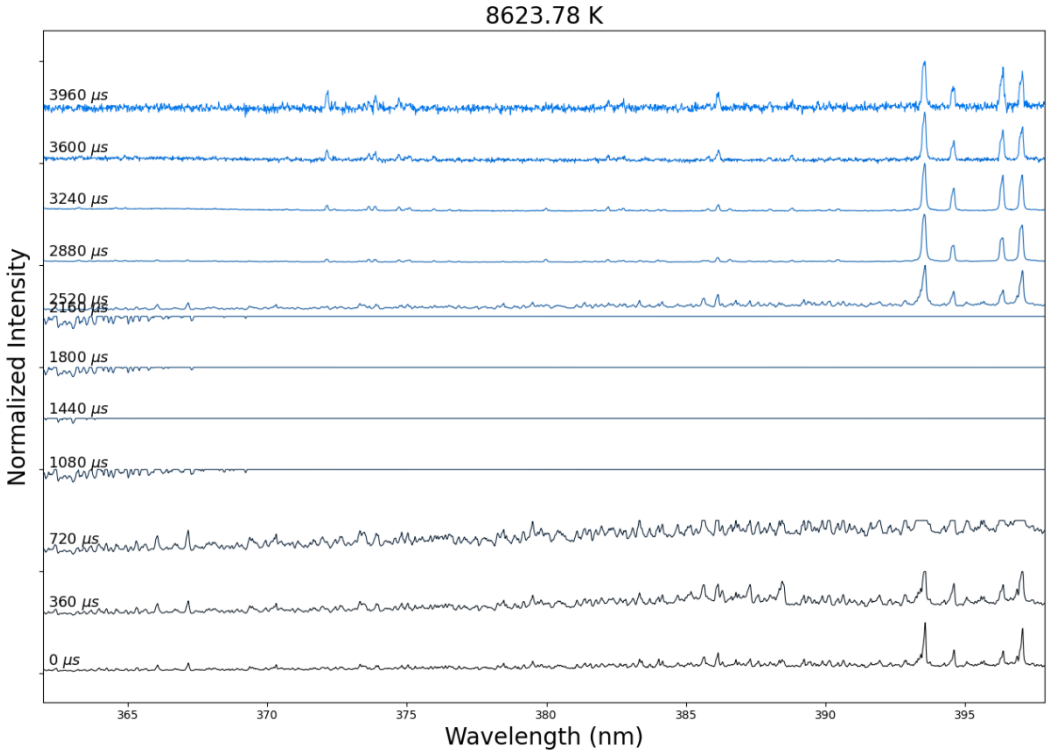
8623.78 K
3960 μs
3600 μs
3240 μs
2880 μs
2520 μs
2160 μs
1800 μs
1440 μs
1080 μs
720 μs
360 μs
0 μs
Normalized Intensity
365
370
375
380
385
390
395
Wavelength (nm)

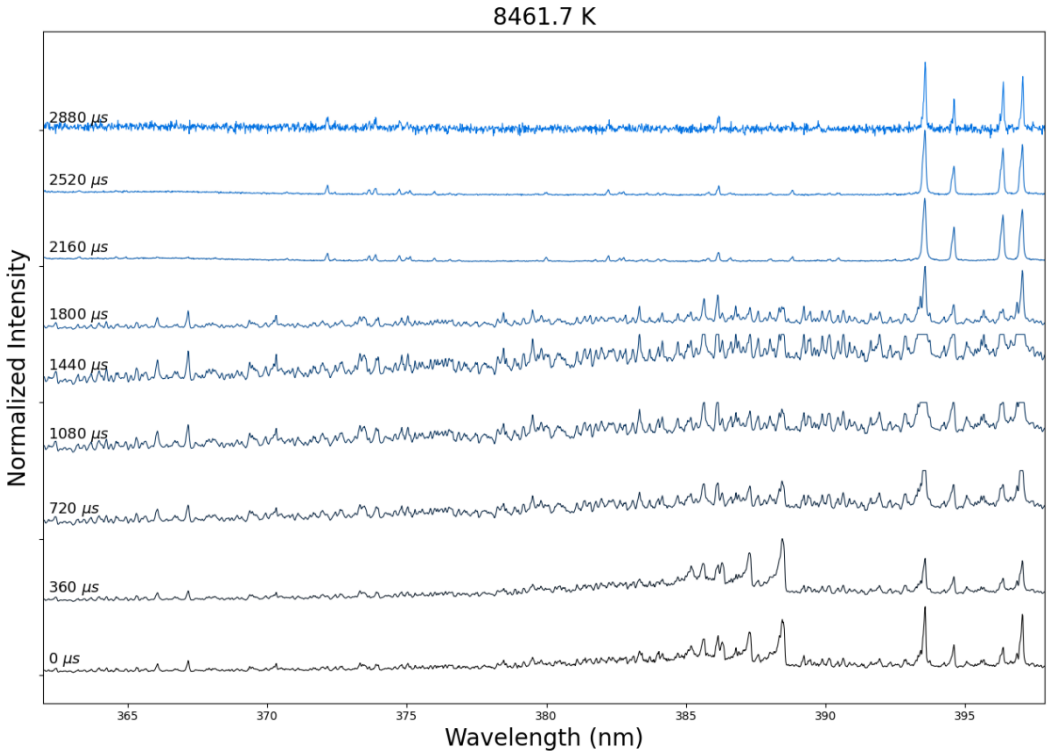
8461.7 K
2880 μs
2520 μs
2160 μs
1800 μs
1440 μs
1080 μs
720 μs
360 μs
0 μs
Normalized Intensity
365
370
375
380
385
390
395
Wavelength (nm)

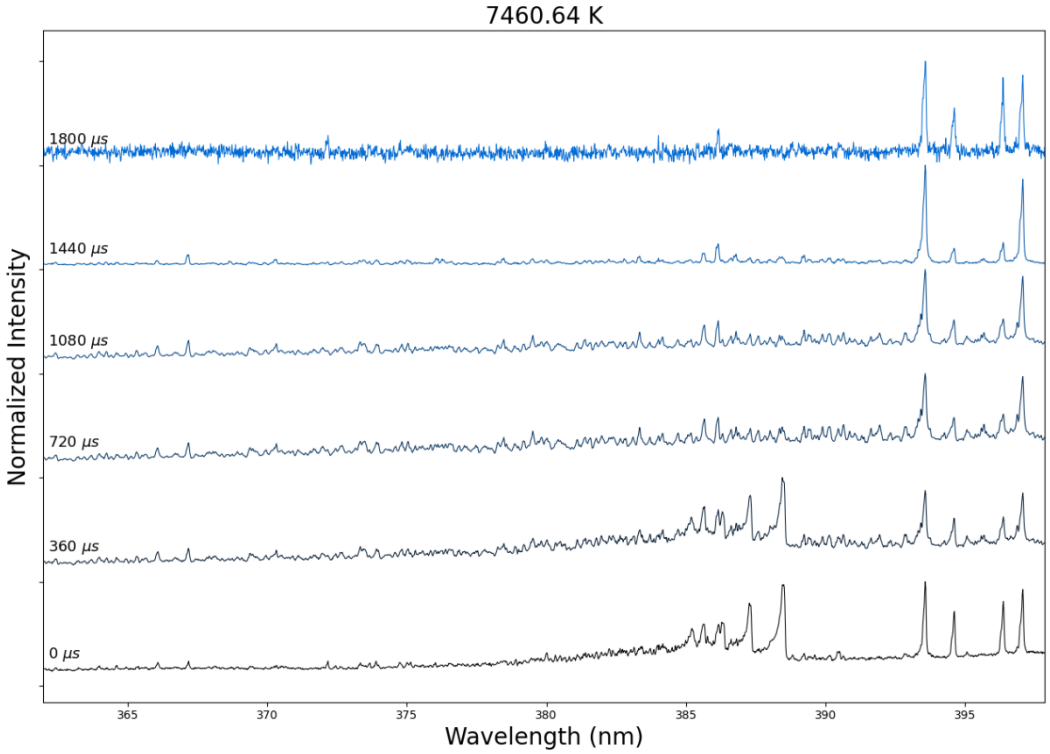
7460.64 K
1800 μs
1440 μs
1080 μs
720 μs
360 μs
0 μs
Normalized Intensity
365
370
375
380
385
390
395
Wavelength (nm)

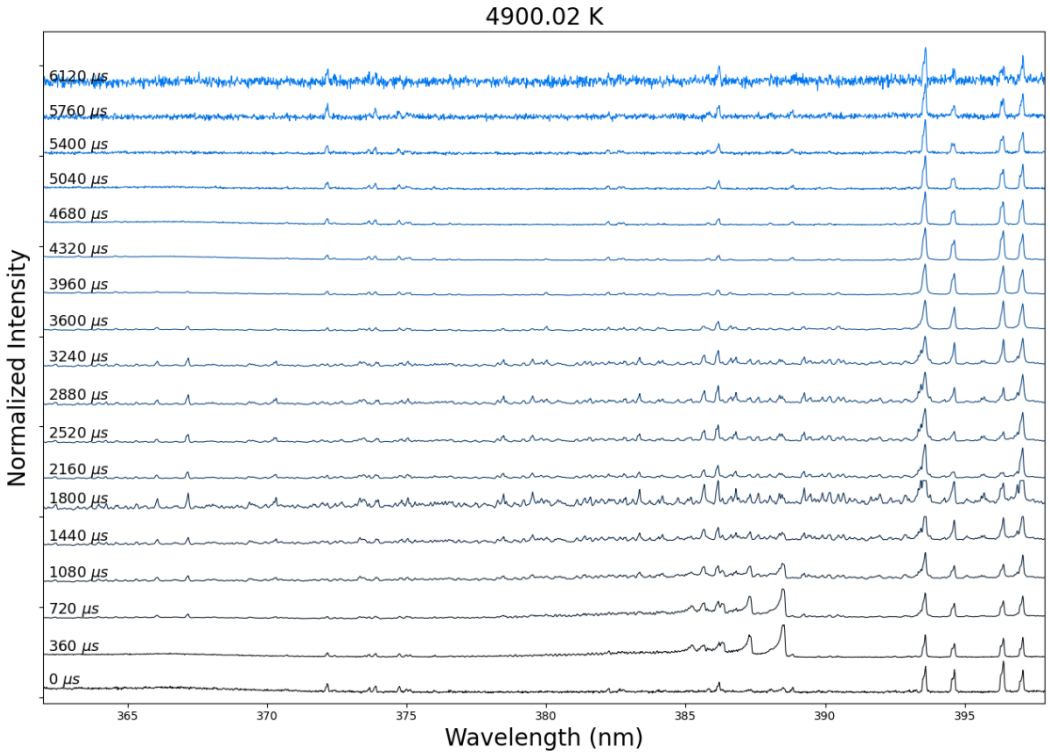
4900.02 K
6120 μs
5760 μs
5400 μs
5040 μs
4680 μs
4320 μs
3960 μs
3600 μs
3240 μs
2880 μs
2520 μs
2160 μs
1800 μs
1440 μs
1080 μs
720 μs
360 μs
0 μs
Normalized Intensity
365
370
375
380
385
390
395
Wavelength (nm)

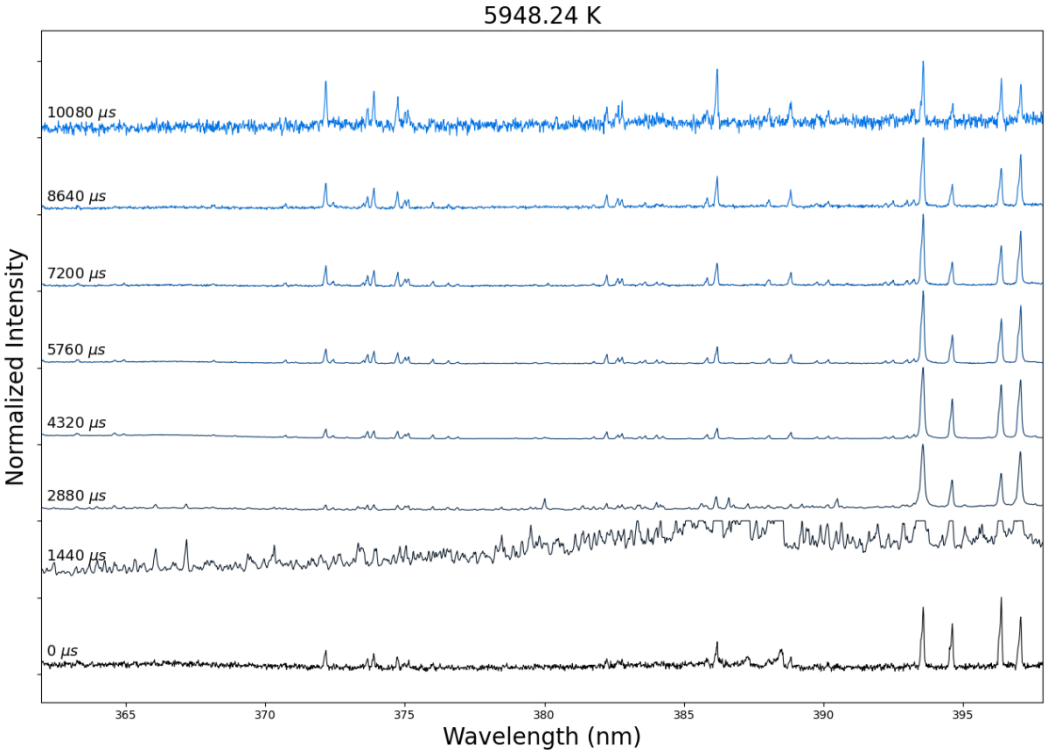
5948.24 K
10080 μs
8640 μs
7200 μs
5760 μs
4320 μs
2880 μs
1440 μs
0 μs
Normalized Intensity
365
370
375
380
385
390
395
Wavelength (nm)

A.2.3. Visible spectra from shock tube experiments with model overlays

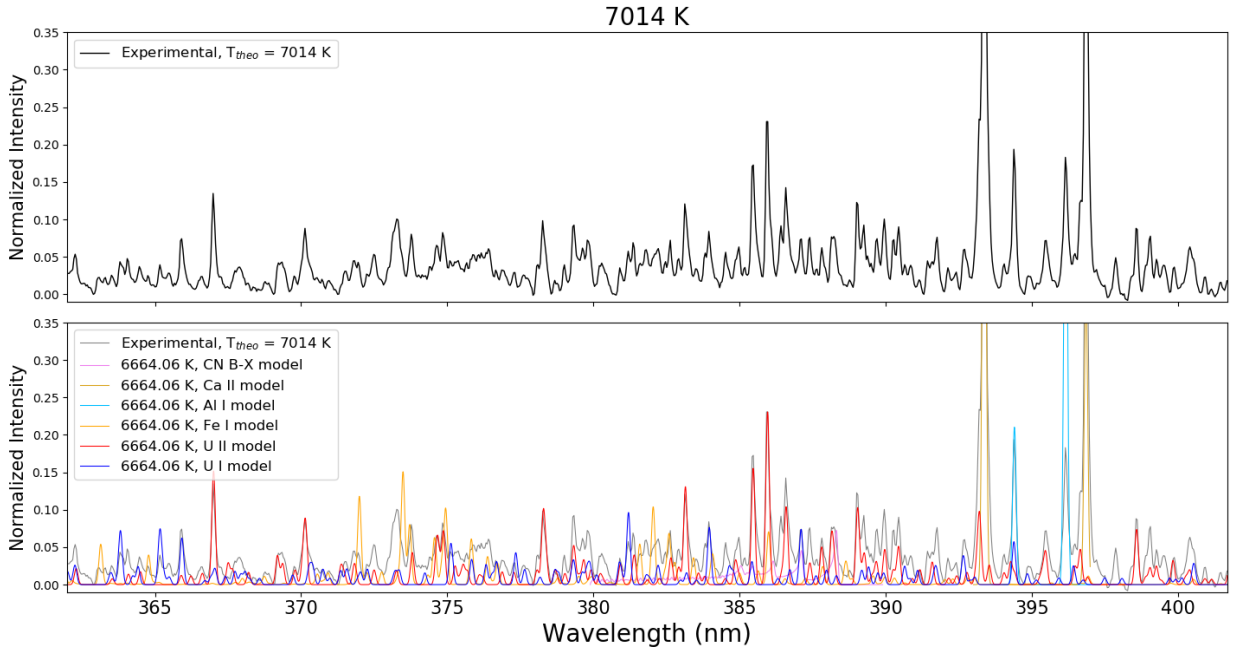

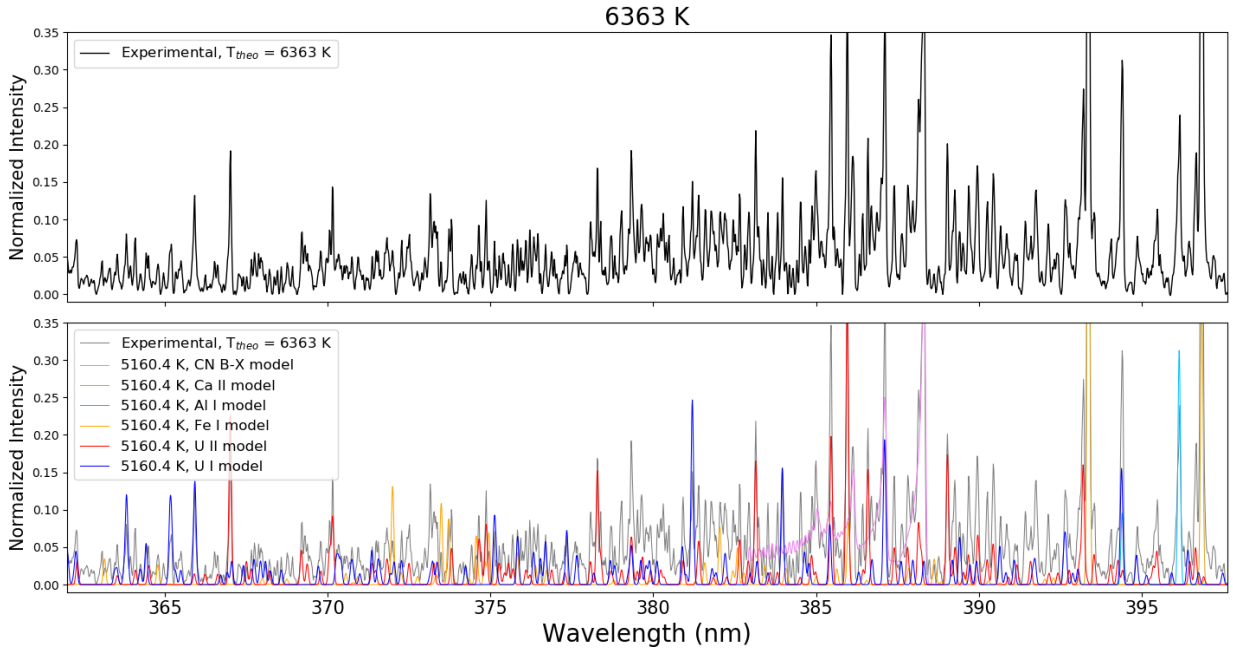

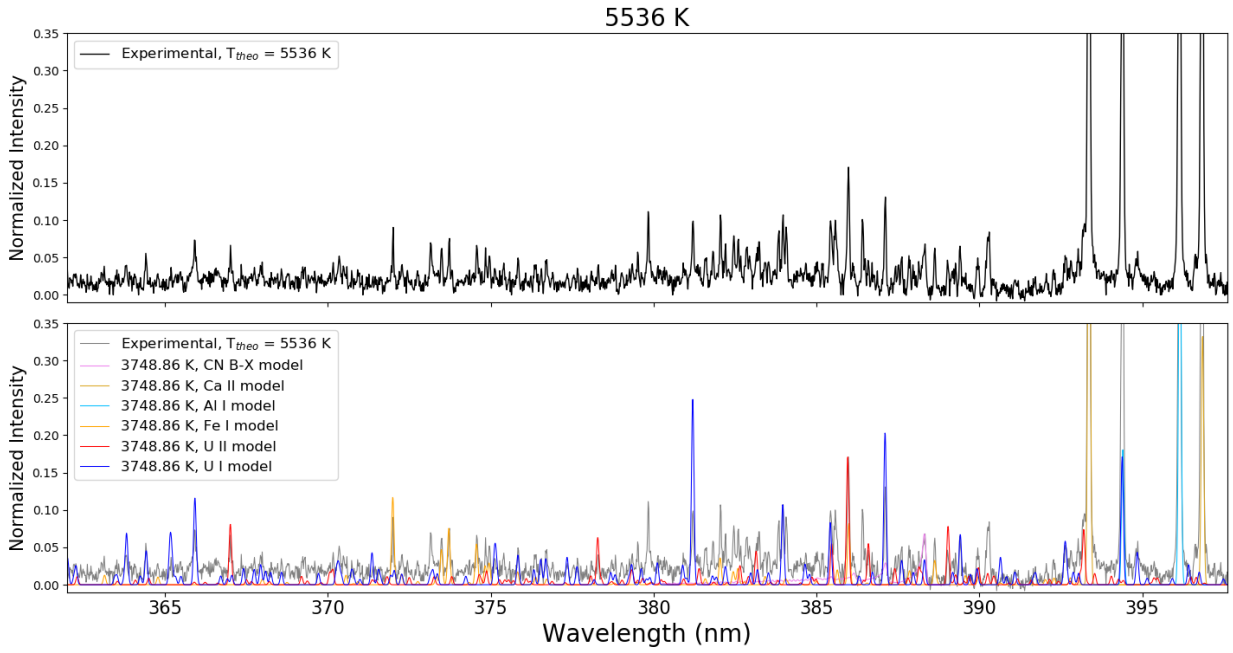
5536 K
Experimental, T_{theo} = 5536 K
Normalized Intensity
Experimental, T_{theo} = 5536 K
3748.86 K, CN B-X model
3748.86 K, Ca II model
3748.86 K, Al I model
3748.86 K, Fe I model
3748.86 K, U II model
3748.86 K, U I model
Normalized Intensity
Wavelength (nm)

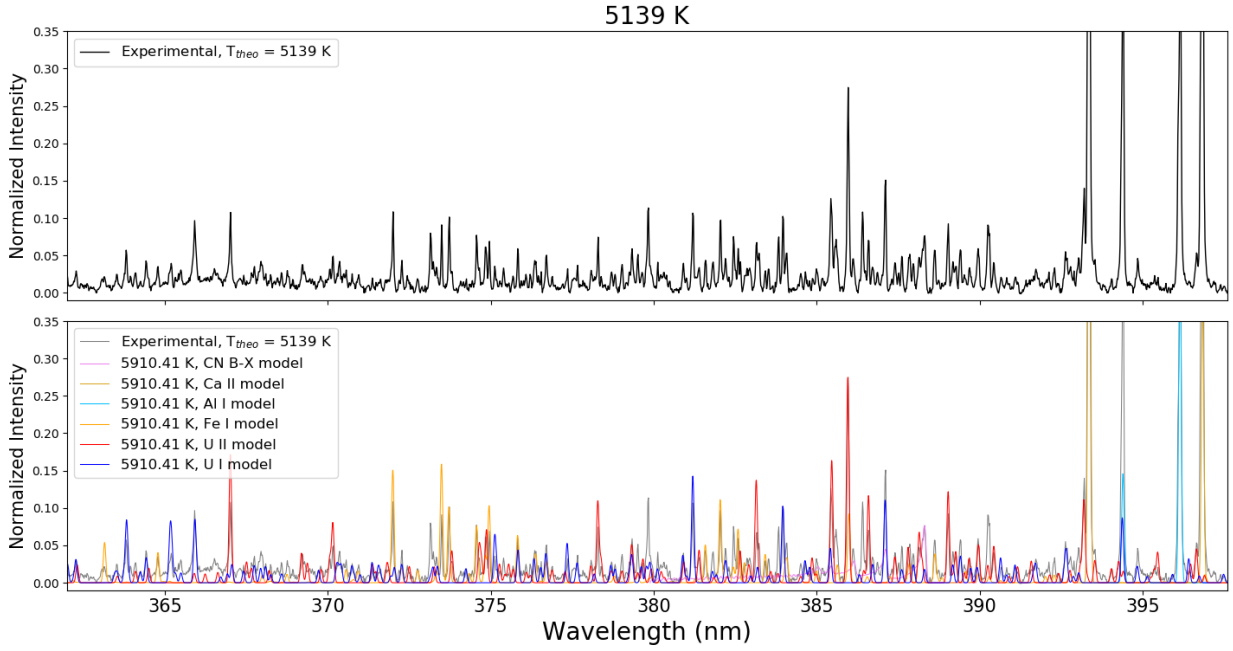
5139 K
Experimental, T_{theo} = 5139 K
Normalized Intensity
Experimental, T_{theo} = 5139 K
5910.41 K, CN B-X model
5910.41 K, Ca II model
5910.41 K, Al I model
5910.41 K, Fe I model
5910.41 K, U II model
5910.41 K, U I model
Normalized Intensity
Wavelength (nm)

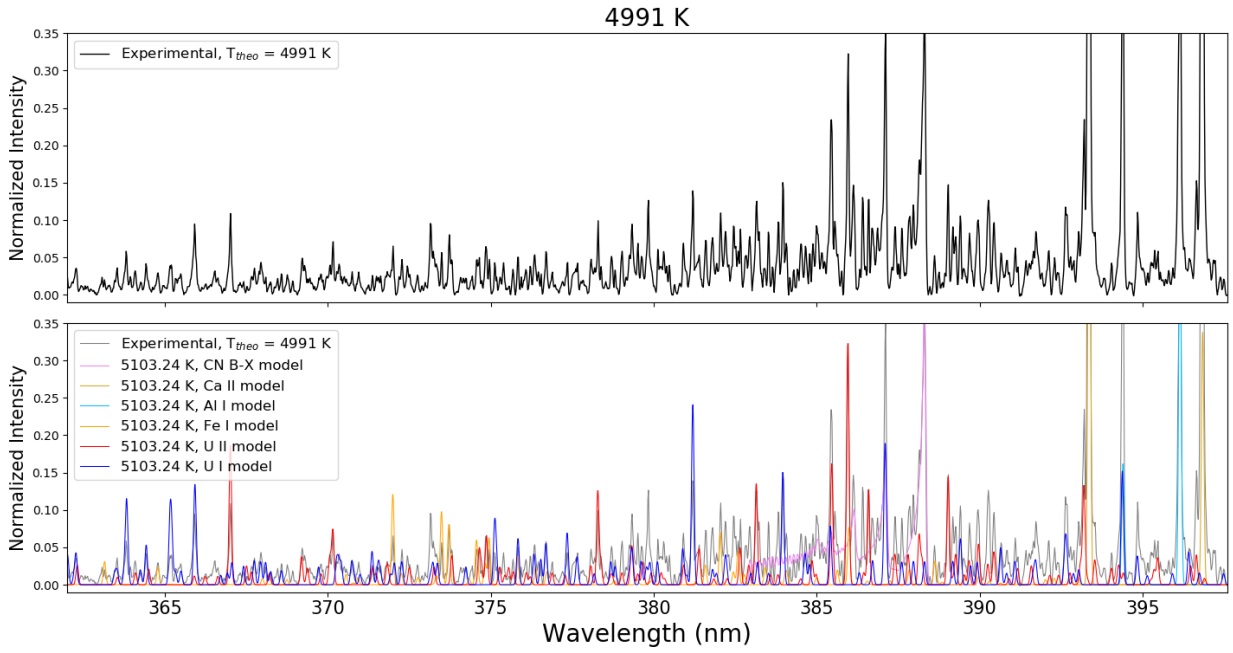
4991 K
Experimental, T_{theo} = 4991 K
Normalized Intensity
Experimental, T_{theo} = 4991 K
5103.24 K, CN B-X model
5103.24 K, Ca II model
5103.24 K, Al I model
5103.24 K, Fe I model
5103.24 K, U II model
5103.24 K, U I model
Normalized Intensity
Wavelength (nm)

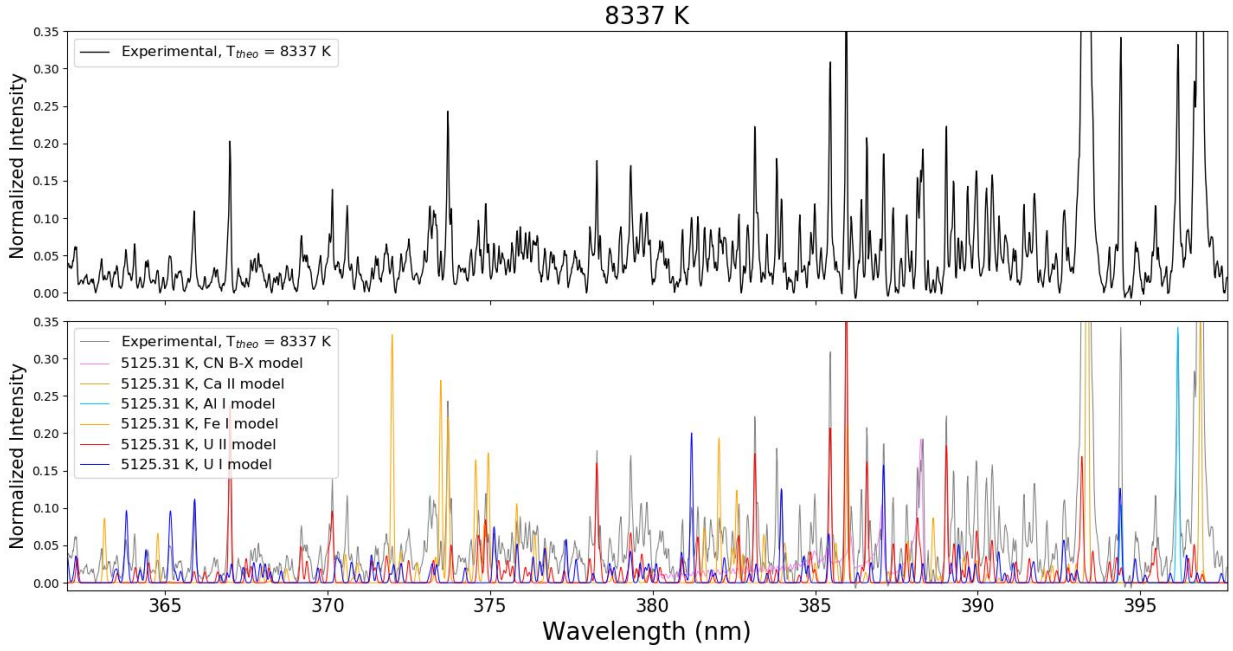
8337 K
Experimental, T_{theo} = 8337 K
Normalized Intensity
Experimental, T_{theo} = 8337 K
5125.31 K, CN B-X model
5125.31 K, Ca II model
5125.31 K, Al I model
5125.31 K, Fe I model
5125.31 K, U II model
5125.31 K, U I model
Normalized Intensity
Wavelength (nm)

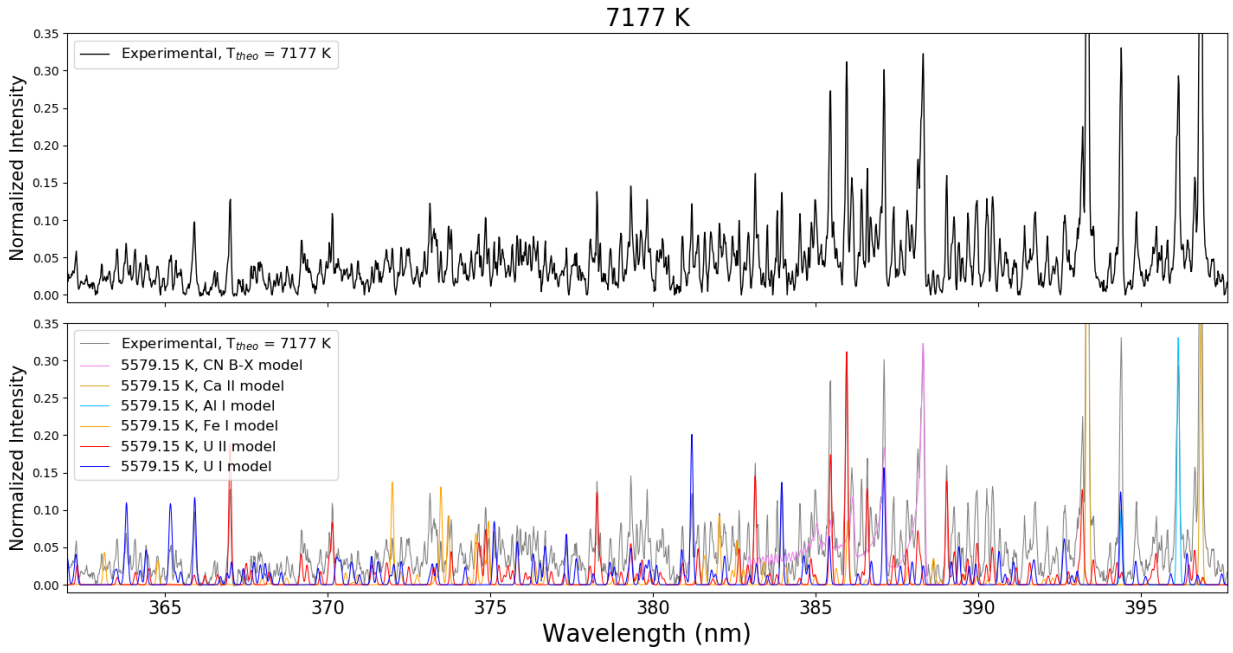
7177 K
Experimental, T_{theo} = 7177 K
Normalized Intensity
Experimental, T_{theo} = 7177 K
5579.15 K, CN B-X model
5579.15 K, Ca II model
5579.15 K, Al I model
5579.15 K, Fe I model
5579.15 K, U II model
5579.15 K, U I model
Normalized Intensity
Wavelength (nm)

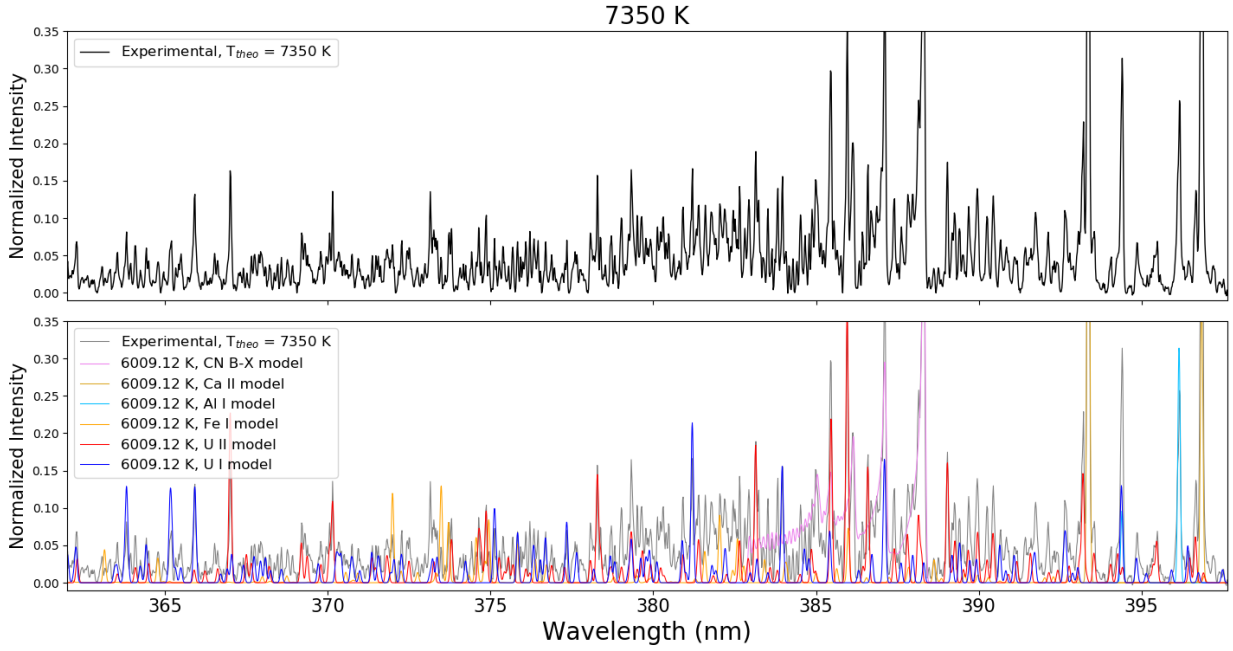
7350 K
Experimental, T_{theo} = 7350 K
Normalized Intensity
Experimental, T_{theo} = 7350 K
6009.12 K, CN B-X model
6009.12 K, Ca II model
6009.12 K, Al I model
6009.12 K, Fe I model
6009.12 K, U II model
6009.12 K, U I model
Normalized Intensity
Wavelength (nm)

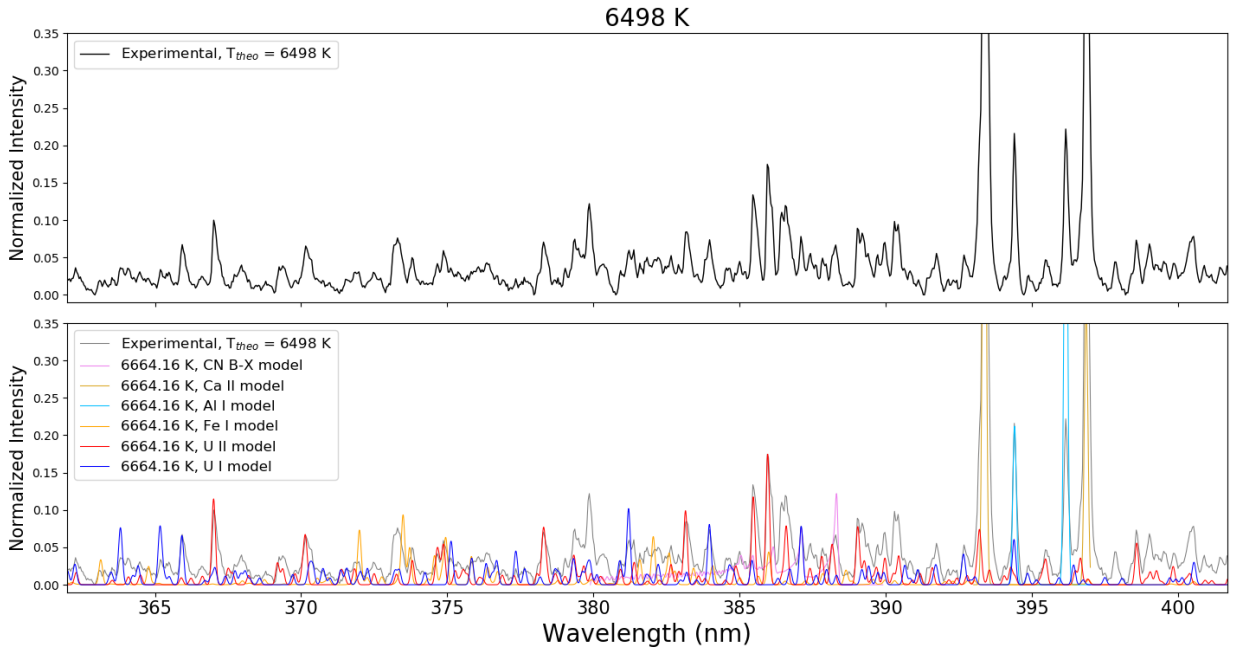
6498 K
Experimental, T_{theo} = 6498 K
Normalized Intensity
Experimental, T_{theo} = 6498 K
6664.16 K, CN B-X model
6664.16 K, Ca II model
6664.16 K, Al I model
6664.16 K, Fe I model
6664.16 K, U II model
6664.16 K, U I model
Normalized Intensity
Wavelength (nm)

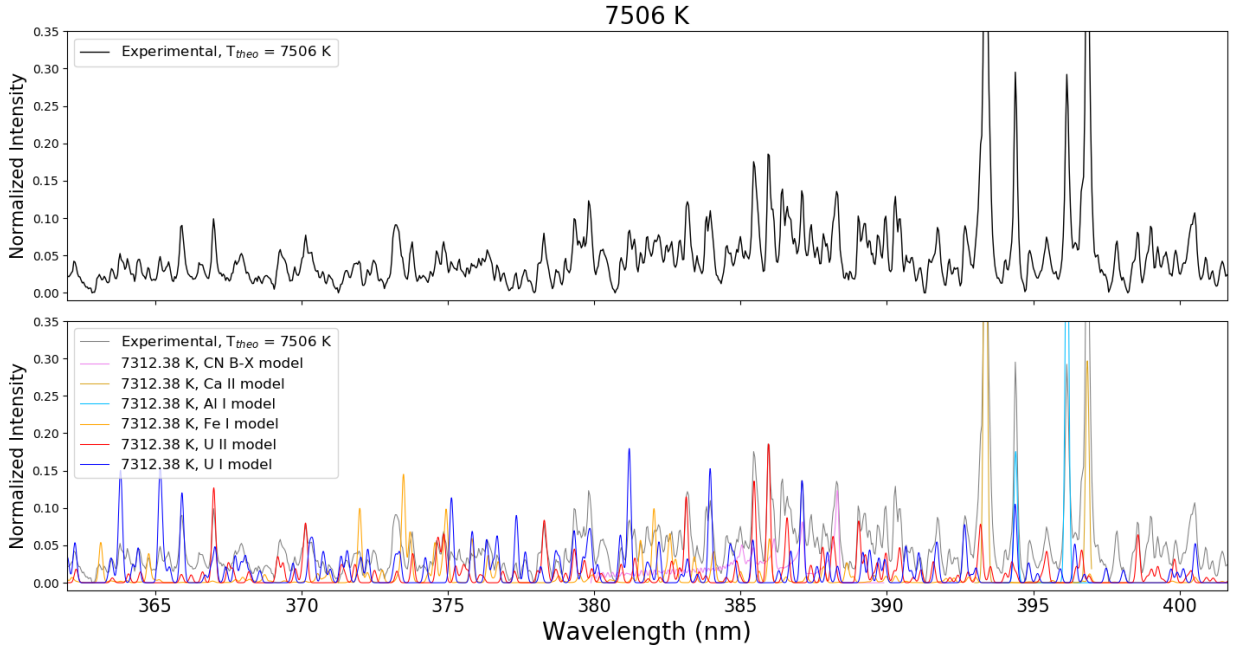
7506 K
Experimental, T_{theo} = 7506 K
Normalized Intensity
Experimental, T_{theo} = 7506 K
7312.38 K, CN B-X model
7312.38 K, Ca II model
7312.38 K, Al I model
7312.38 K, Fe I model
7312.38 K, U II model
7312.38 K, U I model
Normalized Intensity
Wavelength (nm)

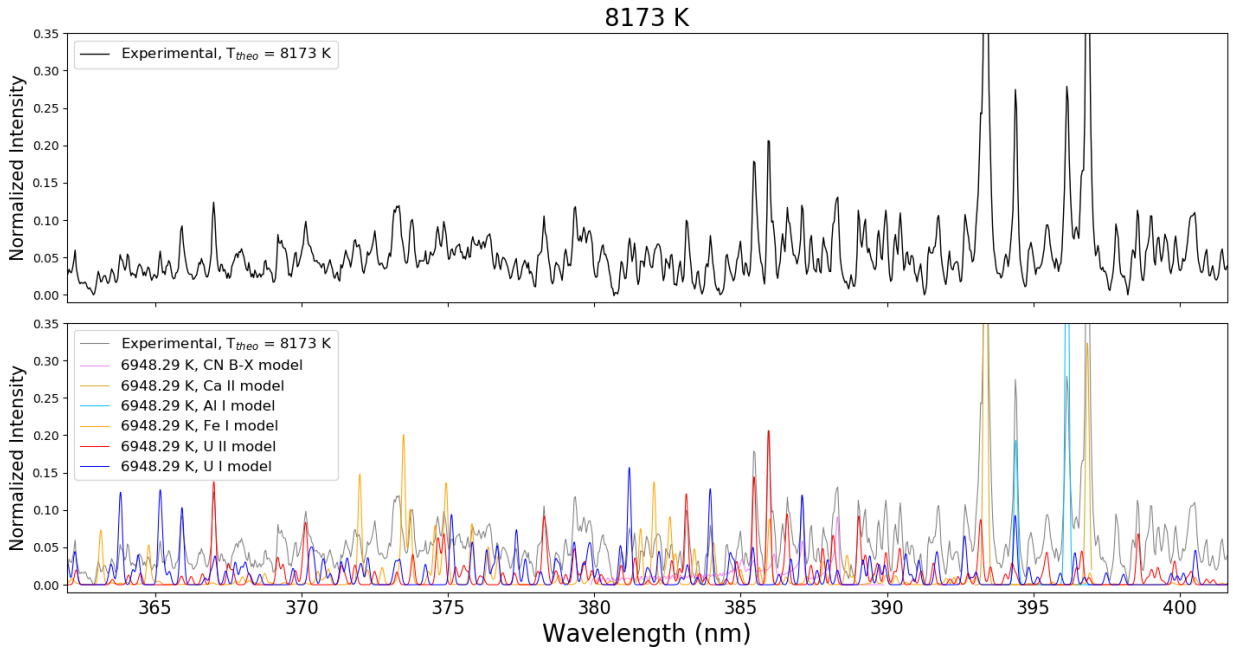
8173 K
Experimental, T_{theo} = 8173 K
Normalized Intensity
Experimental, T_{theo} = 8173 K
6948.29 K, CN B-X model
6948.29 K, Ca II model
6948.29 K, Al I model
6948.29 K, Fe I model
6948.29 K, U II model
6948.29 K, U I model
Normalized Intensity
Wavelength (nm)

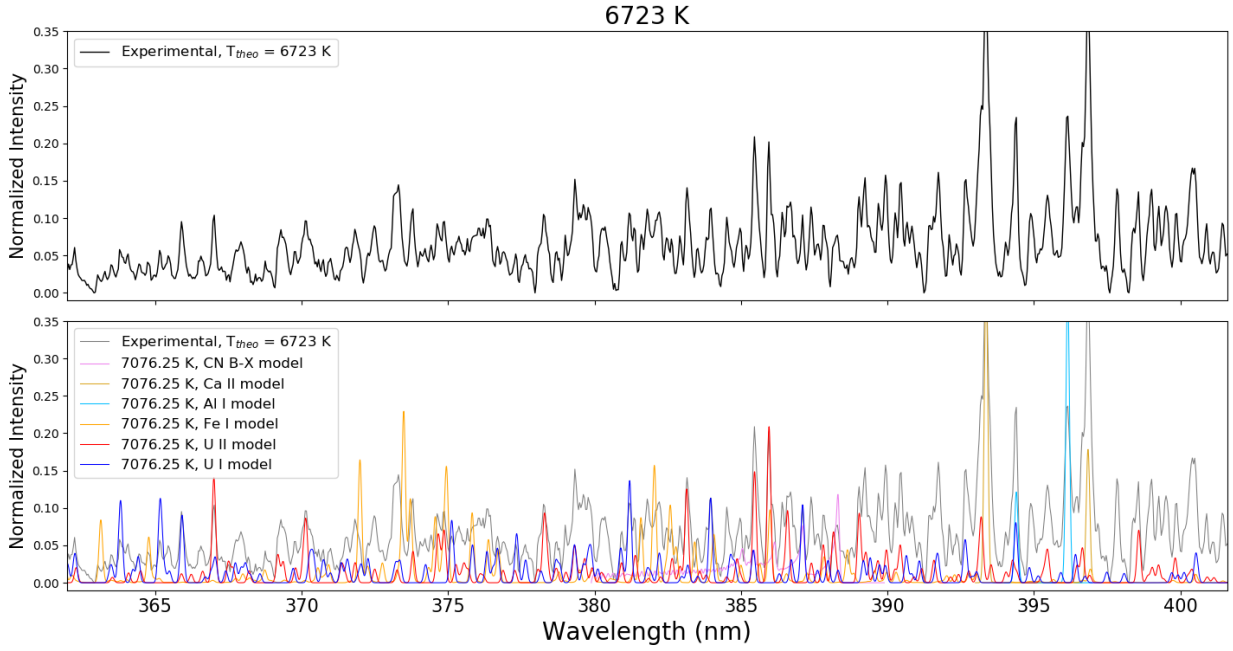
6723 K
Experimental, T_{theo} = 6723 K
Normalized Intensity
Experimental, T_{theo} = 6723 K
7076.25 K, CN B-X model
7076.25 K, Ca II model
7076.25 K, Al I model
7076.25 K, Fe I model
7076.25 K, U II model
7076.25 K, U I model
Normalized Intensity
Wavelength (nm)

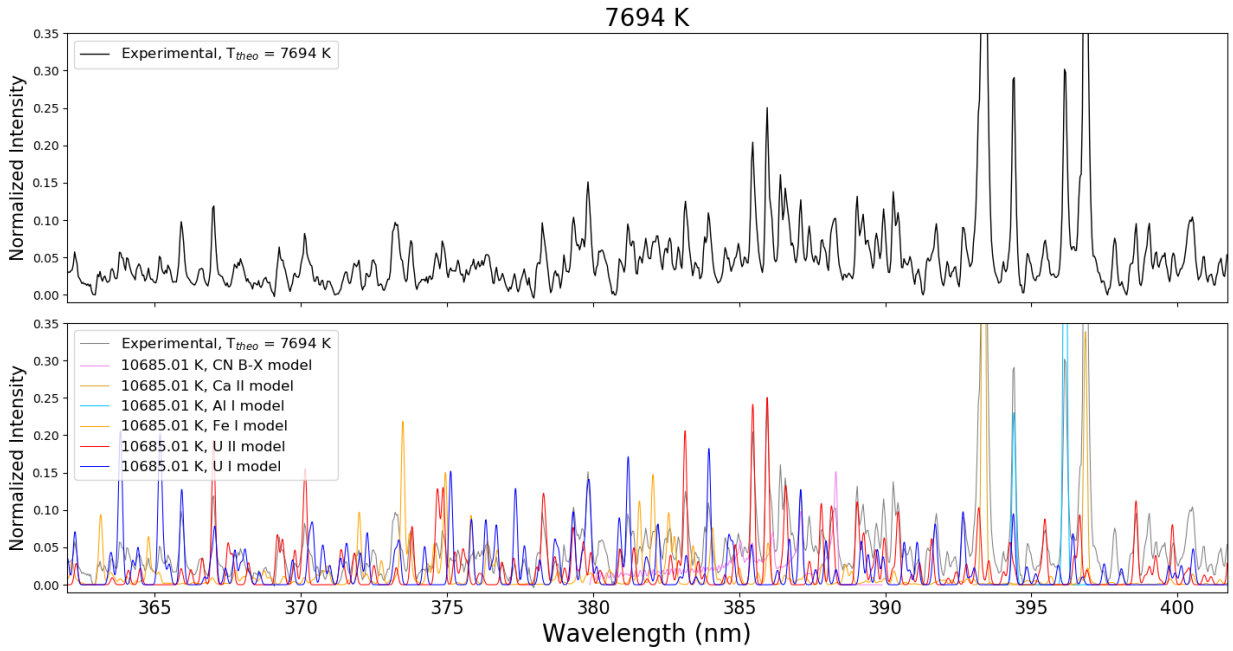
7694 K
Experimental, T$_{theo}$ = 7694 K
Normalized Intensity
Experimental, T$_{theo}$ = 7694 K
10685.01 K, CN B-X model
10685.01 K, Ca II model
10685.01 K, Al I model
10685.01 K, Fe I model
10685.01 K, U II model
10685.01 K, U I model
Normalized Intensity
Wavelength (nm)

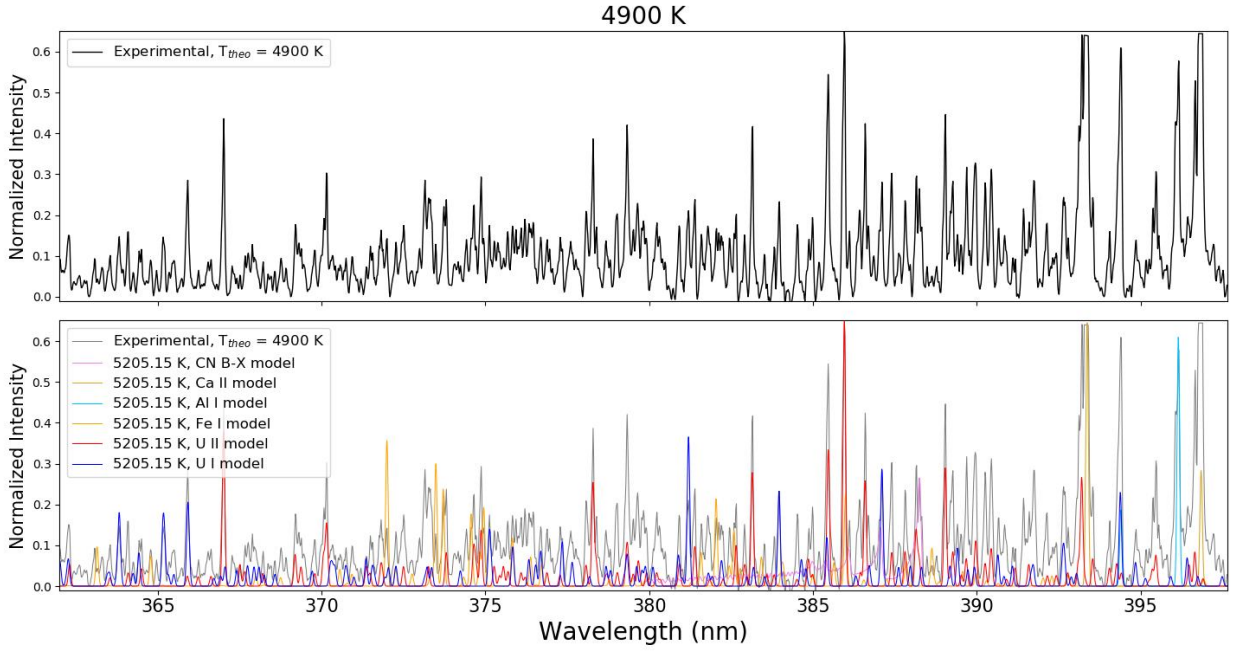
4900 K
Experimental, T$_{theo}$ = 4900 K
Normalized Intensity
Experimental, T$_{theo}$ = 4900 K
5205.15 K, CN B-X model
5205.15 K, Ca II model
5205.15 K, Al I model
5205.15 K, Fe I model
5205.15 K, U II model
5205.15 K, U I model
Normalized Intensity
Wavelength (nm)

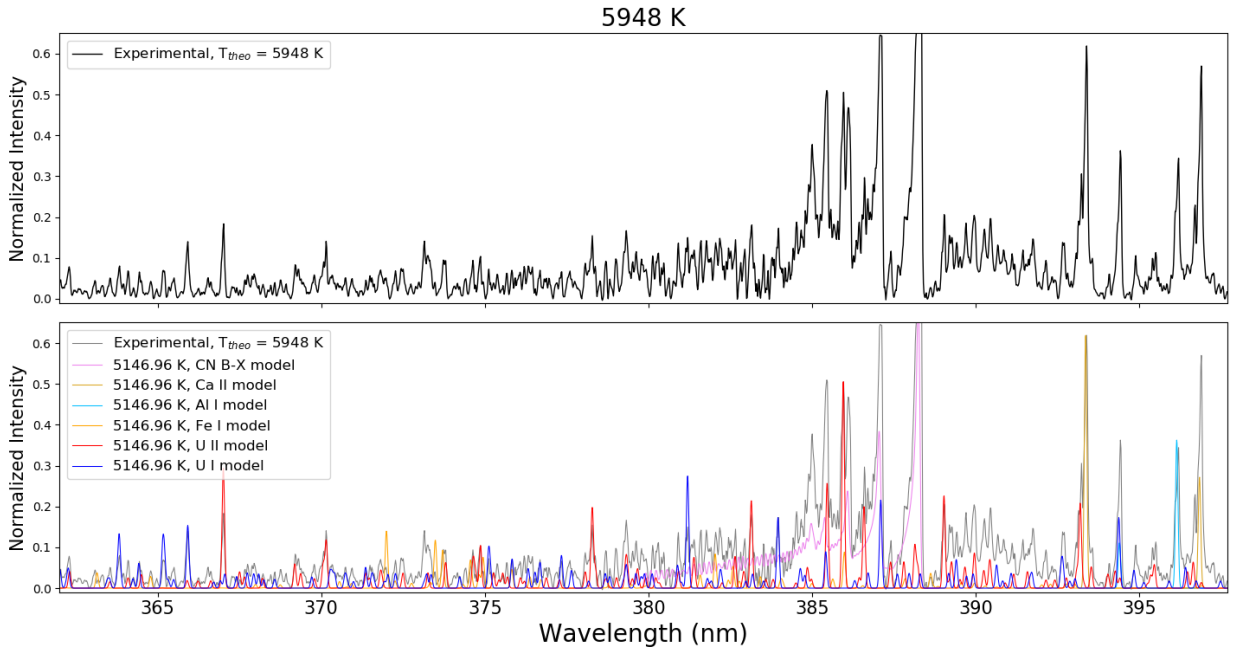
5948 K
Experimental, T_{theo} = 5948 K
Normalized Intensity
Experimental, T_{theo} = 5948 K
5146.96 K, CN B-X model
5146.96 K, Ca II model
5146.96 K, Al I model
5146.96 K, Fe I model
5146.96 K, U II model
5146.96 K, U I model
Normalized Intensity
Wavelength (nm)

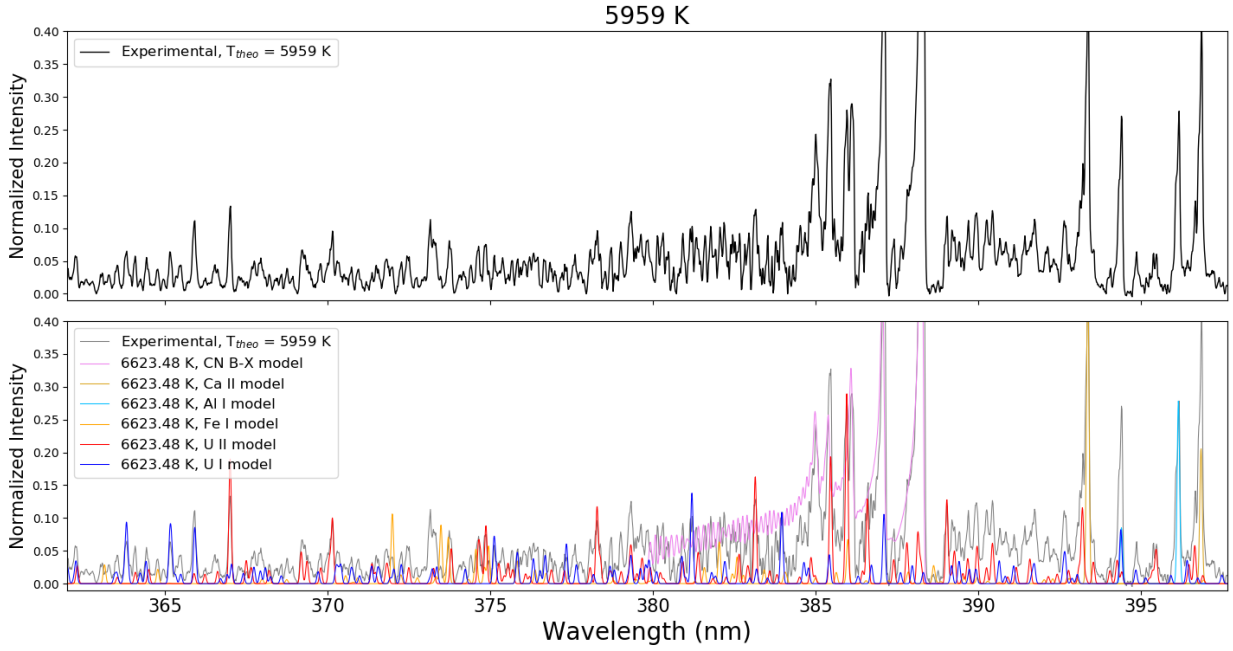
5959 K
Experimental, T_{theo} = 5959 K
Normalized Intensity
Experimental, T_{theo} = 5959 K
6623.48 K, CN B-X model
6623.48 K, Ca II model
6623.48 K, Al I model
6623.48 K, Fe I model
6623.48 K, U II model
6623.48 K, U I model
Normalized Intensity
Wavelength (nm)

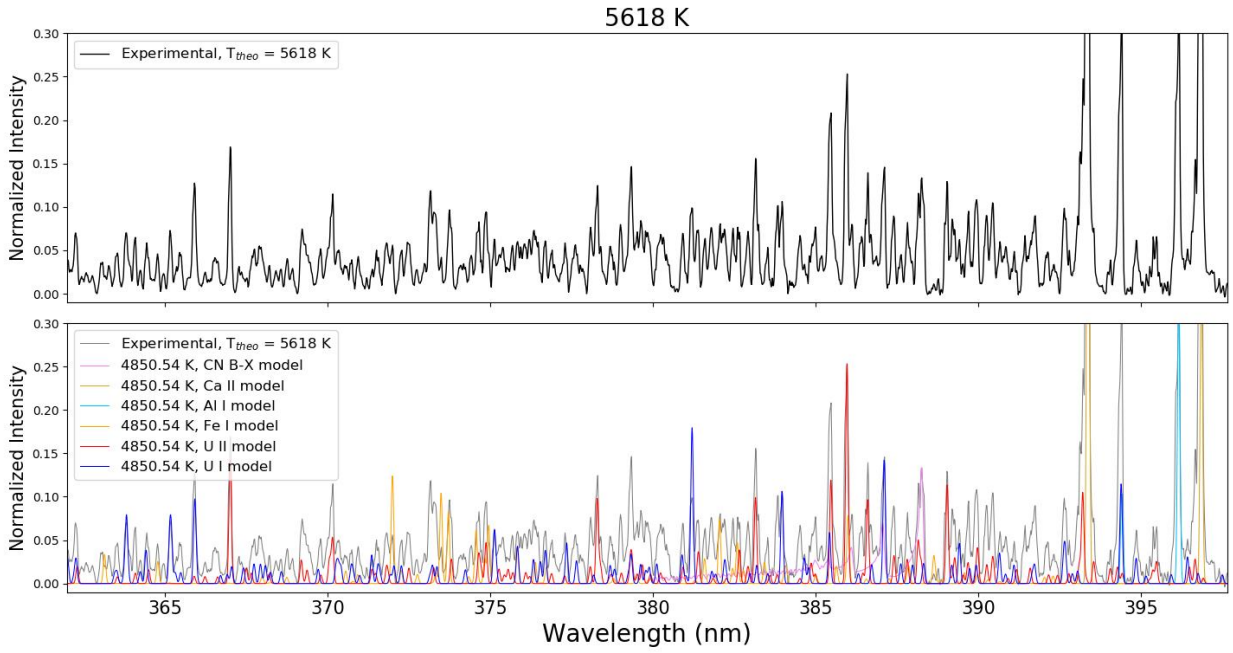
5618 K
Experimental, T_{theo} = 5618 K
Normalized Intensity
Experimental, T_{theo} = 5618 K
4850.54 K, CN B-X model
4850.54 K, Ca II model
4850.54 K, Al I model
4850.54 K, Fe I model
4850.54 K, U II model
4850.54 K, U I model
Normalized Intensity
Wavelength (nm)

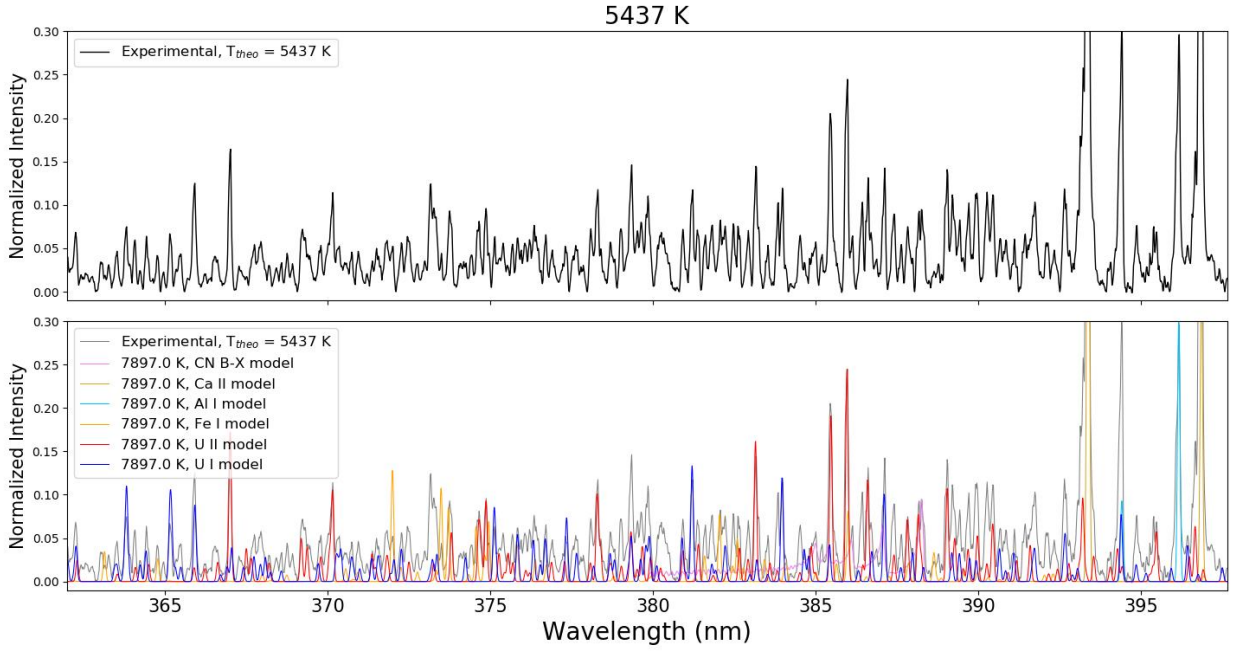
5437 K
Experimental, T_{theo} = 5437 K
Normalized Intensity
Experimental, T_{theo} = 5437 K
7897.0 K, CN B-X model
7897.0 K, Ca II model
7897.0 K, Al I model
7897.0 K, Fe I model
7897.0 K, U II model
7897.0 K, U I model
Normalized Intensity
Wavelength (nm)

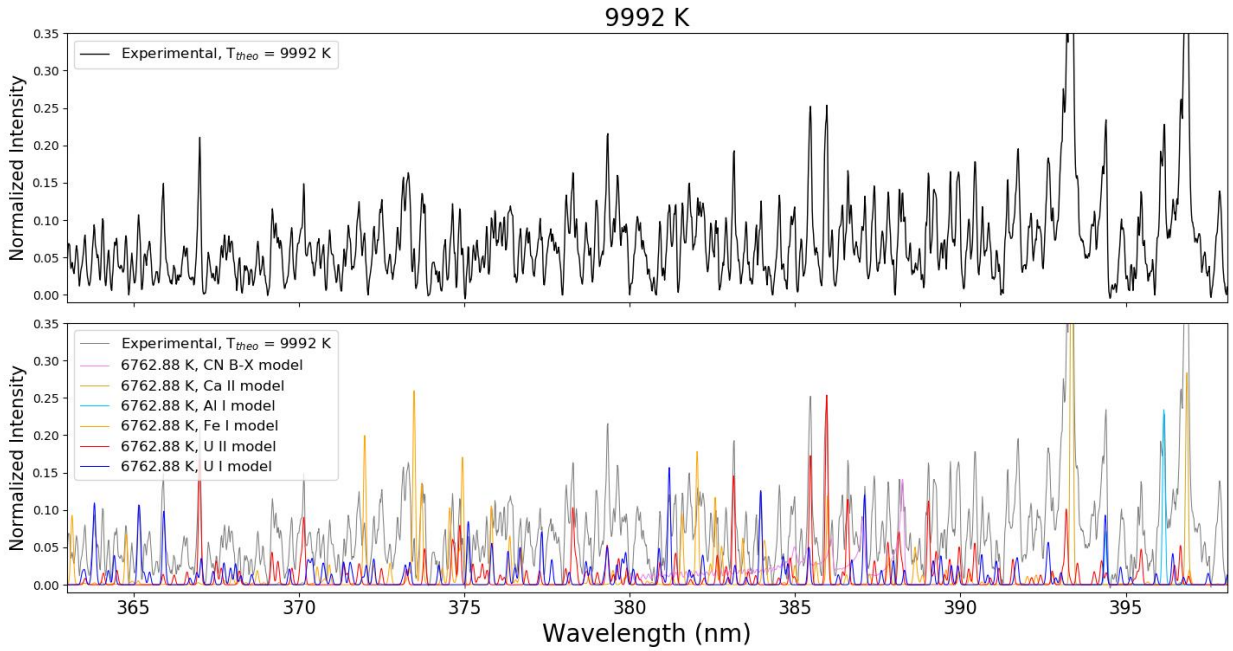
9992 K
Experimental, T_{theo} = 9992 K
Normalized Intensity
Experimental, T_{theo} = 9992 K
6762.88 K, CN B-X model
6762.88 K, Ca II model
6762.88 K, Al I model
6762.88 K, Fe I model
6762.88 K, U II model
6762.88 K, U I model
Normalized Intensity
Wavelength (nm)

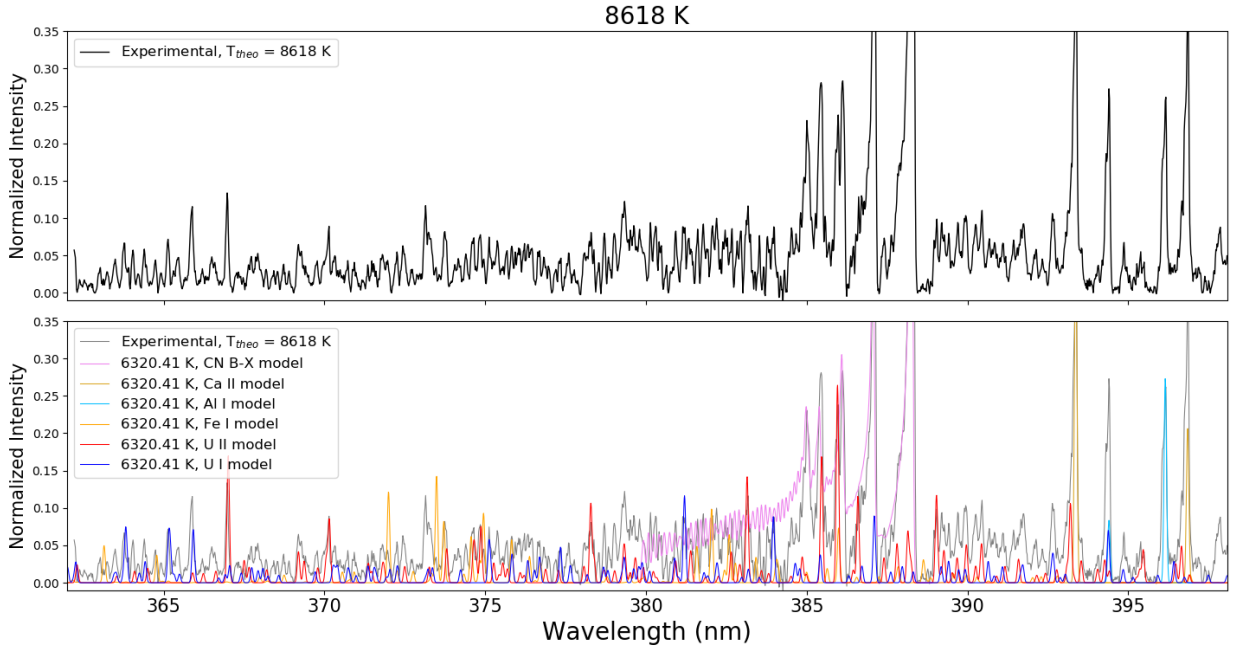
8618 K
Experimental, T_{theo} = 8618 K
Normalized Intensity
Experimental, T_{theo} = 8618 K
6320.41 K, CN B-X model
6320.41 K, Ca II model
6320.41 K, Al I model
6320.41 K, Fe I model
6320.41 K, U II model
6320.41 K, U I model
Normalized Intensity
Wavelength (nm)

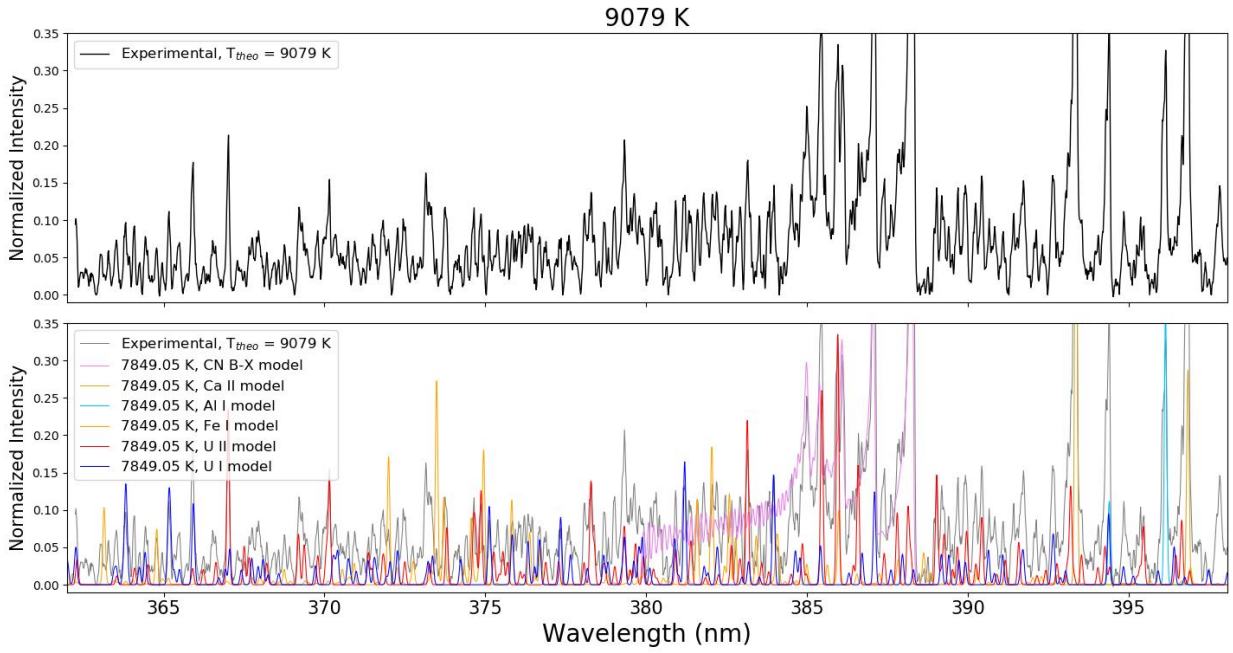
9079 K
Experimental, T_{theo} = 9079 K
Normalized Intensity
Experimental, T_{theo} = 9079 K
7849.05 K, CN B-X model
7849.05 K, Ca II model
7849.05 K, Al I model
7849.05 K, Fe I model
7849.05 K, U II model
7849.05 K, U I model
Normalized Intensity
Wavelength (nm)

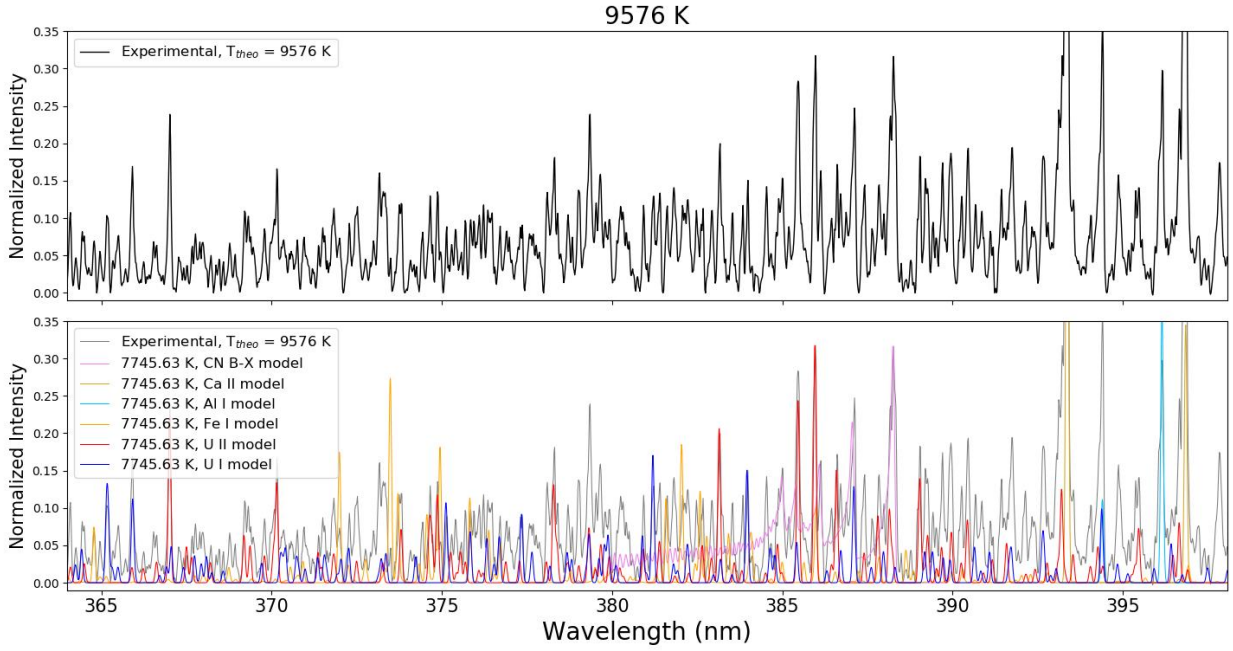
9576 K
Experimental, T_{theo} = 9576 K
Normalized Intensity
Experimental, T_{theo} = 9576 K
7745.63 K, CN B-X model
7745.63 K, Ca II model
7745.63 K, Al I model
7745.63 K, Fe I model
7745.63 K, U II model
7745.63 K, U I model
Normalized Intensity
Wavelength (nm)

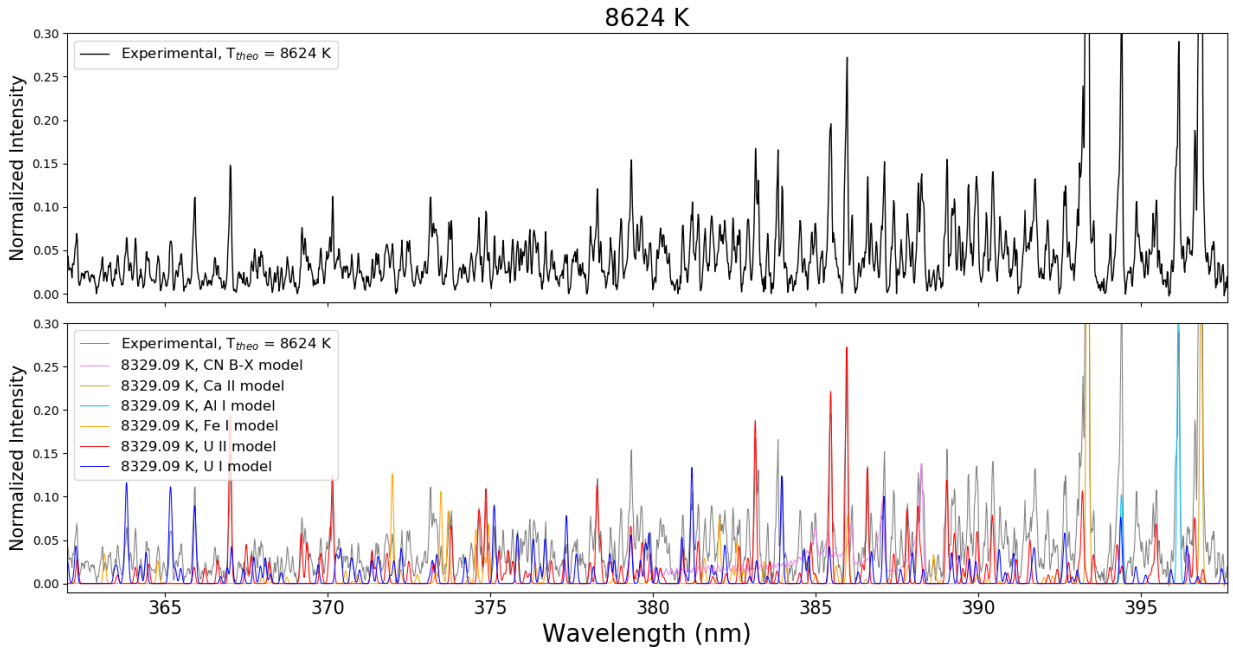
8624 K
Experimental, T_{theo} = 8624 K
Normalized Intensity
0.30
0.25
0.20
0.15
0.10
0.05
0.00
Experimental, T_{theo} = 8624 K
8329.09 K, CN B-X model
8329.09 K, Ca II model
8329.09 K, Al I model
8329.09 K, Fe I model
8329.09 K, U II model
8329.09 K, U I model
365
370
375
380
385
390
395
Wavelength (nm)

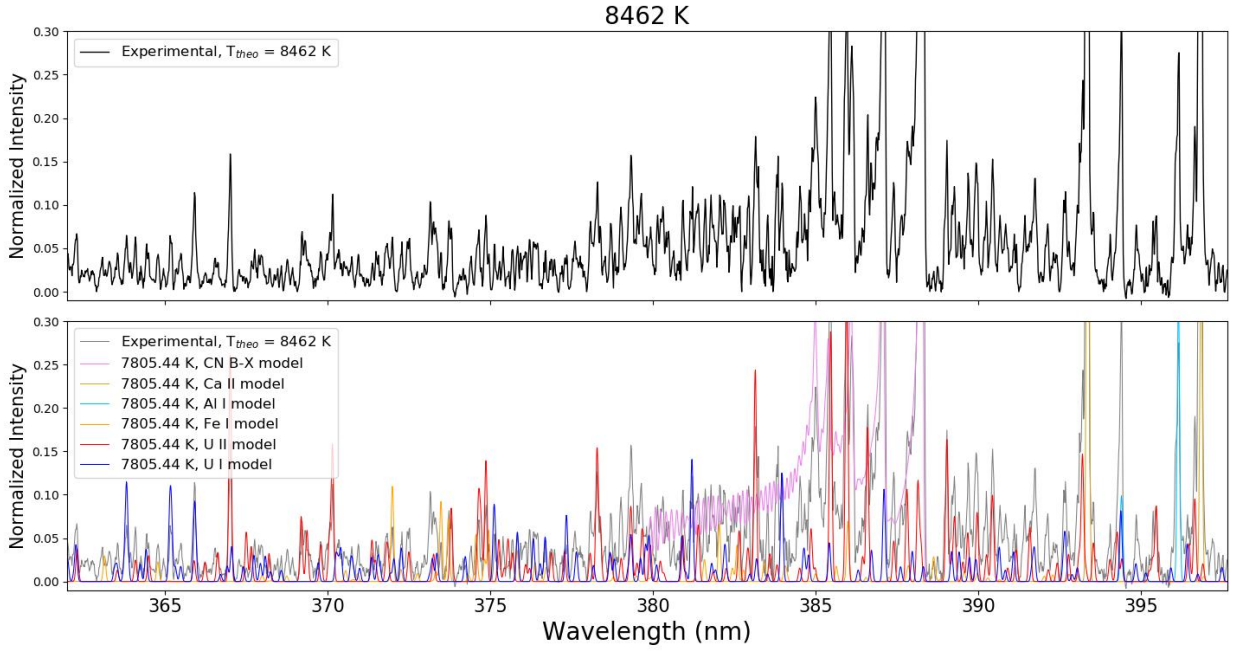
8462 K
Experimental, T_{theo} = 8462 K
Normalized Intensity
0.30
0.25
0.20
0.15
0.10
0.05
0.00
Experimental, T_{theo} = 8462 K
7805.44 K, CN B-X model
7805.44 K, Ca II model
7805.44 K, Al I model
7805.44 K, Fe I model
7805.44 K, U II model
7805.44 K, U I model
365
370
375
380
385
390
395
Wavelength (nm)

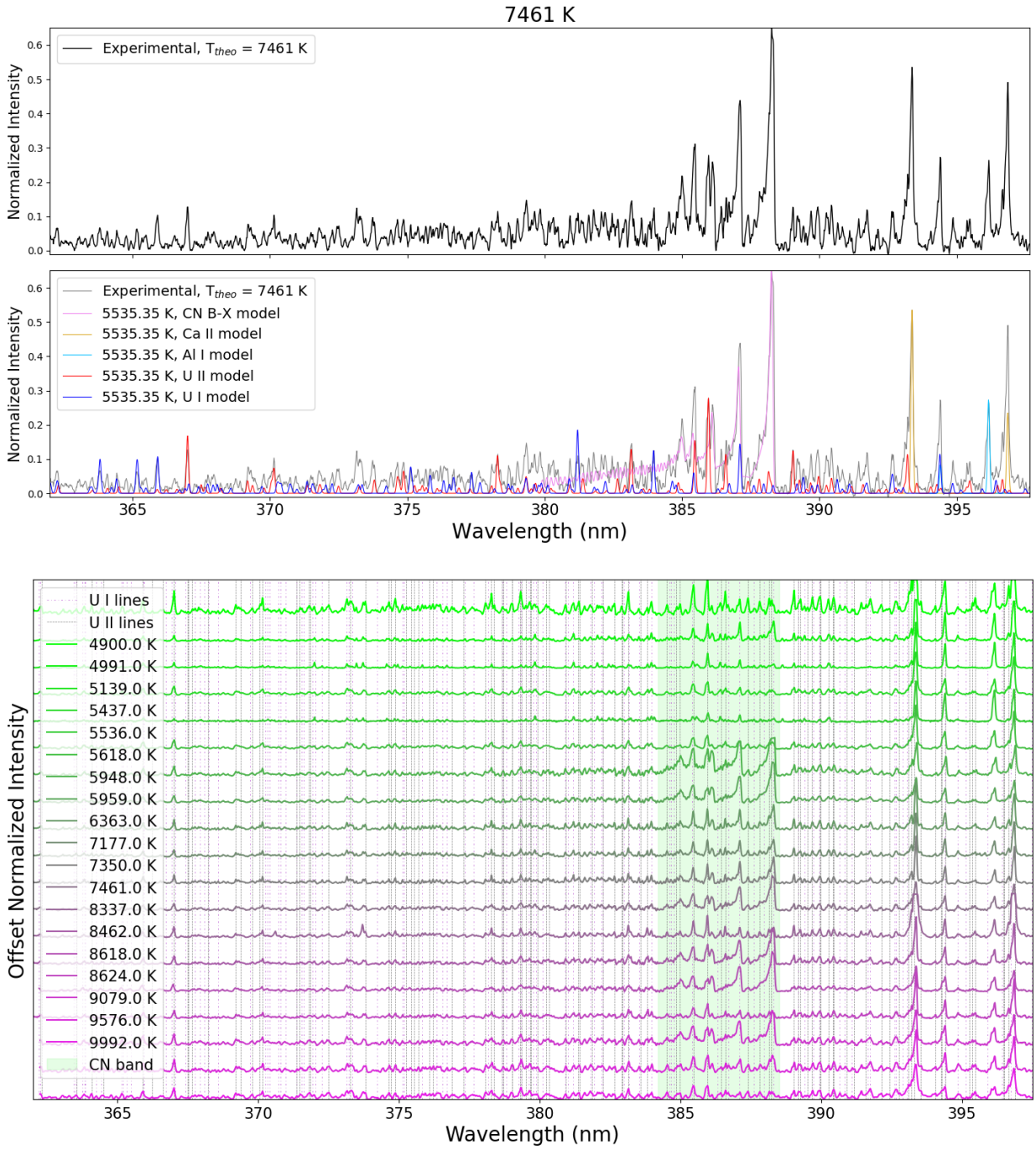
7461 K
Experimental, T$_{theo}$ = 7461 K
Normalized Intensity
Experimental, T$_{theo}$ = 7461 K
5535.35 K, CN B-X model
5535.35 K, Ca II model
5535.35 K, Al I model
5535.35 K, U II model
5535.35 K, U I model
Normalized Intensity
Wavelength (nm)
U I lines
U II lines
4900.0 K
4991.0 K
5139.0 K
5437.0 K
5536.0 K
5618.0 K
5948.0 K
5959.0 K
6363.0 K
7177.0 K
7350.0 K
7461.0 K
8337.0 K
8462.0 K
8618.0 K
8624.0 K
9079.0 K
9576.0 K
9992.0 K
CN band
Offset Normalized Intensity
Wavelength (nm)

A.2.4. Near-infrared spectra from shock tube experiments with model overlays

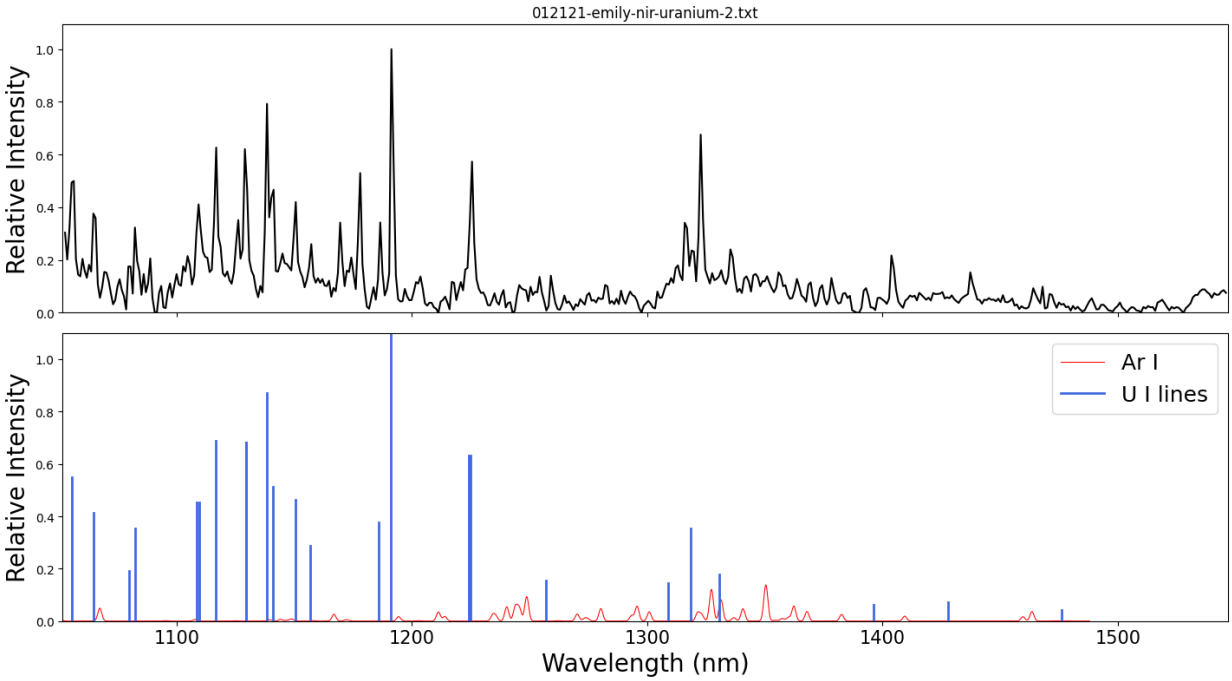

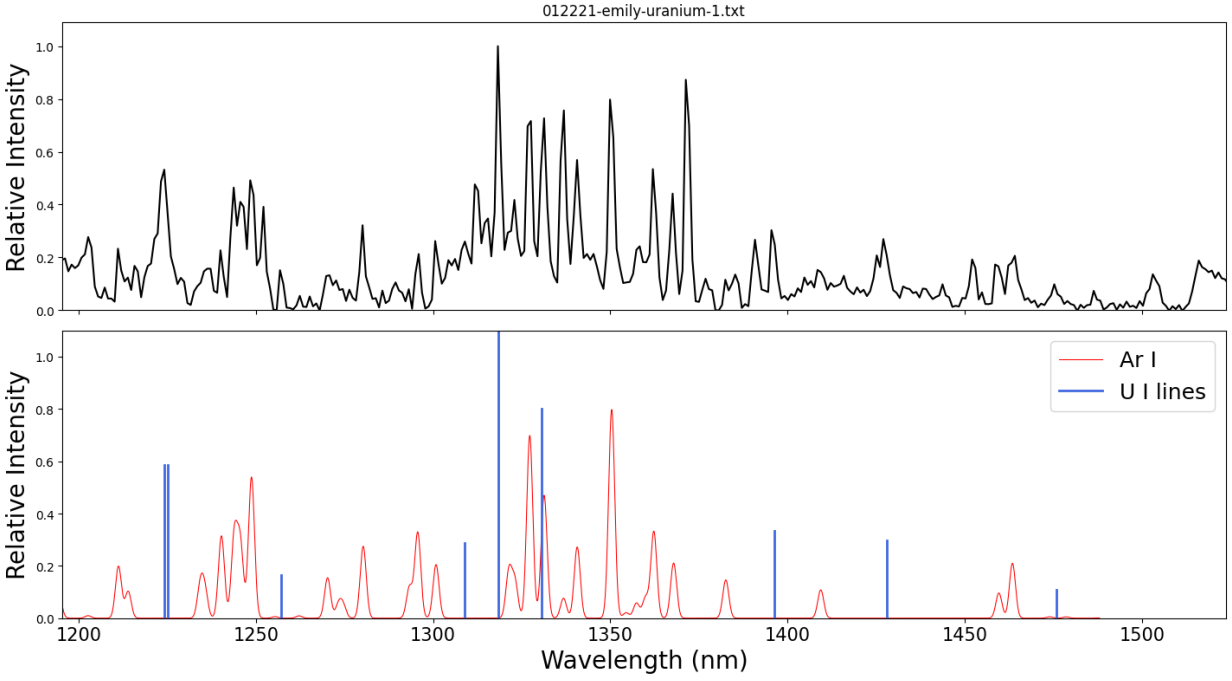

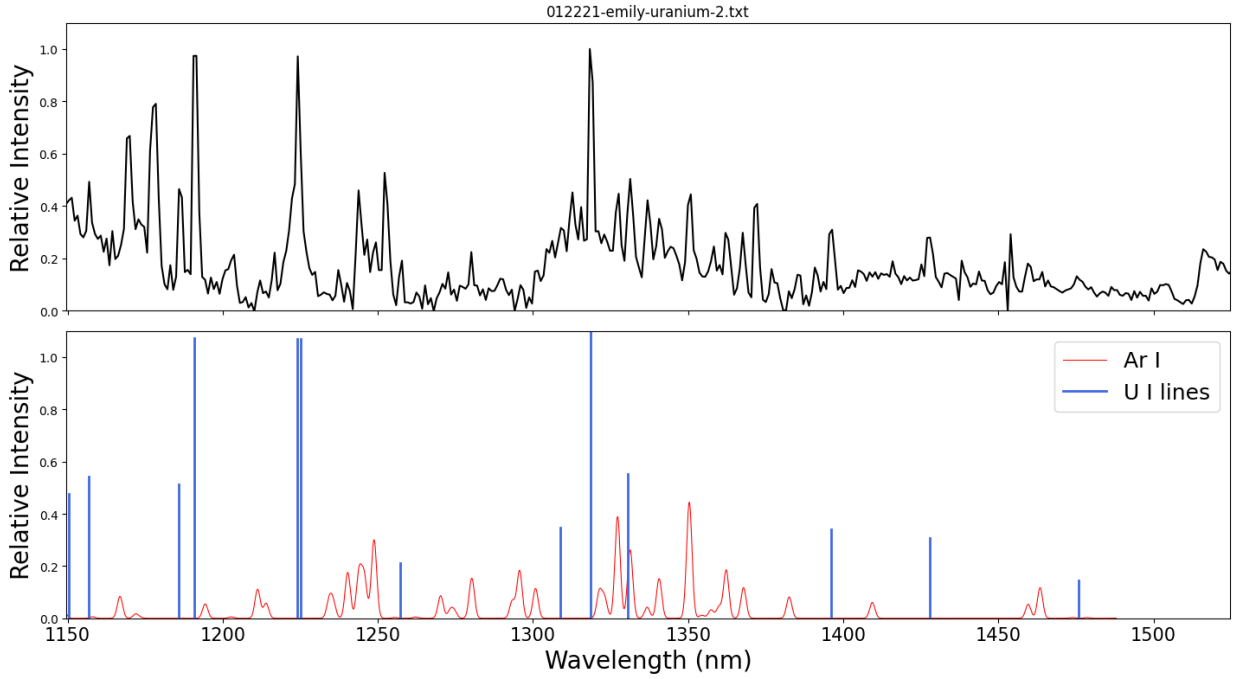
012221-emily-uranium-2.txt
Relative Intensity
Relative Intensity
Ar I
U I lines
Wavelength (nm)

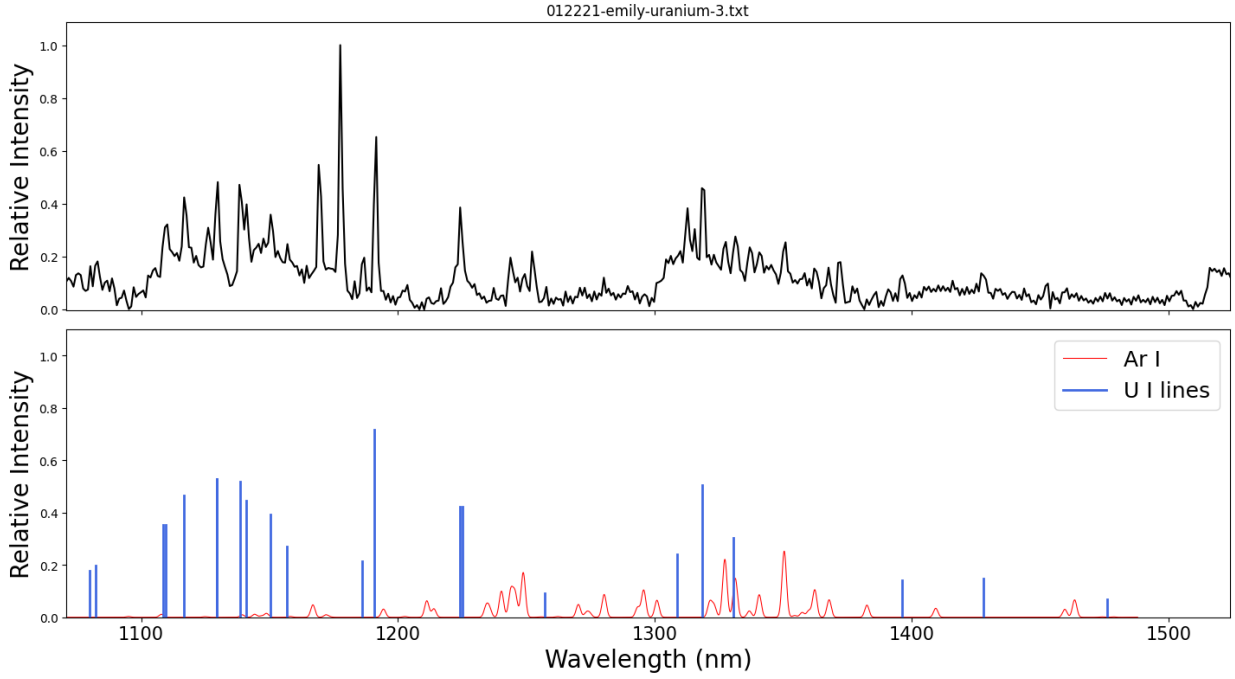
012221-emily-uranium-3.txt
Relative Intensity
Relative Intensity
Ar I
U I lines
Wavelength (nm)

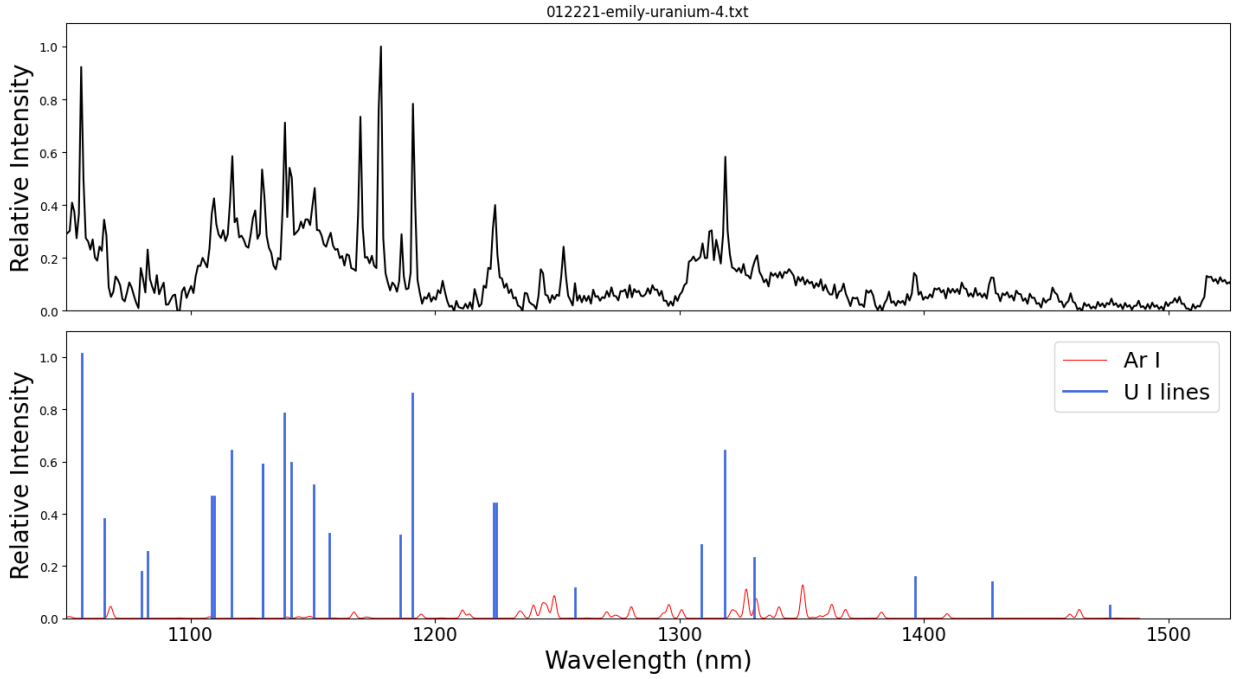
012221-emily-uranium-4.txt
Relative Intensity
Relative Intensity
Ar I
U I lines
1100
1200
1300
1400
1500
Wavelength (nm)

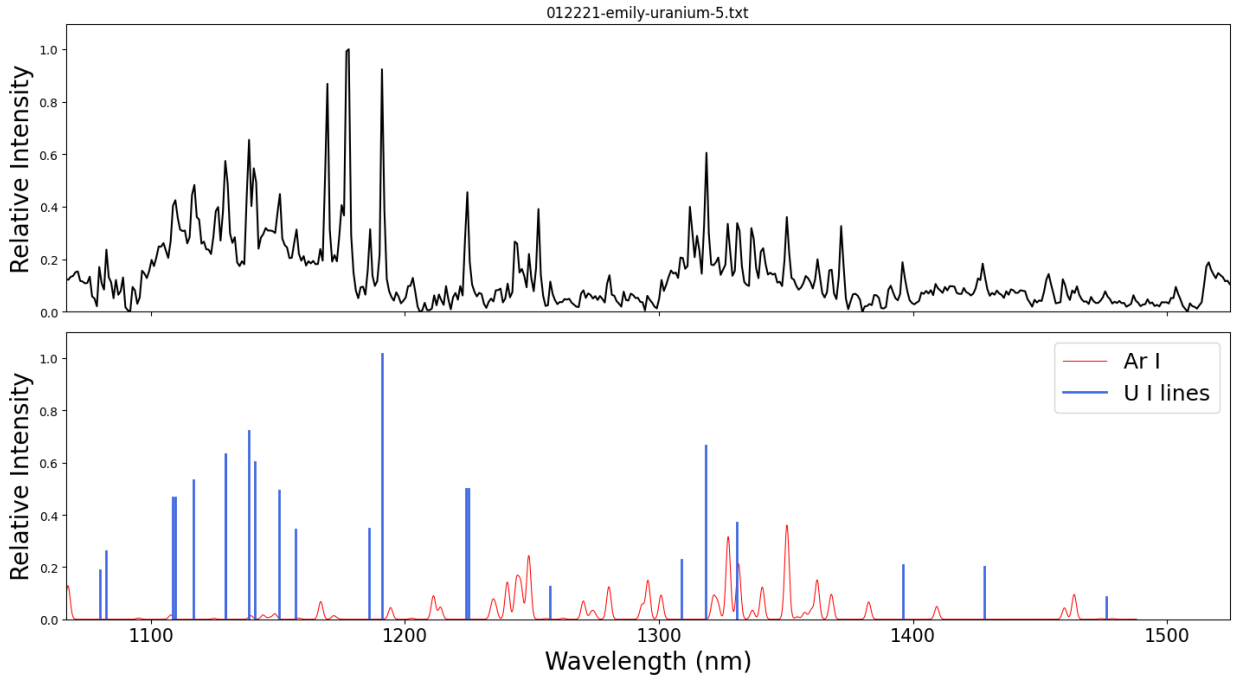
012221-emily-uranium-5.txt
Relative Intensity
Relative Intensity
Ar I
U I lines
1100
1200
1300
1400
1500
Wavelength (nm)

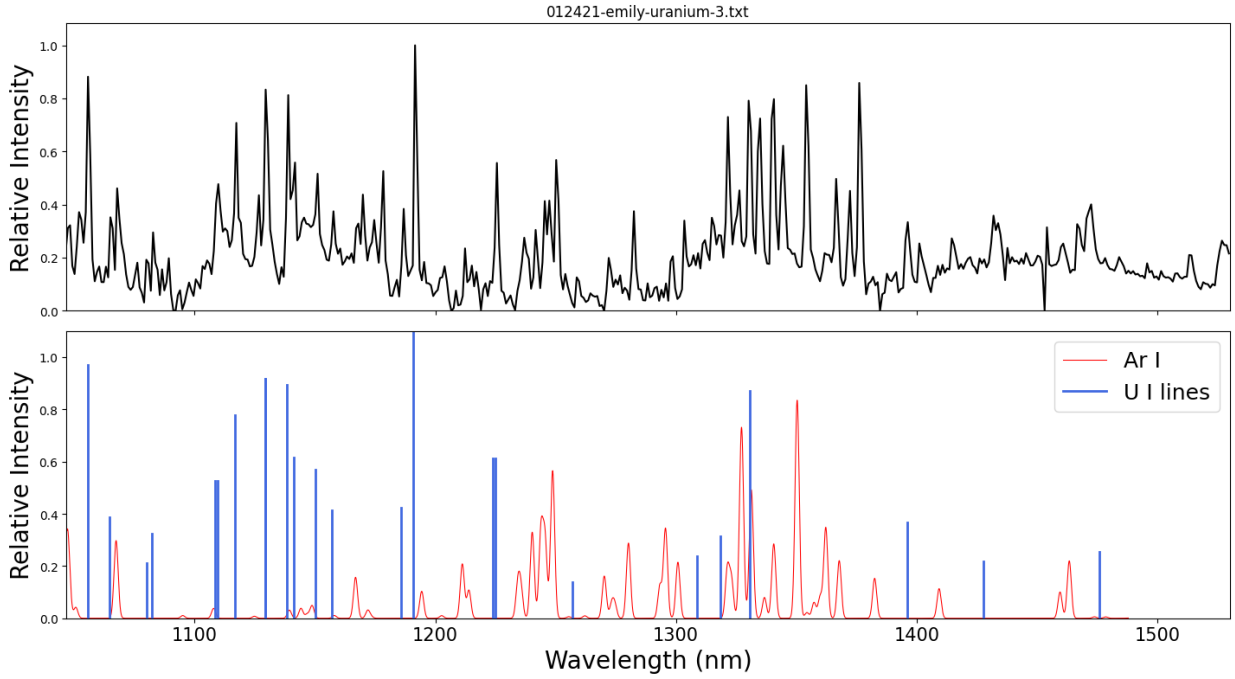
012421-emily-uranium-3.txt
Relative Intensity
Relative Intensity
Ar I
U I lines
1100
1200
1300
1400
1500
Wavelength (nm)

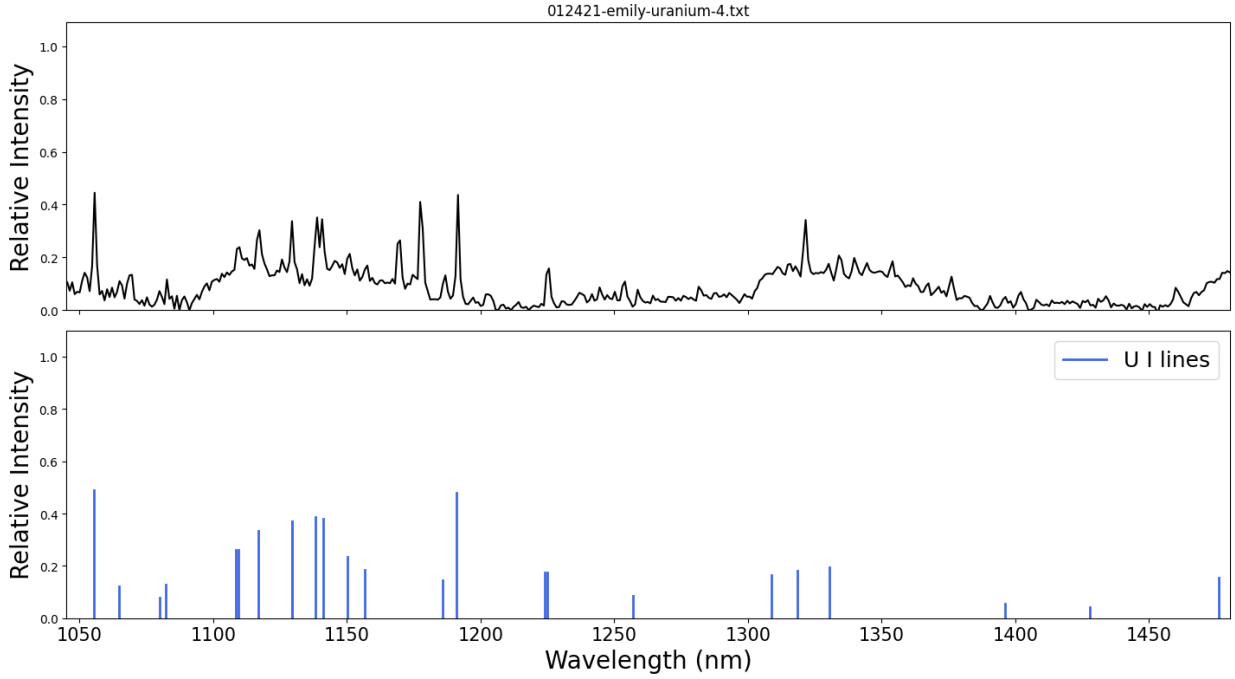
012421-emily-uranium-4.txt
Relative Intensity
Relative Intensity
U I lines
1050
1100
1150
1200
1250
1300
1350
1400
1450
Wavelength (nm)

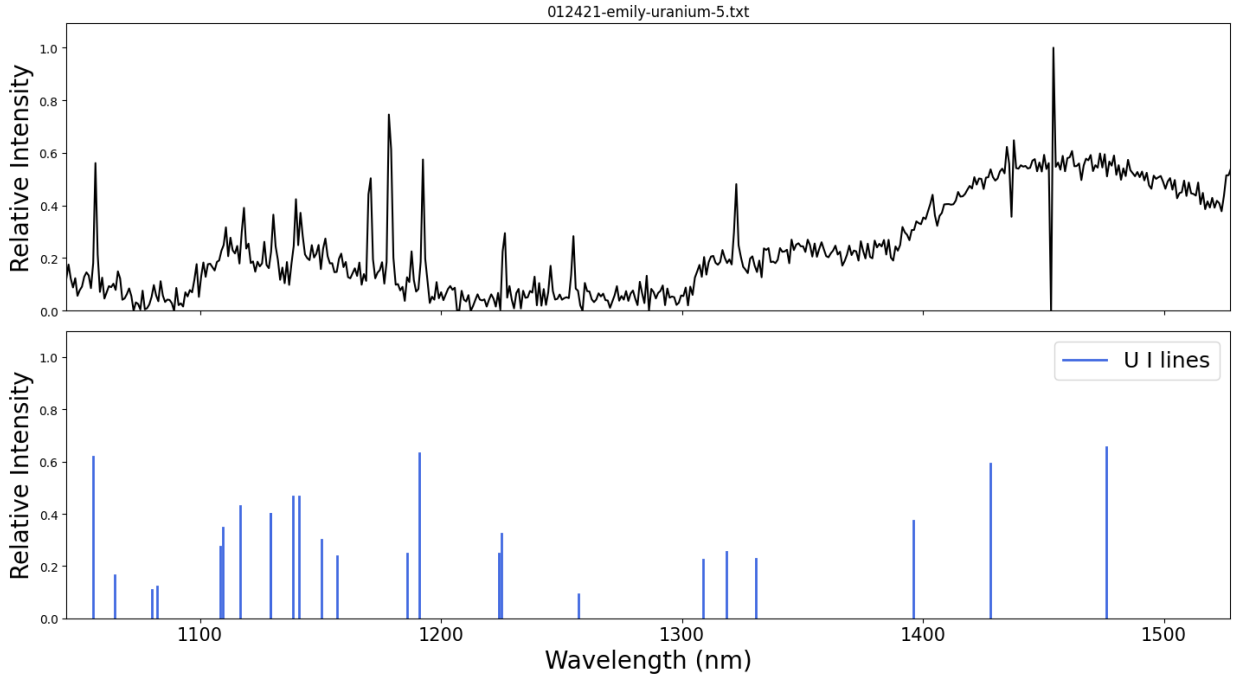
012421-emily-uranium-5.txt
Relative Intensity
U I lines
Relative Intensity
Wavelength (nm)

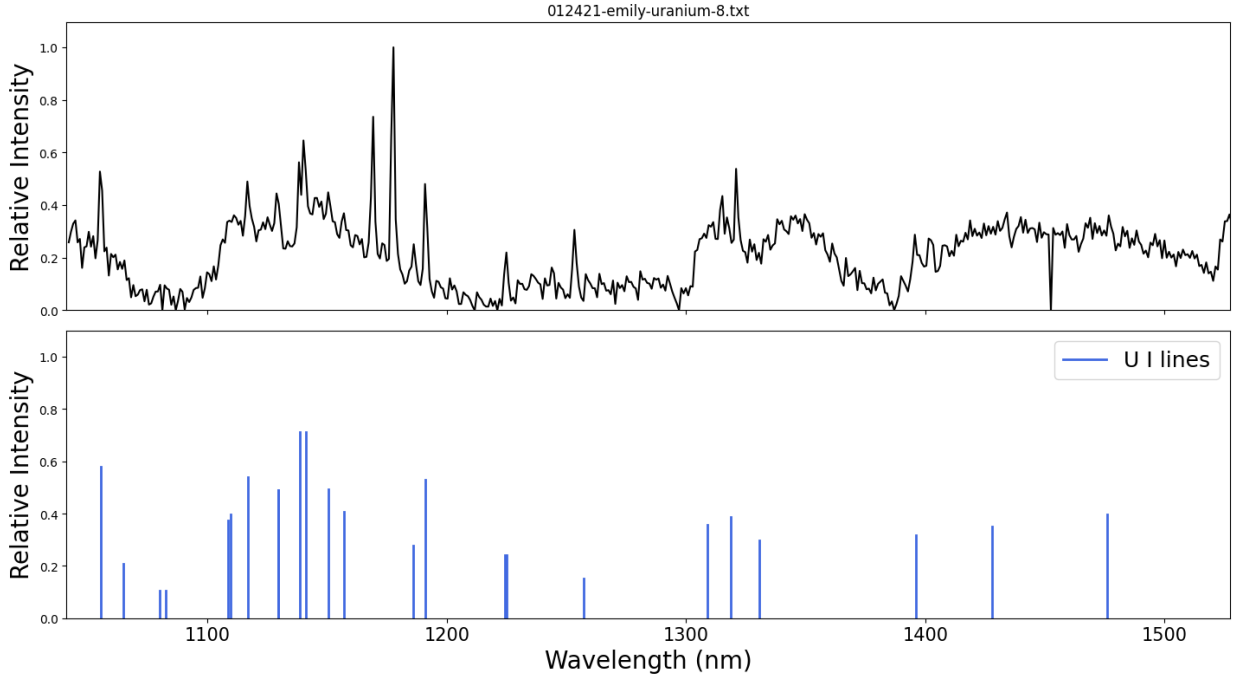
012421-emily-uranium-8.txt
Relative Intensity
U I lines
Relative Intensity
Wavelength (nm)

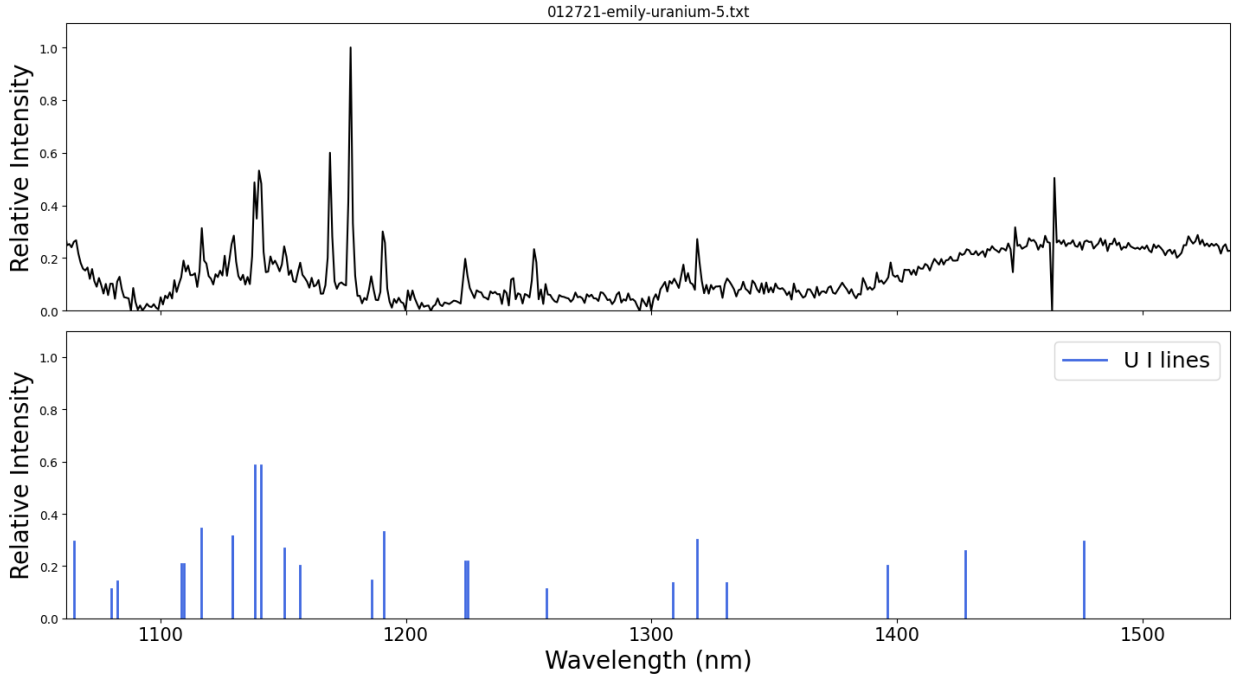
012721-emily-uranium-5.txt
Relative Intensity
U I lines
Wavelength (nm)

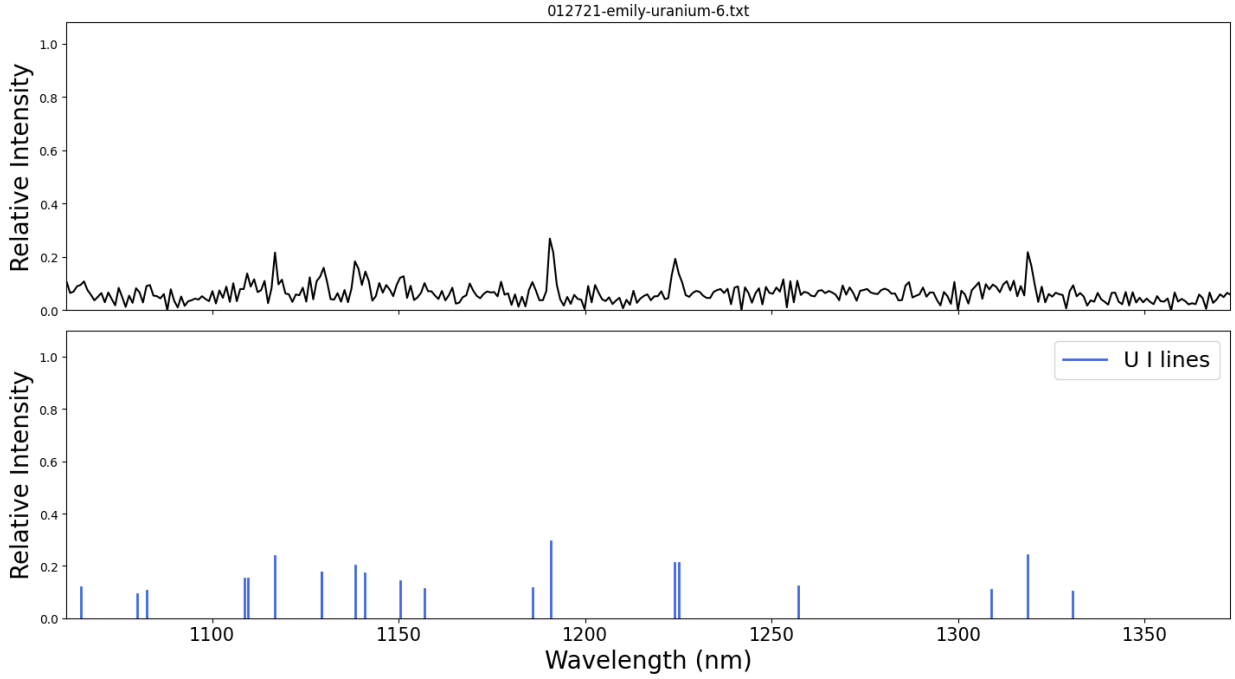
012721-emily-uranium-6.txt
Relative Intensity
U I lines
Wavelength (nm)

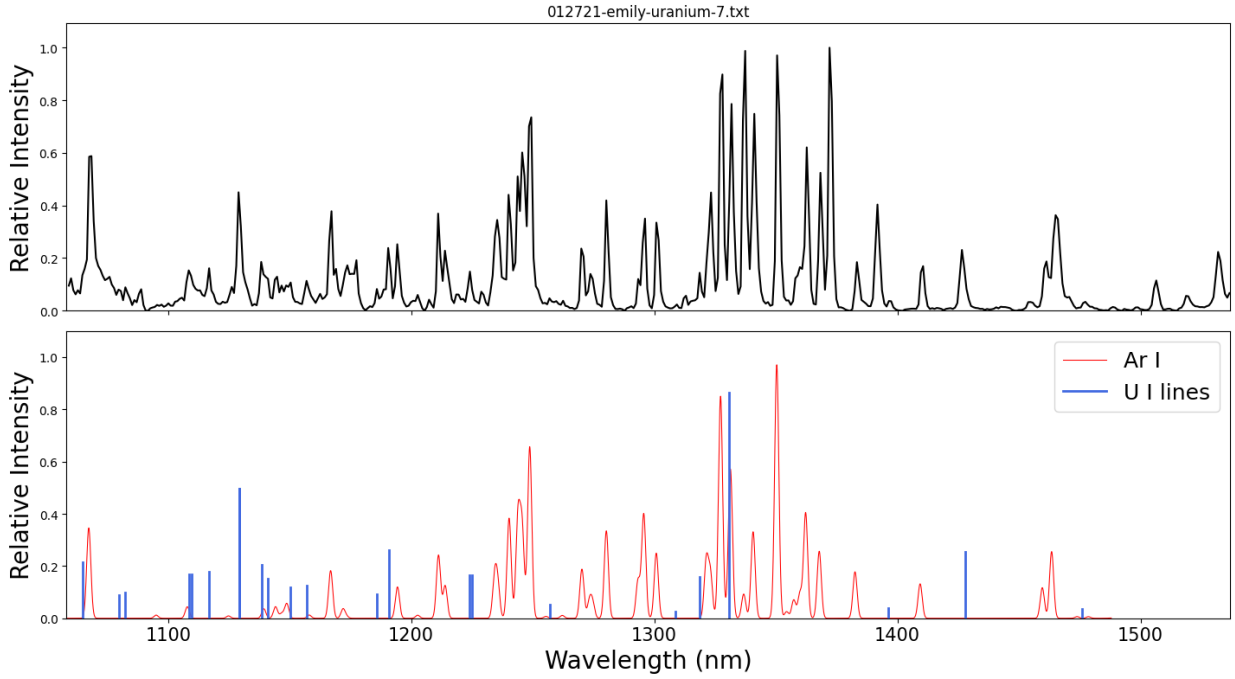
012721-emily-uranium-7.txt
Relative Intensity
Relative Intensity
Ar I
U I lines
1100
1200
1300
1400
1500
Wavelength (nm)

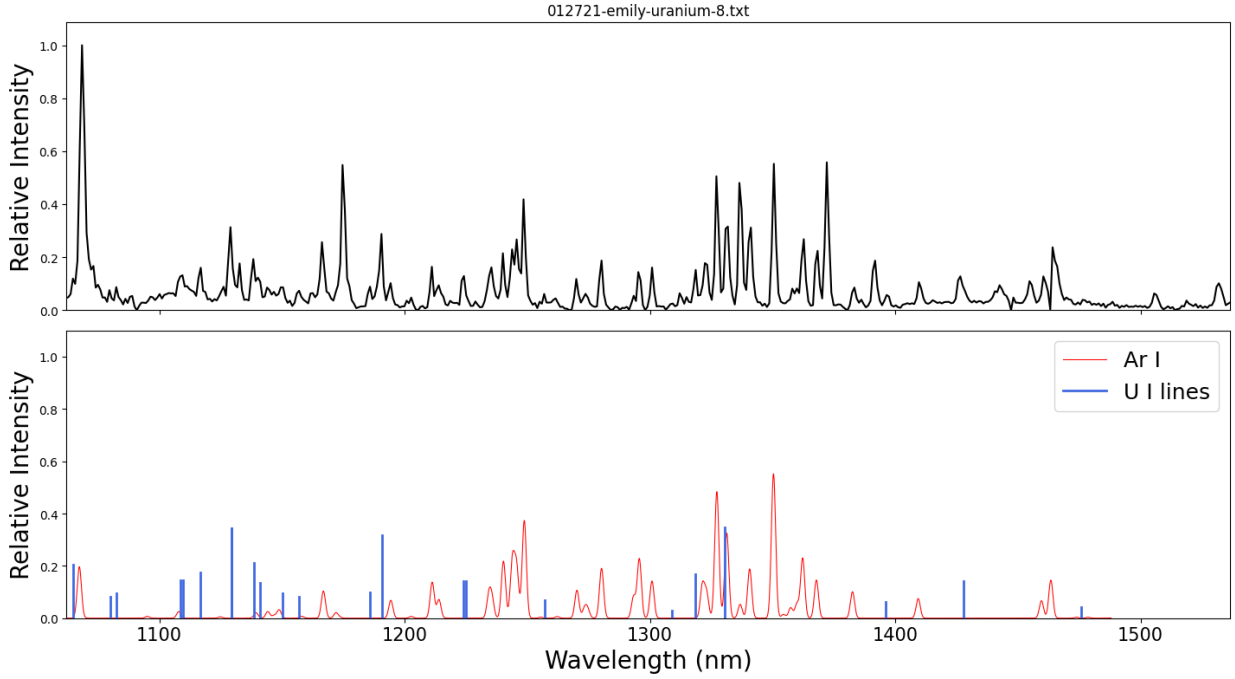
012721-emily-uranium-8.txt
Relative Intensity
Relative Intensity
Ar I
U I lines
1100
1200
1300
1400
1500
Wavelength (nm)

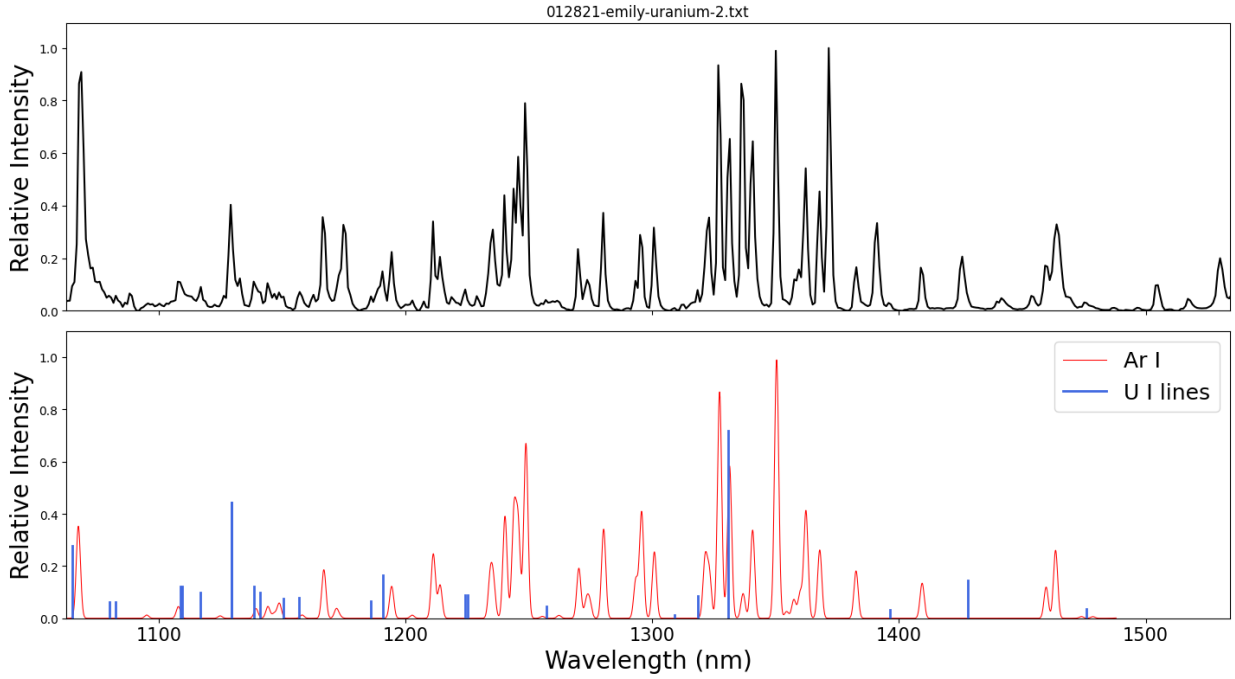
012821-emily-uranium-2.txt
Relative Intensity
Ar I
U I lines
Wavelength (nm)

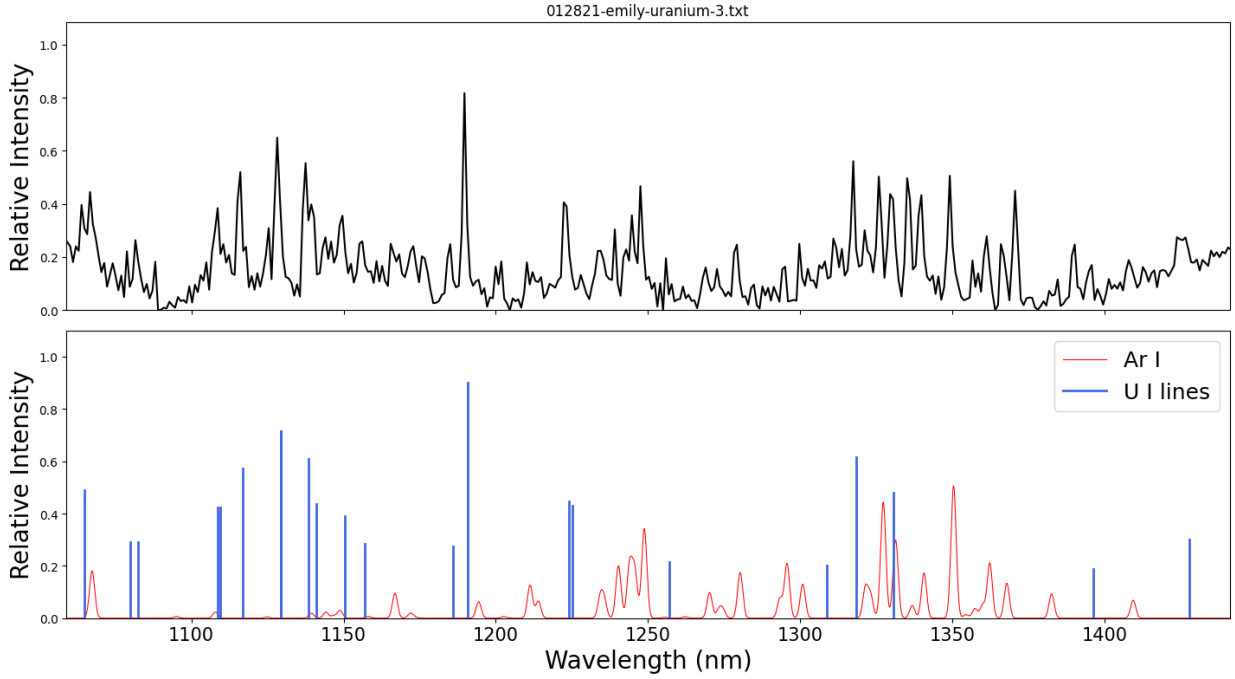
012821-emily-uranium-3.txt
Relative Intensity
Ar I
U I lines
Wavelength (nm)

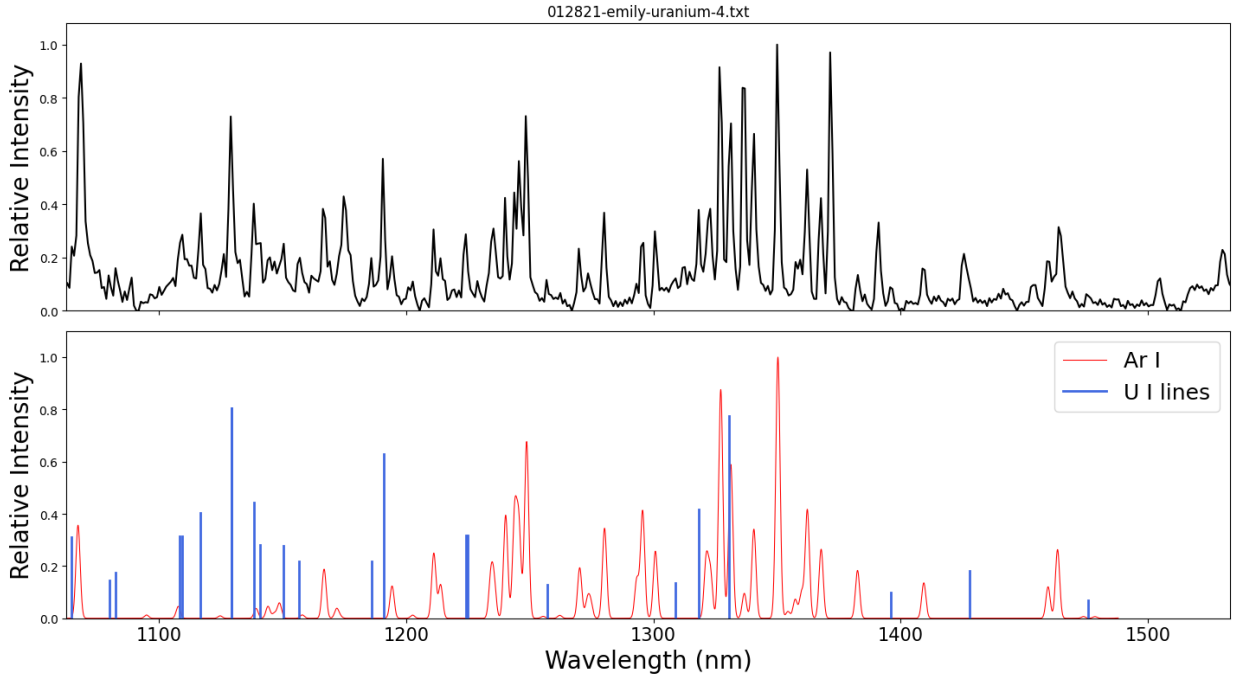
012821-emily-uranium-4.txt
Relative Intensity
Relative Intensity
Ar I
U I lines
1100
1200
1300
1400
1500
Wavelength (nm)

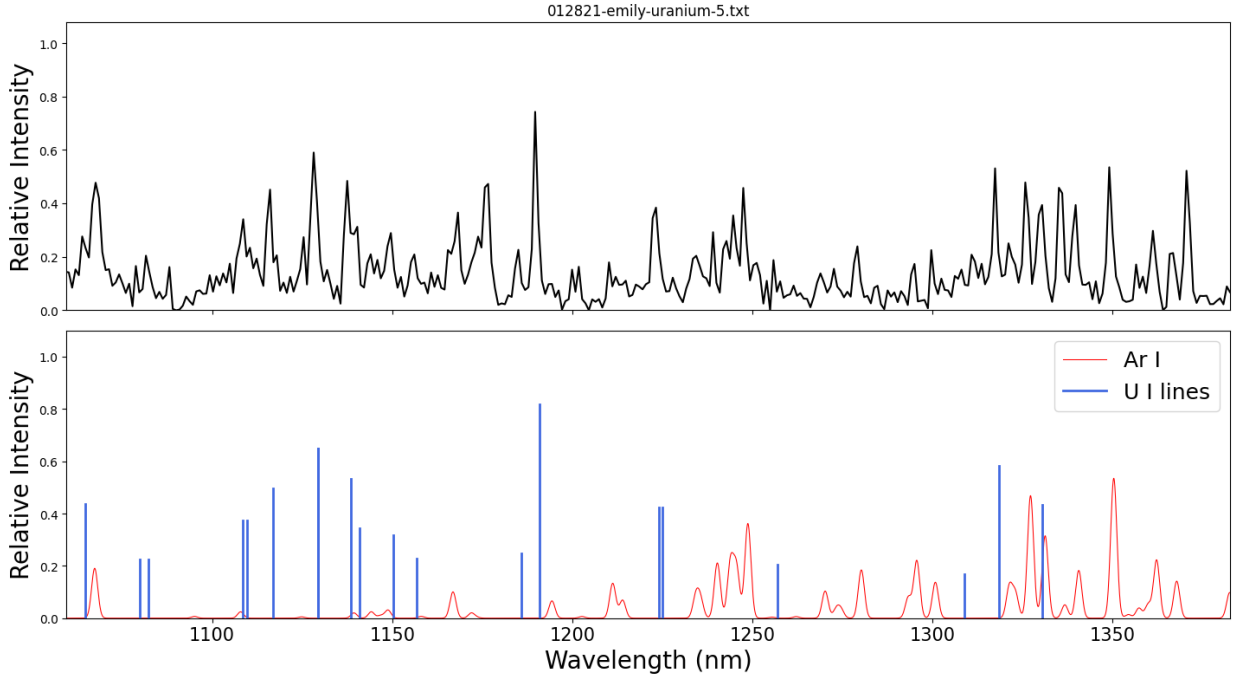
012821-emily-uranium-5.txt
Relative Intensity
Relative Intensity
Ar I
U I lines
1100
1150
1200
1250
1300
1350
Wavelength (nm)

A.3. Using NASA CEA for Shock Tube Calculations

Calculations for shock tube conditions were performed using the web-based interface of NASA CEA (Chemical Equilibrium with Applications), which is a program that determines theoretical equilibrium concentrations from given problem types and initial parameters [67]. Specific information on how calculation are performed are provided in documentation for the Gordon-McBride program [153], [154]. Instructions and discussion of its use in evaluating tests in this document are provided herein:

1. Go to https://cearun.grc.nasa.gov/.
2. Chemical Equilibrium Problem Types: Defines shock tube as the type of problem to be solved.
    a. Select Problem type, ‘shock’.
    b. Enter an alphanumeric code in the field provided if desired.
    c. Click Submit.

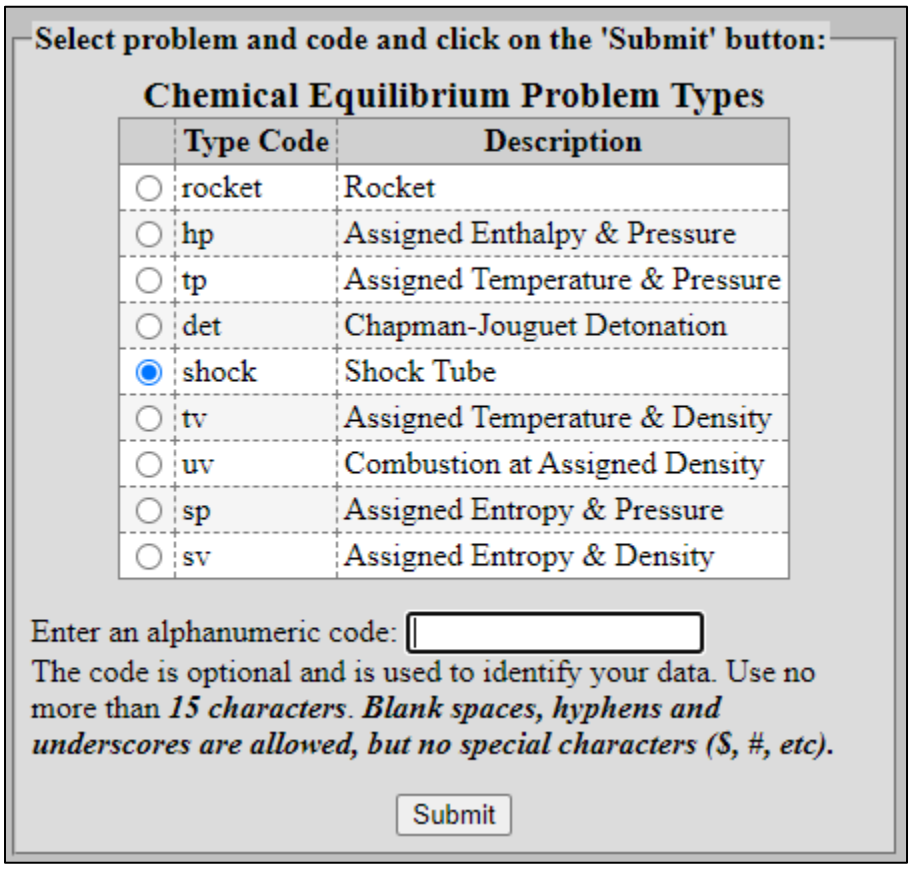

Figure A.1: Chemical Equilibrium Problem Types.

3. Parameters for Shock Problem: Shock parameters are outlined. These are measured experimentally.
    a. Enter the velocity of the shock wave. This can be determined by measuring the times at which the shock wave reaches two piezoelectric pressure transducers of known separation distance and calculating the resulting velocity.
    b. Enter the initial pressure of the driven section of the shock tube. This can be determined from conditions set during the test while factoring in an air leak rate from the room into the shock tube between initially setting the desired driven pressure and the shock wave being set off. The leak rate should be measured periodically as this may change over time with different fittings, etc.
    c. Enter the initial temperature of the driven section of the shock tube. Use the handheld Type K thermocouple to measure this prior to loading the shock tube. It should be room temperature unless the heating system is turned on. (*Note: the new heating system should feature a digital temperature readout, and this measurement can be used instead because it also features a Type K thermocouple.*)
    d. Multiple of each parameter can be input to do multiple calculations simultaneously if desired.
    e. Select the appropriate units, typically m/s, mmHg, and K.
    f. Accept Input and Continue to Next Form.

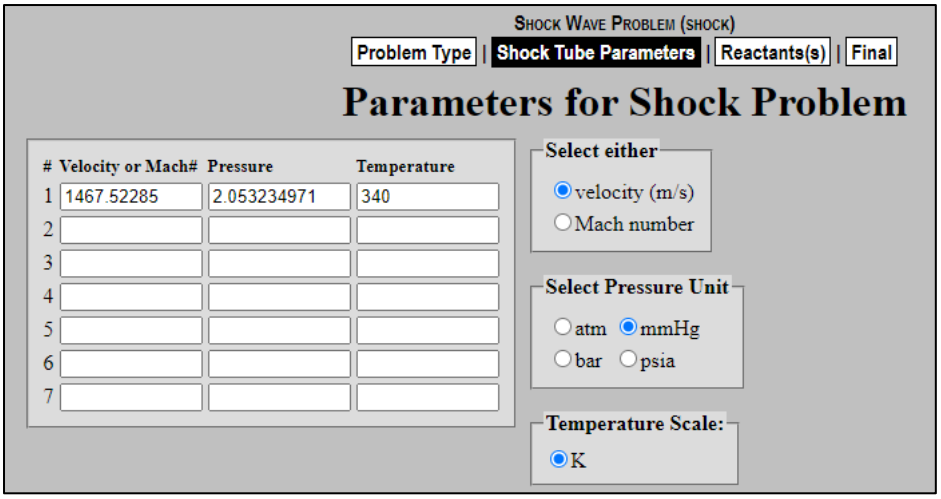

Figure A.2: Parameters for Shock Problem.

4. Select your reactant(s): Input the gases present in the driven section of the shock tube. For tests in this document, Argon was used as the driven gas, but N_2 and O_2 were also factored into calculations due to a small leak into the shock tube that would affect the eventual shock temperature. Theoretical shock temperature was found to be especially sensitive to the amount of O_2 present in the system.
    a. Specify the desired units (wt% or mole)
    b. If air is the only gas present in the driven section, select air and continue.
    c. If any other gases are used, select 'Use periodic table (mixtures)'.

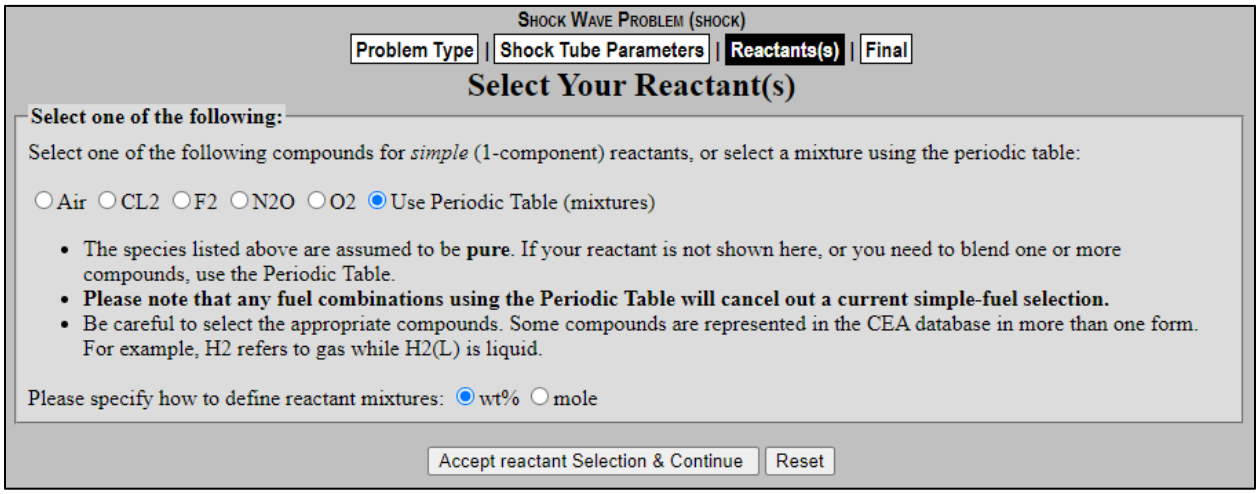

Figure A.3: Select Your Reactant(s).

5. Select Elements for your Reactants from the Periodic Table. NASA CEA features a database containing a multitude of potential reactants and draws necessary information for shock tube calculations from it.
    a. Select the elements appropriate for one of your constituents (i.e. N for N2, N and O for NO, etc.).
    b. Accept Element Selections and Continue to Next form.

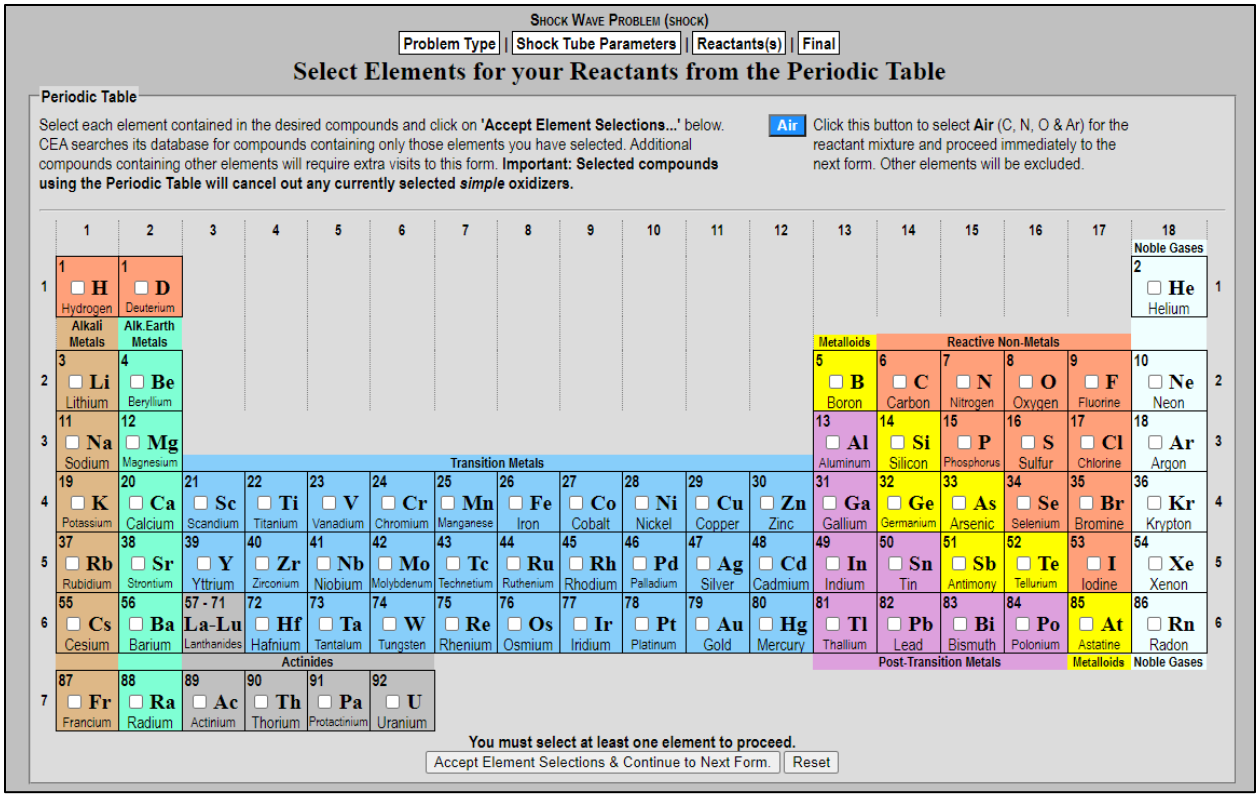

Figure A.4: Select Elements for your Reactants from the Periodic Table.

6. Select Your Fuel(s):
    a. Select the desired constituent(s).
    b. Accepted selected reactants and continue.

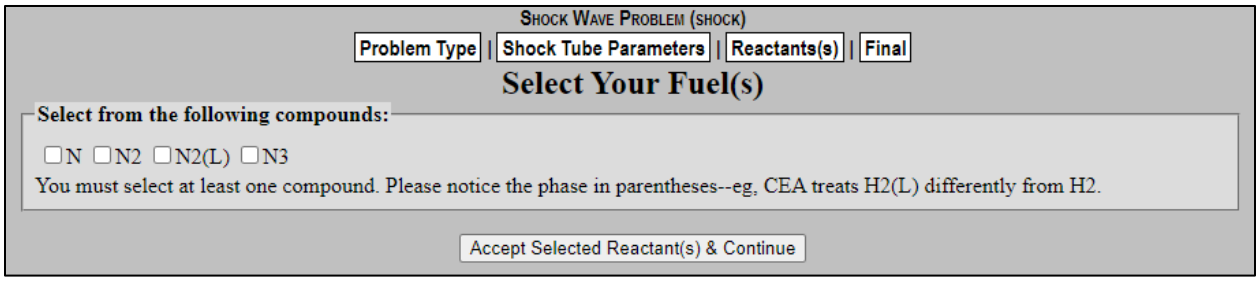

Figure A.5: Select Your Fuel(s).

7. You have selected these reactants:
    a. Check the box if more constituents are desired and repeat steps 5 and 6 for each constituent.

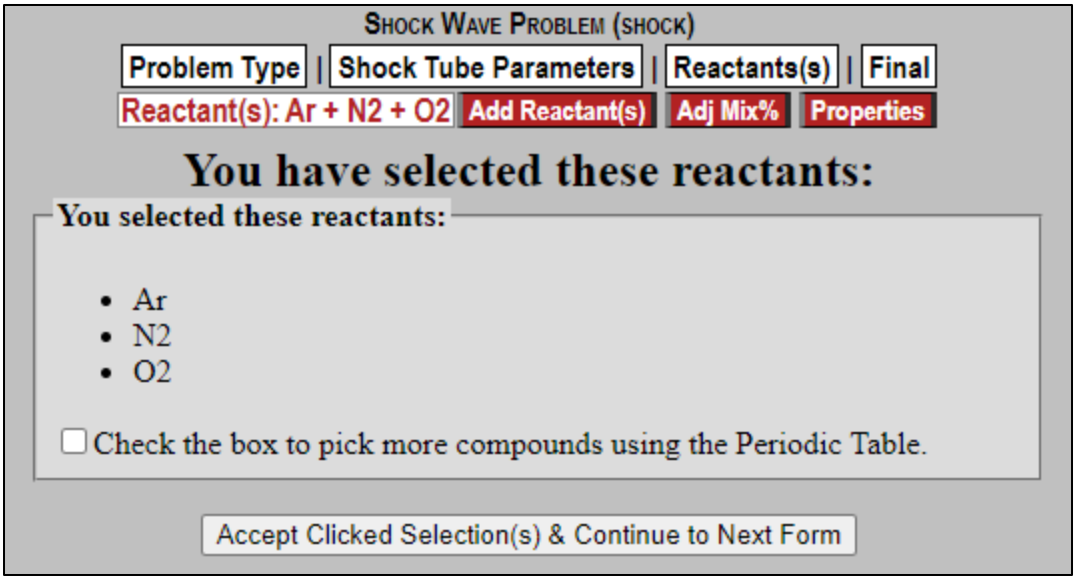

Figure A.6: You have selected these reactants.

8. Set Your Reactants(s) mix: Here, define the proportions of the initial constituents of the driven section after leak calculations (if you had multiple constituents). In this example, Ar was the desired fill gas with calculated O_2 and N_2 impurities from leak into the tube.
    a. Input proportions.
    b. Accept Input and Continue to Next Form.

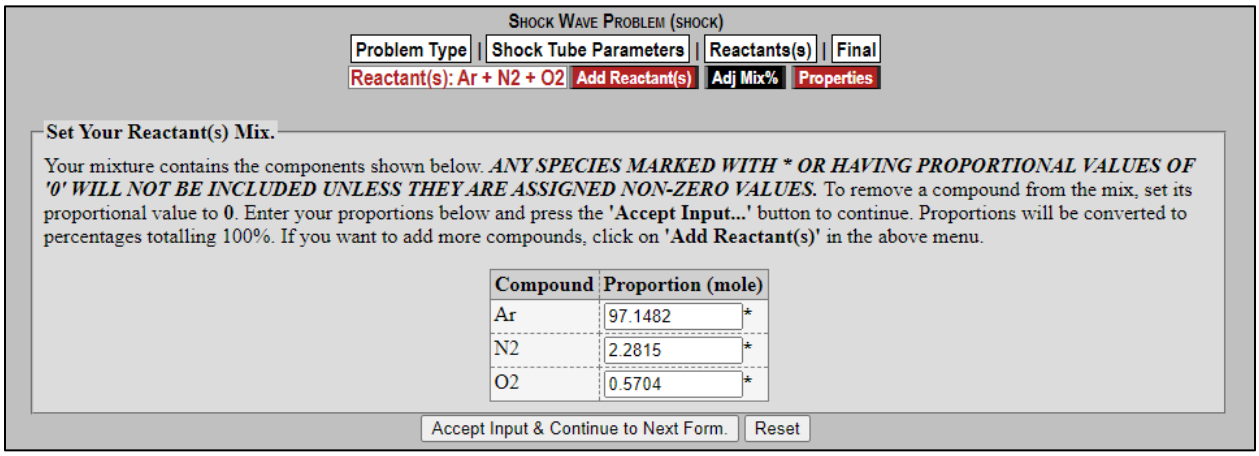

Figure A.7: Set Your Reactant(s) Mix.

9. It is likely, that there is no need to alter the 'Reactant Component Properties'. Advance through this page.
10. Enter Your Final Choices Before Running CEA: Define final parameters for calculation, such as whether to consider initial and reflected shock parameters, ionized species, etc.

a. Check ‘Set Trace Value’. Change 10^-**5** to 10^-**10**.
b. Check ‘Calculate Incident Shock Parameters?’
c. Check ‘Calculate Incident Shock Parameters?’ if shock tube is being used with end wall. (*Note: a dump tank end section can be used in tests which prevents reflected shock.*)
d. ‘Assume Equilibrium Compositions?’ should already be checked.
e. Choose desired units.
f. Submit input and Perform CEA Analysis.

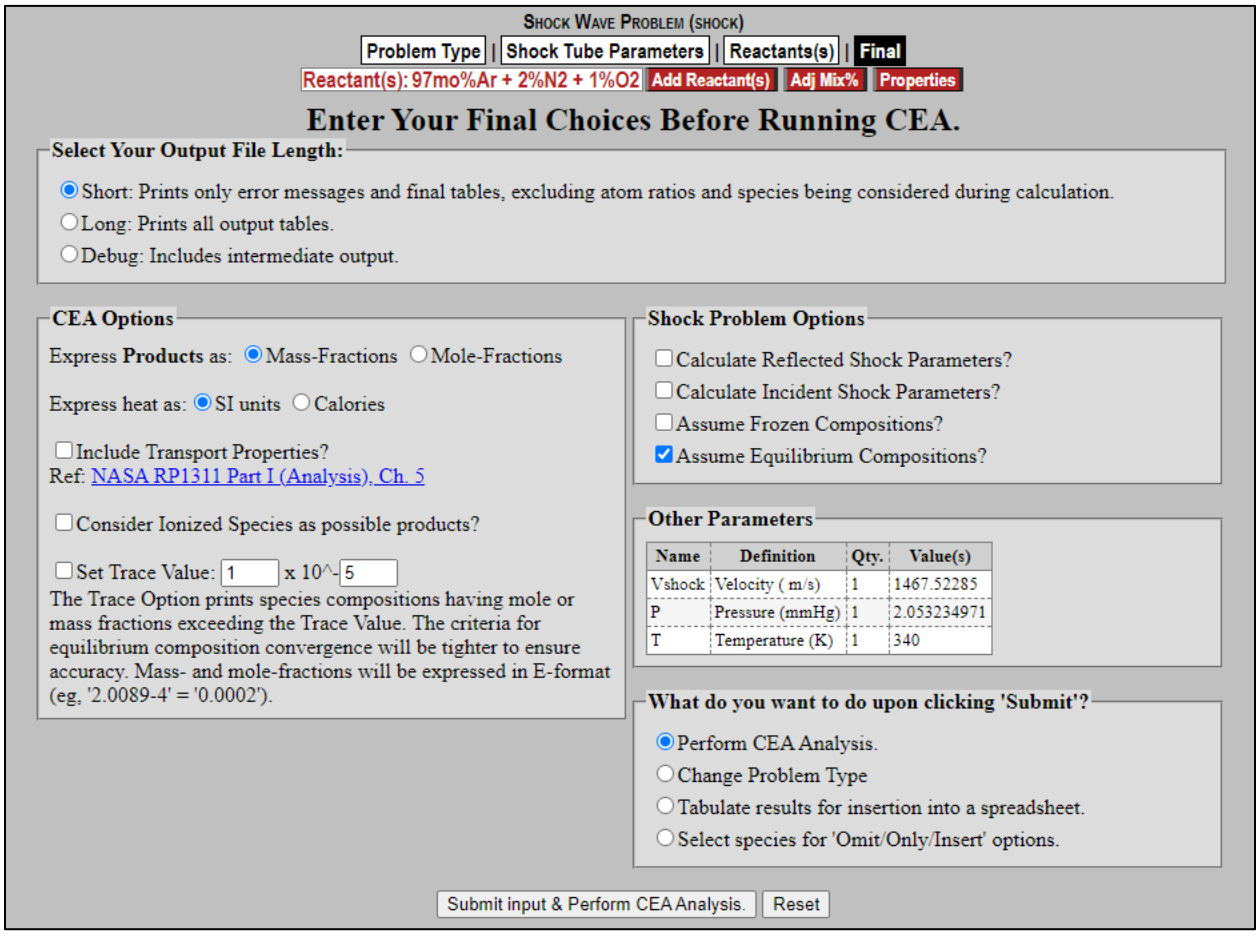

Figure A.8: Enter Your Final Choices Before Running CEA.

11. The calculated shock information and input parameters should be summarized on the next page, and a pdf of the output can be created.